SYNTHESIS AND APPLICATIONS OF NANOSTRUCTURED, MESOPOROUS ORGANOSILICA FILMS AND MONOLITHS

by

JENNY DU

A thesis submitted to the Department of Chemistry

in conformity with the requirements for

the degree of Doctor of Philosophy

Queen's University

Kingston, Ontario, Canada

May, 2011

Abstract

Surfactant-templated, sol-gel based methodologies for the synthesis of tailored, nanostructured, hybrid inorganic–organic materials are incredibly powerful and versatile. Although growth in this field has been explosive in recent decades, a lot of room remains to contribute to the design and synthesis of new materials, as well as the development of advanced applications.

In the work described herein, we firstly explored the synthesis of thick, mesoporous organosilica films and their application as functional coatings for solution-based, fibre-optic heavy metal sensors. Notably, sub-ppm level detection was observed for the detection of Pb(II) in mixed aqueous–organic media in short timeframes, and progress has been made toward synthesizing organotitania films that would allow for heavy metal sensing in purely aqueous solution. Furthermore, the utility of these types of surfactant-templated, organically-functionalized, mesostructured coatings has been preliminarily extended to other types of optical devices for heavy metal sensing.

We have also explored the use of designer amphiphilic, alkyl oligosiloxane precursors for the tightly-controlled formation of thin, self-templated, hybrid nanostructured films. Moreover, films bearing uniaxial 2D hexagonal alignment over macroscopic length scales were obtained using polymer-treated substrates to control the interfacial interactions between the film precursors and the substrate surface. In addition, a relatively mild UV / ozone treatment was employed to remove the alkyl moieties from the films to yield porous materials without catastrophic loss of the as-synthesized, mesostructural order.

Lastly, novel chiral, binaphthylene-based, periodic mesoporous organosilica (PMO) materials have been prepared. With the aim of demonstrating chiral recognition with such materials, porous, co-continuous capillary monoliths have been synthesized and applied as chiral stationary phases in nano-HPLC and CEC. Notably, enantioselective interactions between our materials and a chiral acetal-based analyte have been observed. Quantification of these enantioselective interactions in chiral PMOs by isothermal titration microcalorimetry is also being pursued.

It has thus been demonstrated that a wide array of different functional materials may be accessed through template-based synthetic strategies. By varying parameters such the starting monomers, the sol composition, and the interfacial interactions between reacting species and a given substrate (to name a few), the resulting materials may be tailored to meet the demands of new and emerging technologies.

Acknowledgements

"No act of kindness, no matter how small, is ever wasted." (Aesop)

It is somewhat challenging to definitively separate the 'academic' and 'personal' parts of my life and the people who have played significant roles in positively shaping my experiences, but one thing is certainly true: I have been incredibly fortunate to have received tremendous kindness and support from a wide and varied network of family, friends, mentors, colleagues, and peers. For all of this and more, I am humbled and sincerely grateful. From me to each and every one of you – a heart-felt THANK YOU.

With the practical limitations of space and time, it is not possible to individually acknowledge all of those who have contributed to my passage to this academic 'landmark'. However, there are some people to whom I owe special thanks:

- Prof. Cathleen Crudden – for taking a chance on a quirky student and providing me with all of the necessary tools and extraordinary opportunities to shape an amazing graduate experience. Your love and passion for your life's work have inspired all of us who have had the good fortune of working for you.
- Crudden Group members, in general (past and present graduate students, post-doctoral researchers, undergraduate students, and visiting researchers) – for making *every day* an awesome day to come to work. It has been an absolute pleasure to have shared this time learning, laughing, striving, and evolving alongside each other.
- Drs. Dave Edwards, Daryl Allen, Yonek Hleba, Pedro Montoya-Pelaez, Alex Blanc, Daisuke Imao, Stephanie MacQuarrie, and Abdel El-Kadib – for taking good care of me and for generously passing on all of your valuable wisdom.
- Dr. Judy Cipot-Wechsler, Dr. Steve Dickson, Jose Lobez, Marian Dreher, and Dr. Larbi Benhabib – for all of your contributions and dedication to the sensing project, without which we would not have made the strides that we did.

- Tom Blackburn – for laying down the groundwork for Chapter 4 of this thesis and for continuing to offer ideas from afar.
- Dr. Thomas Wood – for taking the hit on the resolution of BINOL as well as the Masuda Reaction so that I didn't have to on my own.
- The younger generation of Crudden Group members – for injecting new life and earnest into the lab and for keeping us 'oldies' on our toes. Looking forward to seeing all the great things you will accomplish in the years to come.
- Profs. Hans-Peter Loock, Robert Lemieux, and Richard Oleschuk – for making collaborative work such a joy. You've treated me as though I was one of your own students by enthusiastically offering your time, attention, and resources to helping me learn some of the tricks of each of your trades. The members of your labs have also warmly assisted me every step of the way and they deserve much thanks, too.
- Drs. Jack Barnes and Graham Gibson – for doing all of the dirty work on the sensing and chromatography projects, respectively. I couldn't have done any of it without your help.
- The research, technical, administrative, and support staff in the Department of Chemistry, as well as Dr. Louise Weaver (University of New Brunswick), Charlie Cooney (MECH), and Chelsea Elliott (PHYS) – for all of your 'behind the scenes' work, which makes it easier for the rest of us to do our jobs.
- Prof. Ralph Whitney – for your mentorship and guidance over all these years. I have appreciated all of your time and valued all of your input.
- Prof. Bill Newstead – for your love of teaching and for showing me what it means to embody the spirit of effective and meaningful teaching and learning.
- Prof. Kazyuki Kuroda and the Kuroda Group members (Waseda University, Japan) – for welcoming me into your lab, and for giving me the opportunity to enjoy such an incredible and memorable learning and life experience. You are Chapter 3's *raison d'être*.

- Prof. Kazuki Nakanishi, and Drs. Kazuyoshi Kanamori and George Hasegawa (Kyoto University, Japan) – for sharing your knowledge and for your kind and generous support with respect to the synthesis of silica-based monoliths, without which there wouldn't be much to speak of in Chapter 4.
- DE and Jonathan Webb – for your ever curious and inquisitive natures, which inspire creativity and purpose in all those who surround you. You have worked tirelessly to enliven the best scientists in all of us.
- Dr. Jeremy Praetorius, Dr. Mark Mohamed, Vivian Yates, and Michael Lockett – for your camaraderie over countless mornings spent running along the lakefront. There is no better way to kick start each new day.
- SD and Ben Glasspoole – for making our bay an AWESOME good time, and for being like brothers to me.
- 'Goats', 'Froggies', 'Roast Beefs', '346 ½-ers', 'Sitbpeegohn', 'Goodlifers', 'Climbing Crew', 'QVB and PEC Crew', 'Gladiators', 'FMA-ers', 'Cowtowners' and related posse members near and far – for keeping me sane and for always cheering me on.
- My family – for giving me the freedom and encouragement to go down this road, despite this whole 'grad school thing' being kind of a giant mystery to you.
- Rob Hobden – for your selfless and unwavering support of my goals and endeavours, and for standing by me through all of it. *"If I know what love is, it is because of you."* (Harold Hesse)

Statement of Originality

I hereby certify that all of the work described within this thesis is the original work of the author. Any published (or unpublished) ideas and/or techniques from the work of others are fully acknowledged in accordance with the standard referencing practices.

Jenny Du

May 2011

Table of Contents

Abstract ii
Acknowledgements iv
Statement of Originality vii
Table of Contents viii
List of Schemes xii
List of Figures xvi
List of Tables xxv
List of Appendices xxvi
List of Abbreviations, Symbols, and Units xxvii
Chapter 1 Introduction 1
1.1 General 1
1.2 Sol-Gel Chemistry and the Synthesis of Amorphous, Porous Silicas 2
1.3 Surfactant-Templated Mesoporous Silicas 8
1.4 Objectives of This Thesis 21
1.5 References 23
Chapter 2 Surfactant-Templated, Mesoporous Organosilica Films as Functional Overlays for Fibre-Optic Heavy Metal Detection 28
2.1 Introduction 28
2.2 Amorphous Organosilica Sol-Gel Films 42
2.3 Surfactant-Templated Mesporous Organosilica Sol-Gel Films 51
2.3.1 First Generation Pluronic® F127-Templated Materials 54
2.3.2 Brij® 56-Templated Thiol-Functionalized Films, High-Index Tetrasulfide Films, and Preliminary Hg(II) Sensing 56
2.3.3 Tetrasulfide-Functionalized Brij® 56-Templated Films for Pb(II) Sensing 71
2.3.4 Improving the Reproducibility of Film Synthesis and Second Generation F127-Templated Tetrasulfide-Functionalized Films for ppb-Level Pb(II) Detection 73
2.3.5 Pb(II) Sensing in Mixed Metal Solutions 91
2.3.6 Mesoporous Tetrasulfide-Functionalized Titania Films for Pb(II) Sensing in Purely Aqueous Solution Systems 94
2.3.7 Organically-Modified Mesoporous Films as Functional Coatings for Silicon-on-Insulator (SOI) Microchip Sensing Devices 103

2.4 MZ (Mach–Zehnder)-Type Tapered Fibre Interferometers 109
2.5 Future Work 112
2.6 Conclusions 114
2.7 Experimental Procedures 116
2.7.1 General and Materials 116
2.7.2 Substrate Preparation / Activation 118
2.7.3 MPTMS Monolayers and Thin Multilayers 119
2.7.4 TEOS–MPTMS Xerogel Films 119
2.7.5 Polysilsesquioxane Xerogel Films 121
2.7.6 First-Generation Pluronic® F127-Templated Materials 122
2.7.7 Brij® 56-Templated Functionalized Films 123
2.7.8 High-Index Tetrasulfide Films 124
2.7.9 Second-Generation Pluronic® F127-Templated Materials 125
2.7.10 Titania-Based Films 126
2.7.11 Determination of Heavy Metal Concentration in Test Solutions Using Standard Analytical Techniques 128
2.7.12 LPG Calibration and Metal Sensing 129
2.7.13 SOI Microchip Calibration and Metal Sensing 130
2.7.14 Characterization Techniques 132
2.8 References 133
Chapter 3 Uniaxially-Aligned, Mesostructured Films from the Self-Assembly of Amphiphilic, Oligomeric Organosiloxane Precursors 150
3.1 Introduction 150
3.2 Alignment Control of Self-Assembled Nanohybrid Films 155
3.3 Introduction of Porosity Using UV / Ozone Treatment 169
3.4 Improving the Efficacy of Alkyl Chain Removal 176
3.5 The Accommodation of Guest Molecules within the Aligned Films 179
3.6 Chiral, Oligomeric Organosiloxanes 182
3.7 Conclusions and Future Work 186
3.8 Experimental Procedures 187
3.8.1 General and Materials 187
3.8.2 Alkyl Organosiloxane Precursor Synthesis 188
3.8.3 Preparation of Rubbing-Treated Substrates 190

3.8.4 Nanohybrid Film Synthesis 190
3.8.5 Removal of Alkyl Moieties from 2D Hexagonally-Ordered Films 191
3.8.6 Incorporation of TEOS, TTIP, and Organic Guest Molecules 191
3.8.7 Chiral Organosiloxane Precursor Synthesis 193
3.8.8 Characterization Methods 196
3.9 References 196
Chapter 4 Probing Chiral Recognition in Chiral Binaphthylene-Based Periodic Mesoporous Organosilica Powders and Monoliths 205
4.1 Introduction 205
4.1.1 Periodic Mesoporous Organosilicas (PMOs) 205
4.1.2 Chirality Transfer in PMOs 208
4.1.3 Monoliths and Capillary Chromatography 219
4.2 Biphenylene-Based PMO Capillary Monoliths 222
4.3 Chiral Binaphthylene-Doped PMO Capillary Monoliths 231
4.4 Problems with Capillary PMO Monolith Stability in Solution 233
4.5 Nano-HPLC and Continued Problems with Capillary Monolith Shrinkage 236
4.6 Improving the Hydrolytic Stability of Capillary PMO Monoliths 239
4.7 Capillary Electrochromatography 247
4.8 Probing Chiral Recognition by Isothermal Titration Microcalorimetry 250
4.9 Conclusions and Future Work 264
4.10 Experimental Procedures 266
4.10.1 Materials 266
4.10.2 Synthesis of Chiral Binaphthyl Monomer, 2 267
4.10.3 Synthesis of Chiral Acetal Analyte, 3b 267
4.10.4 Fused Silica Capillary Activation 267
4.10.5 100% BTESBP Capillary PMO Monolith Preparation (T_{gel} = 60 °C) 269
4.10.6 Chiral Capillary PMO Monolith Preparation 271
4.10.7 Post-Synthetic Solution Exposure 272
4.10.8 Incorporation of Sol Additives 272
4.10.9 Nano-HPLC and CEC Trials 274
4.10.10 Microcalorimetry Trials 276
4.10.11 Characterization Methods 277
4.11 References 278

Chapter 5 Conclusions 290
Appendix A 294

List of Schemes

Scheme 1-1. Typical inorganic precursors and organosilanes (where X = Cl or OR, and R = Me or Et) used in the sol-gel syntheses of metal oxides and functionalized metal oxides. 4

Scheme 1-2. Some examples of organically-bridged bis-silanes for the synthesis of polysilsesquioxanes (where R = Me, Et). 7

Scheme 1-3. Schematic representation of typical micellar mesophases (from left to right): spherical, rod-like / cylindrical, lamellar / bilayer, inverse spherical, bicontinuous, vesicular. (Scheme taken from reference 9.) 9

Scheme 1-4. Formation of mesoporous silica via a lyotropic liquid crystalline pathway (Pathway A) or a cooperative self-assembly pathway (Pathway B). (Scheme adapted from reference 13.) 10

Scheme 1-5. Schematic representation of a surfactant molecule and the variables involved in the calculation of the surfactant packing parameter (*g*-parameter). (Scheme taken from reference 9.) 12

Scheme 1-6. Typical examples of anionic (SDS = sodium dodecylsulfate), cationic (C_{16}TAB = cetyltrimethylammonium bromide), and nonionic (DA = dodecylamine; F127 = Pluronic®-type nonionic triblock copolymer; B76 = Brij®-type alkyl polyether) surfactants used to template mesoporous sol-gel materials. 14

Scheme 1-7. Schematic representation of the different types of interfacial metal oxide–surfactant interactions taking place in various surfactant-templated systems (where typically the inorganic M = a metal such as Si or Ti). (Scheme taken from reference 9.) 15

Scheme 1-8. Schematic representation of the difference in the distribution of organic groups between typical organically-functionalized mesoporous silica (synthesized by post-synthetic grafting or co-condensation) (left) and periodic mesoporous organosilica (PMO) (where the functionality is embedded in the framework walls) (right). 19

Scheme 1-9. Schematic representation of the formation of FSM-type materials. (Scheme taken from reference 30.) 21

Scheme 2-1. Examples of modified pyrene- (1),[8] calixarene- (2),[9] and heteroatom-substituted crown-type[10] (3) fluorescent probes developed for the detection of Hg(II) ion in solution. 31

Scheme 2-2. Schematic representation of a long-period grating (LPG) inscribed into the core region of a fibre-optic waveguide. At the LPG, the propagating core mode (red) couples (i.e. overlaps) with a higher order cladding mode (blue), which can extend past the cladding–film

interface if the fibre-optic waveguide is coated with an index-matched film at this location. 33
Scheme 2-3. Schematic representation of the various steps involved in the synthesis of mesostructured films by EISA. (Scheme taken from reference 30.)..... 39
Scheme 2-4. Schematic representations of all of the main condensable sol-gel precursors used in the work described in this chapter, along with their acronyms and the refractive indices of each precursor (reported at the sodium D-line wavelength of 589 nm at 20 °C) in its uncondensed state. 43
Scheme 2-5. Schematic representation of the refractometer set-up used for the determination of silica and organosilica film RIs. The path of the laser light (indicated in dark grey) is expanded and focused with a series of mirrors and lenses, respectively. At the CCD detector, part of the screen is illuminated, while another part of the screen is not illuminated (as indicated by the blank / 'white' path). The position of the boundary between the illuminated and non-illuminated regions of the CCD read-out is correlated to the RI of the sample film. (Scheme taken from reference 46b.) 46
Scheme 2-6. Nonionic, polymeric templates used in this project. 54
Scheme 2-7. Schematic representation of a cross-sectional view of the sensing window of a silicon photonic wire waveguide device (image taken from reference 100c). The isolation layer may be composed of SU-8 photoresist or dense silica. 105
Scheme 2-8. Schematic representation of a MZ-type tapered fibre interferometer, showing two tapers of specific length and diameter separated by a distance, *L*, along a single-mode fibre-optic waveguide (SMF). (Image taken from reference 103.)..... 111
Scheme 3-1. Schematic representation of 2D hexagonally-ordered films bearing (a) poor in-plane alignment (i.e. 'polycrystalline-like') and (b) coherent in-plane alignment (i.e. 'single crystalline-like'). (Scheme taken from reference 17.) 151
Scheme 3-2. Preparation of macroscopically oriented, mesostructured films by: (i) hydrolysis of the precursor, C*n*; (ii) dip-coating of the hydrolyzed solution onto a rubbing-treated substrate; and (iii) self-assembly and polycondensation of the amphiphilic hydrolyzed species. The white arrow on the substrate indicates the rubbing direction. 154
Scheme 3-3. Synthesis of C*n* precursors from the corresponding alkyltrichlorosilane. 156
Scheme 3-4. Schematic representation of the various axes manipulated in out-of-plane and in-plane XRD experiments (taken from reference 29b). 158

Scheme 3-5. Schematic representation of the 2D hexagonal mesostructure and the diffraction information obtained in the case of (a) out-of-plane XRD, and (b) in-plane XRD (where q = diffraction vector). (Scheme taken from reference 29a) 158
Scheme 3-6. Illustration of the arrangements of hydrolyzed C*n* molecules in the (a) C*10* and (b) C*16* systems near the film–air interface (top) and substrate–film interface (bottom) viewed from the direction normal to the rubbing direction. 168
Scheme 3-7. In-situ ligand exchange to generate a less-reactive titania precursor. 178
Scheme 3-8. Synthesis of chiral, oligomeric organosiloxanes. Reaction conditions are summarized as follows: (i) $[PdCl(\eta^3\text{-}C_3H_5)]_2$, L*, neat, 40 °C, 2 h; (ii) H_2O, aniline, THF / Et_2O, 0 °C, 2 h, then crystallization in hexane; (iii) $SiCl_4$, hexane / THF; (iv) MeOH, pyridine, hexane; (v) NaH, THF, 45 °C, 48 h; (vi) $H_2PtCl_6{\cdot}6H_2O$ in ACN, and neat at 70 °C for 2 h (Route B), or in toluene at 50 °C for 18 h (Route C); (viii) $(C_2H_5)_2NOH$, EtOH, toluene, room temperature, 16 h. 184
Scheme 4-1. Bis-silylated silsesquioxane monomers used in some of the first reported syntheses of PMO materials. 207
Scheme 4-2. Examples of binaphthyl-based ligands commonly used in metal-catalyzed asymmetric transformations. 209
Scheme 4-3. Axially chiral, bis-silylated monomers designed by the Crudden research group (1, 2, and 3a). The chiral precursor to 3a (3b) was used in this work as a test analyte for chiral capillary chromatography (chiral centers marked by *). 211
Scheme 4-4. Schematic representation of the separation of two peaks (species A and B) at three different resolutions (R_S) and the corresponding chromatographic parameters included in the calculation of R_S. (Scheme taken from reference 26.) 214
Scheme 4-5. Organosilane precursors used in some of the first examples of monolithic organosilica materials prepared by spinodal decomposition (i.e. polymerization-induced phase separation). 221
Scheme 4-6. Protocol and timing of individual steps in the synthesis of PMO capillary monoliths. 224
Scheme 4-7. Ternary phase diagram (left) (with 0.025 mL of 1 M $HNO_{3(aq)}$ as a constant across all sols) showing the variation in the F127 content. An enlarged image of the data points is also shown (right). 227

Scheme 4-8. Ternary phase diagram (with 0.025 mL of 1 M $HNO_{3(aq)}$ as a constant across all sols) showing the variation in the solvent (i.e. DMA) content. 229
Scheme 4-9. Auxiliary reagents added to the BTESBP-based PMO capillary monolith sols with the aim of minimizing monolith shrinkage (where V88 is the radical initiator for the thermally-induced free radical polymerization of the methacrylate groups of γ-MAPS). ... 242
Scheme 4-10. Schematic representation of the MicroCal® VP-ITC instrumental set-up. (a) The system monitors the difference in temperature between the sample cell and the reference cell, as well as the difference in temperature between the reference cell and the surroundings. Power is delivered to or retracted from the sample cell in response to the addition of the syringe reactant (which is usually a solution of the analyte of interest) in order to maintain both the sample cell and the reference cell at the same temperature. (b) The syringe reactant (i.e. a solution of the analyte of interest) is injected into the sample via the action of a stepper motor, and a propeller-style stirrer extends from the syringe into the sample cell medium to promote continuous mixing of the contents of the sample cell. (Both images taken from reference 71.) 252
Scheme 4-11. Amino acids used as analytes in the isothermal titration microcalorimetry experiments. 256
Scheme 4-12. Synthetic route for the preparation of chiral monomer 3a. (Scheme courtesy of Dr. Steven Dickson, Queen's University.) 262
Scheme 4-13. Schematic representation of hydrobenzoin. 263

List of Figures

Figure 1-1. TEM images of surfactant-templated, porous silica materials bearing different mesostructural order: (a) 2D hexagonal (*p6mm*); (b) cubic [100] (*Fm3m*); (c) cubic [100] ($Pm\overline{3}n$) (images taken from references 15a, , and , respectively.) 11

Figure 1-2. Examples of surfactant-templated silica-based mesoporous materials synthesized with different morphologies: (a) silica nanowires; (b) silica nanocubes; (c) benzene-bridged organosilica spheres; and (d) silica-based inverse opals. (Images taken from references , , , and , respectively.) 18

Figure 2-1. Representative attenuation spectra for a standard single-mode fibre (SMF) in air (black trace) in comparison to an LPG-inscribed, cladding-etched SMF (grating length = 25 mm, periodicity = 320 μm) under exposure to air (green trace) and water / DMSO solutions (RI at 1550 nm) (blue and red traces). The blue-shift of the resonant peak with increasing RI of the surrounding environment is indicated by the dashed lines. (Data courtesy of Prof. Hans-Peter Loock, Queen's University.) 34

Figure 2-2. A plot illustrating the non-linear resonant peak shift behaviour for the bare, uncoated LPG of Figure 2-1 as a function of the RI of the surrounding environment. (Data courtesy of Prof. Hans-Peter Loock, Queen's University.) 35

Figure 2-3. A sample of the screen read-out obtained using the software (written by Mr. Nick Trefiak, formerly of Queen's University) coupled to the refractometer. The captured image (left) is vertically binned and the first derivative of the image intensity is taken and displayed (right). The software computes and outputs the pixel at which the turning point in the derivative plot occurs (bottom left). Given the parameters for the calibration of the instrument (bottom right), the pixel position is translated into a value for the RI of the sample sitting on top of the refractometer prism. The image displayed, here, is for a sample solution composed of 60 vol% DMSO in water at a laser wavelength of 589 nm. (Image taken from reference 46.) 47

Figure 2-4. Two different CCD camera images recorded for a the same xerogel film sample (25 mol% MPTMS co-condensed with TEOS, prepared in a sol using *t*-BuOH as the solvent) aligned slightly differently on the refractometer prism. 48

Figure 2-5. TEM images of (a) MCM-41 and (b) SBA-15, displaying the honeycomb mesostructure typically observed for these 2D hexagonally-ordered materials. These images were taken from references 50b and 51a, respectively. 52

Figure 2-6. 3D renderings of (a) rhombohedral $R\bar{3}m$ (distorted face-centered cubic $Fm\bar{3}m$), (b) 2D rectangular *c2mm* (distorted 2D hexagonal *p6mm*), (c) distorted double-gyroid (distorted cubic $Ia\bar{3}d$), and (d) lamellar mesoporous silica films (siloxane framework shown in green) on support (grey substrate). (Images taken from reference 54b.) 53

Figure 2-7. Binary phase diagrams for (a) Pluronic® P123 and (b) Pluronic® F127 nonionic block copolymers in aqueous solution. Note the relatively large area occupied by the hexagonal phase in the case of the P123 block copolymer, and the greater occurrence of a cubic phase with the F127 block copolymer. (Both plots taken from reference 56.) 53

Figure 2-8. Nitrogen isotherm and pore size distribution (inset, BJH desorption branch) for a solvent-extracted 20 mol% APTES / 80 mol% TEOS organosilica material templated with B56. 57

Figure 2-9. Pore size distribution plots (BJH desorption branch) for porous 5 mol% MPTMS / 95 mol% TEOS bulk materials templated by B56 without (open circles) and with (black triangles) ammonia vapour treatment prior to solvent extraction of the templating agent. ... 60

Figure 2-10. Nitrogen isotherms for porous 5 mol% MPTMS / 95 mol% TEOS bulk materials templated by B56 without (open circles) and with (black triangles) ammonia vapour treatment prior to solvent extraction of the templating agent. 60

Figure 2-11. Modeled effective RIs of different linearly polarized (LP) modes for varying thicknesses of an LPG overlay with an RI of 1.58. (Image taken from reference 19.) 63

Figure 2-12. Plot of the film thicknesses of layer-by-layer spin-coated, high-RI, 100% BTESPTS films (prepared without the use of any templating agent) as a function of the number of deposited layers. 65

Figure 2-13. A photograph of layer-by-layer spin-coated, high-RI, 100% BTESPTS films (prepared without the use of any templating agent) with one (blue), two (yellow), three (magenta), and four (green) accumulative layers. 65

Figure 2-14. Calibration curves for an etched LPG (both in its bare (black trace) and coated state (red and blue traces)) (Λ = 320 μm, grating length = 25 mm) showing the resonant peak shifts as a function of the RI of the surrounding water / DMSO solution. Two Hg(II) sensing trials were conducted using the same 2.5 mol% MPTMS / 97.5 mol% TEOS coating on the

LPG in mixed water / DMSO solutions of RIs indicated by the dashed lines (red and blue dashed lines for Trials #1 and #2, respectively)..... 68
Figure 2-15. Plot of the resonant peak shifts for a 2.5 mol% MPTMS / 97.5 mol% TEOS coating on an LPG as a function of the Hg(II) concentration in water / DMSO solutions with an RI of 1.33 (at 1550 nm)..... 70
Figure 2-16. Plot of the resonant peak shifts for a 2.5 mol% MPTMS / 97.5 mol% TEOS coating on an LPG as a function of the Hg(II) concentration in water / DMSO solutions with an RI of 1.36 (at 1550 nm)..... 70
Figure 2-17. Two different TEM images of the same thick, solvent-extracted 5 mol% BTESPTS (Si basis) / 95 mol% TEOS film templated by B56 showing the occurrence of mixed mesophases throughout the material. In particular, (a) 2D hexagonally-ordered and (b) amorphous regions can be observed. 73
Figure 2-18. Plot of as-synthesized film thicknesses for both spin- and dip-coated films prepared on glass microscope slides (open circles and opaque triangles, respectively). The sol composition was 9 mol% BTESPTS (Si basis) / 1 mol% TTIP / 90 mol% TEOS with F127 as the templating agent. The films were prepared in an atmosphere with RH = 50%. 76
Figure 2-19. Nitrogen isotherm and pore size distribution curves (insets) for a large batch of solvent-extracted, scraped PMO films. 81
Figure 2-20. TEM image of the porous, solvent-extracted PMO film displaying a uniform wormhole-type mesostructure..... 83
Figure 2-21. EDX sum spectrum of the solvent-extracted PMO film sample dispersed onto a carbon-coated copper grid..... 83
Figure 2-22. (a) HAADF-STEM image of the solvent-extracted PMO film sample, and chemical maps showing the distribution of (b) Si, (c) Ti, and (d) S in the sample. 84
Figure 2-23. Calibration of an LPG-inscribed fibre-optic waveguide (both in uncoated and coated states) with water / DMSO solutions of increasing RI, noting the shift to lower RI (~ 1.40 at 1550 nm) and broadening of the RI-sensitive region that accompanies coating of the grating with the PMO film. 86
Figure 2-24. Optical response for an LPG coated with the PMO film to aqueous DMSO solutions (RI = 1.402 at 1550 nm) of Pb(II) of increasing concentration as observed by the LPG attenuation spectra and by the shift in the resonant peak position as a function of solution concentration (inset)..... 87

Figure 2-25. A plot of the shifts in the resonant wavelength position for a PMO-coated LPG relative to the peak for the blank solution as a function of exposure to aqueous DMSO solutions (RI = 1.402 at 1550 nm) of increasing Pb(II) concentration. 87
Figure 2-26. No resonant peak shifts were observed in the attenuation spectra recorded for a PMO-coated LPG exposed to aqueous DMSO solutions (RI = 1.387 at 1550 nm) of increasing $NaNO_3$ concentration. 90
Figure 2-27. No resonant peak shifts observed in the attenuation spectra recorded for an uncoated LPG exposed to aqueous DMSO solutions (RI = 1.358 at 1550 nm) of increasing Pb(II) concentration. 90
Figure 2-28. Accumulative resonant peak shifts observed upon repeated exposure of the PMO film–LPG system to aqueous DMSO solutions (RI = 1.402 at 1550 nm) of 10 ppm Pb(II) in alternation with exposures to blank solutions. 91
Figure 2-29. Attenuation spectra for the PMO-coated LPG in a mixed metal solution (RI = 1.402) containing 1 ppm each of Cd(II), Co(II), Ni(II), Fe(III), and Zn(II) both with (blue trace) and without (red trace) added Pb(II) (also at a concentration of 1 ppm). No peak shift is observed relative to the metal-free blank (black trace). 92
Figure 2-30. Attenuation spectra for the PMO-coated LPG in a mixed metal solution (RI = 1.402) containing 10 ppm each of Cd(II), Co(II), Ni(II), Fe(III), and Zn(II) both with (blue trace) and without (red trace) added Pb(II) (also at a concentration of 10 ppm). No peak shift is observed for the PMO-coated LPG in the mixed metal solutions relative to the metal-free blank (black trace), however, a response to a 10 ppm solution of Pb(II) alone (without acid treatment after exposure to the mixed metal solution) results in a blue-shift in the resonant peak position (green trace). 93
Figure 2-31. Optical response for an LPG coated with a solvent-extracted, tetrasulfide-functionalized titania-based film to purely aqueous solutions of Pb(II). Negligible resonant peak shifts occur at low (sub-ppm) concentrations, but a sudden and dramatic blue-shift upon exposure to a 10 ppm Pb(II) solution is observed. 96
Figure 2-32. Attenuation spectra for an LPG coated with a solvent-extracted, tetrasulfide-functionalized titania-based film to purely aqueous solutions of Pb(II) after pre-exposure of the film to a 50 ppm Pb(II) solution. 97

Figure 2-33. Nitrogen isotherms for a large batch of solvent-extracted and scraped tetrasulfide-functionalized titania-based films, both with (black triangles) and without (open circles) ammonia vapour treatment prior to extraction. 98
Figure 2-34. TEM images of solvent-extracted, tetrasulfide-functionalized titania-based films (a) without and (b) with ammonia vapour treatment prior to extraction. 98
Figure 2-35. Attenuation spectra for an ammonia-treated, solvent-extracted, tetrasulfide-functionalized titania-based film on an LPG showing the red-shift of the resonant peak after 10 minutes of exposure to water. 101
Figure 2-36. TEM images of a tetrasulfide-functionalized, nanoparticulate titania-based film at two different magnifications showing (a) the particulate nature of the film, and (b) some of the crystalline anatase planes (with the more evident sections circled). 101
Figure 2-37. Optical micrograph of three different pairs of spiral path MZIs (note the open windows for the sensing arms) on a SOI microchip. The image was taken at 10 × magnification (objective) with dark-field differential interference contrast. 105
Figure 2-38. Normalized electric field distribution profile for the transverse magnetic (TM) mode at λ = 1550 nm for a 0.26 μm × 0.45 μm SOI photonic wire waveguide with a SiO_2 lower cladding and various upper cladding media. Data modeled and provided by Dr. Dan-Xia Xu (NRC, Ottawa). 106
Figure 2-39. (a) Plot of transmitted intensity (normalized) for an unmodified SOI spiral path MZI exposed to water and sucrose solutions of increasing concentration (and RI) showing the interference fringes that arise due to changes in the RI of the ambient environment. (b) Plot of the phase shift measured from 'fringe counting' of the interference fringes in (a) as a function of the RI of the surrounding solution. 107
Figure 2-40. Attenuation spectra for a bare, uncoated tapered fibre interferometer in water / DMSO solutions of varying composition. (Data courtesy of Dr. Judy Cipot-Wechsler, Queen's University.) 111
Figure 3-1. Out-of-plane XRD pattern for the C*10*-derived film measured with the rubbing direction oriented parallel to the projection of the incident X-ray beam. The (20) peak has been magnified by a factor of 10 and the (30) peak has been magnified by a factor of 40. 160
Figure 3-2. Optical micrographs of: (a) a C*10*-derived film prepared on a rubbing-treated substrate; (b) a TEOS-derived film prepared on a rubbing-treated substrate (image taken from reference 29a); and (c) a C*10*-derived film on a non-rubbing-treated substrate. 160

Figure 3-3. Out-of-plane XRD patterns for C*10* films dip-coated onto rubbing-treated substrates at rates of 0.5 mm·s^{-1}, 1.0 mm·s^{-1} and 2.0 mm·s^{-1}. The arrows indicate the positions of higher-order peaks. 161

Figure 3-4. Optical micrographs of *C10*-derived films coated onto (a) a non-rubbing-treated substrate at 2.0 mm·s^{-1}, and rubbing-treated substrates at rates of (b) 0.5 mm·s^{-1}, (c) 1.0 mm·s^{-1} and (d) 2.0 mm·s^{-1}. 161

Figure 3-5. (a) In-plane φ–$2\theta\chi$ scanning profiles for the C*10*-derived film with the rubbing direction oriented parallel (red trace) and perpendicular (black trace) to the projection of the incident X-ray beam at φ = 0 °; and (b) the corresponding φ-scanning profile at $2\theta\chi$ = 4.76 °. 162

Figure 3-6. Cross-sectional TEM image of our C*10*-derived film sliced (a) parallel (inset shows an enlarged image (× 2) of the central region of the film), and (b) perpendicular to the rubbing direction. The polyimide layer is about 10 nm thick. 164

Figure 3-7. Out-of-plane XRD pattern of a C*16*-derived film measured with the rubbing direction oriented parallel to the projection of the incident beam. 165

Figure 3-8. Comparison of the optical micrograph images for (a) a C*10*-derived film and (b) a C*16*-derived film, both prepared on rubbing-treated substrates. 165

Figure 3-9. (a) In-plane φ–$2\theta\chi$ scanning profiles for the C*16*-derived film with the rubbing direction oriented parallel (red trace) and perpendicular (black trace) to the projection of the incident X-ray beam at φ = 0 °; and (b) the corresponding φ-scanning profile at $2\theta\chi$ = 2.56 °. 166

Figure 3-10. Cross-sectional TEM images of the C*16*-derived film sliced parallel to the rubbing direction with (a) the substrate–film interface located at the bottom right corner of the image, and (b) the film–air interface located at the top left corner of the image. 167

Figure 3-11. (a) Out-of-plane XRD pattern and (b) in-plane φ–$2\theta\chi$ scanning profile of C*16*-derived film prepared on a non-rubbing-treated substrate. 169

Figure 3-12. Optical micrographs of C*10*-derived films: (a) as-synthesized on a rubbing-treated substrate; (b) UV-exposed on a rubbing-treated substrate (UV exposure at a 2 mm-separation for 20 minutes at 50 Pa); and (c) calcined on a non-rubbing-treated substrate. 171

Figure 3-13. FT-IR spectra for as-synthesized and UV-exposed (2 mm-separation for 20 minutes at 50 Pa) C*10*-derived films. 172

Figure 3-14. FT-IR spectra for the UV-exposure of a C*10*-derived film at various oxygen pressures at a separation of 1 cm for 30 minutes each. 172
Figure 3-15. Cross-sectional TEM images for an aligned, UV-exposed, C*10*-derived film sliced (a) parallel and (b) perpendicular to the rubbing direction. 173
Figure 3-16. Out-of-plane XRD patterns for as-synthesized, UV-exposed (2 mm-separation for 20 minutes at 50 Pa), and calcined C*10*-derived films..... 175
Figure 3-17. (a) In-plane φ–$2\theta\chi$ scanning profiles for the C*10*-derived film with the rubbing direction oriented parallel (red trace) and perpendicular (black trace) to the projection of the incident X-ray beam at $\varphi = 0$ ° after UV-exposure (2 mm-separation for 20 minutes at 50 Pa); and (b) the corresponding φ-scanning profile for the UV-exposed film in comparison to the as-synthesized film. 175
Figure 3-18. Optical micrograph images showing phase separation in (a) a TIPB-doped C*10*-derived film, and (b) a DO3-doped C*10*-derived film. 180
Figure 4-1. (a) TEM image of the porous, solvent-extracted biphenylene-bridged crystalline PMO material showing lattice fringes in the pore walls with a spacing of 11.6 Å, as well as a 2D hexagonal mesopore arrangement (inset). Scale bars = 10 nm. (b) COMPASS (Condensed-Phase Optimized Molecular Potentials for Atomistic Simulation Studies) force field-optimized structural model of the crystallinity within the walls of the mesoporous biphenylene-bridged PMO. (Both images taken from reference 8b.) 207
Figure 4-2. Reverse phase nano-HPLC chromatograph for the gradient elution of *R,R*- and *S,S*-3b on a capillary column packed with 100% *S*-2 PMO powder (data provided by Dr. Graham Gibson, Queen's University). 217
Figure 4-3. FE-SEM image showing the morphology of the 100% *S*-2 PMO material (image taken from reference 21). 217
Figure 4-4. Cross-sectional SEM image of a monolith prepared from a equimolar mixture of methytrimethoxysilane and tetramethoxysilane inside of a 100 μm-diameter fused silica capillary. (Image taken from reference 33.) 220
Figure 4-5. Composite cross-sectional SEM images of four different capillary monoliths bearing co-continuous structures prepared with the same sol composition, but with different reaction times. The desired skeletal structure for this work is shown in the bottom left quadrant. All monoliths were prepared in capillaries that were 100 μm in diameter. 224

Figure 4-6. Cross-sectional SEM images showing the structural variations of 100% BTESBP-based PMO capillary monoliths with 0.10 mL of BTESBP, 0.40 mL of DMA, 0.025 mL of 1 $HNO_{3(aq)}$, and (a) 0.050 g, (b) 0.055 g, (c) 0.060 g, and (d) 0.070 g of F127 (all capillaries are 100 μm in diameter). 227

Figure 4-7. Cross-sectional SEM images showing the structural variations of 100% BTESBP-based PMO capillary monoliths with 0.10 mL of BTESBP, 0.055 g of F127, 0.025 mL of 1 $HNO_{3(aq)}$, and (a) 0.20 mL, (b) 0.30 mL, (c) 0.50 mL, and (d) 0.70 mL of DMA (all capillaries are 100 μm in diameter). 230

Figure 4-8. Cross-sectional SEM images showing the structural variations of PMO capillary monoliths containing 13 wt% chiral binaphthyl monomer (2) with F127 : 2 mass ratios of (a) 3.9 : 1.0, (b) 6.3 : 1.0, and (c) 7.9 : 1.0 (in 0.40 mL of DMA and 0.025 mL of 1 $HNO_{3(aq)}$) (all capillaries are 100 μm in diameter). 232

Figure 4-9. Cross-sectional SEM images showing the structural variations of 100% BTESBP-based PMO capillary monoliths (a) before (i.e. as-synthesized) and (b) after exposure to ethanol (both capillaries are 100 μm in diameter). 234

Figure 4-10. ^{29}Si CP MAS (solid-state) NMR of a 100% BTESBP-based bulk PMO monolith obtained from the leftover sol of a corresponding capillary monolith – prepared and treated under equivalent conditions. 235

Figure 4-11. Reverse phase nano-HPLC chromatograph for the isocratic elution of *R,R*- and *S,S*-3b on a shrunken 11 wt% *R*-2 PMO capillary monolith (data provided by Dr. Graham Gibson, Queen's University). 237

Figure 4-12. CEC electrograph for injection of a racemic mixture of 3b into a 100% BTESBP-based achiral capillary monolith column (thiourea is an EOF marker). (Data courtesy of Dr. Graham Gibson, Queen's University.) 249

Figure 4-13. VP-ITC traces for adsorption of D- and L-histidine (red and black traces, respectively) onto the chiral zeolite, Goosecreekite, in buffered aqueous media (figure taken from reference 69) 251

Figure 4-14. VP-ITC control traces for the dilution of D-histidine (red trace) and L-histidine (black trace) (each at an initial concentration of 8 mM in buffered water (pH 7)) into buffered water. 253

Figure 4-15. VP-ITC traces for the interaction of D- and L-histidine (each at an initial concentration of 8 mM in buffered water (pH 7)) with (a) 15 wt% *S*-2 PMO, and (b) 15 wt% *R*-2 PMO (both as solid suspensions in buffered water). 256
Figure 4-16. VP-ITC traces for the interaction of D- and L-histidine (each at an initial concentration of 8 mM in buffered water (pH 7)) with (a) MCM-41 (mesoporous inorganic silica), and (b) 100% BTESBP-based PMO (both as solid suspensions in buffered water). 257

List of Tables

Table 1-1. Summary of the different value ranges for surfactant packing parameter (*g*-parameter) and their corresponding micellar structures and mesophases. (Table adapted from references 9 and 19.) 13

Table 1-2. Summary of the different types of metal oxide–template systems used to prepare sol-gel-based mesoporous materials. (Table taken from reference 9.) 16

Table 2-1. Summary of strategies explored to improve the quality and integrity of thick, organosilica xerogel films. 50

Table 2-2. Heavy metal uptake data for mesoporous organosilica thin films and bulk material immersed in aqueous solutions of Hg(II). 58

Table 2-3. Summary of refractive indices of B56-templated thick films and surfactant-free thin films (as measured by VASE). 62

Table 2-4. Extraction efficiency of several solvents for the removal of P123 from bulk ethene-bridged periodic mesoporous organosilica materials (taken from reference 79). 78

Table 2-5. Summary of nitrogen porosimetry data for a large batch of solvent-extracted, scraped PMO films. 81

Table 2-6. Heavy metal uptake data for a large batch of scraped and solvent-extracted tetrasulfide-functionalized titania-based films immersed in aqueous solutions of Pb(II). 99

Table 3-1. Summary of experimental trials conducted to incorporate various dopants into C*10*-based films. 180

Table 4-1. Summary of sol compositions and resultant structures of 100% BTESBP-based capillary PMO monoliths (prepared inside 100 μm-ID fused silica capillaries at T_{gel} = 60 °C). 226

Table 4-2. Summary of CEC data from Figure 4-12 for a 100% BTESBP-based achiral monolithic column. 249

Table 4-3. Summary of the isothermal titration microcalorimetry experiments. 254

List of Appendices

Appendix 1. Table of saturated salt solutions used to control atmospheric relative humidity at various temperatures. (Tables obtained from Chapter 2, reference 75.) 294

Appendix 2. Device map for half of a SOI microchip designed and fabricated by NRC, Ottawa. (Figure courtesy of Dr. Dan-Xia Xu, NRC, Ottawa.) 295

Appendix 3. Photo of the experimental set-up for the charging of activated, fused silica capillaries with monolith-forming sols. 296

Appendix 4. Summary of additional achiral PMO capillary monolith syntheses. 297

Appendix 5. Summary of additional achiral and chiral PMO capillary monolith syntheses (in all instances, T_{gel} = 60 °C). 298

List of Abbreviations, Symbols, and Units

α	selectivity factor
Å	Angstrom (unit equivalent to 10^{-10} m)
AAS	atomic absorption spectrometry
ACN	acetonitrile
ads	adsorption (i.e. adsorption branch of a nitrogen isotherm)
AES	atomic emission spectrometry
APTES	(3-aminopropyl)triethoxysilane
ATMS	allyltrimethoxysilane
B56	poly(ethylene oxide)$_{10}$ hexadecyl ether
B76	poly(ethylene oxide)$_{10}$ octadecyl ether
BJH	Barrett-Joyner-Halenda
BTESE	1,2-bis(triethoxysilyl)ethane
BTESEY	1,2-bis(triethoxysilyl)ethylene or 1,2-bis(triethoxysilyl)ethene
BTESB	1,4-bis(triethoxysilyl)benzene
BTESBP	4,4'-bis(triethoxysilyl)-1,1'-biphenyl
BTESO	1,8-bis(triethoxysilyl)octane
BTESPTS	bis[3-(triethoxysilyl)propyl]tetrasulfide

BTMSE	1,2-bis(trimethoxysilyl)ethane
BTMSH	1,6-bis(trimethoxysilyl)hexane
BTMSM	1,1-bis(trimethoxysilyl)methane
BTMSP	1,3-bis(trimethoxysilyl)propane
CCD	charge-coupled device
CD	circular dichroism
CEC	capillary electrochromatography
CEPA	Canadian Environmental Protection Act
cm	centimeter
cm^{-1}	wavenumber
COMPASS	Condensed-Phase Optimized Molecular Potentials for Atomistic Simulation Studies
CP	cross-polarized
CSP	chiral stationary phase
$C_{16}TAB$	cetyltrimethylammonium bromide or hexadecyltrimethylammonium bromide
cum	cumulative
CV-AAS	cold-vapor atomic absorption spectrometry
δ	chemical shift

d	d-spacing (spacing between lattice planes, as measured by diffraction)
D4R	double-four-ring (a type of cubic, octasilane POSS) unit
DA	dodecylamine
dB	decibel
des	desorption (i.e. desorption branch of a nitrogen isotherm)
DEW	Distant Early Warning
DI	deionized
diam	diameter
DMA	dimethylacetamide
DMDES	dimethyldiethoxysilane
DMSO	dimethyl sulfoxide
DO3	disperse orange 3 or 4-(4-nitrophenylazo)aniline
DOI	digital object identifier
D*o*M	directed *ortho*-metalation
EA	elemental analysis
EDX	energy-dispersive X-ray
ee	enantiomeric excess
EISA	evaporation-induced self-assembly

EPA	Environmental Protection Agency (US)
Et	ethyl
EtOH	ethanol
F127	poly(ethylene oxide)$_{106}$–poly(propylene oxide)$_{70}$–poly(ethylene oxide)$_{106}$
FE-SEM	field emission scanning electron microscopy
FIB	focused ion beam
FSM	Folded Sheets Mesoporous Materials
FT-IR	Fourier Transform infra-red spectroscopy
g	gram
γ_{LV}	surface tension of a given liquid at the liquid–vapour interface
γ-MAPS	γ-methacryloxypropyltrimethoxysilane
GC	gas chromatography
GIXRD	grazing-incidence X-ray diffraction
H	plate height
h	hour
HAADF	high-angle annular dark field
HOAc	acetic acid
HPLC	high-performance liquid chromatography

i	order of an electromagnetic mode
ICP-MS	inductively coupled plasma mass spectrometry
ICP-OES	inductively coupled plasma optical emission spectrometry
ID	internal diameter (of fused silica capillaries)
i-Pr or ^{i}Pr	isopropyl
i-PrOH	isopropanol
IR	infrared
ITC	isothermal titration calorimetry
K	Kelvin
K_i	partition coefficient for species *i*
k'_i	capacity factor for species *i*
KLE	poly(ethylene-*co*-butylene)-*b*-poly(ethylene oxide)
kV	kiloVolt
λ	wavelength
λ_f	resonant wavelength (in LPG spectra)
Λ	periodicity (of LPG)
L	(i) distance between two fibre tapers; and (ii) column length
LC	liquid crystal

LP	linearly polarized
LPG	long period grating
μm	micrometer
m	meter
M	molar or mole·litre^{-1}
MAS	magic angle spinning
mbar	millibar
MCM	Mobil Crystalline Material or Mobil Composition of Matter
Me	methyl
MeOH	methanol
min	minute
mL	millilitre
mm	millimeter
mM	millimolar
mmol	millimole
mol	mole
MPTES	(3-mercaptopropyl)triethoxysilane
MPTMS	(3-mercaptopropyl)trimethoxysilane

MTMS	methyltrimethoxysilane
mW	milliWatt
MZ	Mach–Zehnder
MZI	Mach–Zehnder interferometer
N	number of theoretical plates
n_a	refractive index of the ambient / external environment
n-Bu or ^{n}Bu	*n*-butyl
n-BuOH	*n*-butanol
n_{clad}	refractive index of the cladding
n_{core}	refractive index of the core
n_D^{20}	refractive index at the sodium D-line (589 nm) at a temperature of 20 °C
$n^{i}_{eff,\ clad}$	effective refractive index of the i^{th} order cladding mode
$n_{eff,\ core}$	effective refractive index of the core mode
nL	nanolitre
nm	nanometer
NMR	nuclear magnetic resonance spectroscopy
n-Pr or ^{n}Pr	*n*-propyl
NRC	National Research Council

°C	degree Celsius
$Ø_{ID}$	diameter (specifically, internal diameter of fused silica capillary tubing)
OD	outer diameter
O^{i}Pr	isopropoxy
OSA	optical spectrum analyzer
P123	poly(ethylene oxide)$_{20}$–poly(propylene oxide)$_{70}$–poly(ethylene oxide)$_{20}$
P_c	capillary pressure within a pore
PEEK	polyether-ether-ketone
PFDF	Protein Function Discovery Facility
PMO	periodic mesoporous organosilica
POSS®	polyhedral oligosilsesquioxanes
ppb	parts-per-billion (or $\mu g \cdot kg^{-1}$)
ppm	parts-per-million (or $mg \cdot kg^{-1}$)
psig	pounds per square inch (gauge pressure)
PTFE	polytetrafluoroethylene (or Teflon®)
r	pore radius
RBF	round-bottomed flask
RI	refractive index

RH	relative humidity
rpm	rotations (or revolutions) per minute
R_S	column resolution
rt	room temperature
s	second
SBA	Santa Barbara Amorphous type materials
SDS	sodium dodecylsulfate
SEM	scanning electron microscopy
SERS	surface-enhanced Raman spectroscopy
SMF	single-mode fibre
S_N2	bimolecular nucleophilic substitution
SOI	silicon-on-insulator
SPR	surface plasmon resonance
STEM	scanning transmission electron microscopy
θ	contact angle for a liquid at a given liquid–solid interface
T	temperature
T_{gel}	gelation temperature
t	time

t_0	time zero
$t_{1/2}$	half-life
t-BuOH	*tert*-butanol
TEM	transmission electron microscopy
TEOS	tetraethoxysilane or tetraethyl orthosilicate
THF	tetrahydrofuran
$Ti(O^iPr)_4$	titanium(IV) tetraisopropoxide
$Ti(O^nBu)_4$	titanium(IV) tetrabutoxide
TIPB	1,3,5-triisopropylbenzene
TLC	thin-layer chromatography
t_M	column 'dead time'
TM	transverse magnetic
TMES	trimethylethoxysilane
TMOS	tetramethoxysilane or tetramethyl orthosilicate
TPAOH	tripropylammonium hydroxide
t_R	retention time
TTBO	titanium(IV) tetrabutoxide
TTIP	titanium(IV) tetraisopropoxide

TUV	tunable UV
u	linear velocity of the mobile phase (in chromatography)
UPLC	ultra performance liquid chromatography
UV	ultraviolet
V88	VAZO® 88 (1,1′-azobis(cyclohexanecarbonitrile))
VASE	variable angle spectroscopic ellipsometry
VOC	volatile organic compound
vol	volume
VTMS	vinyltrimethoxysilane
W_i	peak width (at the base of the peak) for the peak corresponding to species i
wt	weight
XRD	X-ray diffraction

Chapter 1
Introduction

1.1 General

Silica (SiO_2) is – fascinatingly – both an ordinary and commonplace mineral found in commodity items such as window panes and glass bottles, as well as a unique and incredibly exciting material being widely developed for novel and advanced applications ranging from the capture of interstellar comet dust[1] to oral drug delivery.[2] The prevalent implementation of silica-based materials in conventional applications is largely a result of properties such as: (i) its occurrence in both crystalline and amorphous forms; (ii) low thermal conductivity; (iii) a low coefficient of thermal expansion and high thermal shock resistance; (iv) tunable optical properties (from perfectly transparent to completely opaque); (v) electrical resistance; (vi) chemical stability in solution over a relatively large pH range; (vii) tailorable chemical functionality; as well as (viii) a relatively high elastic modulus and resistance to abrasion, all of which can be tuned depending on the method of processing and thus making it *incredibly* useful.[3,4] Correspondingly, it is these properties (and more!) that make silica equally as attractive a material for utilization in advanced optical, biological, and heterogeneous catalytic applications, to name a few.

Although 'silica' is a broad and all-encompassing term, it is really *porous silica* that is of particular interest to our work as it is the high surface areas and large porous volumes of such materials that allow for the realization of interesting physical and chemical behaviour. An important advancement promoting the continued interest in

silicas has been the development of sol-gel methods for the facile synthesis of both non-porous and porous silicas in diverse morphologies such as particles of various uniform shapes and sizes, films, fibres, and monoliths.[5] For the most part, bulk silica and glass are manufactured using energy-intensive high-temperature melting, sintering, and hot-pressing processes. However, sol-gel methods allow for the preparation of non-porous and porous silicas using wet chemistry at moderate temperatures (for example, < 120 °C) and ambient or autogenous pressure to yield materials of controlled homogeneity in a number of different forms. Although sol-gel chemistry is a significantly less economical method for producing bulk glass, the ability to affect silica synthesis through the infinite possibilities for modification of the starting condensable components, variation of the solvent media, implementation of additives, optimization of post-synthetic treatment processes, and so forth, provides access to new types of materials with properties that could not easily be realized by other synthetic methodologies.[6]

1.2 Sol-Gel Chemistry and the Synthesis of Amorphous, Porous Silicas

Formally, a *sol* is defined as a colloidal suspension of solid particles in a liquid medium. Meanwhile, a *gel* is formally defined as a colloidal suspension of a liquid phase in a solid medium,[7] or a substance consisting of a continuous solid skeleton enclosing a continuous liquid phase.[5] In the sol-gel process, amorphous metal oxides are formed from precursors (either monomeric, oligomeric, or particulate species) that undergo hydrolysis and condensation in a given liquid reaction medium to form the colloidal sol.

Continued polymerization / condensation of the solid phase then progresses to a point where a gelatin gel (an entanglement of chains), polymeric gel (a covalently bound, extended network), or particulate gel (an agglomeration of particles to form an extended bulk structure) is formed, with the sol-to-gel transition point (i.e. a degree of reaction or length of time) defined as the *gel point* or *gel time*.[5]

Silicon alkoxides such as **1** are very common precursors for forming silicon oxides (see Scheme 1-1 for some examples) because they readily undergo hydrolysis (particularly under mineral acid- or hydroxy or ammonia base-catalyzed conditions) to give hydroxy-substituted species (**2**).

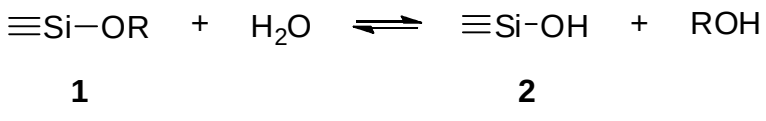

1 **2** (**1-1**)

These compounds typically then proceed to condense with other hydroxy- or alkoxy-substituted silanes to yield siloxanes (**3**), as outlined below in equations (1-2) and (1-3), respectively.[5]

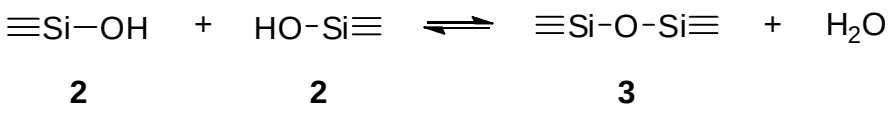

2 **2** **3** (**1-2**)

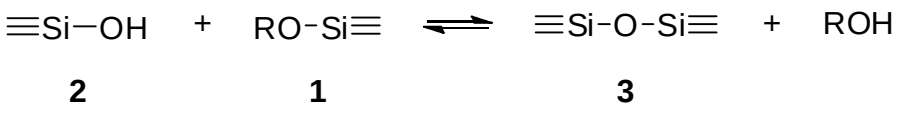

2 **1** **3** (**1-3**)

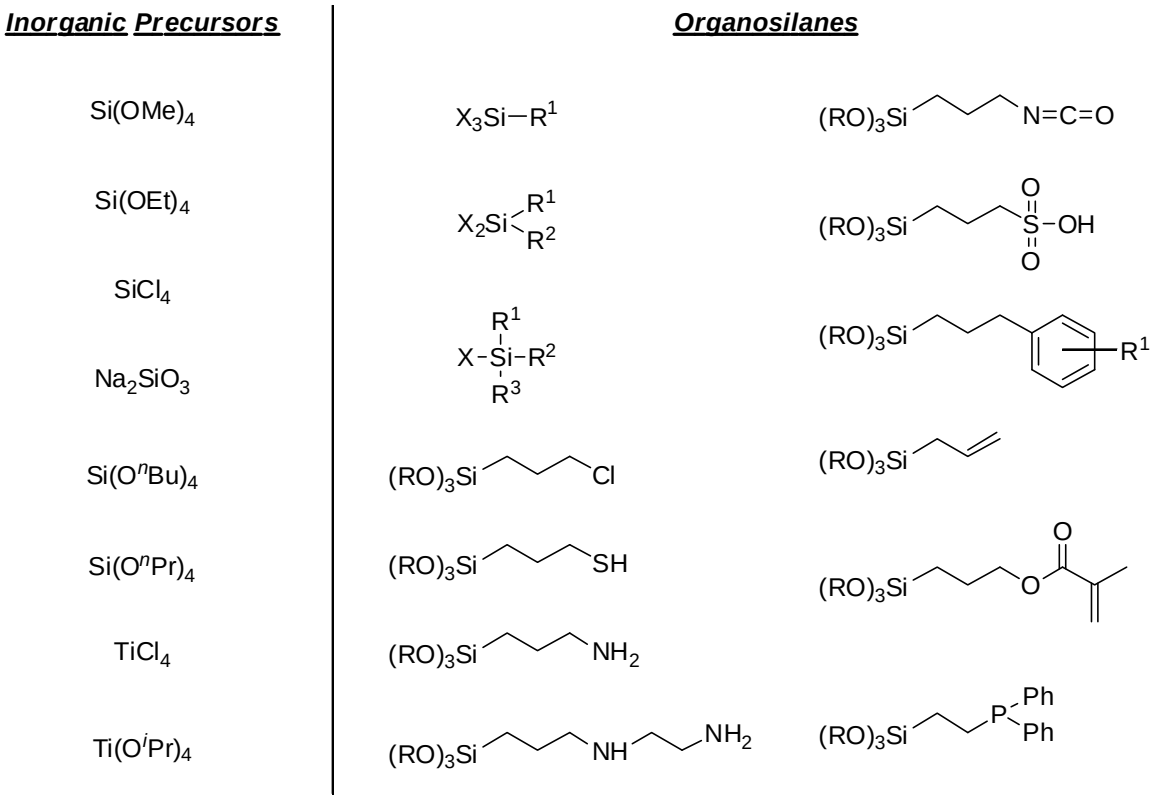

Scheme 1-1. Typical inorganic precursors and organosilanes (where X = Cl or OR, and R = Me or Et) used in the sol-gel syntheses of metal oxides and functionalized metal oxides.

The most commonly used metal alkoxide precursors are tetraalkoxysilanes such as tetramethoxysilane ($Si(OMe)_4$, TMOS) and tetraethoxysilane ($Si(OEt)_4$, TEOS), although silanes substituted with bulkier –OR alkoxy substituents are also known and commercially available (for example, R = *i*-Pr, *n*-Bu, or *t*-Bu). These metal alkoxides are not intrinsically miscible in water. However, as these precursors undergo hydrolysis and release alcohol as a by-product (see equation 1-1), this alcohol acts as a co-solvent that increases the miscibility of the precursors in an aqueous reaction medium.[5] Alternatively, to prevent this liquid–liquid phase separation, polar organic solvents such as methanol

(MeOH), ethanol (EtOH), isopropanol (*i*-PrOH), *n*-butanol (*n*-BuOH), or tetrahydrofuran (THF) are often employed as co-solvents or as the majority solvent phase. Additionally, the choice of solvent system can influence the processability of the sol as well as the morphology of the final product as intermolecular interactions in the growing silica structures are dissimilarly modulated in different solvent systems.[5]

Common acid catalysts are hydrochloric acid (HCl), nitric acid (HNO_3), sulfuric acid (H_2SO_4), and acetic acid (HOAc), whereas common base catalysts are ammonium hydroxide (NH_4OH), sodium hydroxide (NaOH), and potassium hydroxide (KOH). Notably, for these amorphous silicas, use of an acid- or base-catalyzed hydrolysis and condensation process will influence the microstructure and morphology of the final product. In general, it has been documented that hydrolysis of metal alkoxides occurs more rapidly under acid-catalyzed conditions while condensation occurs more rapidly under base-catalyzed conditions.[5] Furthermore, acid-catalyzed condensation reactions tend to yield more extended structures showing lower degrees of condensation.[5] This is in contrast to base-catalyzed condensation reactions that tend to yield highly condensed, particulate networks.[5]

It should be emphasized that upon gelation or precipitation of a given sol-gel system, siloxane bond formation does not suddenly stop. Dynamic bond-forming and bond-breaking processes are still at play and the silica framework continues to evolve. This process of continued framework restructuring after gelation is referred to as *aging*.[5] Some of the consequences of the aging process may be any combination of strengthening, stiffening, densification, and shrinkage of the silica networks. The structural changes that

take place during the aging process may then also be observed during the subsequent *drying* stage, in addition to affecting the drying process itself (which formally involves the removal of residual solvent, monomer, etc.).[5] These factors greatly affect the physical, mechanical, and chemical properties of the final product (for example, the material's degree of porosity, pore size, modulus, and concentration of surface silanols).

Although pure, inorganic silica (SiO_2) is undoubtedly a valuable material, the ability to add additional functionality (either mixed inorganic, organic, or organometallic, and so forth) to this material tremendously expands its usefulness for various applications. Appealingly, sol-gel chemistry allows for the facile introduction of additional functionality into the silica-based materials. For example, using organosilanes (some of which are exemplified in Scheme 1-1), functionality may be introduced via grafting of the organosilanes onto a pre-formed silica support through condensation with residual silanols on the surface of the support, or via co-condensation of the organosilanes with the tetraalkoxide precursors.

As an extension to the synthesis of organosilicas through the grafting or co-condensation processes mentioned above, organosilicas having organic moieties embedded in the framework may also be synthesized using silsesquioxanes precursors (see Scheme 1-2).[8] These are bridge-bonded organosilanes bearing two or more condensable silyloxy groups, and the products of their condensation are often referred to as polysilsesquioxanes. These bridge-bonded silsesquioxanes may additionally be used in combination with, for example, tetraalkoxysilanes as well as organotrialkoxysilanes to yield further combinations of hybrid silica sol-gel materials.

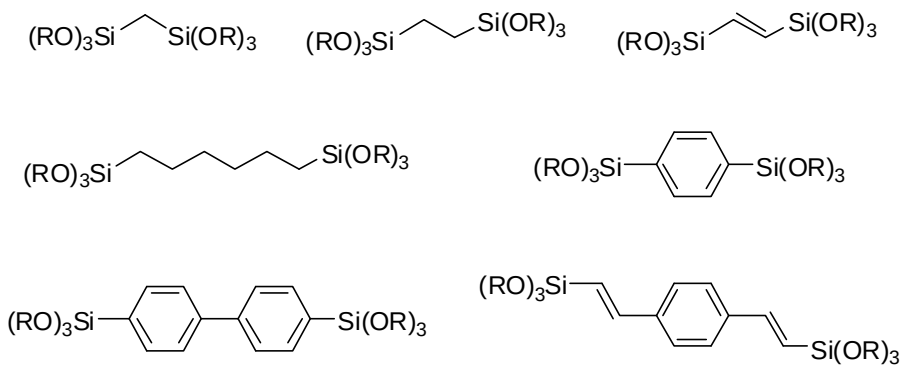

Scheme 1-2. Some examples of organically-bridged bis-silanes for the synthesis of polysilsesquioxanes (where R = Me, Et).

Lastly, hybrid silica–transition metal oxide materials are also possible using precursors such as titanium(IV) tetraalkoxides (for example, $Ti(OR)_4$, where R = Et, *i*-Pr, or *n*-Bu) (see Scheme 1-1). Mixed metal oxides comprising zirconia, alumina, and others, may likewise be formed using analogous metalorganic precursors.[5] Consequently, boundless possibilities exist for the formation of hybrid silica species with transition metal oxide and / or organic functionality.

In brief summary, it can be seen that the preparation of a given silica-based sol and the resulting product will be affected by the choice and consequent concentration of each of the following components: (i) inorganic, metal alkoxide precursor(s); (ii) organosilane(s); (iii) aqueous acid and / or base catalyst; (iv) water content; (v) polar organic solvent; and (vi) additives (e.g. salts, swelling agents, or drying control agents). In addition, the material properties may be further adjusted by modifying parameters such

as the aging and drying conditions. It, therefore, comes as no surprise that an extremely rich variety of hybrid silica-based materials are accessible via sol-gel chemistry.

1.3 Surfactant-Templated Mesoporous Silicas

The same principles of hydrolysis and polycondensation of silicon alkoxides to form both non-porous and porous silicas (and organosilicas), as described in Section 1.2, also apply to the synthesis of silica-based materials with periodically ordered porosity. The main difference with this particular sol-gel methodology, however, is the addition of low molecular weight surfactants and / or amphiphilic block copolymers as templating agents for control of the shape and size of the pores, and concomitant organization of the pores into regular 1-, 2-, and 3-D arrays.[9,10] This surfactant-based, 'soft templating' approach (with the term 'surfactant' being applied, herein, to all appropriate amphiphilic templating species) takes advantage of the ability for amphiphilic molecules and polymers to self-assemble not only into spherical micelles, but also into higher order, lyotropic liquid crystalline mesophases (exemplified in Scheme 1-3), which act as scaffolds for the pore structure of the final, condensed silica material.[9,10]

This is in contrast to zeolite-based materials,[9,10,11] which are synthesized using small organic molecules as templates (for example, ammonium salts such as tripropylammonium hydroxide (TPAOH) or amines) at elevated temperatures (up to 300 °C) and pressures (up to 50 atm) over longer reaction times (up to days) in strongly alkaline solutions. Under these conditions, highly crystalline aluminosilicates bearing

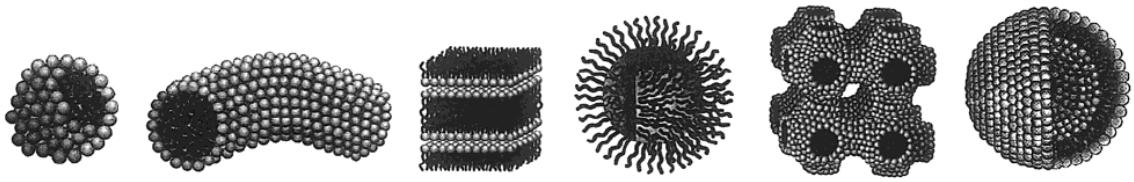

Scheme 1-3. Schematic representation of typical micellar mesophases (from left to right): spherical, rod-like / cylindrical, lamellar / bilayer, inverse spherical, bicontinuous, vesicular. (Scheme taken from reference 9.)

molecular scale order in the zeolite walls as well as periodic order in their pore arrangement are formed after removal of the organic templating molecules. Notably, with zeolites, removal of the template may only be achieved by high-temperature calcination. Furthermore, the pore sizes of zeolitic materials lie in the microporous range (i.e. pore diameters < 2 nm) while the surfactant-templated materials have pores with diameters in the mesoporous range (i.e. 2–50 nm).[9,10] In fact, the discovery of the archetypal M41S family of surfactant-templated, silica-based mesoporous sieves was largely a result of efforts dedicated to preparing larger-pore analogues of zeolitic materials, as ordered materials with mesoscale porosity would allow for interactions with molecules larger than those allowed by the microporous systems.[12]

Formation of a given hybrid silica-surfactant mesophase may occur by one of two common pathways:[9,10,13] (i) a true, lyotropic liquid crystalline phase;[14] or (ii) a co-operative self-assembly process.[15] In the first instance, the templating agent is present in solution at a concentration that gives a particular mesophase. The condensable precursors are then added to the reaction mixture, and the hydrolyzed, hydrophilic silica

precursors interact with the hydrophilic head groups of the template located at the corona of the micellar structures. Condensation of the hydrolyzed precursors then progresses around these micellar structures to yield the ordered, as-synthesized (i.e. surfactant-containing) material (see Scheme 1-4, Pathway A).[9,10,13,14]

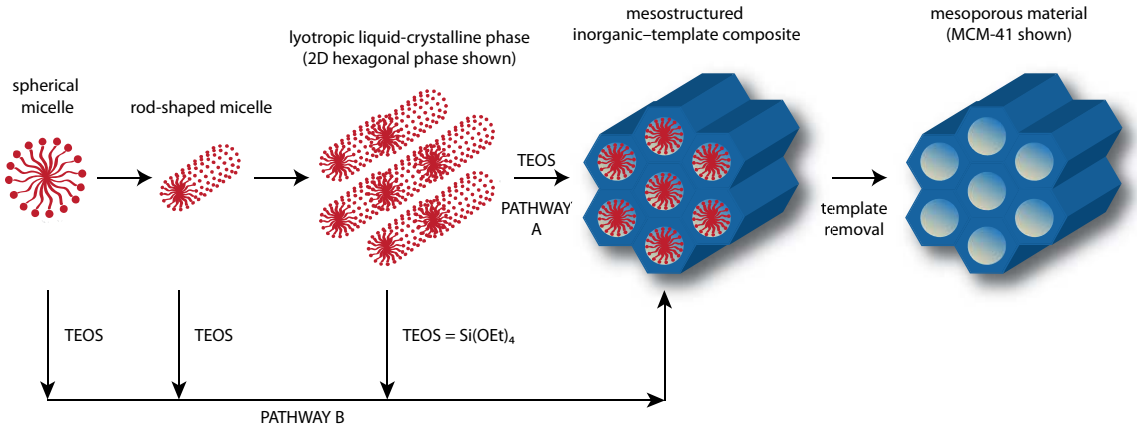

Scheme 1-4. Formation of mesoporous silica via a lyotropic liquid crystalline pathway (Pathway A) or a cooperative self-assembly pathway (Pathway B). (Scheme adapted from reference 13.)

For the case of co-operative self-assembly, pre-association of hydrolyzed silica-based monomers and oligomers with the surfactant molecules occurs (also via hydrophilic–hydrophilic interactions), which induces mesophase formation.[9,10,13,15] Condensation of the hydrolyzed precursors proceeds to, again, yield the ordered, as-synthesized material (see Scheme 1-4, Pathway B). For both pathways, after condensation of the silica into an amorphous network and removal of the non-covalently bound templating agent (most commonly by solvent extraction or high-temperature

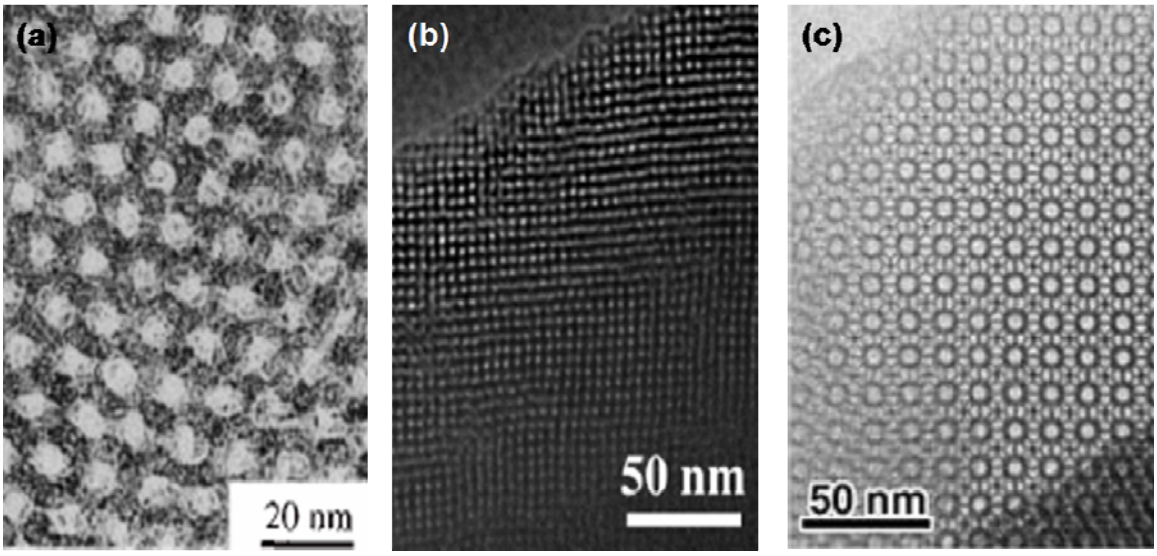

Figure 1-1. TEM images of surfactant-templated, porous silica materials bearing different mesostructural order: (a) 2D hexagonal (*p6mm*); (b) cubic [100] (*Fm3m*); (c) cubic [100] ($Pm\bar{3}n$) (images taken from references 15a, 16, and 17, respectively.)

calcination), a high surface area material is obtained (up to ~ 1000 $m^2 \cdot g^{-1}$) with an ordered pore structure mimicking that of the surfactant phase.[9,10,13] Examples of some of the accessible mesostructures may be seen by the TEM images in Figure 1-1.

The establishment of a certain mesophase depends heavily on the interfacial curvature at the surfactant–siloxane interface. Consequently, the packing geometry of the amphiphilic templating species plays an important role in determining the final mesophase of the condensed material. A popular and intuitive model was devised by Israelachivili and co-workers to explain and predict the mesophases obtained in micellar systems,[18] and has since been applied to the surfactant-templated mesporous metal oxide systems. In particular, the steric hinderance imposed by the hydrophobic surfactant tail is

taken into account through consideration of the tail length as well as the hydrophobic volume occupied by the tail. Furthermore, a balance between the hydrophobicity of the tail and hydrophilicity of the polar head group is also included in the model. The resulting relationship is that of the *g*-parameter, and is expressed as follows:[9,18]

$$g = \frac{V}{a_o l} \qquad \textbf{(1-4)}$$

where g is an index of interfacial curvature or the 'packing parameter', V is the hydrophobic volume occupied by the surfactant tail, a_o is the effective head group area, and l is the effective length of the surfactant tail (which is less than the length of the fully extended tail) (see Scheme 1-5). Different values for g correspond to different micellar phases, and the values and trends are summarized in Table 1-1.[9,19]

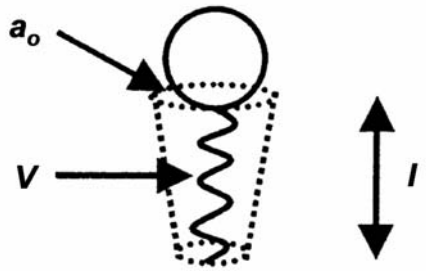

Scheme 1-5. Schematic representation of a surfactant molecule and the variables involved in the calculation of the surfactant packing parameter (*g*-parameter). (Scheme taken from reference 9.)

Table 1-1. Summary of the different value ranges for surfactant packing parameter (*g*-parameter) and their corresponding micellar structures and mesophases. (Table adapted from references 9 and 19.)

***g*-Parameter Value**	**Resulting Micellar Structures and Mesophases**
< 1/3	spherical micelles / primitive cubic
1/3 – 1/2	cylindrical micelles / 2D hexagonal
1/2 – 2/3	bicontinuous cubic
1/2 – 1	bilayer micelles / vesicles
1 – 2	bilayer micelles / lamellar
2 – 3	inverse cylindrical micelles
> 3	inverse spherical micelles

The templating species may be cationic, anionic, neutral, or nonionic. Examples of some of the most common templating agents are cationic alkylammonium salts bearing one or more charged head groups, nonionic alkylpolyethers, nonionic block copolymers, and neutral alkylamines, with their chemical structures depicted in Scheme 1-6.[9,10]

The variety of synthetic routes to obtaining templated, mesoporous materials is summarized in Scheme 1-7 and Table 1-2. Here, 'S' represents the surfactant, while 'I' represents the inorganic precursor. Additionally, where applicable, 'M^+' and 'X^-' denote charge-matching counterions, 'N' denotes an organic amine or aminosilane, and 'H^+' denotes a proton. The corresponding superscripts '+', '–', and '0' refer to the charge of a given species (i.e. positive, negative, and neutral or nonionic, respectively).[9,10,15]

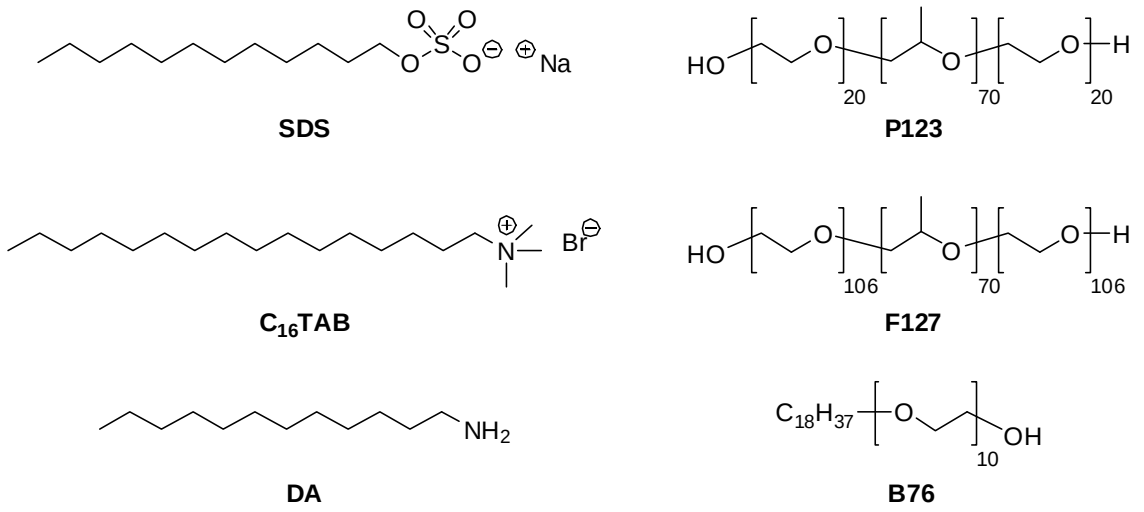

Scheme 1-6. Typical examples of anionic (**SDS** = sodium dodecylsulfate), cationic (**C_{16}TAB** = cetyltrimethylammonium bromide), and nonionic (**DA** = dodecylamine; **F127** = Pluronic®-type nonionic triblock copolymer; **B76** = Brij®-type alkyl polyether) surfactants used to template mesoporous sol-gel materials.

The most famous examples of ordered, mesoporous silicas are MCM-41[12] and SBA-15,[20] both of which possess 2D hexagonal symmetry (the TEM image depicting the benchmark 'honeycomb structure' for 2D hexagonal mesostructures may be seen for SBA-15 in Figure 1-1a). MCM-41 belongs to the M41S family of molecular sieves originally discovered by researchers at Mobil Corporation, and is formed via a S^+I^- templating route using a cationic alkylammonium surfactant (cetyltrimethylammonium bromide, **C_{16}TAB**) under base-catalyzed conditions.[9,10,12] On the other hand, SBA-15 – developed by the research group of Prof. Galen D. Stucky at the University of California, Santa Barbara – is formed through a $N^0X^-I^+$ (or $S^0(IX)^0$) process using a nonionic triblock copolymer (Pluronic® **P123**) as the templating agent under acid-catalyzed conditions.[9,10,20]

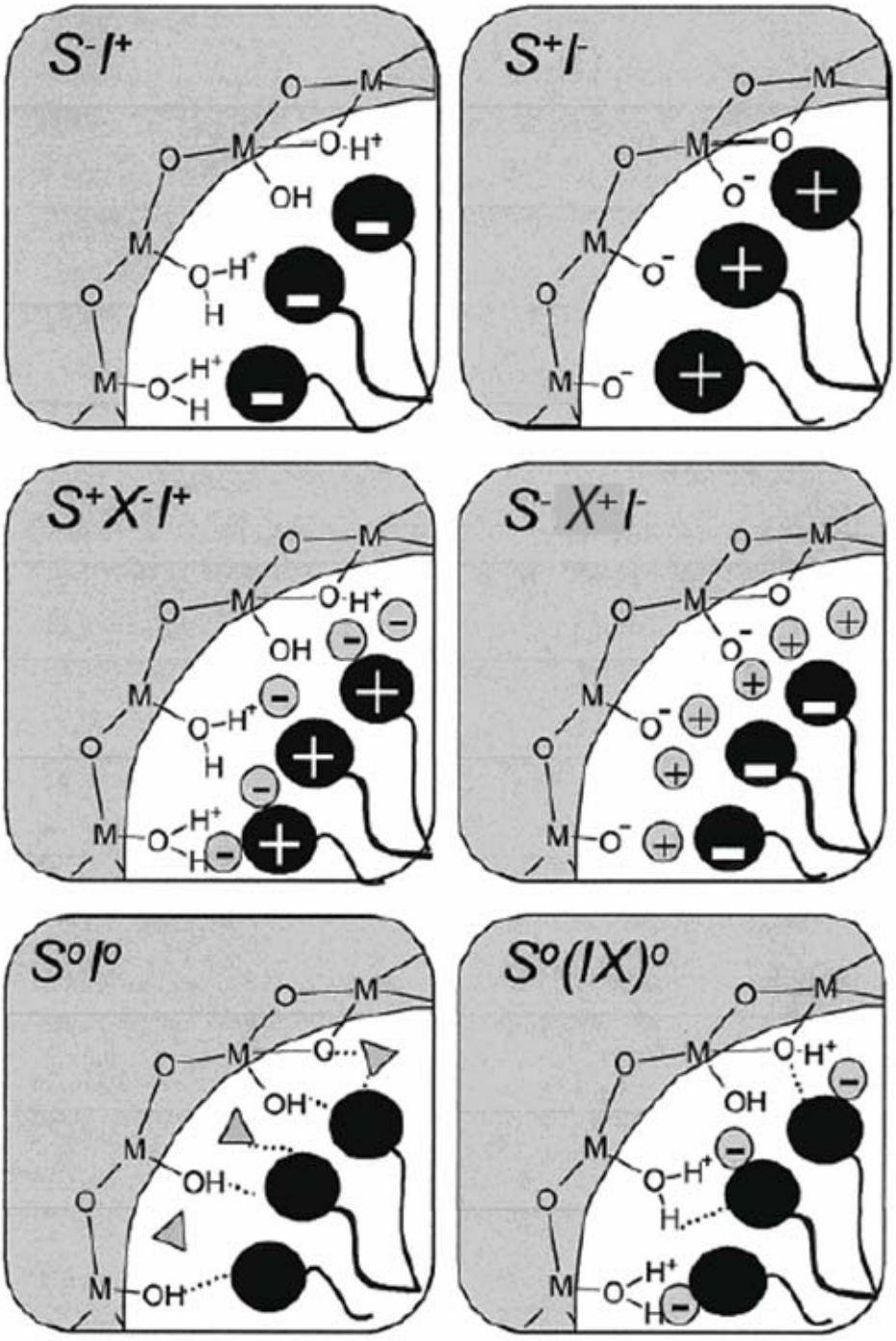

Scheme 1-7. Schematic representation of the different types of interfacial metal oxide–surfactant interactions taking place in various surfactant-templated systems (where typically the inorganic M = a metal such as Si or Ti). (Scheme taken from reference 9.)

Table 1-2. Summary of the different types of metal oxide–template systems used to prepare sol-gel-based mesoporous materials. (Table taken from reference 9.)

Surfactant Type	Interaction Type	Example Materials (Structure)[a]
cationic S^+	S^+I^-	silica: MCM-41 (hex) MCM-48 (cub) MCM-50 (lam) tungsten oxide (lam, hex) antimony oxide (lam, hex, cub) tin sulphide (lam) aluminum phosphate (lam, hex)
	$S^+X^-I^+$	silica: SBA-1 (cub) SBA-2 (3D hex) SBA-3 (hex) zinc phosphate (lam) zirconium oxide (lam, hex) titanium dioxide (hex)
	$S^+F^-I^0$	silica (hex)
anionic S^-	S^-I^+	Mg, Al, Ga, Mn, Fe, Co, Ni, Zn oxides (lam) lead oxide (lam, hex) aluminum oxide (hex) tin oxide (hex) titanium oxide (hex)
	$S^-X^+I^-$	zinc oxide (lam) aluminum oxide (lam)
neutral S^0 or N^0	S^0I^0	silica: HMS (hex)
	N^0I^0	MSU-X (hex) silica (lam, hex, cub) Ti, Al, Zr, Sn oxides (hex)
	$N^0X^-I^+$	silica: SBA-15 (hex)
	$N^0F^-I^+$	silica (hex)
	$(N^0M^{n+})I^0$	silica (hex)

[a] – cub = cubic; hex = hexagonal; lam = lamellar.

Although both MCM-41 and SBA-15 bear the same 2D hexagonal porous mesostructure, differences arise when their physical properties are compared. MCM-41 typically has a mean pore diameter of 3.7 nm (which can be increased to ~ 10 nm through

the use of swelling agents),[12] while SBA-15 has a mean pore diameter of 4.7 nm (which can be expanded to ~ 30 nm through the use of swelling agents).[20] The larger diameter pores of the SBA-type materials are interesting as they could arguably allow for more facile mass transport of various analytes through the pore network. Another important difference is that the silica walls of SBA-15 tend to be thicker than those of MCM-41 (3.1–6.4 nm for SBA-15 compared to 1.0–1.5 nm for MCM-41),[10,20] leading to the dramatically improved hydrothermal stability of the SBA-type materials over MCM-type materials.[10,20] For these reasons (and more, which will be discussed in the following chapters), the synthesis of mesoporous organosilica materials using nonionic block copolymers and alkylpolyethers are the routes explored for much of the work presented in this thesis.

In similar fashion to the non-templated sol-gel chemistry described in Section 1.2, the preparation of surfactant-templated, ordered mesoporous silicas as powders, films, fibres, monoliths, and so forth (a few different morphologies are exemplified in Figure 1-2) may be customized by modifying synthetic parameters such as the type and relative concentrations of the condensable metalorganic precursors, catalyst (i.e. acid or base), solvent, and additives (i.e swelling agents or salts) used, in addition to the choice of surfactant species (or added exotemplates[21]) and its concentration as additional variables to morphology control.[9,10] Moreover, the material synthesis will further be affected by the choice of reaction temperature, aging time, surfactant removal procedure, and drying process.[9,10] Along with the usual metal(IV) tetraalkoxides such as TMOS, TEOS, and titanium(IV) tetraisopropoxide (TTIP), the options for organosilanes for use in this

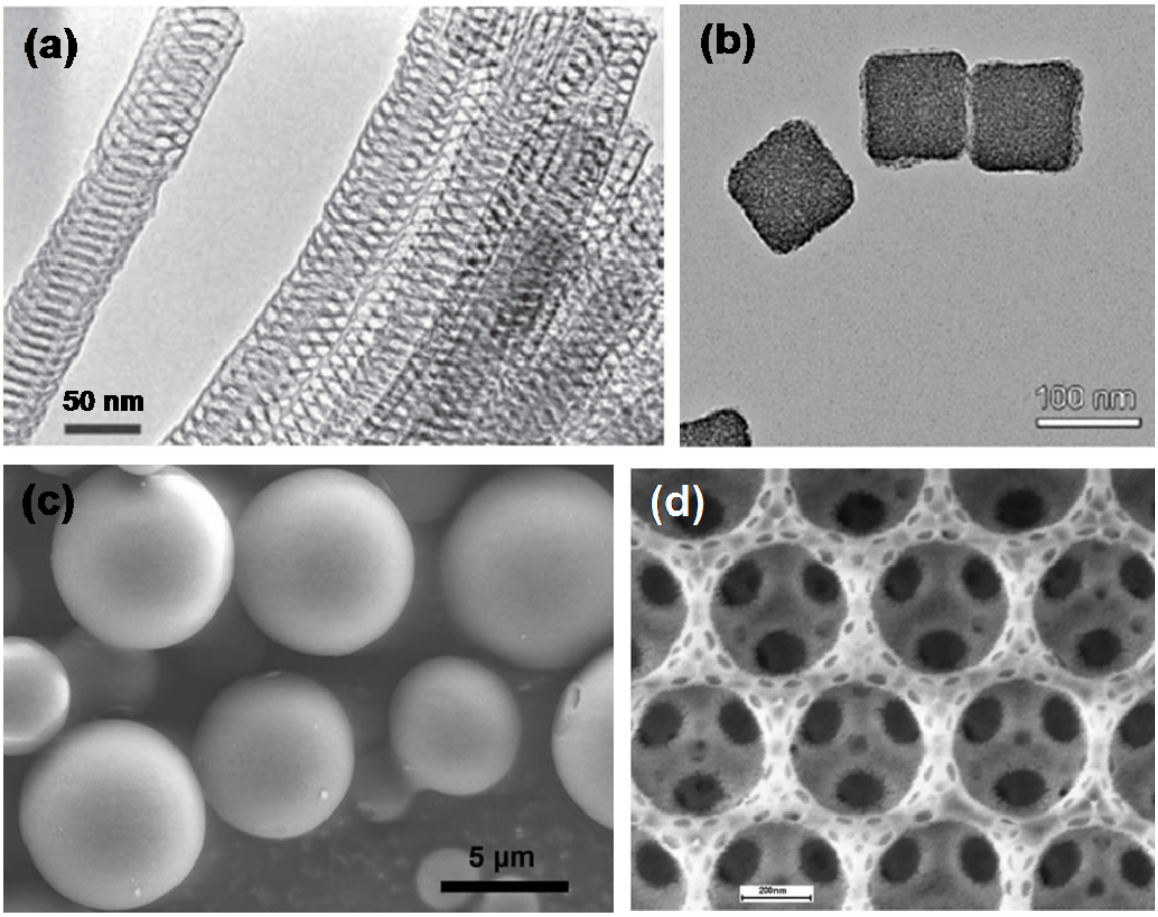

Figure 1-2. Examples of surfactant-templated silica-based mesoporous materials synthesized with different morphologies: (a) silica nanowires; (b) silica nanocubes; (c) benzene-bridged organosilica spheres; and (d) silica-based inverse opals. (Images taken from references 22, 23, 24, and 25, respectively.)

surfactant-templated materials synthesis methodology are also the same as those exemplified in Scheme 1-1.[9,10]

Furthermore, silsesquioxane precursors, as exemplified in Scheme 1-2, may also be incorporated into this template-based strategy for preparing mesostructured

materials.[13,26,27] The resulting materials have been specially termed 'periodic mesoporous organosilicas' (PMOs). This class of materials is of particular value because by conventional functionalization routes such as co-condensation, a maximum of approximately only 25 mol% incorporation of the organotrialkoxysilane may be achieved in the starting sol as increased loading of the organosilanes leads to poorly structured and potentially phase-separated materials (as a result of significant disruption of the template—precursor interactions).[28] However, the use of silsesquioxane precursors in conjunction with the surfactant-templated approach notably allows for the synthesis of ordered, porous materials with essentially 100% incorporation of the desired organic functionality, further expanding the potential for designing novel hybrid materials with well-tailored properties (see Scheme 1-8).

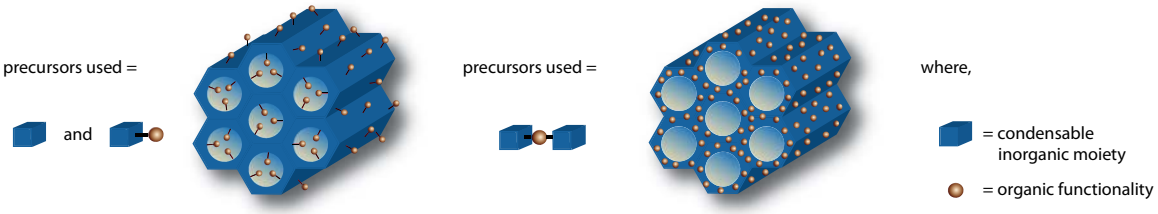

Scheme 1-8. Schematic representation of the difference in the distribution of organic groups between typical organically-functionalized mesoporous silica (synthesized by post-synthetic grafting or co-condensation) (left) and periodic mesoporous organosilica (PMO) (where the functionality is embedded in the framework walls) (right).

Lastly, although not a focus of this thesis, it should be noted, here, that a summary of the history of the discovery and development of ordered mesoporous materials is not complete without the mention of the pioneering work of Kuroda et al. in preparing ordered, mesoporous silicates from alkylammonium–clay intercalation complexes. Prior to the 1992 publication of Krege et al. regarding the discovery and synthesis of MCM-41, Kuroda et al. showed in 1990 that mesoporous materials bearing a network of pores with diameters in the range of 2–4 nm and surface areas of approximately 900 $m^2 \cdot g^{-1}$ could be formed by treating kanemite (a single-layered polysilicate with the chemical composition $NaHSi_2O_5 \bullet 3H_2O$) with alkyltrimethylammonium chlorides under hydrothermal conditions at alkaline pH and subsequent removal of the organic species by calcination.[29] Here, the pore size could be tuned by changing the alkyl chain length of alkyltrimethylammonium chlorides ($C_nH_{2n+1}N^+(CH_3)_3Cl^-$) from n = 12–18. This offered an alternative route to preparing porous materials from layered clays as, up to this point, most of the methodologies explored involved the synthesis of pillared clay structures.

This synthesis strategy was then optimized by Kuroda et al. and the results were reported in 1993.[30] In this latter report, the authors demonstrated that a well-ordered, mesoporous 2D hexagonal material (strikingly similar in structure to MCM-41) could be prepared (using the hexadecyltrimethylammonium chloride species, n = 16) via a lamellar-to-2D-hexagonal phase transition in solution. Interlayer siloxane bond formation was postulated from the solid state ^{29}Si MAS NMR data, implying folding / deformation of the lamellar polysilicate sheets around the intercalated alkylammonium ions to give the final product. This material was consequently named FSM-16 (Folded

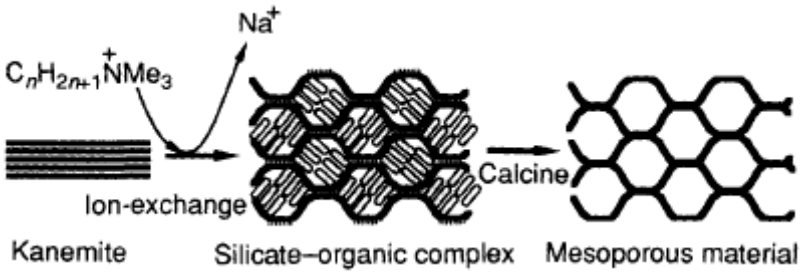

Scheme 1-9. Schematic representation of the formation of FSM-type materials. (Scheme taken from reference 30.)

Sheets Mesoporous Materials) with the number identifier making reference to the alkyl chain length of the alkylammonium species used in the particular synthesis (see Scheme 1-9).[31]

Therefore – to re-emphasize the point – as illustrated with the small handful of classic examples above, the surfactant-templated sol-gel methodology is a not only a flexible and potent means for preparing silica-based materials with a wide variety of both physical and chemical pore properties (as well as bulk morphologies), but more importantly, allows for a significant amount of control over the synthesis to yield materials with a high degree of uniformity in their porosity and functionality.

1.4 Objectives of This Thesis

In the years following the discoveries of the FSM-, MCM-, SBA-, and PMO-type mesoporous silica-based materials, the field of materials synthesis employing the

surfactant-templated sol-gel process has indisputably exploded.[9,10,27,32,33] The literature is replete with reports demonstrating the synthesis of new and novel materials bearing properties such as hierarchical porosity,[9,34] tricontinuous pore networks,[35] crystallinity in the framework walls,[36] mechanized drug-release,[37] chirality transfer,[38] and luminescence[39] to name only a few.

Remarkably, the development of novel applications employing these versatile materials has progressed to a far lesser extent despite the impressive achievements realized using these designed systems for obtaining tailored materials. Furthermore, in general, the vast majority of studies published in the mesoporous silica literature to date have explored the synthesis of these materials as bulk powders. However, for many applications, morphologies such as films, fibres, tubes, and monoliths are critical. With this in mind, this thesis, therefore, explores the following themes with respect to the design and synthesis of mesoporous organosilicas in some of these technologically important morphologies and their subsequent application to selected areas of commercial interest:

(i) periodic mesoporous organosilica (PMO) films as functional coatings for fibre-optic heavy metal sensing devices;

(ii) self-assembly of amphiphilic, hybrid, designer precursors to yield uniaxially-aligned nanostructured films; and

(iii) synthesis of chiral PMO capillary monoliths for chiral separations.

1.5 References

1. (a) Brownlee, D.; Tsou, P.; Aléon, J.; Alexander, C. M. O'D.; Araki, T.; Bajt, S.; Baratta, G. A.; et al. *Science* **2006**, *314*, 1711–1716; (b) Hörz, F.; Bastien, R.; Borg, J.; Bradley, J. P.; Bridges, J. C.; Brownlee, D. E.; Burchell, M. J.; et al. *Science* **2006**, *314*, 1716–1719; (c) McKeegan, K. D.; Aléon, J.; Bradley, J.; Brownlee, D.; Busemann, H.; Butterworth, A.; Chaussidon, M.; et al. *Science* **2006**, *314*, 1724–1730; (d) Flynn, G. J.; Bleuet, P.; Borg, J.; Bradley, J. P.; Brenker, F. E.; Brennan, S.; Bridges, J.; et al. *Science* **2006**, *314*, 1731–1735.

2. (a) Liong, M.; Angelos, S.; Choi, E.; Patel, K.; Stoddart, J. F.; Zink, J. I. *J. Mater. Chem.* **2009**, *19*, 6251–6257; (b) Vivero-Escoto, J. L.; Slowing, I. I.; Trewyn, B. G.; Lin, V. S.-Y. *Small* **2010**, *6*, 1952–1967; (c) Rosenholm, J. M.; Sahlgren, C.; Lindén, M. *Nanoscale* **2010**, *2*, 1870–1883.

3. Housecroft, C. E.; Sharpe, A. G. *Inorganic Chemistry*, 1st ed.; Prentice Hall: Harlow, 2001.

4. Accuratus Corporation website: http://accuratus.com/fused.html (accessed March 25, 2011).

5. Brinker, C. J.; Scherer, G. W. *Sol-Gel Science: The Physics and Chemistry of Sol-Gel Processing*; Academic Press: New York, 1990.

6. Zarzycki, J. *J. Sol-Gel Sci. Tech.* **1997**, *8*, 17–22.

7. Shaw, D. J. *Introduction to Colloid and Surface* Chemistry, 4th ed.; Butterworth-Heinemann: Oxford, 1992.

8. Loy, D. A.; Shea, K. J. *Chem. Rev.* **1995**, *95*, 1431–1442.

9. Soler-Illia, G. J. A. A.; Sanchez, C.; Lebeau, B.; Patarin, J. *Chem. Rev.* **2002**, *102*, 4093–4138.

10. Wan, Y.; Zhao, D. *Chem. Rev.* **2007**, *107*, 2821–2860.

11. Cundy, C. S.; Cox, P. A. *Chem. Rev.* **2003**, *103*, 663–701.

12. (a) Kresge, C. T.; Leonowicz, M. E.; Roth, W. J.; Vartuli, J. C.; Beck, J. S. *Nature* **1992**, *359*, 710–712; (b) Beck, J. S.; Vartuli, J. C.; Roth, W. J.; Leonowicz, M. E.; Kresge, C. T.; et al. *J. Am. Chem. Soc.* **1992**, *114*, 10834–10843.

13. Hoffmann, F.; Cornelius, M.; Morell, J.; Fröba, M. *Angew. Chem. Int. Ed.* **2006**, *45*, 3216–3251.

14. Attard, G. S.; Glyde, J. C.; Göltner, C. G. *Nature* **1995**, *378*, 366–368.

15. (a) Huo, Q. S.; Margolese, D. I.; Ciesla, U.; Feng, P. Y.; Gier, T. E.; Sieger, P.; Leon, R.; Petroff, P. M.; Schuth, F.; Stucky, G. D. *Nature* **1994**, *368*, 317–321; (b) Huo, Q. S.; Margolese, D. I.; Ciesla, U.; Demuth, D. G.; Feng, P. Y.; Gier, T. E.; Sieger, P.; Firouzi, A.; Chmelka, B. F.; Schüth, F.; Stucky, G. D. *Chem. Mater.* **1994**, *6*, 1176–1191.

16. Liu, N.; Assink, A.; Smarsly, B.; Brinker, C. J. *Chem. Commun.* **2003**, 1146–1147.

17. Sakamoto, Y.; Kaneda, M.; Terasaki, O.; Zhao, D. Y.; Kim, J. M.; Stucky, G.; Shin, H. J.; Ryoo, R. *Nature* **2000**, *408*, 449–453.

18. (a) Israelachvili, N.; Mitchell, D. J.; Niham, B. W. *J. Chem. Soc., Faraday Trans. 2* **1976**, *72*, 1525–1568; (b) *Intermolecular and Surface Forces*, 2nd ed.; Israelachvili, J., Ed.; Academic Press: New York, 1992.

19. Huo, Q.; Margolese, D. I.; Stucky, G. D. *Chem. Mater.* **1996**, *8*, 1147–1160.

20. (a) Zhao, D.; Feng, J.; Huo, Q.; Melosh, N.; Fredrickson, G. H.; Chmelka, B. F.; Stucky, G. D. *Science* **1998**, *279*, 548–522; (b) Zhao, D.; Huo, Q.; Feng, J.; Chmelka, B. F.; Stucky, G. D. *J. Am. Chem. Soc.* **1998**, *120*, 6024–6036.

21. 'Exotemplates' are macroscopic templates that maintain their shape under the mesoporous synthesis conditions, but then are etched away from the as-synthesized materials to reveal the final product. These may include, for example: (i) colloidal latex spheres that may be used as a template for the formation of macroscale pores; (ii) porous, anodic alumina membranes that may be used as molds for the formation of nanowires; and (iii) mesoporous silica that may be used as a template for the formation of mesoporous carbon.

22. Wu, Y.; Cheng, G.; Katsov, K.; Sides, S. W.; Wang, J.; Tang, J.; Fredrickson, G. H.; Moskovits, M.; Stucky, G. D. *Nature Mater.* **2004**, *3*, 816–822.

23. Li, F.; Wang, A.; Stein, A. *Angew. Chem. Int. Ed.* **2007**, *46*, 1885–1888.

24. Rebbin, V.; Schmidt, R.; Fröba, M. *Angew. Chem. Int. Ed.* **2006**, *45*, 5210–5214.

25. Wang, J.; Li, Q.; Knoll, W.; Jonas, U. *J. Am. Chem. Soc.* **2006**, *128*, 15606–15607.

26. (a) Inagaki, S.; Guan, S.; Fukushima, Y.; Ohsuna, T.; Terasaki, O. *J. Am. Chem. Soc.* **1999**, *121*, 9611–9614; (b) Melde, B. J.; Holland, B. T.; Blanford, C. F.; Stein, A. *Chem. Mater.* **1999**, *11*, 3302–3308; (c) Asefa, T.; MacLachlan, M. J.; Coombs, N.; Ozin, G. A. *Nature* **1999**, *402*, 867–871.

27. (a) Hoffmann, F.; Fröba, M. *Chem. Soc. Rev.* **2011**, *40*, 608–620; (b) Hunks, W. J.; Ozin, G. A. *J. Mater. Chem.* **2005**, *15*, 3716–3724.

28. Hatton, B.; Landskron, K.; Whitnall, W.; Perovic, D.; Ozin, G. A. *Acc. Chem. Res.* **2005**, *38*, 305–312.

29. (a) Yanagisawa, T.; Shimizu, T.; Kuroda, K.; Kato, C. *Bull. Chem. Soc. Jpn.* **1990**, *63*, 988–992; (b) Yanagisawa, T.; Shimizu, T.; Kuroda, K.; Kato, C. *Bull. Chem. Soc. Jpn.* **1990**, *63*, 1535–1537; (c) for a review, see: Kimura, T.; Kuroda, K. *Adv. Mater.* **2009**, *19*, 511–527.

30. Inagaki, S.; Fukushima, Y.; Kuroda, K. *J. Chem. Soc., Chem. Commun.* **1993**, 680–682.

31. Inagaki, S.; Fukushima, Y.; Kuroda, K. *Stud. Surf. Sci. Catal.* **1994**, *84*, 125–132.

32. Sanchez, C.; Rozes, L.; Ribot, F.; Laberty-Robert, C.; Grosso, D.; Sassoye, C.; Boissiére, C.; Nicole, L. *C. R. Chimie* **2010**, *13*, 3–39.

33. Sanchez, C.; Julián, B.; Belleville, P.; Popall, M. *J. Mater. Chem.* **2005**, *15*, 3559–3592.

34. Nakanishi, K.; Tanaka, N. *Acc. Chem. Res.* **2007**, *40*, 863–873.

35. Han, Y.; Zhang, D.; Chng, L. L.; Sun, J.; Zhao, L.; Zou, X.; Ying, J. Y. *Nature Chem.* **2009**, *1*, 123-127.

36. (a) S. Inagaki, S.; Guan, S.; Ohsuna, T.; Terasaki, O. *Nature* **2002**, *416*, 304–307; (b) Kapoor, M. P.; Yang, Q.; Inagaki, S. *J. Am. Chem. Soc.* **2002**, *124*, 15176–15177.

37. Cotí, K. K.; Belowich, M. E.; Liong, M.; Ambrogio, M. W.; Lau, Y. A.; Khatib, H. A.; Zink, J. I.; Khashab, N. M.; Stoddart, J. F. *Nanoscale* **2010**, *1*, 16–39.

38. MacQuarrie, S.; Thompson, M. P.; Blanc, A.; Mosey, N. J.; Lemieux, R. P.; Crudden, C. M. *J. Am. Chem. Soc.* **2008**, *130*, 14099–14101.

39. Tani, T.; Mizoshita, N.; Inagaki, S. *J. Mater. Chem.* **2009**, *19*, 4451–4456.

Chapter 2

Surfactant-Templated, Mesoporous Organosilica Films as Functional Overlays for Fibre-Optic Heavy Metal Detection

2.1 Introduction

Presently, the acquisition and analysis of water samples from the areas surrounding industrial plants, mines, and landfills is a time-consuming and costly process. For example, after first identifying an area and the target analytes to survey, as well as physically collecting the samples for an environmental assessment of a given site, a number of intermediate steps may have to be carried out by a technician before actual measurement of the analytes.[1] These steps may include sample pretreatments such as the concentration of the sample, extraction of the analyte from the sample matrix, or acidification of the sample, among others. With all of these added steps, care must be taken to avoid issues such as loss, contamination, and decomposition of the sample during handling and storage, which would compromise the integrity of the sample. Furthermore, the risk for encountering such complications increases particularly when the sampling is conducted at a remote site without on-site access to analytical laboratory facilities.[1] However, no alternatives are presently available that significantly improve upon this process. The overarching objective of this project is to design and build a chemically-selective fibre-optic sensor for heavy metal contaminants that would be able to affect on-line detection, measurement, and monitoring of water quality with relatively short response times.

The release of toxic heavy metals into the environment significantly impacts both the quality of the environment and human health. With the aim of, "respecting pollution prevention and the protection of the environment and human health in order to contribute to sustainable development," the Government of Canada put forth the *Canadian Environmental Protection Act, 1999* (CEPA, 1999), and has notably listed the following heavy metal species on its 'List of Toxic Substances': mercury; lead; inorganic cadmium compounds; and hexavalent chromium compounds.[2] The heavy metal species of main interest in our research are mercury(II) and lead(II).

Mercury, in its stable, geological form, can be released into the environment through several different processes. These include, for example, the release due to natural geological activity (such as volcanic eruptions), the burning of coal to produce electricity, as well as release resulting from the manufacture, use, and disposal of mercury-containing products, and discharge from industrial plants that directly use mercury in their processing activities. Total global mercury emissions are estimated to be 5,000 tonnes per year with 50–80% of that number being attributed to anthropogenic activity.[3] Elevated levels of mercury in the environment are cause for concern due to the conversion of metallic and inorganic mercury into its more toxic organic forms (namely, methylmercury), which has been demonstrated to have devastating health effects in animals and humans.[3,4] Organic mercury can accumulate biologically and appear in more concentrated levels further up the food chain, increasing the risk of human exposure to potentially poisonous levels of organic mercury. Once accumulated in the body, mercury

can, for example, cause birth defects, as well as damage to the brain, central nervous system, and kidneys.[2,3,4,5]

In similar fashion, the release of lead into the environment is largely affected by human activity, as well. For example, lead is released into the air via industrial emissions, as well as the activities of smelters and refineries. Furthermore, it is commonly found in lead-based solder, old pipes, as well as some paints and types of glass, further increasing the number of pathways through which lead can be introduced into the air, water, soil, and food supply, resulting in its bioaccumulation. As with mercury, once accumulated in the body, lead can also give rise to disorders of the central nervous system, affect intellectual development, and have many other devastating biological effects.[1,6]

The standard techniques presently used for the detection and measurement of mercury and lead species in environmental samples are atomic absorption spectrometry (AAS), atomic emission spectrometry (AES), and inductively coupled plasma mass spectrometry (ICP-MS) and their variations.[1,4] However, despite their high sensitivities to trace levels of heavy metals, these techniques are expensive, time-consuming, and not easily amenable to on-site and on-line testing.

More recently, heavy metal detection and measurement based on electrochemical, surface-enhanced Raman scattering (SERS), surface plasmon resonance (SPR), bio-sensing, colorimetric, and fluorescence-based techniques have been of popular interest in the chemical literature.[7] For example, in the case of fluorescence-based approaches, a

wide variety of probe / tag molecules such as modified pyrenes,[8] calixarenes,[9] and related heteroatom-substituted macrocycles[10] have been synthesized (Scheme 2-1) and are reported to have excellent sensitivities and selectivity.[5,11] These approaches work by employing specially designed ligands to chelate or react with target metal analytes, resulting a change in either the fluorescence emission or quenching behaviour of the metal–ligand complex relative to the free ligand in either aqueous, organic, or mixed aqueous–organic solution. However, many of these methods and their embodiments still rely largely on classical, benchtop spectroscopic instrumentation for the detection read-out and are thus also not easily amenable to on-line / in-situ environmental monitoring.

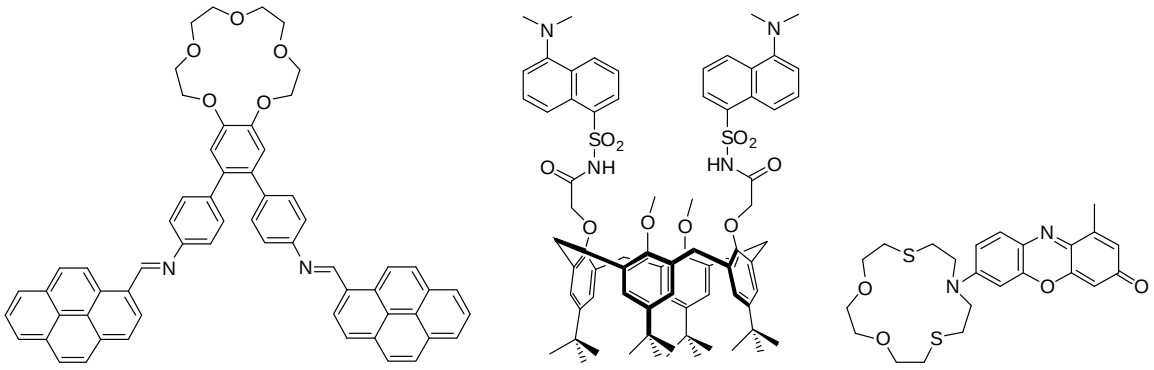

1 **2** **3**

Scheme 2-1. Examples of modified pyrene- (**1**),[8] calixarene- (**2**),[9] and heteroatom-substituted crown-type[10] (**3**) fluorescent probes developed for the detection of Hg(II) ion in solution.

To address the high demand for a quick and efficient method for the detection and measurement of toxic heavy metals in the environment, fibre-optic sensors are an attractive option for several reasons. Firstly, being electrically passive, fibre-optic sensors are unaffected by external electromagnetic interference and can therefore be used in close proximity to other electrical devices and power sources.[12,13] Fibre-optic sensors are also small in diameter (generally 125 μm) and flexible. Hence, the sensor and the related instrumentation can be packaged in a more portable form, allowing for a "lab-on-a-chip" type of device that can be used for on-site testing. Additionally, traditional spectroscopic methods of detection and measurement may be integrated into the fibre-optic platform, along with the possibility of multiplexing sensor arrays to allow for the simultaneous detection of several different analytes.[14] Moreover, fibre-optic cables can be designed to send information by telemetry,[14] providing access to remote locations such as the DEW Line (Distant Early Warning Line) sites in the Canadian Arctic, which are otherwise inaccessible or very expensive to monitor by personnel in the field, as is the current practice.

The optical sensing element employed in this research is a long-period grating (LPG) (Scheme 2-2). This is a diffraction grating that consists of a periodic modulation of the refractive index (RI) in the core region of a single mode fibre-optic (SMF) waveguide. This grating is commonly etched into the waveguide by laser irradiation of the fibre-optic cable while it is covered with a mask designed to yield an LPG of a given length and periodicity.[15] Light guided by the fibre-optic cable travels within the core until it encounters the grating, at which point the guided core mode may couple with

discrete cladding modes, resulting in attenuation of the propagated light at specific wavelengths (Figure 2-1). The wavelengths (otherwise known as resonant wavelengths, λ_f) at which coupling losses are observed are described by Equation 2-1:[15,16]

$$\lambda_f = \Lambda[n_{eff,\,core}(\lambda, n_{core}, n_{clad}) - n^i_{eff,\,clad}(\lambda, n_{core}, n_{clad}, n_a)] \qquad \textbf{(2-1)}$$

where Λ is the period of the grating (which is on the order of hundreds of microns), and $n_{eff,\,core}$ and $n^i_{eff,\,clad}$ correspond to the effective RIs of the core and cladding, respectively (for a mode of order i). Importantly, $n_{eff,\,core}$ and $n^i_{eff,\,clad}$ are functions of the operating wavelength, λ, as well as of n_{core}, n_{clad}, and n_a, which are the actual RIs of the core, cladding, and ambient environment, respectively.[17]

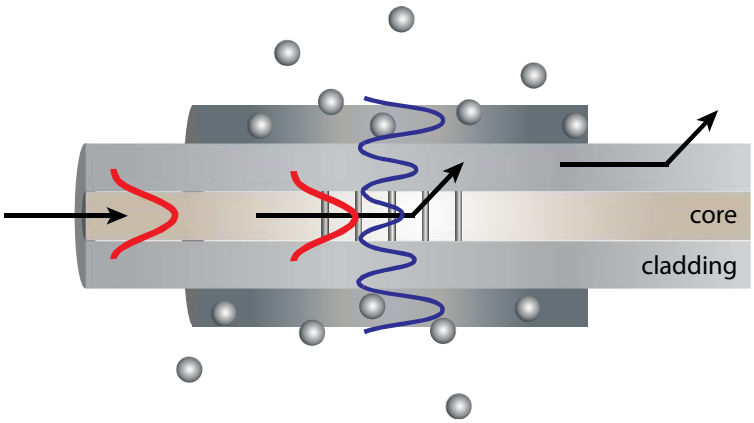

Scheme 2-2. Schematic representation of a long-period grating (LPG) inscribed into the core region of a fibre-optic waveguide. At the LPG, the propagating core mode (red) couples (i.e. overlaps) with a higher order cladding mode (blue), which can extend past the cladding–film interface if the fibre-optic waveguide is coated with an index-matched film at this location.

In addition to the order, i, of the cladding mode of interest, the effective RI of the cladding, $n^{i}_{eff,\ clad}$, is affected by the interaction of the evanescent field (generated at the cladding–environment interface) with the external environment.[18] Consequently, the effective RI of the cladding is a function of both the RI of the cladding and that of the surrounding environment. A change in the RI of the external environment (e.g. by absorption of a target chemical species) will, therefore, cause a shift in the position of the resonant wavelength, λ_f, according to Equation 2-1 (Figure 2-1). ***An LPG-based sensor thus is an optical sensor that responds to changes in RI***, which is in contrast to other types of optical sensors that operate on the principles of, for example, changes in reflectance, absorption, or fluorescence.

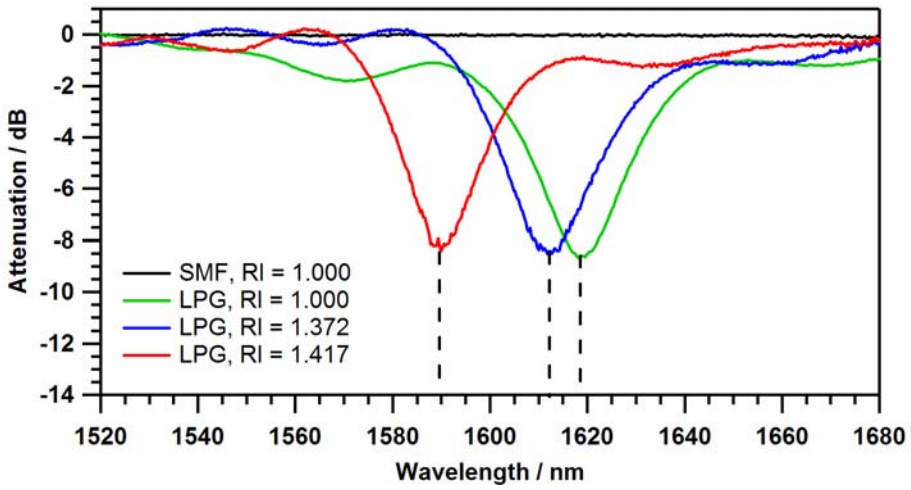

Figure 2-1. Representative attenuation spectra for a standard single-mode fibre (SMF) in air (black trace) in comparison to an LPG-inscribed, cladding-etched SMF (grating length = 25 mm, periodicity = 320 μm) under exposure to air (green trace) and water / DMSO solutions (RI at 1550 nm) (blue and red traces). The blue-shift of the resonant peak with increasing RI of the surrounding environment is indicated by the dashed lines. (Data courtesy of Prof. Hans-Peter Loock, Queen's University.)

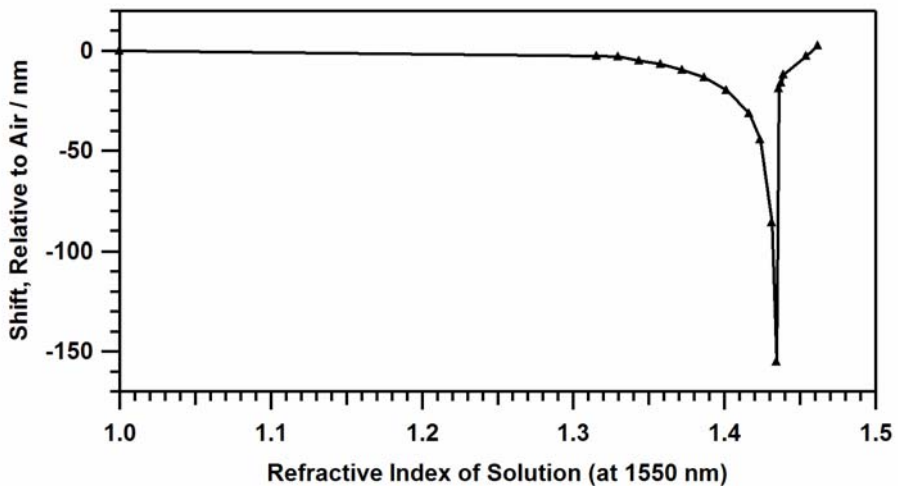

Figure 2-2. A plot illustrating the non-linear resonant peak shift behaviour for the bare, uncoated LPG of Figure 2-1 as a function of the RI of the surrounding environment. (Data courtesy of Prof. Hans-Peter Loock, Queen's University.)

As can be seen in Figure 2-2, the sensitivity of the LPG increases as the RI of the external environment approaches that of the cladding (~ 1.44 at 589 nm).[15,19,20] Therefore, the sensitivity of an LPG's response to changes in the external environment can be maximized by depositing an overlay on the cladding with an RI that – when immersed in solution – closely matches that of the cladding. In this RI region, the overlay may then effectively act as an extension of the cladding (i.e. a layer without an optical discontinuity with respect to the cladding), maximizing the evanescent field present in the region of the overlay[21] and allowing for dramatic shifts in the position of the resonant peak upon binding of a target analyte.

Various fibre-optic sensor platforms have been previously established.[22a] For example, in the simplest case, unmodified fibre-optic waveguides have been configured

to directly measure the absorbance of heavy metal species in solution.[22b] However, these 'plain fibre sensors' lack analyte specificity and can only detect metals at relatively high concentrations due to the inherently low molar absorptivities of the metal species.[22a] In more sophisticated assemblies, the fibre-optic waveguides are used to transmit light to and / or from a solution containing indicator dyes that interact with metal analytes from which absorbance or emission data may be obtained.[22c] In another variation, the ends of cleaved fibre-optic cables may also be coated with functionalized materials that interact with the metal analytes from which either reflectance or fluorescence data may also be obtained.[22d,22e] However, only a very limited number of examples employing LPGs as RI sensors for chemical detection have been reported in the peer-reviewed literature. These include PDMS-[16] and zeolite-coated[23] LPG sensors for the detection of small, hydrophobic, organic compounds, as well as bare LPGs used for the determination of chromium,[24] and sodium and calcium[25] salt solution concentrations. Although relatively high RI sensitivity has been observed in some of these embodiments, the metal sensors either detected the presence of the metal species indirectly or, in a critical flaw, lacked functionalization that would allow for the detection of specific analytes.

The research described herein focuses on the design and synthesis of high-affinity and chemically-selective thin film coatings that meet both the optical and physical requirements of the fibre-optic LPG sensor. In addition to the issue of closely matching the RI of the material to that of the cladding (as previously discussed), there are several other criteria that need to be satisfied. The film should be chemically-selective for a given target analyte, relatively thick (i.e. > ~ 1–3 μm in thickness), and have a high

degree of interconnected porosity to maximize through-film diffusion and ensure accessibility of the binding sites within the material to the analyte. In addition, of course, the film should be mechanically robust and chemically stable.

To meet many of the above criteria for the overlay, organically-modified porous silicas have been explored in this research to create functional materials. Silica is a natural choice for the matrix material because the fibre-optic waveguides are also silica-based, thus allowing for better matching of the physical and optical properties between the film and fibre. In addition, silica – once condensed – is less likely to swell upon exposure to water and / or organic solvents (in contrast to some conventional cross-linked polymers), improving the reliability of the sensor response in solution media. For all of the aforementioned reasons, it was decided that organosilicas were ideal candidates for functional sensor overlay materials.

At the outset of this project, the preparation of porous, amorphous, organosilica xerogel films by sol-gel processing was first explored. However, after encountering significant complications with respect to the reliable synthesis of thick films (> 1 μm in thickness) by this route, surfactant-templated sol-gel methodologies were instead pursued with much greater success.

The first report detailing the synthesis of mesoporous silica films by a surfactant-templating strategy was presented by Ogawa in 1994[26] and the field has since experienced unrelenting growth and expansion. Surfactant-templated sol-gel silica films[27] may be prepared by a few different methods, the most common of which are by:

(i) evaporation; and (ii) spontaneous growth from solution.[28,29,30] In the case of the mesostructured film formation by evaporative methods, 'evaporation-induced self-assembly' (EISA) has taken over as the synthetic method of choice.[31,32,33] Importantly, this synthetic methodology is amenable to conventional processing methods presently used in industrial / commercial settings such as spin-coating, dip-coating, casting, or spray-coating for the preparation films.

Typically, a dilute and homogeneous sol composed of the templating agent (present at a concentration below its critical micelle concentration), the inorganic precursor(s), and an aqueous catalyst is prepared in a polar and volatile organic solvent, and is subsequently deposited onto the desired substrate by one of the aforementioned methods. Immediately after deposition of the coating onto the substrate, evaporation of the solvent occurs and self-assembly of the surfactant and silica precursors is initiated as the effective concentration of these species increases within the film. At the same time, the water content within the deposited film equilibrates with respect to the relative humidity of the surrounding atmosphere, and condensation of the siloxane network progresses around the supramolecular template structures to form a solid matrix.[28,29,30,31,32,33] The interplay and interdependent nature of these steps is illustrated in Scheme 2-3.

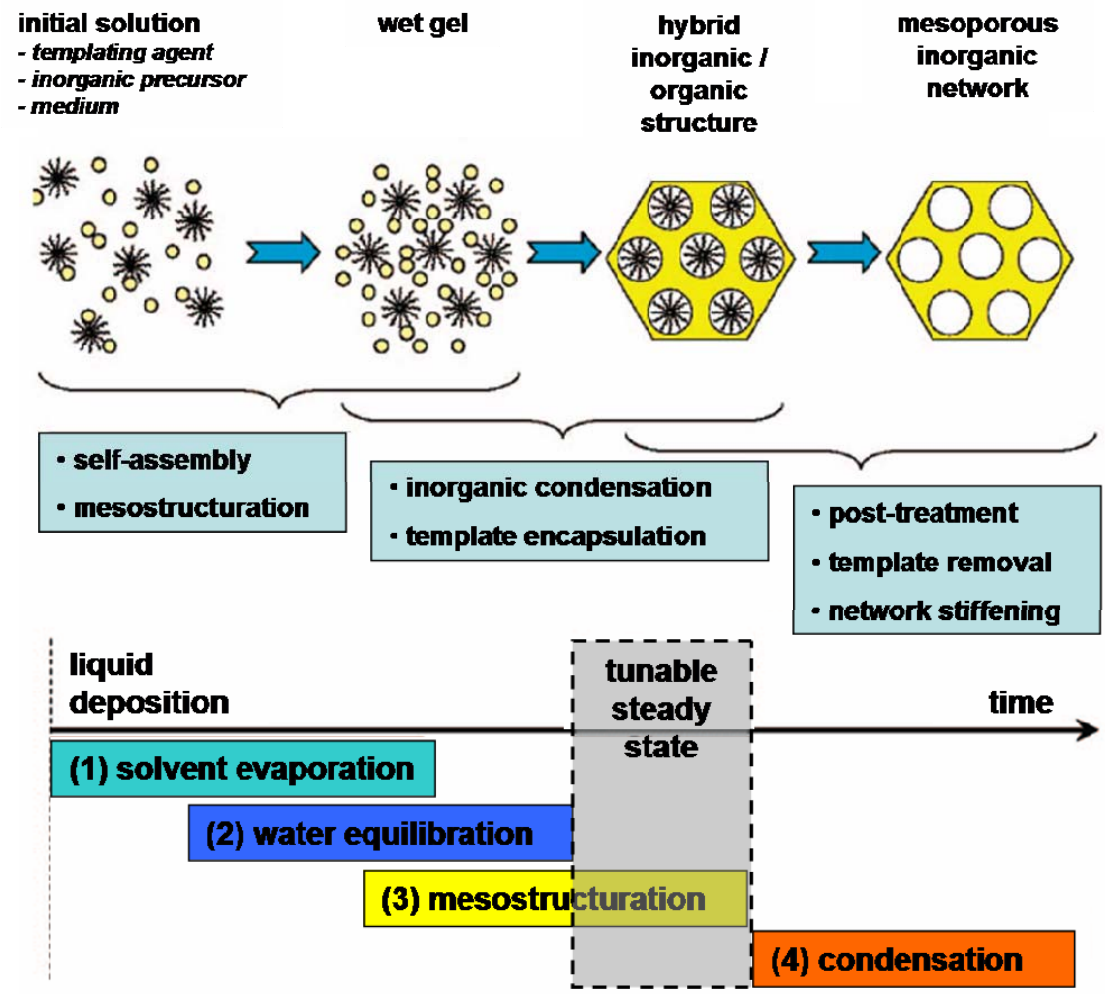

Scheme 2-3. Schematic representation of the various steps involved in the synthesis of mesostructured films by EISA. (Scheme taken from reference 30.)

It should also be noted that in the time period between establishing an ordered surfactant–silica array and reaching a high extent of siloxane condensation within the silica framework, the as-synthesized film lies within a 'tunable (or modulable) steady state'. Here, a change in the atmospheric conditions (i.e. the vapour pressures of water

and / or solvent) surrounding the wet, as-synthesized film can potentially lead to a transformation in the mesostructural order within the film.[34]

Therefore, the critical parameters that affect the mesostructure of the final product may be divided in three different categories, which include: (i) the chemistry of the starting sol (prior to coating); (ii) the conditions of the coating process itself; and (iii) the post-synthetic treatment conditions used to consolidate the siloxane network and remove the templating species. Furthermore, among these categories, the following variables are of particular interest: (i) the surfactant-to-silane ratio in the starting sol; (ii) the extent of siloxane condensation within the coating sol prior to deposition (which is affected by the amount of catalyst in the sol and the aging conditions leading up to film deposition); (iii) the relative humidity of the surrounding environment; (iv) the rate of film deposition (which influences the resulting film thickness and the rate of solvent evaporation from the surface of the film); (v) the final treatments employed to stabilize the mesostructure (usually a thermal treatment step); and (vi) the template removal conditions.[28,29,30,31,32,33]

Consequently, surfactant-templated, mesostructured film synthesis by EISA is an appealing approach as the final properties of the resulting films may be tuned via modification of a number of different variables and the films may be prepared using industrially-relevant processes. Moreover, the large number of possible combinations of synthetic conditions can lead, in principle, to a rich variety of films. However, the dynamic relationship between all of these interdependent parameters can make tuning of the film synthesis procedure relatively complex. Strict control of the various processing

conditions is, therefore, of paramount importance if reproducible film synthesis is to be achieved.

In the case of film growth from solution (occasionally referred to as 'hydrothermal growth'), two major variants exist: (i) the formation of free-standing films at a water–oil or water–air interface; and (ii) the growth of a substrate-attached film from a substrate submerged in solution (i.e. film growth from the substrate–solution interface).[28,29,30] With these approaches, film formation is encouraged through the concentration of the sol reagents at the interface of interest. Typically, film formation takes much longer with these methods than with the EISA method (e.g. several hours or days versus minutes, respectively), but offer a means of obtaining films with unique properties. For example, thick, free-standing membranes may be obtained,[35] in addition to films bearing 'single-crystalline' mesostructuration.[36]

Additional strategies for the formation of mesostructured metal oxide-based films also exist such as vapour impregnation of a pre-formed block copolymer template, electrodeposition, and laser deposition, to name a few.[30] However, given the relative ease with which films can be produced in a short stretch of time, as well as the ability to extend such coating strategies to commercial platforms – which would be of importance in our proposed fibre-optic sensing device – EISA is the method of choice for the work presented in this chapter.

Eventually, both Hg(II) and Pb(II) detection in mixed aqueous–organic systems was demonstrated using these templated, mesoporous organosilica films bearing thiol and

tetrasulfide ligands, respectively, in conjunction with the LPG sensing platform.[37,38,39] The details regarding our endeavours with this project are documented in the following sections.

Additionally, in the sections below, we will also present our efforts toward the demonstration of heavy metal ion detection in purely aqueous systems using mesoporous, titania-based hybrid films, as well as our attempts to employ these mesoporous organosilica materials as functional coatings with other evanescent wave sensing devices (namely silicon-on-insulator (SOI) microchip interferometers).

At this time, it should be noted that given the limited availability of LPGs supplied to us by our industrial partner, Avensys / ITF Labs (Montréal, QC), the majority of the films produced in this project have been coated onto glass microscope slides, high-index glass wafers, or single-crystalline silicon wafers (all activated by base or Piranha etching – ***CAUTION: Piranha solution is an extremely energetic and potentially explosive mixture!*** – to expose fresh surface silanol groups prior to coating) for characterization and optimization. Thereafter, films were only coated onto LPGs on selected occasions to evaluate the optical response upon interfacing the films with the optical sensing element.

2.2 Amorphous Organosilica Sol-Gel Films

The solution-based synthesis of both non-porous and porous silica materials dates back several decades.[40] Given the ease with which silica-based materials may be

prepared using sol-gel chemistry (as discussed in Chapter 1), it is not surprising that these materials have been explored in a variety of compositions, morphologies, and applications. Accordingly, we first explored the synthesis of non-templated, amorphous, porous silica and organosilica coatings as functional overlays for our proposed fibre-optic sensor.

Thiol functionalities were employed to provide selectivity for the absorption of Hg(II) ions since these have previously been shown in the literature to be extremely effective ligands for Hg(II) binding (even in the presence of competing metal ions).[41,42,43] The ligands were incorporated into the silica-based films using (3-mercaptopropyl)trimethoxysilane (**MPTMS**) as the co-condensable precursor (see Scheme 2-4).

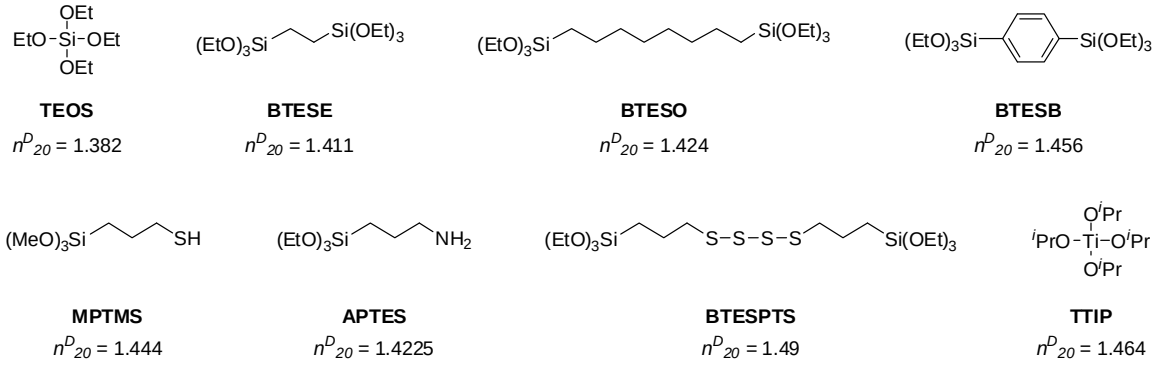

Scheme 2-4. Schematic representations of all of the main condensable sol-gel precursors used in the work described in this chapter, along with their acronyms and the refractive indices of each precursor (reported at the sodium D-line wavelength of 589 nm at 20 °C) in its uncondensed state.[44]

Firstly, though, we briefly explored the silylation of the surface of LPGs with a monolayer (or – more likely – a thin multilayer) of mercaptopropyl moieties to see if a concentrated presence of the metal-binding ligands at the cladding–solution interface would be enough to generate an optical response upon Hg(II) absorption. However, no resonant peak shifts were observed upon exposure of the functionalized LPGs to aqueous Hg(II) solutions of concentrations up to 1000 ppm.

We then turned to silica xerogel films as a launching point for our attempts at preparing suitable LPG overlays. The majority of our efforts were centered on a process we adapted from the reports of Plawsky and co-workers for a two-step both acid- and base-catalyzed procedure for the synthesis of spin-coated films using **TEOS** as the precursor.[45] Our general procedure for synthesizing silica and thiol-modified organosilica xerogel films is outlined in Section 2.6.4.

Both **TEOS**-only and **MPTMS–TEOS** films processed using relatively freshly prepared sols yielded thin films (~ 500 nm in thickness, as determined by profilometry) that showed excellent surface coverage and reasonably good adherence to the test substrates (either microscope slides, high-index glass wafers, or silicon wafers) after solution aging and subsequent curing at temperatures up to 120 °C.

To determine the RI of these films and to see if the RIs could be tuned by varying the amount of thiol incorporated into the starting sols and other synthetic parameters, an in-house built Abbé-type refractometer (built and generously provided for our use by the Loock research group at Queen's University) was used. With this particular set-up, a

beam of light refracted by the sample of interest floods a charge-coupled device (CCD) camera over a certain area. If the sample RI lies within the RI range for which the instrument is calibrated, the CCD camera will show an image comprised of two distinct regions: one illuminated and one not illuminated. The position (i.e. pixel) at which this boundary appears correlates to a given value for sample RI that depends on the configuration and calibration of the instrument (see Scheme 2-5 and Figure 2-3 for an example).[46] Unfortunately, reliable and reproducible measurements of RI were not possible on this instrument with our silica-based films. It was rare to see a distinct and sharp interface / boundary in the images captured by the CCD camera, which lead to wide variability in the interpretation of the corresponding RI of the film. Two examples of some of our better – yet still ambiguous – CCD images obtained with these films are shown in Figure 2-4. In particular, it should be noted that Figure 2-4 shows two images recorded for one particular film, but both images are quite different in appearance. In Figure 2-4a, an interface may be deciphered, but the fringe pattern observed in Figure 2-4b complicates the identification of the position of the true interface.

Complications with film RI determination aside, despite the seeming ease with which continuous and relatively robust thin silica xerogel films could be synthesized, the adaptation of such procedures to yield thick and continuous sol-gel-derived films (> 1 μm in thickness) proved significantly challenging. Specifically, after evaporating solvent from the coating sols through either ambient evaporation or heating at moderate temperatures (i.e. between 45–70 °C) to yield more viscous sols, thick films were prepared by spin-coating, dip-coating, or drop-casting. Importantly, it should be

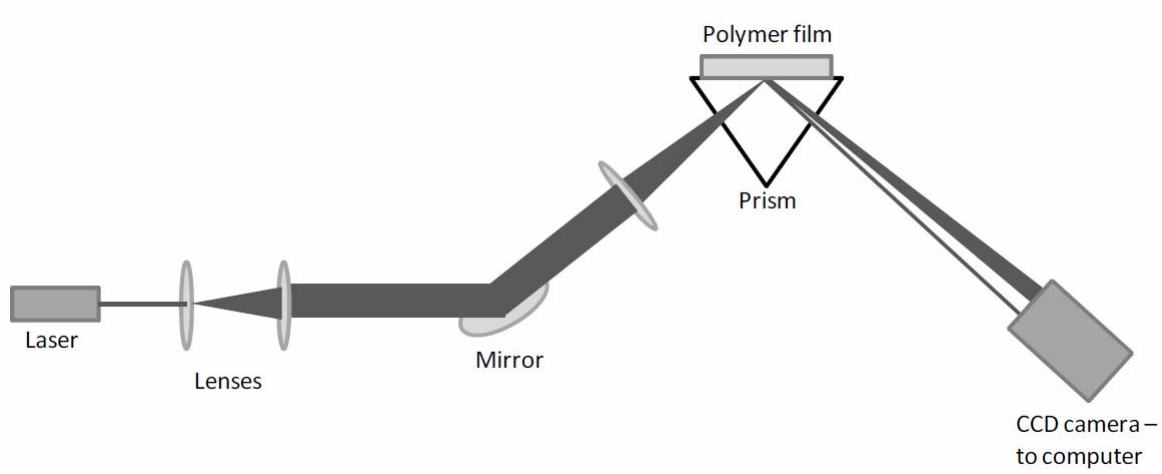

Scheme 2-5. Schematic representation of the refractometer set-up used for the determination of silica and organosilica film RIs. The path of the laser light (indicated in dark grey) is expanded and focused with a series of mirrors and lenses, respectively. At the CCD detector, part of the screen is illuminated, while another part of the screen is not illuminated (as indicated by the blank / 'white' path). The position of the boundary between the illuminated and non-illuminated regions of the CCD read-out is correlated to the RI of the sample film. (Scheme taken from reference 46b.)

noted that the window within which viscous sols could be obtained and used for coating was quite narrow as the onset of sol gelation occurred very quickly – and beyond this point, the sol could no longer be used for preparing coatings. In addition, the resulting thick films notoriously cracked catastrophically and often pulled away from the substrates while they were dried either ambiently or at moderately elevated temperatures.[47]

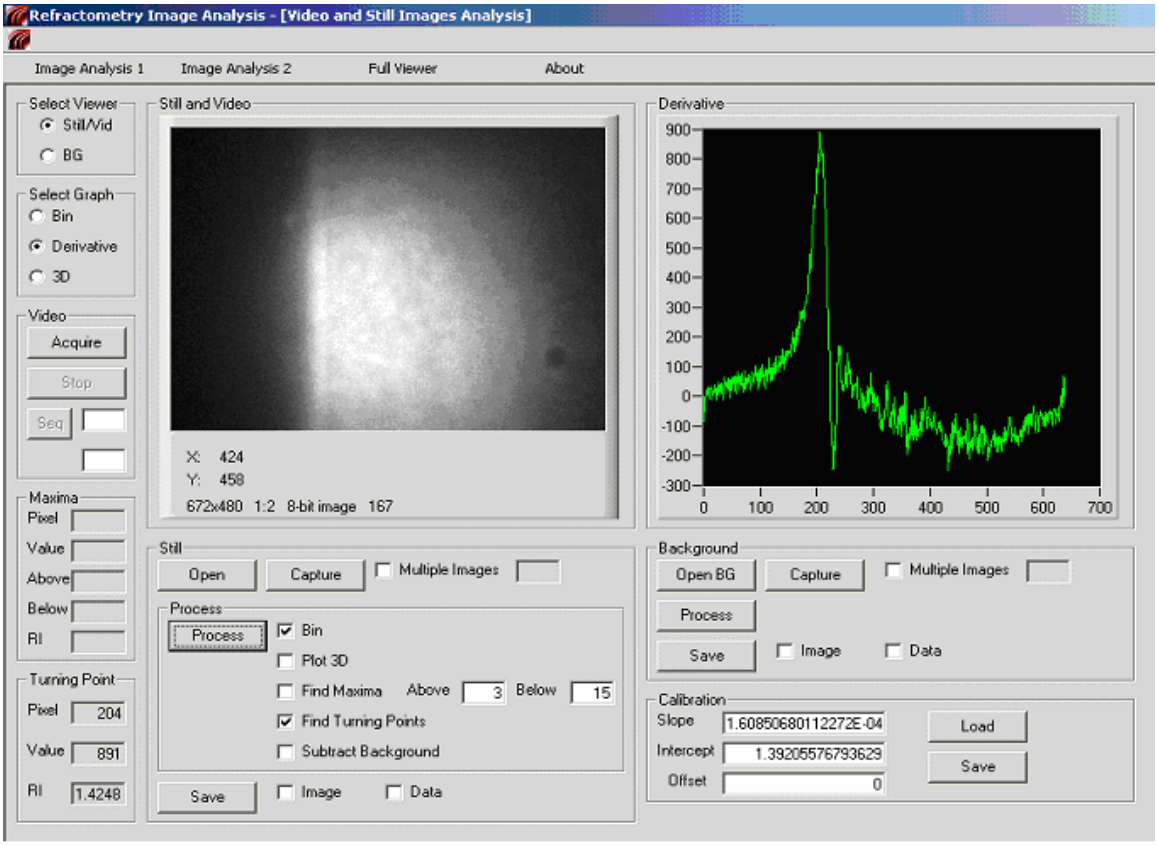

Figure 2-3. A sample of the screen read-out obtained using the software (written by Mr. Nick Trefiak, formerly of Queen's University) coupled to the refractometer. The captured image (left) is vertically binned and the first derivative of the image intensity is taken and displayed (right). The software computes and outputs the pixel at which the turning point in the derivative plot occurs (bottom left). Given the parameters for the calibration of the instrument (bottom right), the pixel position is translated into a value for the RI of the sample sitting on top of the refractometer prism. The image displayed, here, is for a sample solution composed of 60 vol% DMSO in water at a laser wavelength of 589 nm. (Image taken from reference 46.)

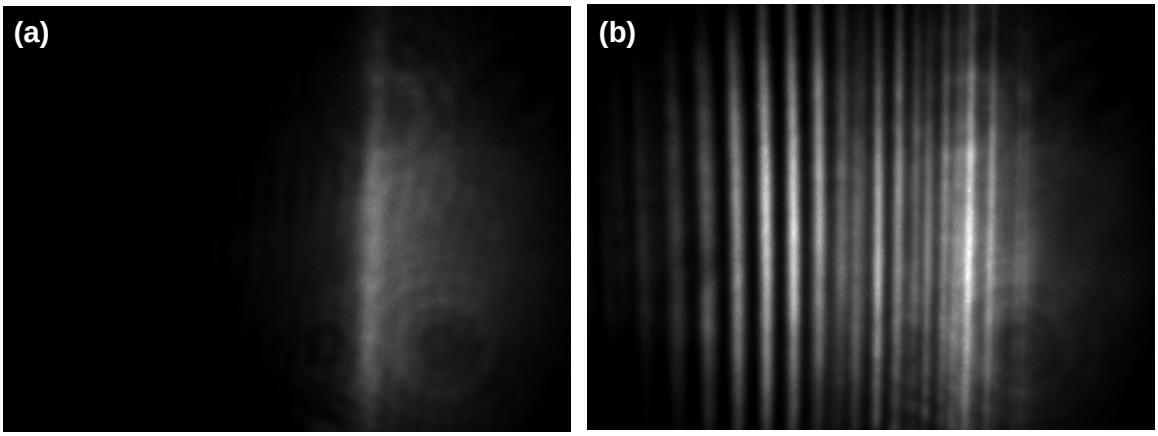

Figure 2-4. Two different CCD camera images recorded for a the same xerogel film sample (25 mol% **MPTMS** co-condensed with **TEOS**, prepared in a sol using *t*-BuOH as the solvent) aligned slightly differently on the refractometer prism.

A number of different strategies were pursued in an effort to mitigate the cracking and subsequent disintegration of these films during drying. Shrinkage and cracking of the films during the drying stage is most commonly attributed to the inability of the porous material to withstand the capillary pressure (P_c) exerted on its framework due to the receding meniscus of the solvent at the solvent–skeleton interface, which is quantified by:

$$P_c = -\frac{2\gamma_{LV}\cos(\theta)}{r} \qquad \textbf{(2-2)}$$

where the negative sign implies that the liquid is in tension, γ_{LV} is the surface tension of a given solvent at the liquid–vapour interface, θ is the contact angle for the solvent in contact with the skeleton surface, and r is the radius of the pore from which the solvent is emptying.

The strategies subsequently explored in this work were thus applied with the intention of either reducing the solvent–skeleton interfacial tension, improving the stiffness of the silica skeleton, or a combination thereof, and are summarized below in Table 2-1.[48] To our disappointment, none of these strategies proved sufficient to overcome the drying stress exerted on the thick films. Additionally, particularly after post-synthetic treatment by aging the films in an alkaline environment, some of the films exhibited heterogeneous, macroscopic phase separation as evidenced by the appearance of opaque particulate silica matter embedded in the films and on the surface of the films, which was also undesirable.

We next decided to briefly explore hybrid silica–organic polysilsesquioxane-type materials. For example, as demonstrated nicely by Shea and co-workers, condensable bridge-bonded bis-silanes could also be used as precursors to prepare inherently porous bulk materials using base-catalyzed procedures.[49] These hybrid silica-organic materials were also reported to have a greater degree of mechanical robustness due to the flexibility imparted on the materials depending on the choice of organic bridging moieties. In particular, we attempted the synthesis of hybrid films using 1,2-bis(triethoxysilyl)ethane (**BTESE**), 1,8-bis(triethoxysilyl)octane (**BTESO**), and 1,4-bis(triethoxysilyl)benzene (**BTESB**) silsesquioxane precursors (see Scheme 2-4).

Unfortunately, yet again, the synthesis of thick films could not be successfully realized. It should also be noted, that although the as-synthesized films satisfactorily covered the substrate surfaces, fine silica-based particulate matter embedded within the

Table 2-1. Summary of strategies explored to improve the quality and integrity of thick, organosilica xerogel films.

Strategy	Purpose	General Outcome and Comments
film processing in a solvent-saturated atmosphere	• decrease the rate of solvent evaporation from the freshly-coated films and thus decrease the drying stress on the siloxane skeleton • allow the skeleton more time to stiffen and thus better withstand the drying stress	• no significant improvements observed • cracking and delamination of the thick films still occurred upon drying
aging of freshly-coated films in an ammonia-based atmosphere	• allow for stiffening of the skeleton through the promotion of further siloxane condensation in order for the films to better withstand the drying stress	• no significant improvements observed • cracking and delamination of the thick films still occurred upon drying
solvent-exchange by immersing freshly-coated films in non-polar solvent (e.g. hexanes)	• exchange the polar, pore-filling solvent in the as-synthesized films for a less polar / non-polar solvent of decreased surface tension in order to decrease the capillary pressure upon solvent evaporation during the drying process	• no significant improvements observed • as-synthesized films were occasionally washed off the substrate surface when immersed into the new solvent • cracking and delamination of films still occurred during the drying of the thick films that survived the solvent-exchange process
aging of freshly-coated films in an alkaline, aqueous solution	• allow for stiffening of the skeleton through the promotion of further siloxane condensation in order for the films to better withstand the drying stress	• no significant improvements observed • precipitation of particulate silica from within the films was frequently observed, resulting in heterogeneous materials • cracking and delamination of the thick films still occurred upon drying
freeze-drying of films prepared with *t*-butanol as the solvent in the coating sol	• freeze-drying of the films theoretically eliminates any capillary pressure within the pores of the films because sublimation of the solvent eliminates the existence of any liquid surface tension at the solvent–skeleton interface	• some improvements observed • transparent and homogeneous films were obtained after freeze-drying • however, upon exposure to aqueous test solutions (e.g. solutions of Hg(II) in acidified DI H_2O), precipitation of particulate silica from within the films was frequently observed – resulting in heterogeneous materials and indicating that the films were not hydrolytically stable

films could often be found with these base-catalyzed polysilsesquioxane syntheses after film aging and drying despite first passing the sols through syringe filters (bearing 0.45 μm Nylon® or Teflon® membranes) prior to film formation by either spin- or dip-coating or solution casting, which is again undesirable.

In the end, despite our best efforts, we found it to be considerably problematic to form thick, homogeneous, and continuous films by either spin-coating, dip-coating, or drop-casting that showed good adherence to the test substrates using these classic sol-gel systems. It was then decided that alternative options for porous silica and organosilica film synthesis should be pursued.

2.3 Surfactant-Templated Mesporous Organosilica Sol-Gel Films

Surfactant-templated materials were next considered as an option for forming functional films due to the increased likelihood of producing porous materials in comparison to the non-templated materials that had previously failed to yield useable results. Furthermore, surfactants have been previously shown to work as *drying control chemical additives* in non-templated sol-gel silica syntheses due to their modification of the surface tension at the interface between the solvent and silica framework.[47] It was thus expected that film processing may be facilitated using this surfactant-templating approach.

As introduced in Section 1.3, the most famous examples of surfactant-templated mesoporous silicas are MCM-41 and SBA-15 materials, both of which possess a 2D

hexagonal mesostructure (see Figure 2-5).[50,51] This 2D hexagonal structure turns out to be a relatively accessible phase using a variety of different surfactants over a wide range of reagent compositions. Despite the ease with which this mesophase may be formed, the relatively low degree of interconnected porosity in this type of structure makes these materials less useful for applications that demand full mass transport through the solid support. Also, when the sols for 2D hexagonal materials are spin-coated or dip-coated to form films, the resultant cylindrical channel arrays tend to align with their long axis lying parallel to the substrate surface,[31,52,53] which further impairs diffusion through the film in the direction normal to the substrate surface. Fortunately, films bearing 3D interconnected pore networks have been synthesized – providing materials that facilitate mass transport through the matrix (see Figure 2-6 for representative examples).[31,54,55]

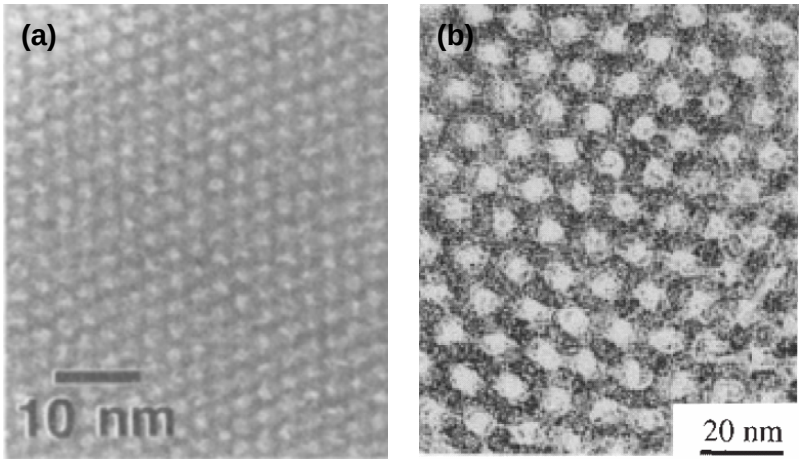

Figure 2-5. TEM images of (a) MCM-41 and (b) SBA-15, displaying the honeycomb mesostructure typically observed for these 2D hexagonally-ordered materials. These images were taken from references 50b and 51a, respectively.

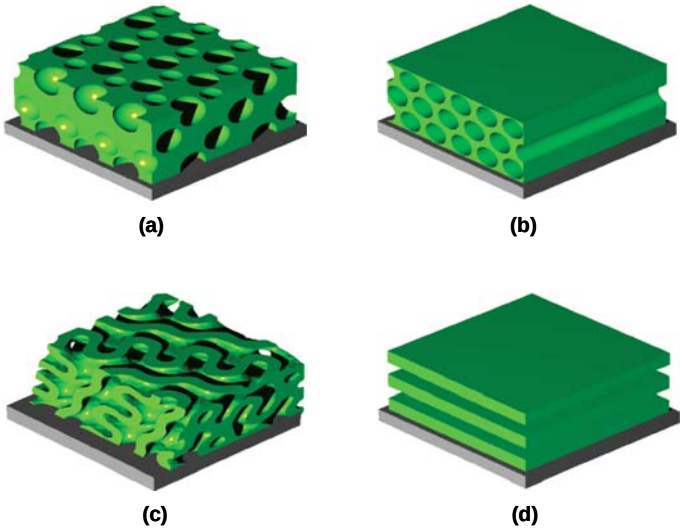

Figure 2-6. 3D renderings of (a) rhombohedral $R\bar{3}m$ (distorted face-centered cubic $Fm\bar{3}m$), (b) 2D rectangular *c2mm* (distorted 2D hexagonal *p6mm*), (c) distorted double-gyroid (distorted cubic $Ia\bar{3}d$), and (d) lamellar mesoporous silica films (siloxane framework shown in green) on support (grey substrate). (Images taken from reference 54b.)

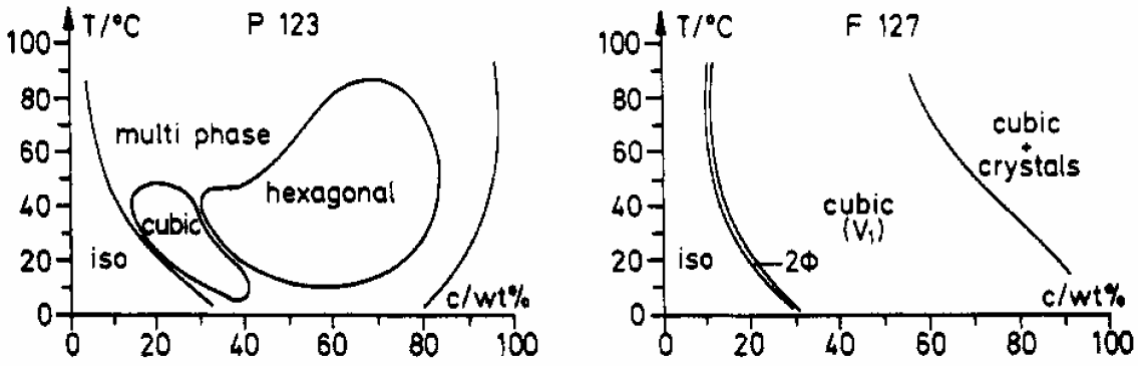

Figure 2-7. Binary phase diagrams for (a) Pluronic® **P123** and (b) Pluronic® **F127** nonionic block copolymers in aqueous solution. Note the relatively large area occupied by the hexagonal phase in the case of the **P123** block copolymer, and the greater occurrence of a cubic phase with the **F127** block copolymer. (Both plots taken from reference 56.)

Depending on the surfactant employed in a given synthetic procedure, cubic and bicontinuous phases are accessible in different regions of a particular surfactant's phase diagram, and some surfactants more readily adopt these mesostructures than others (see Figure 2-7).[56]

2.3.1 First Generation Pluronic® F127-Templated Materials

The synthesis of SBA-type cubic materials by evaporation-induced self-assembly[31,32,33] (EISA) was first attempted following a procedure obtained directly from researchers in the Stucky group at the University of California at Santa Barbara.[57] This synthesis used the nonionic, amphiphilic, triblock copolymer Pluronic® **F127** ($PEO_{106}PPO_{70}PEO_{106}$) (where PEO = poly(ethylene oxide), and PPO = poly(propylene oxide)) (see Scheme 2-6) as the surfactant in acidic media. This block copolymer has been shown to be more effective in preparing cubically ordered materials than the Pluronic® **P123** block copolymer ($PEO_{20}PPO_{70}PEO_{20}$) (see Scheme 2-6) used to synthesize SBA-15,[51b,57] and was thus deemed appropriate for investigation in this particular project.

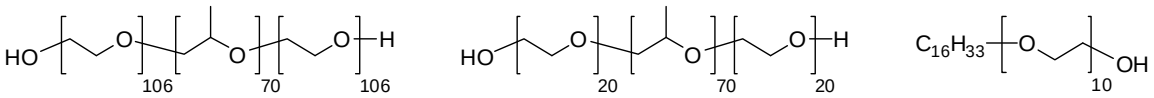

F127 **P123** **B56**

Scheme 2-6. Nonionic, polymeric templates used in this project.

The aged sol for this material (and all surfactant-containing sols prepared hereafter) was much easier to handle in comparison to the non-surfactant-containing sols. The transition from the solution to the gel phase was far less abrupt as the viscosity of the sol increased more gradually with time. This provided a wider window within which to work with the sol. Also, as expected, the films coated at a given spin- or dip-coating rate also became progressively thicker as the sol became more viscous. Experimenting with different sol viscosities and spin- and dip-coating rates allowed for the preparation of as-synthesized films (i.e. with the template still in the pores of the material) in a wide range of film thicknesses (as determined by profilometry) – including those thick enough to be useful in coating the LPG.

Difficulties arose, however, at the surfactant removal stage. Despite long exposure to refluxing acidic ethanol in a continuous (Soxhlet) extractor, solid-state ^{13}C CP MAS NMR showed evidence of a significant amount of residual surfactant in the treated bulk materials (formed by gelation of the residual sol not used for film preparation), and nitrogen adsorption porosimetry analyses on these bulk materials showed a complete lack of porosity. Calcination to remove the block copolymer template, however, was not an option because the fibre-optic waveguide cannot withstand prolonged exposure to such elevated temperatures (e.g. 500 °C for up to 8 hours). Even if the extraction process had been successful at removing the template from the material's pores, the thick films did not survive the solvent extraction. The extracted films were either severely cracked or nearly completely washed away from the surfaces of both glass

and silicon test substrates. We thus turned to an alternative procedure in our attempts to prepare functional films.[58]

2.3.2 Brij® 56-Templated Thiol-Functionalized Films, High-Index Tetrasulfide Films, and Preliminary Hg(II) Sensing

The nonionic alkyl polyether Brij® 56 ($C_{16}H_{33}EO_{10}$, **B56**) (Scheme 2-6) was previously shown to yield aminopropyl-functionalized cubic, ordered mesoporous silicas as thin films when employed under acidic conditions.[58] This material was successfully replicated in our laboratory and thiol-functionalized derivatives of this material were also successfully prepared using the original Brinker procedure as a guide.[59]

Bulk materials were first prepared following the original procedure published by Brinker.[58] Removal of the template did not require Soxhlet extraction, as reported in the published procedure, but instead could be achieved by simply refluxing the material in acidic ethanol. The resulting materials were highly porous as evidenced by nitrogen porosimetry, although borderline microporous in nature (surface area = 423 $m^2 \cdot g^{-1}$; BJH pore diameter (desorption branch) = 17 Å) (see Figure 2-8). Elemental analysis (EA) showed a high degree of incorporation of the aminopropyl moiety (2.17 mmol $NH_2 \cdot g^{-1}$ material).[60] Although complete template removal could not be achieved (as is typical with template removal by solvent extraction),[61] more than 98% of the surfactant is consistently removed from the materials (as determined by elemental analysis), which is more than sufficient to open up the porous network.

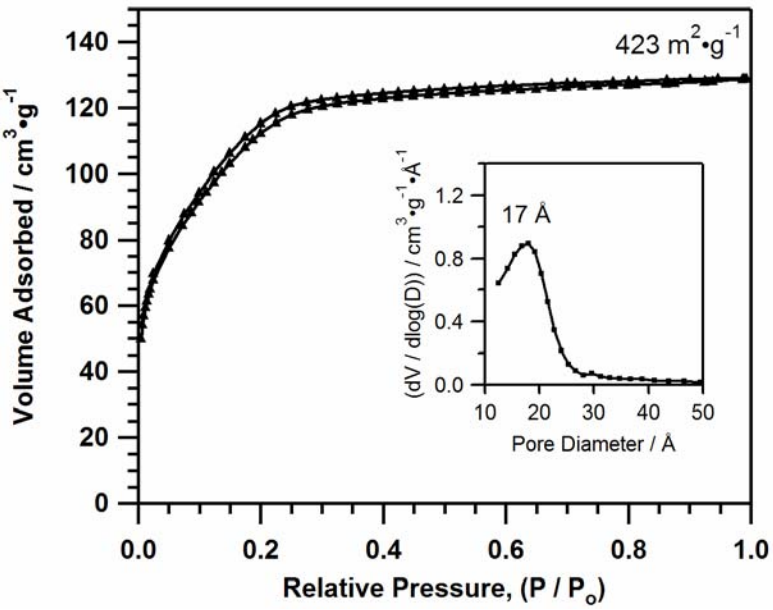

Figure 2-8. Nitrogen isotherm and pore size distribution (inset, BJH desorption branch) for a solvent-extracted 20 mol% **APTES** / 80 mol% **TEOS** organosilica material templated with **B56**.

To make this material more suitable as a mercury-binding material, the synthesis was modified from the original addition of 20 mol % of (3-aminopropyl)triethoxysilane (**APTES**) to include **MPTMS** (5 mol%) instead (see Scheme 2-4). Again, this bulk material was prepared with a high degree of incorporation of the organic component (0.65 mmol $SH \cdot g^{-1}$ material, as determined by EA), showed successful removal of the surfactant, and had a reasonable degree of porosity (58%) (calculated as a ratio of 'pore volume' to sample volume if the density of fused silica is assumed to be 2.2 $g \cdot cm^{-3}$).[62] This material was then tested for its ability to absorb Hg(II) from aqueous solution. Under our optimized conditions (see Section 2.6.11), 0.18 $mmol \cdot g^{-1}$ (35 $mg \cdot g^{-1}$) of Hg(II)

Table 2-2. Heavy metal uptake data for mesoporous organosilica thin films and bulk material immersed in aqueous solutions of Hg(II).

Sample	Initial Hg(II) Concentration [ppm]	Final Hg(II) Concentration [ppm]
5 mol% **MPTMS** / 95 mol% **TEOS** (*as-synthesized film*)	0.84	0.32
5 mol% **MPTMS** / 95 mol% **TEOS** (*solvent-extracted film*)	0.84	0.33
5 mol% **MPTMS** / 95 mol% **TEOS** (*solvent-extracted bulk*)	69	25
100% **BTESPTS** (*non-templated film*)	0.84	0.57

were taken up by the material (see Table 2-2), as measured by cold-vapour atomic absorption spectrometry (CV-AAS). These values closely match those reported in the literature by other groups who have also prepared high affinity mercury adsorbents,[41,42,43] demonstrating this material's potential as a suitable LPG overlay.

However, initial attempts to remove the surfactant from *thick* Brij® 56-templated films by solvent extraction were again unsuccessful at the outset of experimentation. Although thin films (< 400 nm) survived the extraction process, thick films (especially those ≥ 1 μm, which are necessary for the sensing system) were easily destroyed. A search of the literature and a recollection of our previous experience with the non-templated film systems gave insight into a variety of different post-synthesis treatments that could be performed to reinforce the silica matrix and increase the material's resistance to the stresses of template removal. In particular, exposure of the as-

synthesized materials (in both bulk and film form) to a saturated atmosphere of ammonia vapour has been shown to consolidate the silica matrix, which improves its mechanical integrity.[63,64,65] The more condensed silica network that results from this treatment also mitigates pore contraction during subsequent thermal treatments and surfactant removal, improving the material's final physicochemical properties relative to the untreated material. As shown in Figure 2-9, when this ammonia vapour post-synthetic treatment was applied to our materials, the resultant pore diameter of the extracted bulk material was significantly larger than for the untreated extracted materials. This was also evident in the dramatic change in the shape of the nitrogen adsorption–desorption isotherm and its hysteresis loop (Figure 2-10), which shows more mesoporous character as well as an increased degree of pore connectivity for the case of the ammonia-treated materials. With the subsequent incorporation of an ammonia vapor treatment step to the film synthesis protocol, thick films (>> 1 μm) have consistently survived solvent extraction of the templating agent without significantly compromising the film thickness, film uniformity, or continuity.

As with the bulk materials, these films (~ 2 cm^2 in area and 150–500 nm in thickness, coated and left intact on their respective substrates) were subjected to mercury uptake tests and demonstrated an even larger capacity for Hg(II) uptake (0.9 $mmol \cdot g^{-1}$, 180 $mg \cdot g^{-1}$) (see Table 2-2). This reinforces the suitability of these materials as coatings for a metal sensor.

Both as-synthesized and extracted films were analyzed in these experiments, and surprisingly, both types of materials demonstrated mercury absorption. This was

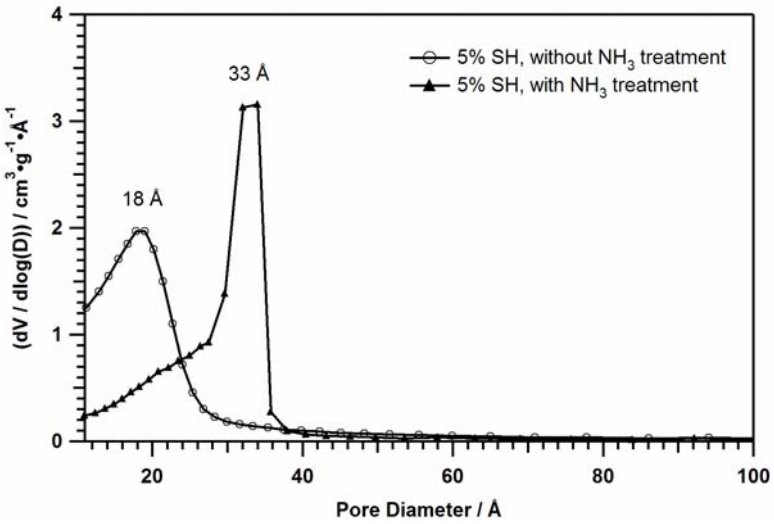

Figure 2-9. Pore size distribution plots (BJH desorption branch) for porous 5 mol% **MPTMS** / 95 mol% **TEOS** bulk materials templated by **B56** without (open circles) and with (black triangles) ammonia vapour treatment prior to solvent extraction of the templating agent.

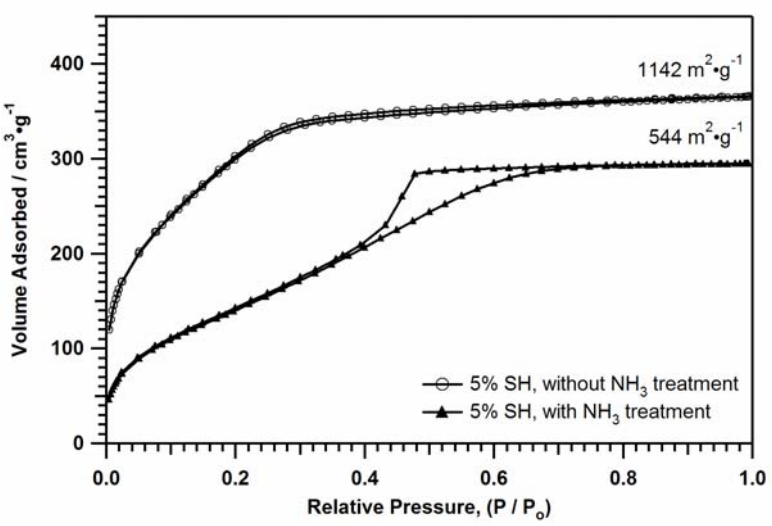

Figure 2-10. Nitrogen isotherms for porous 5 mol% **MPTMS** / 95 mol% **TEOS** bulk materials templated by **B56** without (open circles) and with (black triangles) ammonia vapour treatment prior to solvent extraction of the templating agent.

encouraging news because the residual surfactant left behind in the extracted materials did not appear to impair the function of the films at all.[66] Instead, removal of the surfactant is of interest in terms of lowering the RI of the film to a value slightly below that of the cladding. Furthermore, if the surfactant was to be left inside of the films in the final device configuration, it would be expected that the RI of the coating would drift with time due to leaching of the surfactant into the external environment. This in turn would affect the operation and calibration of the sensor at the testing site.

After gaining a handle on preparing **MPTMS–TEOS**-based films, it was necessary to get estimates of the RI of the films (both as-synthesized and extracted) at the operating wavelength of the sensor (1550 nm). Turning to refractometry, the RIs of as-synthesized films of varying composition were measured. Although the precision of the values was questionable, the values were used to at least try and obtain some 'ballpark' estimates for the RIs of the as-synthesized films. Unfortunately, extraction of the films caused the RIs of the films to fall out of the range of the refractometer (i.e. lower than 1.42 with that particular set-up). The inability to measure the RIs of the extracted films using the refractometer was more likely due to the significantly decreased RI of the extracted films after removal of the surfactant than changes in other properties of the film (e.g. thickness, uniformity, and continuity), since measurements of the film thickness and roughness by profilometry before and after extraction showed little changes in these film properties.

Variable angle spectroscopic ellipsometry (VASE) was simultaneously investigated as an alternative means of measuring the RIs of both the as-synthesized and

solvent-extracted films (see Table 2-3). Unfortunately, the results also did not appear to be reliably accurate or reproducible due to difficulties in fitting a model to the experimental data from which the desired optical properties could be extracted. The modeling of the data becomes exceptionally complex with such thick films of multi-component systems. Consequently, both this technique and refractometry were used where appropriate to mainly identify trends in film RI, as opposed to pin-pointing absolute values for film RIs. Our confidence in the results from refractometry and VASE was judged on a case-by-case basis and relied on the outcome of multiple measurements for every sample analyzed.

Table 2-3. Summary of refractive indices of **B56**-templated thick films and surfactant-free thin films (as measured by VASE).

Film Composition	RI at 1550 nm (*as-synthesized film*)	RI at 1550 nm (*solvent-extracted film*)
20 mol% **APTES** / 80 mol% **TEOS**	1.4630	1.3625
5 mol% **MPTMS** / 95 mol% **TEOS**	1.4664	1.3026
100% **BTESPTS**	1.5746	N/A

Despite the fact that the RIs of the thiol-functionalized silica films prepared with the **B56** system were likely too low to be in the sensitive region of the LPG, these films were nonetheless coated onto LPGs to test their ability to effectively interface with the optical sensing element. Both as-synthesized and solvent-extracted films were calibrated for their RI sensitivity using water / DMSO solutions of varying composition. When

immersed in solution, the as-synthesized films induced peculiar and incomprehensible changes in the appearance of the LPG attenuation spectra, which was eventually attributed to the RI of the as-synthesized films exceeding that of the fibre cladding. However, once solvent-extracted, these films only showed RI sensitivity when immersed in relatively high RI solutions – not in water, as ideally desired – implying that the RI of the porous films was conversely too low. Not surprisingly, then, Hg(II) sensing in aqueous solutions did not yield any LPG response.

At this point, publications detailing the use of high RI overlays (i.e. higher than the RI of the fibre cladding) on LPG-inscribed fibre-optic waveguides were encountered.[67,68] In these reports, very thin films (only a few hundred nanometers in thickness) of specific thickness and RIs greater than the cladding were used to coat LPGs, and resonant peak shifts were obtained in response to changes in RI of the external

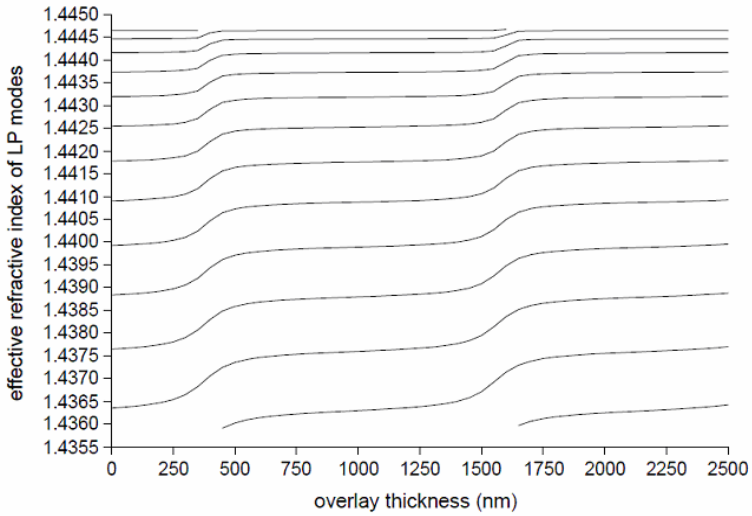

Figure 2-11. Modeled effective RIs of different linearly polarized (LP) modes for varying thicknesses of an LPG overlay with an RI of 1.58. (Image taken from reference 19.)

environment surrounding the overlay. Such high RI films were then briefly pursued as potential LPG coatings for Hg(II) sensing.

Thin films (not surfactant-templated) were thus prepared using 100% **BTESPTS** (bis[3-(triethoxysilyl)propyl]tetrasulfide) for Hg(II) uptake following a previously published procedure,[69] as powdered / bulk **BTESPTS**-functionalized mesoporous organosilica materials have been shown to be highly effective Hg(II) adsorbents.[70] Since this was essentially a one-component thin film, VASE was used to determine its RI. After determining that the RI of this film was ~1.58 at 1550 nm (see Table 2-3), our collaborators at Dalhousie University (Prof. Peter Wentzell and Dr. Hannes Hochreiner) were able to model the LPG response to external changes in RI using this type of film. Their results (see Figure 2-11) suggested that a film of 400 nm-thickness was necessary to see any shifts in the resonant wavelength. Layer-by-layer deposition of the sol was consequently used to build up an overlay of sufficient thickness in a spin-coating experiment to successfully prepare a high refractive index film that was 400 nm in thickness. As seen in Figure 2-12, there was a high degree of control in preparing the 400 nm film.

An analogous layer-by-layer coating procedure was followed to coat an LPG by dip-coating, after which the coated LPG was exposed to solutions of different Hg(II) concentration and analyzed on the OSA. At this point, it should be noted that no porosity was expected for this non-templated film as it was thought that a film of only a few hundred nanometers in thickness may potentially be thin enough to allow surface-bound analytes to still interact with the tail of the evanescent wave. However, to our

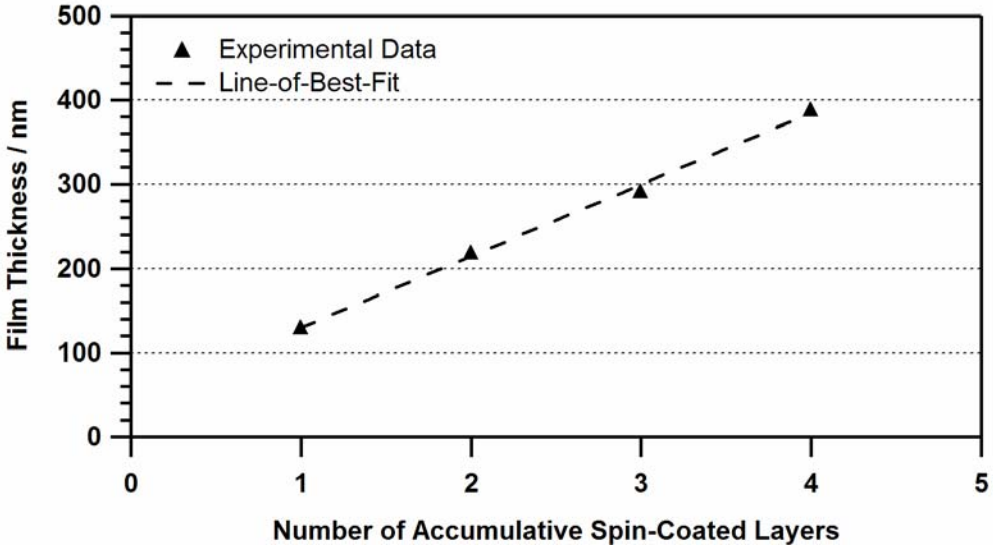

Figure 2-12. Plot of the film thicknesses of layer-by-layer spin-coated, high-RI, 100% **BTESPTS** films (prepared without the use of any templating agent) as a function of the number of deposited layers.

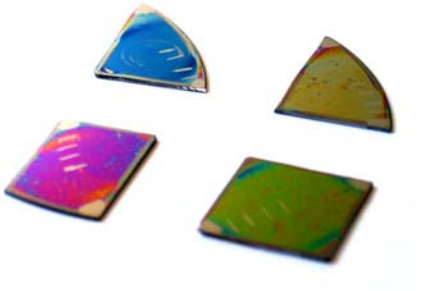

Figure 2-13. A photograph of layer-by-layer spin-coated, high-RI, 100% **BTESPTS** films (prepared without the use of any templating agent) with one (blue), two (yellow), three (magenta), and four (green) accumulative layers.

disappointment, again, no shifts in the resonant peak were observed. Although high RI films are potential materials for the mercury sensor and the issue of introducing porosity into these high RI films could be addressed, the LPG response to changes in the RI of the surrounding environment is governed by phenomena that differ from that of the low RI materials described earlier and is not as well understood. Troubleshooting these high RI materials on LPGs becomes a more convoluted task, and as such, it was decided that research efforts should be concentrated on fine tuning the system using low RI films containing **MPTMS** and templated by **B56**.

Knowing that relatively robust, thick, porous, mercury-binding, and low RI films could be reliably prepared by the modified Brinker method using **B56** as a surfactant and mercaptopropyl moieties as the metal binding ligands, it was anticipated that it could be possible to see shifts in the resonant peaks in the LPG attenuation spectrum by tuning the RI of the environment surrounding the LPG overlay through modification of the solution medium instead of the overlay itself (see equation 2-1). Again, the LPG attenuation is more sensitive to changes in the RI of the surrounding environment when that RI (in combination with the RI of the film) approaches that of the fibre cladding. If the RI of the film is too low – even when water occupies the pore space – the effective RI of the environment could be increased to a value closer to that of the cladding through the use of water / DMSO mixtures, as opposed to purely aqueous solutions. The DMSO volume fraction in the mixtures can be increased until the effective RI of the film–water–DMSO system resides in this region of highest sensitivity. Although this is not an ideal set of conditions (i.e. the system will eventually have to work in a purely aqueous system in the

field), water / DMSO mixtures were nonetheless employed to give us at least a preliminary idea of whether or not the sensing device would work before investing further effort into tuning the RI of the overlay.

Water has an RI of 1.3330 at 589 nm (i.e. n_D^{20}) (1.3157 at 1550 nm), while DMSO has an RI of 1.4783 at 589 nm (1.4619 at 1550 nm) (recalling that 1550 nm is the wavelength of interest in our sensing application).[71] Consequently, by changing the volumetric ratios of water and DMSO, solutions mixtures with RIs between these values may easily be prepared and tested with the LPG. A series of different water / DMSO solutions were, therefore, prepared and then used to calibrate a coated LPG with the purpose of identifying a water / DMSO mixture that would bring the effective RI of the film–solution system into a range that more closely matches the RI of the cladding and enhance the sensitivity of the response (see Figure 2-14). Specifically, the calibration curve is a plot of the resonant peak shift (relative to a reference peak position such as that for the LPG in air) as a function of the RI of the surrounding water / DMSO solution. The region of curve with the steepest negative slope is identified, in this case, as being the region of highest RI sensitivity, and thus a water / DMSO medium for Hg(II) sensing is chosen from within this region.

In an additional move to improve the sensitivity of the LPG to changes in RI, we were able to obtain LPGs produced with a shorter periodicity (specifically, Λ was modified from 548 μm to 320 μm) from our suppliers. Furthermore, the cladding diameter surrounding the grating was reduced by etching with a concentrated aqueous

solution of ammonium hydrogen bifluoride, which increases the intensity of the evanescent field that extends into the environment surrounding the LPG.[72]

A fibre was therefore etched, coated, calibrated, and then subjected to mercury uptake tests using Hg(II) solutions prepared in water / DMSO mixed solvent systems. From the calibration curve for the cladding-etched LPG bearing a solvent-extracted porous coating (2.5 mol% **MPTMS**-functionalized) obtained in Figure 2-14 (Coated LPG, Trial #1), it was first decided that a water / DMSO solution with a

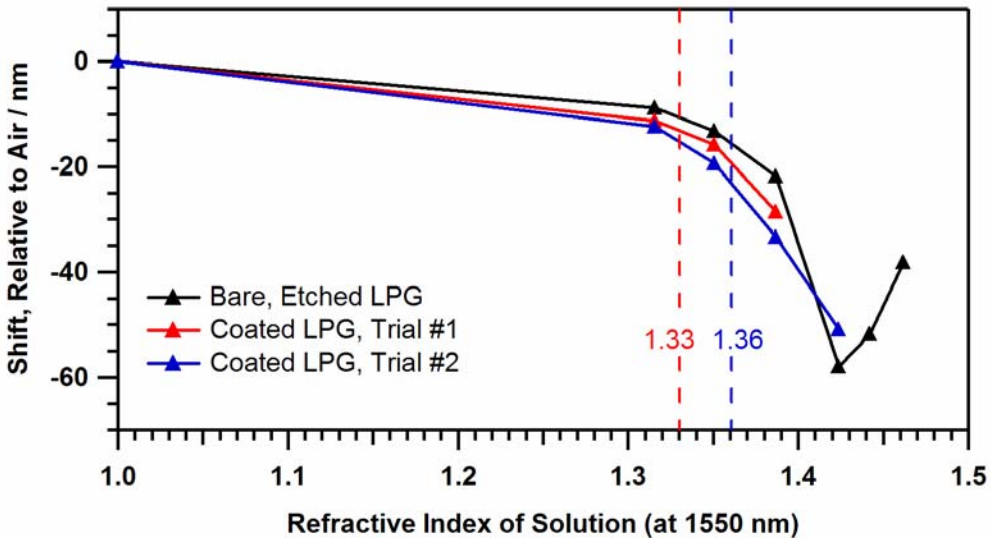

Figure 2-14. Calibration curves for an etched LPG (both in its bare (black trace) and coated state (red and blue traces)) (Λ = 320 μm, grating length = 25 mm) showing the resonant peak shifts as a function of the RI of the surrounding water / DMSO solution. Two Hg(II) sensing trials were conducted using the same 2.5 mol% **MPTMS** / 97.5 mol% **TEOS** coating on the LPG in mixed water / DMSO solutions of RIs indicated by the dashed lines (red and blue dashed lines for Trials #1 and #2, respectively).

refractive index of 1.33 (at 1550 nm) would be a reasonable starting point. Although 1.33 does not lie directly at the steepest point of the calibration curve, it was hypothesized that the absorption and concentration of Hg(II) in the film might be sufficient to drive the RI of the film–solution system into the sensitive region of the response curve.

This coated LPG was then exposed to Hg(II) solutions of different concentration (1–100 ppm) prepared in a water / DMSO mixture consisting of 13 vol% DMSO (4 mol% DMSO) (RI = 1.33 at 1550 nm). Much to our delight, this experiment returned an overall blue-shift of 2.5 nm in the resonant peak position (an accumulative value) with respect to the blank solution (Figure 2-15).[73]

This film was subsequently rinsed with 6 M $HCl_{(aq)}$ to remove any thiol-bound Hg(II) and 'regenerate' the film, and the experiment was performed a second time using the same film–LPG system. However, to see if any improvements in the magnitude of the shift could be realized, the water / DMSO solution was adjusted to 33 vol% DMSO (11 mol% DMSO) to give a solution with a slightly higher RI of 1.36 (Coated LPG, Trial #2 in Figure 2-14). Although the profile of the response is different for the second trial (Figure 2-16), the overall response to Hg(II) was still observed and in fact had increased to a magnitude of 5 nm.

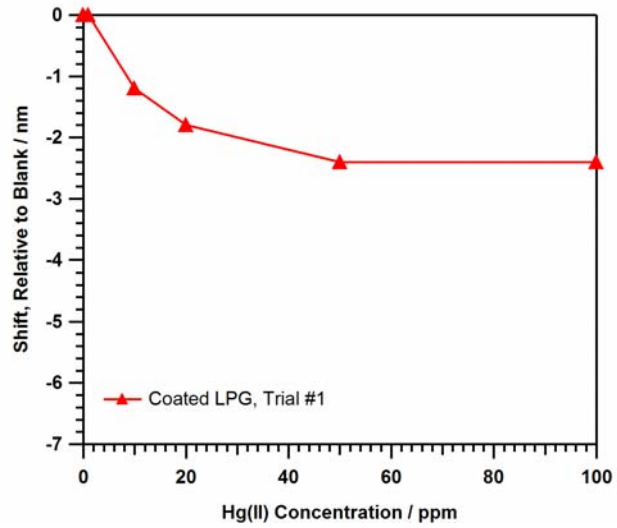

Figure 2-15. Plot of the resonant peak shifts for a 2.5 mol% **MPTMS** / 97.5 mol% **TEOS** coating on an LPG as a function of the Hg(II) concentration in water / DMSO solutions with an RI of 1.33 (at 1550 nm).

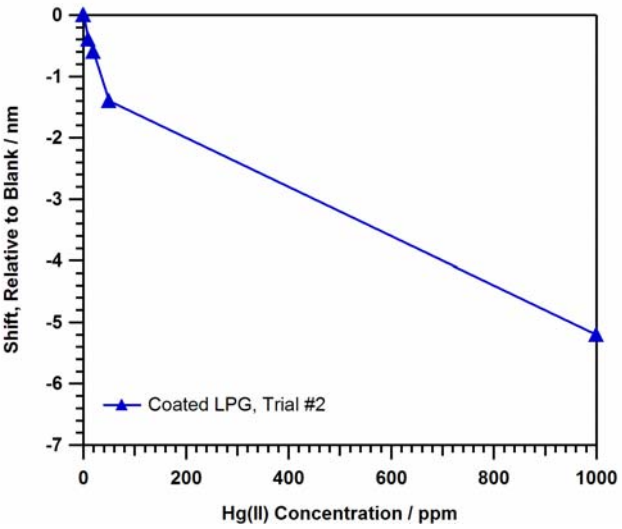

Figure 2-16. Plot of the resonant peak shifts for a 2.5 mol% **MPTMS** / 97.5 mol% **TEOS** coating on an LPG as a function of the Hg(II) concentration in water / DMSO solutions with an RI of 1.36 (at 1550 nm).

Encouraged by these results, other modifications to the overlay were attempted to try to further increase the magnitude of the peak shift. Firstly, the thiol content was increased to see if larger changes in RI could be experienced as a result of the increased Hg(II) binding capacity. Films of 5, 10, and 20 mol% thiol were prepared and subjected to a similar sequence of analyses as outlined with the 2.5 mol% thiol-functionalized film above. Unfortunately, no significant improvements in the RI sensitivity and in the resonant peak shifts were observed in these additional cases.

2.3.3 Tetrasulfide-Functionalized Brij® 56-Templated Films for Pb(II) Sensing

A more thorough survey of the physical data for Hg(II) revealed a very low polarizability volume for this species (1.25 $Å^3$).[74] Therefore, the absorption of Hg(II) may not, in fact, result in overly significant changes in the effective RI of the film–solution system surrounding the LPG. It was then decided that Pb(II) could instead be a more appropriate heavy metal candidate to explore as a test compound that could serve as a proof-of-concept for this optical metal sensor. The polarizability volume of Pb(II) (5 $Å^3$) is much larger than that of Hg(II),[74] and could, therefore, result in a more easily detectable change in RI of the film upon absorption of Pb(II).

Consideration was also given to the heavy metal-binding ligand itself. In particular, we returned to the **BTESPTS** precursor explored for the high-RI films as an alternative to **MPTMS**. Notably, in addition to its high affinity for 'soft metals', its RI in its uncondensed form exceeds that of **MPTMS** (see Scheme 2-4). This factor could

potentially aid in boosting the RI of the porous films into a more effective range whereby metal sensing in pure aqueous systems could be realized. In addition to this aspect regarding RI, the incorporation of a bis-silylated ligand into the silica framework may advantageously improve film flexibility, which would then enhance the material's ability to withstand mechanical and physical stresses experienced during film processing and subsequent sensing trials. It was then decided that the focus of this fibre-optic sensing project would be shifted from the detection of Hg(II) using thiol-based ligands to the detection of Pb(II) using tetrasulfide-based ligands.

The **B56**-based film synthesis was thenceforth modified to accommodate the incorporation of the bis-silylated tetrasulfide-based ligand. The corresponding 5 mol% **BTESPTS** (Si basis) / 95 mol% **TEOS**[75] bulk materials demonstrated porosity (905 $m^2 \cdot g^{-1}$), as well as evidence for tetrasulfide incorporation (1.61 $mmol \cdot g^{-1}$, as determined by EA). Unfortunately, despite possessing respectable material properties and metal detection in mixed water / DMSO systems with the film–LPG system, still no Pb(II) detection in water was experienced. Of notable importance was the fact that if, for example, two films of the same starting composition were deposited on to two LPGs of equivalent specifications, the calibration of those two systems would often show dissimilar calibration behaviour – implying that the RIs of those films were not as similar as we would otherwise have hoped them to be. This was a critical issue not only in terms of RI matching, but because it was a reflection of the limitations of truly reproducing our films as film RI is intimately connected to the physical properties of the films (e.g. degree of ligand incorporation, porous volume, degree of siloxane condensation within the

framework, and so forth). This was also glaringly apparent when, for example, TEM images for a given sample showed a wide variety of mesoscopic ordering, indicating that the materials are not necessarily always formed with uniform structural control (see Figure 2-17).

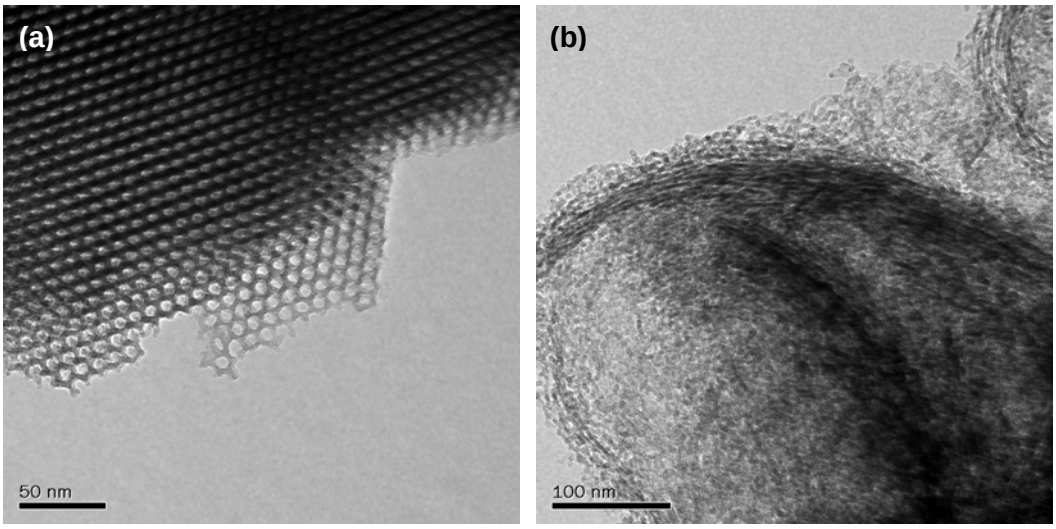

Figure 2-17. Two different TEM images of the same thick, solvent-extracted 5 mol% **BTESPTS** (Si basis) / 95 mol% **TEOS** film templated by **B56** showing the occurrence of mixed mesophases throughout the material. In particular, (a) 2D hexagonally-ordered and (b) amorphous regions can be observed.

2.3.4 Improving the Reproducibility of Film Synthesis and Second Generation F127-Templated Tetrasulfide-Functionalized Films for ppb-Level Pb(II) Detection

The challenges with respect to forming materials by sol-gel chemistry became increasingly apparent at this point. Despite the rich variety of materials that can be

accessed through sol-gel chemistry and the versatility of the methodology, the condensation products obtained by this process are not, in fact, 'thermodynamic products', but rather 'kinetic products' whereby metastable states and structures are 'frozen' in the framework of the network solid.[47] Thus the final form of the material is dependent on competing rates of the different constituent processes and the overall degree of siloxane condensation. It is, therefore, highly likely that sensitivities to processing conditions (for example, the timing and temperature of certain steps, as well as the humidity of the surrounding environment during the preparation of the siliceous structures) are significant.[30,33,34,76] Furthermore, given the interdependence of many of the synthetic and processing variables, it is also extremely likely that the modification of any one parameter will result in a perturbation of several other physical and chemical processes that will correspondingly affect the properties of the final product.

With this in mind, we ventured to control the film processing conditions as rigorously yet practically as possible. The parameters that were consequently highlighted included: (i) the order of reagent addition; (ii) time allotted for each of the pre-hydrolysis steps; (iii) sol stir rate; (iv) sol aging temperature; (v) sol density at the time of coating; (vi) spin- and dip-coating rates; (vi) relative humidity (RH) of the surrounding environment during the coating step; (vii) drying and curing temperatures and times; (viii) ammonia vapour treatment time; (ix) surfactant extraction conditions (temperature, reflux rate, and elapsed time); and when applicable, (x) LPG exposure conditions. In particular, sol density at the time of coating and the RH of the surrounding environment during the coating step were identified as two of the most crucial parameters.

Elaboration on the details pertaining to the control and influence of these two parameters is included in the paragraphs that follow.

As previously mentioned, thick films were obtained by using viscous, aged sols for the coating processes. However, the actual viscosity of the sol was quantitatively unknown, and although the spin- and / or dip-coating rates could be changed to qualitatively adjust for the relative viscosity of the coating sol so that the resultant films were always of sufficient thickness to be of use as LPG overlays, it was reasoned that a better way of monitoring sol viscosity was needed. In our case, an increasingly viscous sol is one consisting of a continuously advancing degree of siloxane condensation. Therefore, two films prepared from the same sol at different sol viscosities but the same coating rates would not only yield films of differing thickness, but also films of differing RIs (and perhaps of different mesostructuring, as well) because the two sols will be at different degrees of condensation. Furthermore, as uniform and continuous thick films are inherently difficult to prepare and maintain, it was also suspected that there was a range of film thicknesses within which the coatings could be optically useful on LPGs, but beyond which film integrity would be drastically compromised. It would thus be important to find a reasonable target for film thickness, and to be able to consistently prepare films of that thickness.

Without access to an actual viscometer, we decided instead to use sol density as a marker for sol viscosity.[77] 0.5-mL aliquots of the aging sol were weighed at various time points during the sol aging / evaporation process in order to determine the instantaneous sol density. For each composition explored thereafter, a plot of the resultant film

thickness as a function of measured sol density (for films dip-coated at a withdrawal rate of 10 mm·s^{-1}) was generated and used to identify a target sol density that would yield films of ~ 2–3 μm in thickness (for example, see Figure 2-18). This method proved to be a much more reliable means of preparing films of a desired thickness in comparison to monitoring, for example, elapsed aging time because aging times varied from sol to sol due to fluctuations in ambient environment such as the air flow rates within the fumehoods.

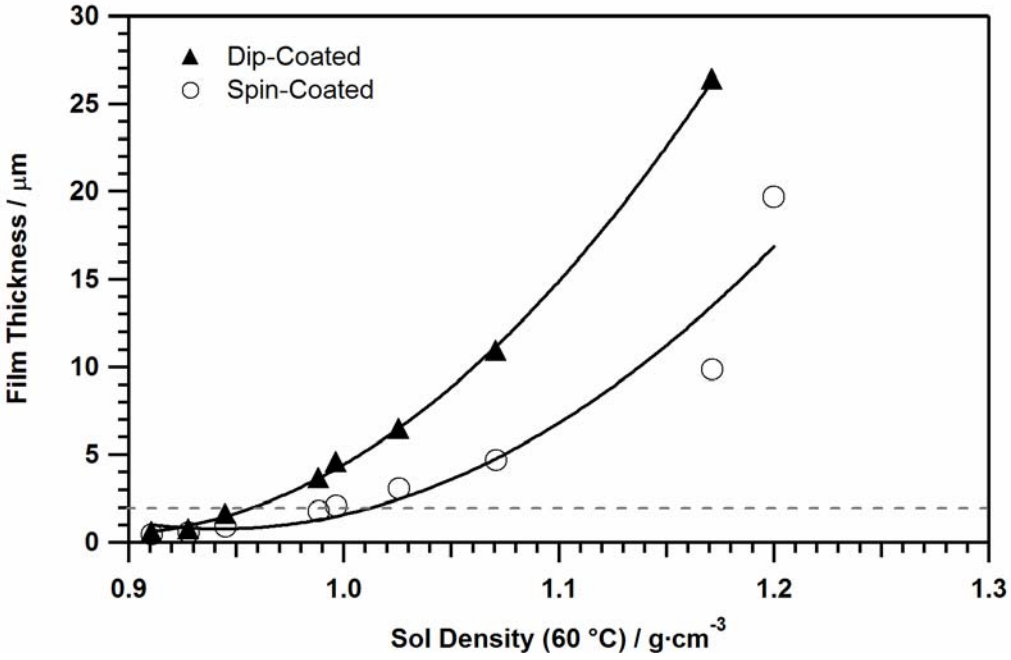

Figure 2-18. Plot of as-synthesized film thicknesses for both spin- and dip-coated films prepared on glass microscope slides (open circles and opaque triangles, respectively). The sol composition was 9 mol% **BTESPTS** (Si basis) / 1 mol% **TTIP** / 90 mol% **TEOS** with **F127** as the templating agent. The films were prepared in an atmosphere with RH = 50%.

In order to control the RH of the surrounding environment during the coating process, an old, decommissioned glove box was converted into a relative humidity chamber that housed the dip- and spin-coating apparatuses, and the RH of the ambient atmosphere was maintained at an intended level using an appropriate saturated salt solution (see Appendix 1 for a comprehensive list of saturated salt solutions that should be used to attain an atmosphere of a given RH)[78].

Given the mixed mesophases obtained in the films prepared using **B56** as the templating agent and the prevalence of the 2D hexagonal phase within these materials, we re-surveyed the literature for other options for possible templating agents, and it appeared that **F127** (the first surfactant explored in this work) was an overwhelmingly popular choice as a surfactant for preparing materials with cubically ordered porosity. Despite the complications initially encountered with the solvent extraction of the block copolymer from **F127**-templated materials, we decided to reconsider its use for the preparation of our LPG overlays.

In our previous attempts to prepare films and bulk materials using **F127**, template extraction was conducted using a Soxhlet extractor. However, in the case of the **B56**-templated films, hot extraction in a round-bottomed flask (RBF) followed by a rinsing of the organosilica films or bulk powders with fresh, hot solvent appeared to be an effective and more expedient procedure for obtaining porous materials. Additionally, a report by Van Der Voort and co-workers demonstrated that the use of acetone instead of the more commonly used acidified ethanol to extract **P123** (which belongs to the same family of triblock copolymers as **F127**) from ethylene-bridged periodic mesoporous organosilicas

(PMOs) not only removed more the template from the as-synthesized materials, but also resulted in materials bearing more favorable porous properties when compared to extraction with ethanol or acidified ethanol.[79] These data are summarized as follows in Table 2-4.

Table 2-4. Extraction efficiency of several solvents for the removal of **P123** from bulk ethene-bridged periodic mesoporous organosilica materials (taken from reference 79).

Extraction Solvent	Amount of P123 Extracted After 5 h [mol%]
dichloromethane	66.7
chloroform	69.9
acidified ethanol	71.8
ethyl acetate	77.0
isopropanol	78.6
acetone	94.2

Lastly, in a further attempt to boost the RI of the films to decrease the dependence on DMSO-modified aqueous solutions for the demonstration of metal detection, a condensable titania (TiO_2) precursor (**TTIP**, $Ti(O^iPr)_4$, titanium tetraisopropoxide) was co-condensed into a sol comprising **TEOS** and **BTESPTS**.[80] A similar strategy was also employed in the work pursued by the research groups of Profs. Hans-Peter Loock and R. Stephen Brown for index-matched PDMS-coated LPGs for the detection of volatile organic compounds (VOCs).[16] Therefore, our second generation **F127**-templated films[81]

were tetrasulfide-modified silica–titania hybrid materials processed in a humidity-controlled environment with concomitant monitoring of the density of the coating sol, which were then exposed to post-synthetic treatment of the as-synthesized films with ammonia vapour to improve the condensation of the framework (followed by, in some cases, trimethylethoxysilane (TMES) vapour treatment to cap residual silanols[82]) before subsequent template removal in an RBF with acetone as the extracting solvent. In the final embodiment, an **F127**-templated film with a molar composition of **TEOS** : **BTESPTS** : **TTIP** = 1 : 0.05 : 0.01 (i.e. 9 mol% **BTESPTS** (Si basis) / 1 mol% **TTIP** / 90 mol% **TEOS**[30]) (herein referred to as the 'PMO film' and variations thereof) was prepared for the proof-of-concept of Pb(II) sensing using LPG-inscribed fibre-optic waveguides.

Markedly, the importance and sensitivity of the resulting material properties to the solvent extraction conditions was realized at this point through the work of this project and others in our research group. Certainly, with a Soxhlet-based extraction process, template removal could be highly dependent not only on the overall elapsed time of the extraction, but also on the solvent drip rate, the temperature of the condensed solvent while collecting in the sample reservoir, the 'residence time' of the hot solvent while in contact with the sample in the reservoir, and the efficiency with which the reservoir periodically empties. Given the efficiency with which the **B56** template could be extracted from our materials in the RBF-based set-up (see Section 2.3.3), we stayed with this methodology of extraction for the remainder of this particular project.

In addition, we also hypothesized that the porous properties of bulk material (obtained through the gelation of the remaining, unused coating sol) may not necessarily be an accurate reflection of the porous properties of the materials in film morphology. A large batch of more than 60 organosilica–titania films were thereafter dip-coated onto glass slides, subjected to the routine post-synthetic treatments (i.e. NH_3 and TMES treatments), and solvent extracted in acetone prior to being scraped off of the substrates and collected for nitrogen porosimetry analysis. Encouragingly, evidence for the occurrence of porosity in these **F127**-based films was obtained (see

Table **2-5** and Figure 2-19).

The physical properties of the surfactant-templated organosilica films were expected to differ from those of their corresponding bulk materials for a few reasons. Firstly, the bulk material is obtained upon gelation of the unused sol under ambient conditions. At the point at which gelation of the sol occurs, the siloxane condensation within the sol will have progressed to a much greater degree than in the case of the preparation of the films, which are synthesized using a sol of lesser siloxane condensation. The final mesostructure and physical properties of the resultant material may then be noticeably different due to differences in the sol composition at the point of mesostructure formation and gelation.[33] In addition, differences in the final properties of the material may be evident if the difference in the extent of siloxane condensation within the matrix of the materials significantly affects the ability of the material to withstand the capillary stresses exerted upon the material during solvent extraction, drying, and curing.

Furthermore, the drying and curing of bulk materials in comparison to films (supported on a substrate) may result in more dramatic yet more uniform pore shrinkage as an unsupported bulk matrix is free to shrink in all three dimensions. In contrast, due to

Table 2-5. Summary of nitrogen porosimetry data for a large batch of solvent-extracted, scraped PMO films.

Sample	BET Surface Area [$m^2 \cdot g^{-1}$]	BHJ Ads. Pore Diam. [Å]	BJH Cum. Ads. Pore Vol. [$cm^3 \cdot g^{-1}$]	BHJ Des. Pore Diam. [Å]	BJH Cum. Ads. Pore Vol. [$cm^3 \cdot g^{-1}$]
solvent-extracted scraped films	203	60	0.189	31	0.200

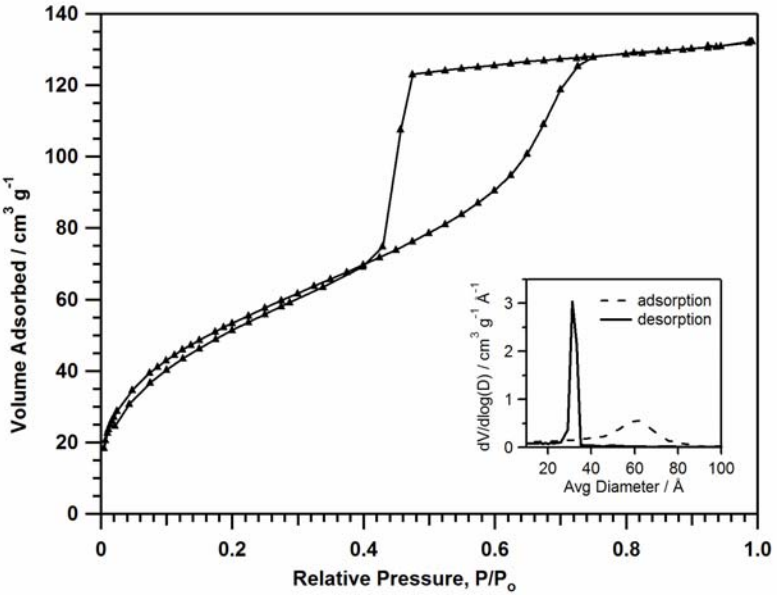

Figure 2-19. Nitrogen isotherm and pore size distribution curves (insets) for a large batch of solvent-extracted, scraped PMO films.

their adherence against a solid substrate, the films are largely supported in the plane parallel to the substrate surface – leading to pore shrinkage predominantly in a direction perpendicular to the substrate plane.[47] However, pore collapse due to anisotropic shrinkage in the case of supported films may then become more of an issue.

The effectiveness of post-synthetic treatments such as the ammonia vapour treatment and / or solvent-extraction of as-synthesized materials may also differ due to variations in mass transport through the materials. For example, as-synthesized bulk gels typically consist of large and thick organosilica pieces, which is in contrast to the bulk morphology of the films. Ammonia vapour treatment may then proceed more efficiently through films than through bulk materials. On the other hand, during solvent-extraction, extensive contraction of the bulk gel pieces typically occurs, causing the bulk to turn into an increasingly fine (but relatively granular) powder and augmenting the interfacial surface area between the particulate matter and the extraction medium. However, this is not the case for films where the interfacial surface area between the films and the extraction medium remains constant (and relatively low). Once more, this could affect the degree to which the siloxane framework may be stabilized and hence affect the final textural properties of the corresponding materials.

From TEM images that were collected for these as-synthesized and extracted films (see Figure 2-20 for an example of the solvent-extracted film), a wormhole-type structure (which is often described as being an interconnected pore system of high permeability[83]) was consistently observed.[84] Furthermore, pores of very uniform

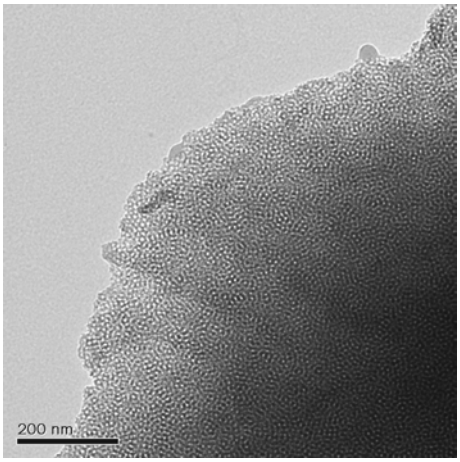

Figure 2-20. TEM image of the porous, solvent-extracted PMO film displaying a uniform wormhole-type mesostructure.

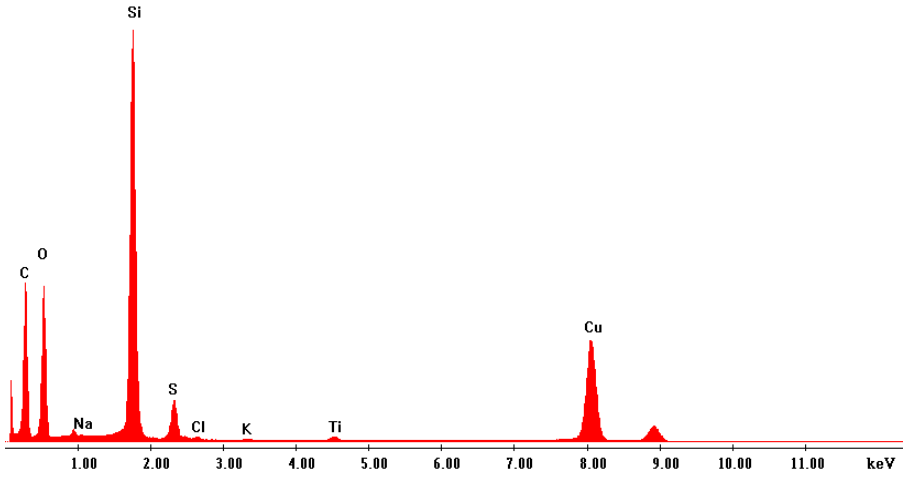

Figure 2-21. EDX sum spectrum of the solvent-extracted PMO film sample dispersed onto a carbon-coated copper grid.

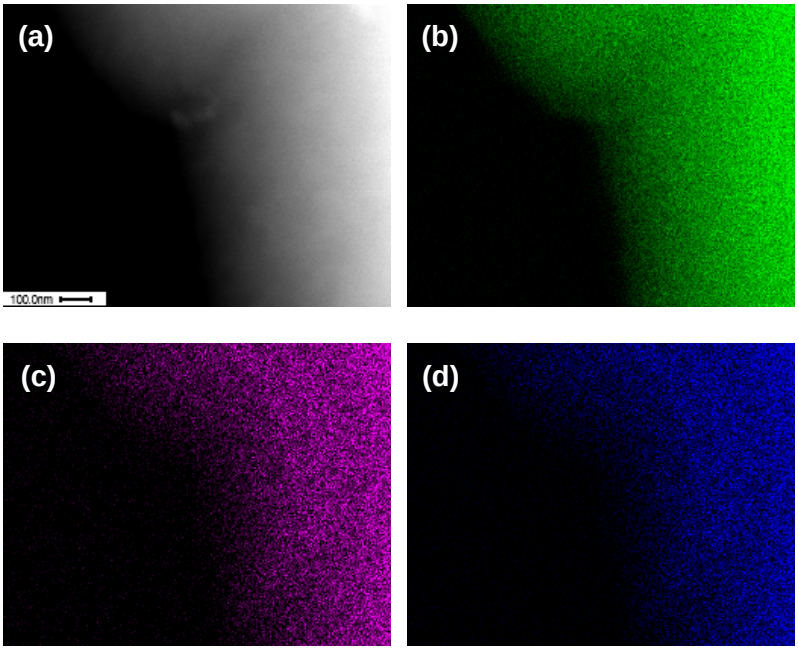

Figure 2-22. (a) HAADF-STEM image of the solvent-extracted PMO film sample, and chemical maps showing the distribution of (b) Si, (c) Ti, and (d) S in the sample.

diameter were observed, with the size of the pores as estimated from TEM well-correlated to the values obtained through nitrogen porosimetry for the same samples.

S and Ti content were confirmed by EA and energy-dispersive X-ray (EDX) analysis (Figure 2-21) with reasonable agreement between the two methods. S content was found to be 1.5 and 1.9 mmol·g^{-1}, with Ti content at 0.1 and 0.2 mmol·g^{-1}, respectively.[85] High-angle annular dark field scanning transmission electron microscopy (HAADF-STEM) and chemical mapping were also employed to confirm that the sulfur and titanium were well distributed throughout the material (Figure 2-22). Notably, no TiO_2 agglomeration was detected.

The response of the resulting coated LPGs to changes in the RI of the surrounding environment was, as before, evaluated by water / DMSO calibration of the devices. On one particular occasion, a film processed with a 9 mol% **BTESPTS** (Si basis) / 5 mol% **TTIP** / 86 mol% **TEOS** formulation demonstrated a resonant peak blue-shift of ~ 1 nm in response to exposure to a 50 ppb solution of Pb(II) in a purely aqueous (i.e. 100% H_2O) solution and an overall accumulative blue-shift of nearly 50 nm for exposure to solutions of up to 100 ppm Pb(II).[86,87] Notably, the resonant peak in the attenuation spectrum for the coated LPG in air was observed to blue-shift ~ 55 nm on the optical spectrum analyzer (OSA) upon immersing the sensing element in water. Such a dramatic shift in moving the coated LPG from air to water was hereafter established as a necessary occurrence in order for metal sensing in purely aqueous systems to be affected. Unfortunately, however, metal sensing using these silica-based mesoporous coatings has not since been replicated in purely aqueous media on any subsequent LPGs and new batches of films, despite repeated demonstrations of Pb(II) detection in water / DMSO solutions with compositions from 25–60 vol% DMSO (i.e. 8–28 mol% DMSO).[88] Consequently, we carried on with the demonstration and characterization of Pb(II) sensing in index-matched water / DMSO media.

When coated with a PMO film of 9 mol% **BTESPTS** (Si basis) / 1 mol% **TTIP** / 86 mol% **TEOS** composition, the steepest part of this particular water / DMSO response curve shifts to a solution of RI ~ 1.40 from ~ 1.43 for the bare, cladding-etched, uncoated LPG (Figure 2-23, green and blue traces, respectively). Furthermore, the broadening of

the RI-response window is observed, which has the added advantage of extending the RI range in which this particular sensor will be effective.

Having used the response curve for the coated LPG (Figure 2-23) to determine the optimum RI of the solution in which sensing will occur (i.e. RI = 1.402 at 1550 nm, which corresponds to a 60 vol% (28 mol%) DMSO solution), attenuation spectra with $Pb(NO_3)_2$ solutions of increasing concentration were recorded. As expected, a blue-shift

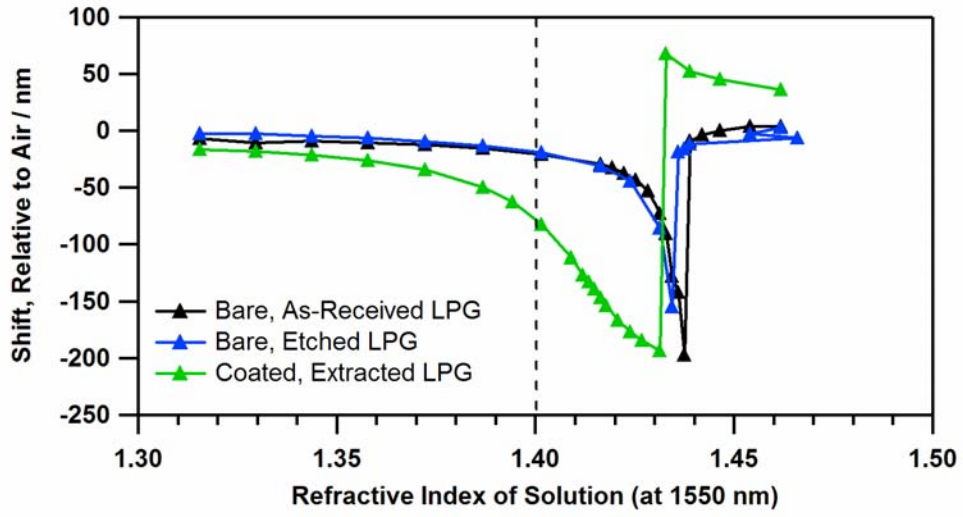

Figure 2-23. Calibration of an LPG-inscribed fibre-optic waveguide (both in uncoated and coated states) with water / DMSO solutions of increasing RI, noting the shift to lower RI (~ 1.40 at 1550 nm) and broadening of the RI-sensitive region that accompanies coating of the grating with the PMO film.

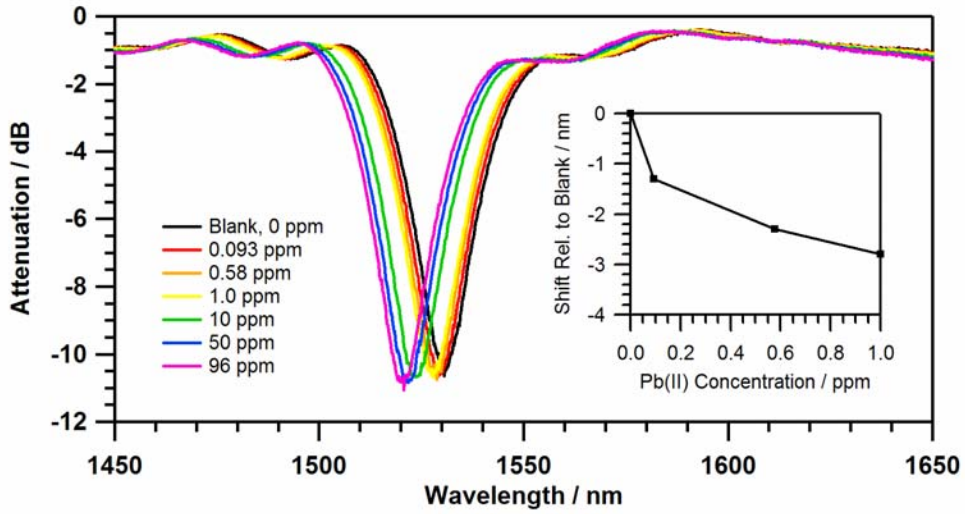

Figure 2-24. Optical response for an LPG coated with the PMO film to aqueous DMSO solutions (RI = 1.402 at 1550 nm) of Pb(II) of increasing concentration as observed by the LPG attenuation spectra and by the shift in the resonant peak position as a function of solution concentration (inset).

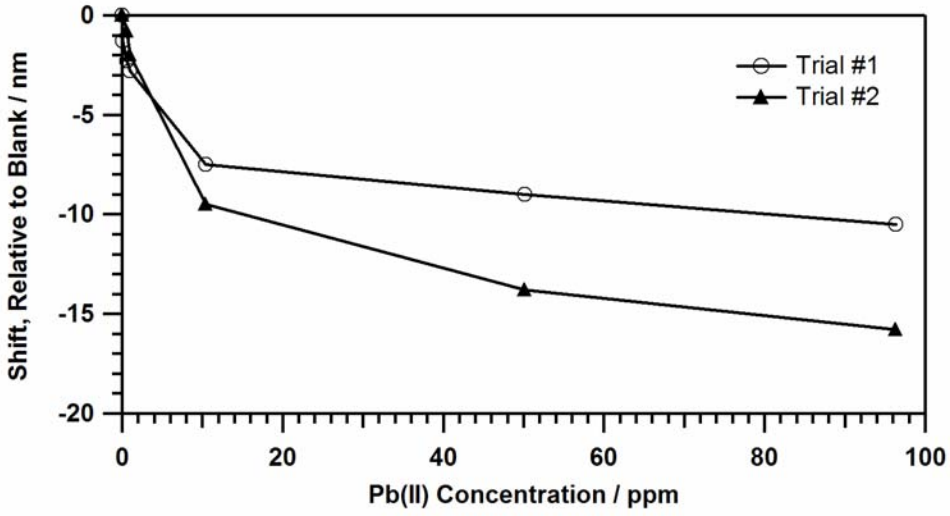

Figure 2-25. A plot of the shifts in the resonant wavelength position for a PMO-coated LPG relative to the peak for the blank solution as a function of exposure to aqueous DMSO solutions (RI = 1.402 at 1550 nm) of increasing Pb(II) concentration.

in the spectrum is observed as the concentration of Pb(II) increases (Figure 2-24). The inset to Figure 2-24 shows a plot of this shift with respect to the Pb(II)-free solution reference peak. Notably, exposure to a 90 ppb Pb(II) solution resulted in a shift greater than 1.0 nm, which is five times that of the resolution of our instrumentation.

The response plateaus after exposure to a 10 ppm Pb(II) solution with an overall peak shift of approximately 10 nm (Figure 2-25, Trial #1). The sensitivity of the device to changes in Pb(II) concentration is nonlinear and is highest at low Pb(II) concentrations. For concentrations below 100 ppb, the response exceeds 1 nm · 100 ppb^{-1} Pb(II). Taking into consideration that the resolution of our OSA is 0.2 nm, the potential detection limit for Pb(II) can then be extrapolated to 20 ppb.[89] This value is encouragingly close to the maximum permissible Pb(II) concentration in drinking water according to the US Environmental Protection Agency (EPA) (15 ppb), Health Canada, and the German Federal Ministry for the Environment (both 10 ppb).[90] Of course, in an ideal scenario, this Pb(II) detection would be carried out in a purely aqueous medium. Nonetheless, a pre-dilution of a test sample with the requisite amount of DMSO could easily be accomplished in the field with a simple pump, which we argue is easier to employ than the current use of off-site measurement techniques such as ICP-MS.

In a series of control experiments conducted over the course of our explorations with this film formulation on this batch of LPGs, it was demonstrated that the PMO-coated LPG did not exhibit any peak shifts upon exposure to $NaNO_3$ solutions of increasing concentration, indicating that the observed response is not due to interaction with the counter ion or a change in the ionic strength of the solution (Figure 2-26).[91]

Additionally, an uncoated LPG showed no shift in the resonance peak position upon exposure to Pb(II) solutions of increasing concentration in an index-matched solution medium (Figure 2-27),[91] providing evidence for the importance of the mesoporous organosilica coating for enhancing the chemical sensitivity of the optical element.

The sensor could be reused with little loss in sensitivity to solutions of low Pb(II) concentration after regeneration with a 1 M HCl solution for 20 minutes to remove any bound Pb(II) from the film (Figure 2-25).[92] Additionally, a cumulative response to Pb(II) in solution was also noted (Figure 2-28), which implies that the sensor may be used for several consecutive readings without requiring acid treatment between each sensing event. However, ultimately, degradation of the coating after >> 36 h of exposure to the various test solutions and >> 2 h of aqueous HCl exposure led to a loss in overall response to Pb(II) solutions. This is attributed to the inherently low degree of silica condensation in these silica sol-gel films in comparison to, say, condensed powders,[47] which we anticipate results in the material being only limitedly stable to acid over prolonged periods of time. A reduced capacity for metal binding by a siliceous powder incorporating this ligand after exposure to acid was also previously reported.[70]

In brief summary, despite the challenges with being able synthesize mesoporous sol-gel derived functional films with strict control and targeting of a very specific film RI, the unique demonstration of thick, porous, tetrasulfide-modified silica–titania films as functional overlays on LPGs to create a fibre-optic based Pb(II) sensor that responded to changes in solution RI was nonetheless accomplished.[38,39]

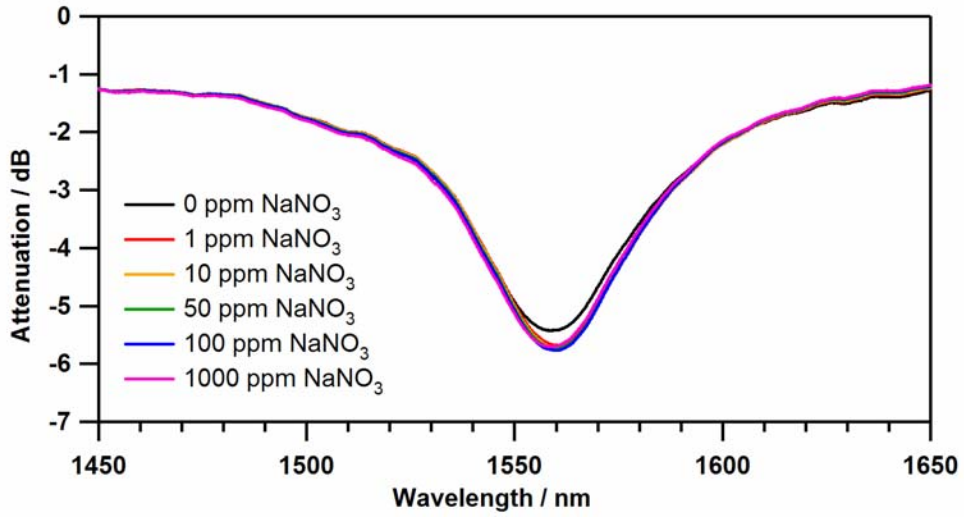

Figure 2-26. No resonant peak shifts were observed in the attenuation spectra recorded for a PMO-coated LPG exposed to aqueous DMSO solutions (RI = 1.387 at 1550 nm) of increasing $NaNO_3$ concentration.

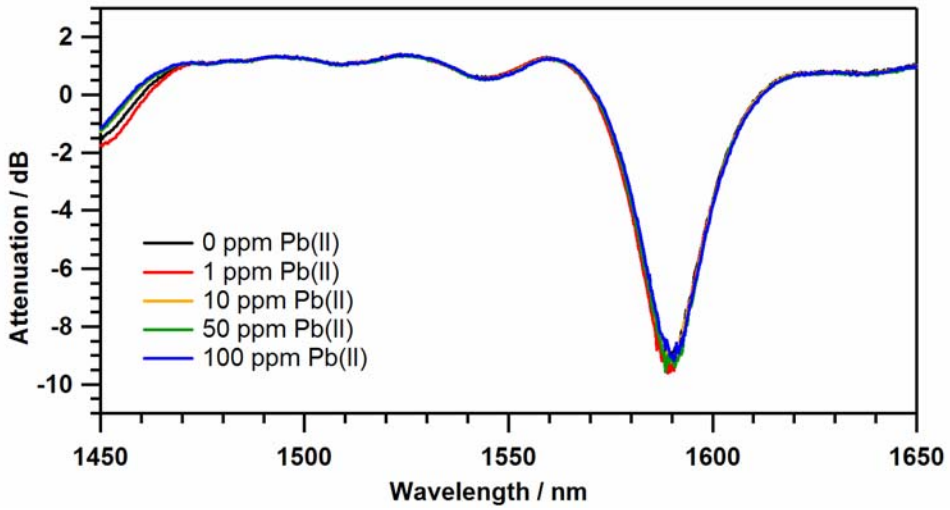

Figure 2-27. No resonant peak shifts observed in the attenuation spectra recorded for an uncoated LPG exposed to aqueous DMSO solutions (RI = 1.358 at 1550 nm) of increasing Pb(II) concentration.

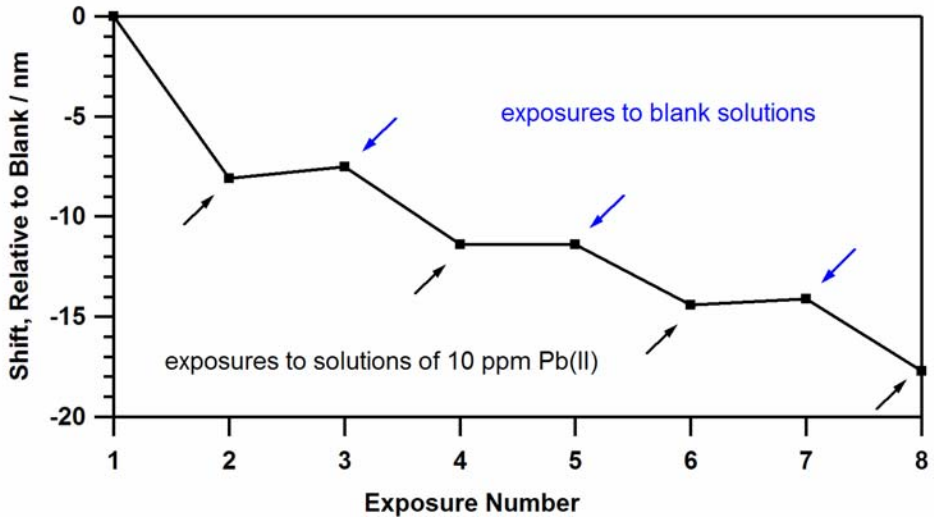

Figure 2-28. Accumulative resonant peak shifts observed upon repeated exposure of the PMO film–LPG system to aqueous DMSO solutions (RI = 1.402 at 1550 nm) of 10 ppm Pb(II) in alternation with exposures to blank solutions.

2.3.5 Pb(II) Sensing in Mixed Metal Solutions

Having demonstrated relatively high sensitivity to Pb(II) binding in mixed aqueous–organic systems, the selectivity of the PMO-coated LPG system for Pb(II) was briefly investigated. The same film–LPG system was subjected to 60 vol% (28 mol%) DMSO solutions (RI = 1.402) containing 1 ppm each of Cd(II), Co(II), Ni(II), Fe(III), and Zn(II) – both with and without the added presence of Pb(II) – and the resonant peak position of the coated LPG was monitored using the OSA.

To our disappointment, no shifts in the resonant peak positions were observed for the mixed metal solutions (both with and without Pb(II) present in the mixture) relative to the blank solution (see Figure 2-29). The concentrations of the metal ions in the solutions

were then each increased to 10 ppm to see if larger magnitude optical changes might be observed. However, again, no shifts in the resonant peak positions were observed for the mixed metal solutions (both with and without Pb(II) present in the mixture) relative to the blank solution (see Figure 2-30).

Interestingly, though, removal of the PMO-coated LPG from the 10 ppm mixed metal solution and immediate immersion of the PMO-coated LPG into a solution of 10 ppm Pb(II) alone (i.e. without acid treatment of the LPG in between exposure to the mixed metal solution and the Pb(II)-only solution as no metal binding event was observed in the mixed metal solution, and the film appeared to still be in good condition)

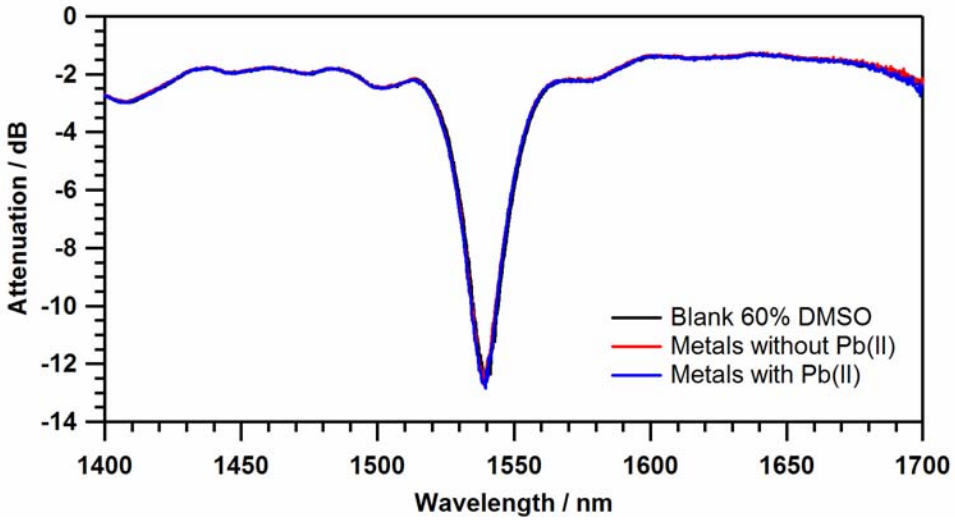

Figure 2-29. Attenuation spectra for the PMO-coated LPG in a mixed metal solution (RI = 1.402) containing 1 ppm each of Cd(II), Co(II), Ni(II), Fe(III), and Zn(II) both with (blue trace) and without (red trace) added Pb(II) (also at a concentration of 1 ppm). No peak shift is observed relative to the metal-free blank (black trace).

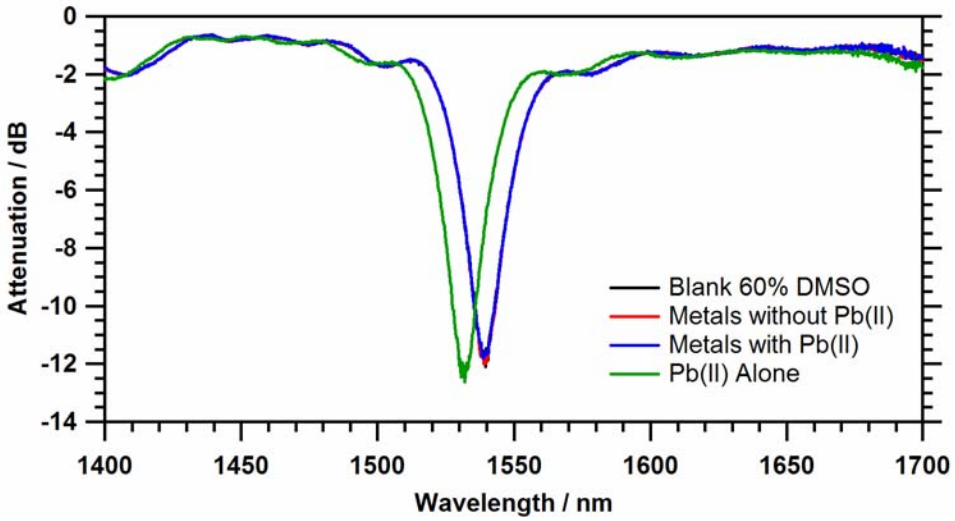

Figure 2-30. Attenuation spectra for the PMO-coated LPG in a mixed metal solution (RI = 1.402) containing 10 ppm each of Cd(II), Co(II), Ni(II), Fe(III), and Zn(II) both with (blue trace) and without (red trace) added Pb(II) (also at a concentration of 10 ppm). No peak shift is observed for the PMO-coated LPG in the mixed metal solutions relative to the metal-free blank (black trace), however, a response to a 10 ppm solution of Pb(II) alone (without acid treatment after exposure to the mixed metal solution) results in a blue-shift in the resonant peak position (green trace).

lead to an observable blue-shift in the resonant peak of nearly 8 nm (see Figure 2-30, green trace).

Our initial explanation of these facts was that some degree of competitive binding between Pb(II) the other metal species might be at play. Cd(II) – also being a soft metal similar in nature to Pb(II) – was thus deemed to be the most likely suspect. Therefore, metal sensing trials were conducted using the same mixture of heavy metal ions (each at a concentration of 10 ppm) both with and without the presence of Pb(II), but

with the complete exclusion of Cd(II) from the solution. Unfortunately, once more, no resonant peak shifts were detected.[93]

Although the reasons for such responses for the PMO-coated LPG presently remain unclear, the metal sensing experiments and their interpretation were complicated by the fact that we were using a mixed aqueous–organic solvent medium. Since the binding behaviour between the metal ions and the tetrasulfide-functionalized films may reasonably be assumed to differ in a mixed aqueous–organic system in comparison to a purely aqueous system, it was decided that further detailed investigations into the heavy metal selectivity of our PMO-coated LPG sensing system be left until the system was first optimized for heavy metal detection in purely aqueous systems.

2.3.6 Mesoporous Tetrasulfide-Functionalized Titania Films for Pb(II) Sensing in Purely Aqueous Solution Systems

As demonstrated in Section 2.3.4, ppb-level Pb(II) sensing was achieved in mixed water / DMSO solution media using silica-based LPG overlays. However, in an effort to execute Pb(II) sensing in purely aqueous media (i.e. the ideal scenario and one that would best mimic 'real world' testing conditions), films that were mainly titania were also explored.

For our first attempts at synthesizing organically-functionalized, surfactant-templated mesoporous titania films, we turned to a report by Soller-Illia and co-workers.[94] Again, **F127** was used at the templating agent, but with titanium tetrachloride

($TiCl_4$) as the main condensable precursor and the substitution of **BTESPTS** for the monosilylated organotrialkoxysilanes (e.g. **APTES**) used in the original publication. Furthermore, sol aging to form a viscous sol, and sol density monitoring along with solvent extraction in acetone (as performed with the silica-based films of the previous sections) were applied to this titania-based film synthesis.

When calibrated with water / DMSO solutions, the first LPGs coated with films prepared from sols consisting of a molar loading of $TiCl_4$: **BTESPTS** = 1 : 0.05 appeared to behave as though the film RI exceeded that of the fibre cladding (recall the anomalous behaviour mentioned with the 100% **BTESPTS** films in Section 2.3.2). It was next decided that **TEOS** could be re-introduced into the coating sols in order to decrease the film RI into a useful range.

With a film of composition $TiCl_4$: **TEOS** : **BTESPTS** = 1 : 0.33 : 0.067 (9 mol% **BTESPTS** (Si basis) / 23 mol% **TEOS** / 68 mol% $TiCl_4$) , we were thrilled to see a significant blue-shift (~ 40 nm) in moving the coated LPG from air to immersion in water.[95] This device was then tested for its optical response upon exposure to purely aqueous Pb(II) solutions. Unfortunately, at sub-ppm levels, no resonant peak shifts were observed. However, a slight blue-shift (< 1 nm) was observed in response to a 1 ppm Pb(II) solution. This was next followed by an astounding ~ 35 nm blue-shift in response to a 10 ppm Pb(II) solution (see Figure 2-31) and a total blue-shift of 140 nm overall after accumulative exposure to Pb(II) solutions up to 100 ppm! Additionally, this strange and sudden onset of a peak shift at higher Pb(II) concentrations was observed on more than

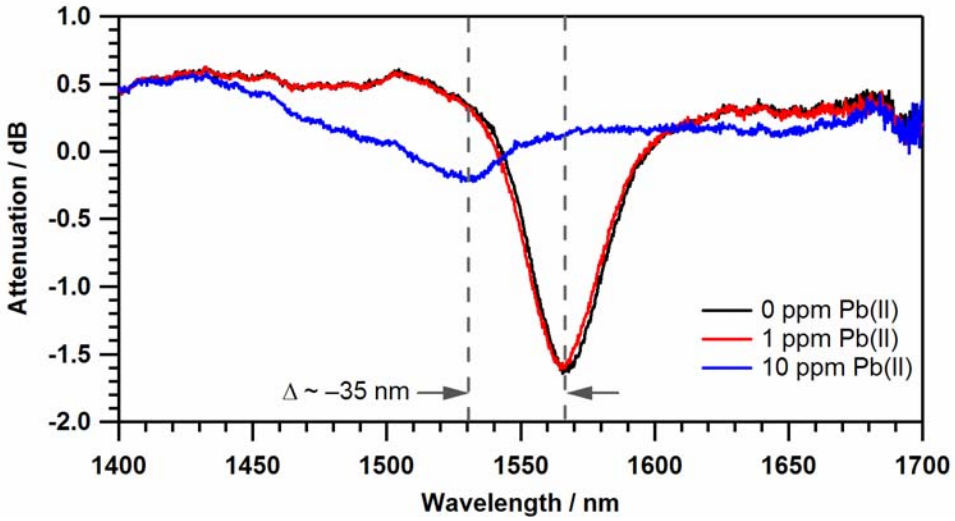

Figure 2-31. Optical response for an LPG coated with a solvent-extracted, tetrasulfide-functionalized titania-based film to purely aqueous solutions of Pb(II). Negligible resonant peak shifts occur at low (sub-ppm) concentrations, but a sudden and dramatic blue-shift upon exposure to a 10 ppm Pb(II) solution is observed.

one occasion with repeated syntheses of films of this formulation on a second LGP-inscribed waveguide.[96]

Given the large, never-before-seen magnitude resonant peak shift upon exposure to a higher concentration Pb(II) solution and the absence of any detectable shifts with less concentrated solutions, a few hypotheses were proposed to rationalize the occurrence of such an optical response. One possibility was that the binding affinity of the films for Pb(II) may have somehow been changed as a result of the incorporation of the tetrasulfide ligand into a matrix of high titania content. A pre-conditioning of the coated LPGs in high concentration Pb(II) solutions (i.e. 50 ppm Pb(II)) was thus conducted prior to exposing the films to ppb-level Pb(II) solutions. With this procedure,

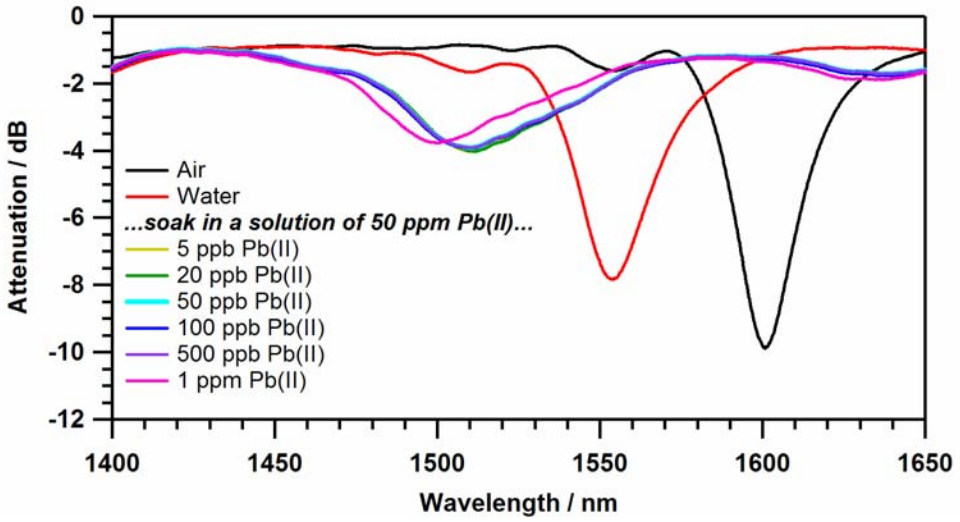

Figure 2-32. Attenuation spectra for an LPG coated with a solvent-extracted, tetrasulfide-functionalized titania-based film to purely aqueous solutions of Pb(II) after pre-exposure of the film to a 50 ppm Pb(II) solution.

a response to an aqueous solution of 50 ppb Pb(II) (~ 1 nm blue-shift) ***was encouragingly detected*** (see Figure 2-32). This was followed by another 10 nm blue-shift upon exposure of the coated LPG to a solution of 1 ppm Pb(II).

To obtain more quantitative insight into the Pb(II) affinity of these materials, a large batch of scraped, solvent-extracted organotitania–silica films was prepared and the Pb(II) uptake in aqueous solution was to be evaluated by ICP-OES. However, these thick films did not firstly demonstrate any notable porosity by nitrogen porosimetry (see Figure 2-33, open circles) nor TEM imaging (see Figure 2-34a), which might account for the

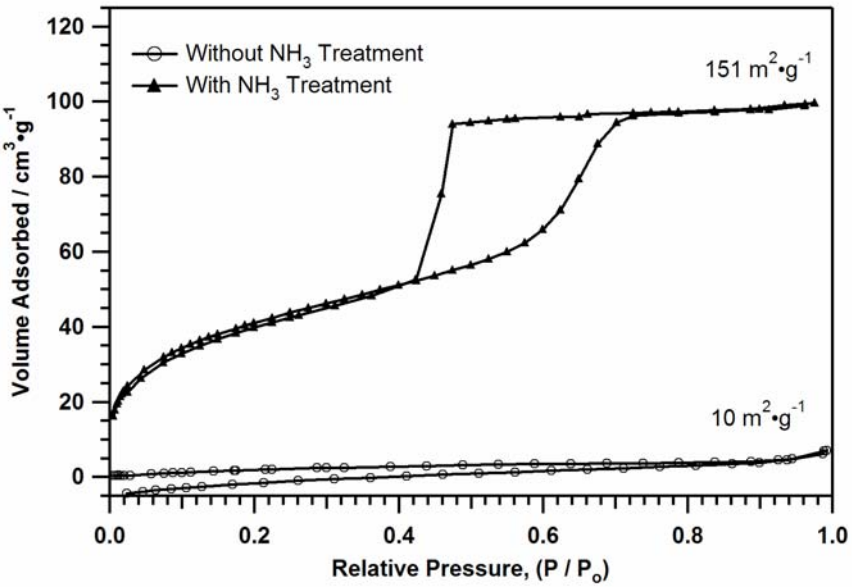

Figure 2-33. Nitrogen isotherms for a large batch of solvent-extracted and scraped tetrasulfide-functionalized titania-based films, both with (black triangles) and without (open circles) ammonia vapour treatment prior to extraction.

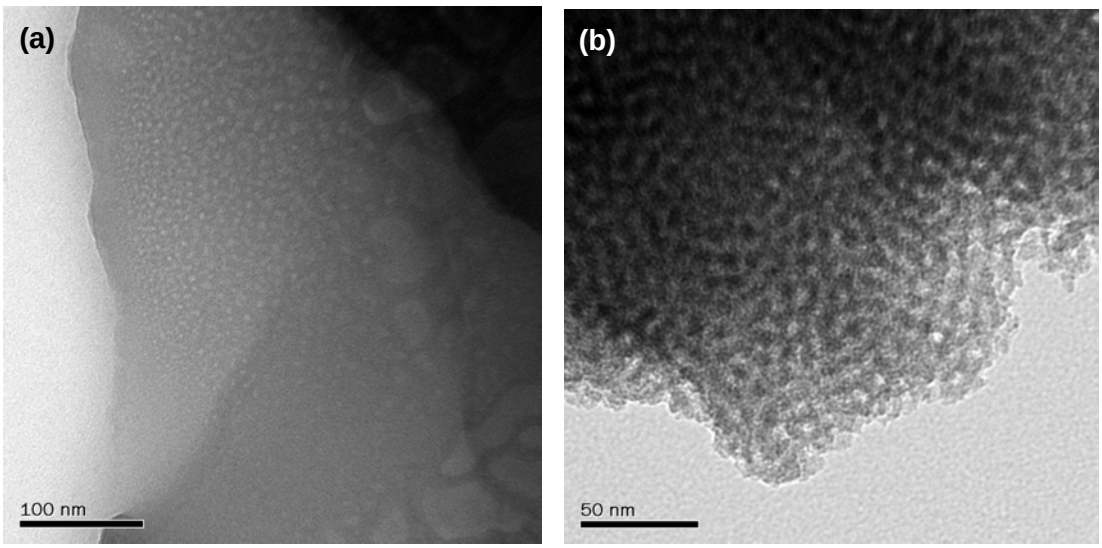

Figure 2-34. TEM images of solvent-extracted, tetrasulfide-functionalized titania-based films (a) without and (b) with ammonia vapour treatment prior to extraction.

low sensitivity to dilute Pb(II) solutions. Consequently, an ammonia vapour treatment step was applied in this film synthesis procedure, after which wormhole-type porosity was regained in these thick, titania-based films (see Figure 2-33 (black triangles) and Figure 2-34b).

Table 2-6. Heavy metal uptake data for a large batch of scraped and solvent-extracted tetrasulfide-functionalized titania-based films immersed in aqueous solutions of Pb(II).

Initial Pb(II) Concentration [ppm]	Final Pb(II) Concentration [ppm]	Pb(II) Absorption [%]	Pb(II) Absorption [mmol·g^{-1}]	Pb(II) Absorption [mg·g^{-1}]	Ratio of Tetrasulfide to Pb(II)
0.057	0	100	2.67×10^{-3}	0.55	87.9
3.50	0	100	1.60×10^{-2}	3.31	14.7
19.9	0	100	9.03×10^{-2}	18.7	2.59
42.0	0.032	99.9	0.192	39.8	1.22
48.7	0.14	99.7	0.234	48.6	1.00
71.9	2.66	96.3	0.318	66.0	0.71
91.1	7.20	92.1	0.352	73.0	0.61
120	26.8	77.7	0.418	86.7	0.44
193	84.9	56.0	0.514	106.5	0.26

A large batch of scraped, ammonia-treated, porous organotitania–silica films was then prepared for evaluation of its Pb(II) uptake behaviour. These data are displayed in Table 2-6. Favourably, we found the binding affinity of these materials for Pb(II) to be on the order of 10^5 (in the case of a ligand : metal molar ratio of 1 : 1), which is still incredibly high. With heavy metal affinity not appearing to be a barrier to sub-ppm level

Pb(II) detection using LPGs in water, we repeated the coating of LPGs with these **F127**-templated, ammonia-treated, porous organotitania–silica films for further Pb(II) sensing.

A promising ~ 35–45 nm blue-shift in the resonant peak position upon moving from air to immersion in water (indicative of the suitability for such a film–LPG system to effect metal sensing in a purely aqueous solution) was consistently observed with subsequently prepared coatings. Unfortunately, though, these films appeared to lack sufficient hydrolytic stability as extended exposure to water in the early stages of the calibration and sensing trials lead to progressive red-shifting of the resonant peak. By the time the peak position stabilized in water, the coated LPG no longer resided in an optimal RI-sensitive region to allow for metal sensing in water (see Figure 2-35).

In a search for other possible routes to preparing films of satisfactory hydrolytic stability, a report by Ozin and co-workers was of noteworthy interest.[97] Here, the authors describe a low-temperature route to preparing mesoporous titania films incorporating pre-formed anatase phase titania nanocrystallites from TTBO (titanium(IV) tetrabutoxide, $Ti(O^nBu)_4$) as the precursor. This is in contrast to the majority of the other reports in the literature dealing with titania-based materials, which often involve a transformation of amorphous titania to one of its crystalline phases by high-temperature calcination (typically $\geq$ 500 °C) of the as-synthesized materials, which is not a viable option in the case of our organically-functionalized film–LPG systems. Consequently, up to this point, only amorphous titania-based films synthesized under relatively low temperature conditions were used to meet the objectives of this project.

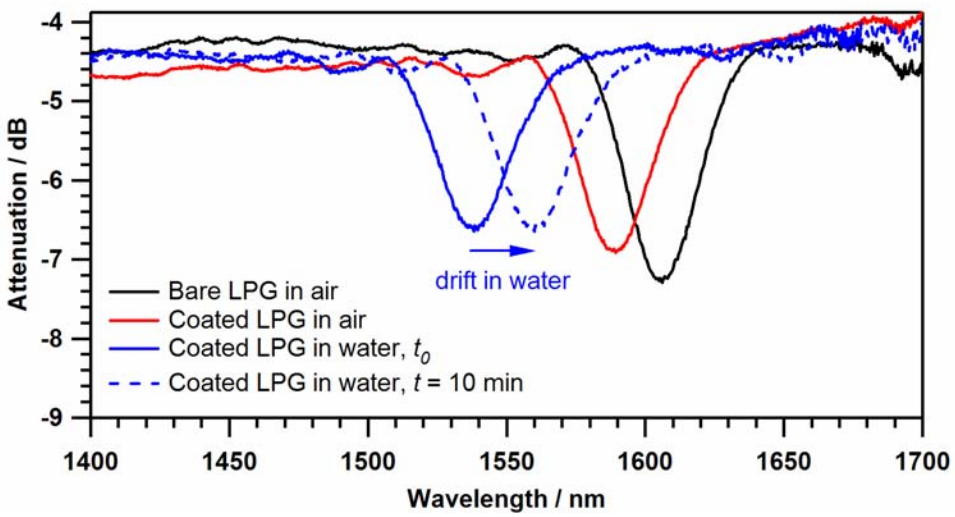

Figure 2-35. Attenuation spectra for an ammonia-treated, solvent-extracted, tetrasulfide-functionalized titania-based film on an LPG showing the red-shift of the resonant peak after 10 minutes of exposure to water.

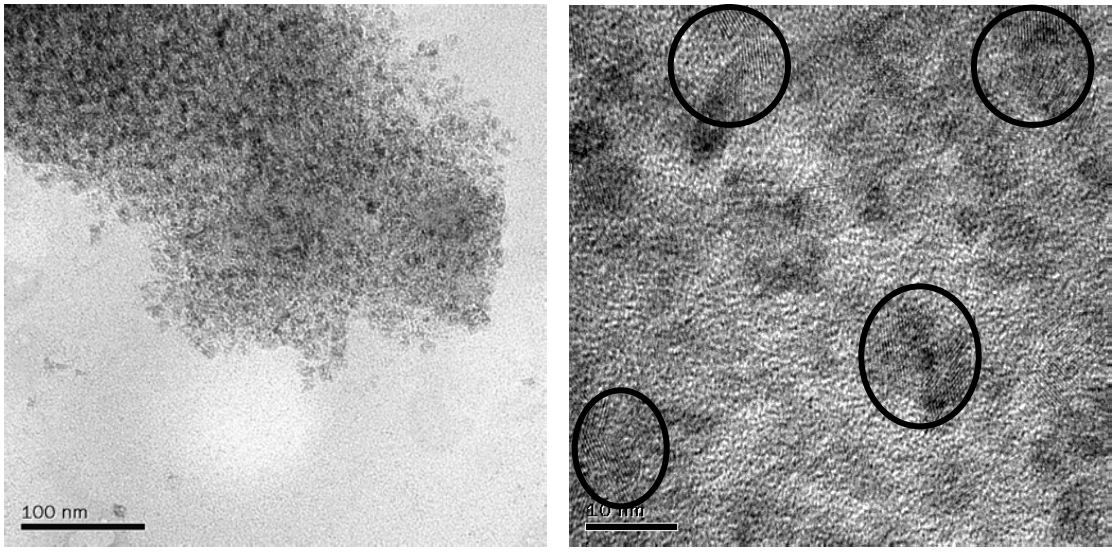

Figure 2-36. TEM images of a tetrasulfide-functionalized, nanoparticulate titania-based film at two different magnifications showing (a) the particulate nature of the film, and (b) some of the crystalline anatase planes (with the more evident sections circled).

Films were thus prepared with a composition of 9 mol% **BTESPTS** (Si basis) and 91 mol% TTBO following the Ozin procedure.[97,98] Unfortunately, these materials did not exhibit any porosity by TEM analysis (Figure 2-36).[99] Futhermore, the application of an ammonia vapour treatment step did not succeed in recovering any visible or significant porosity in this case. However, distinct fringes can be identified in the TEM images of these materials, corresponding to the crystalline planes of titania nanoparticles embedded within the films (see Figure 2-36b).

In spite of the initial unfavourable data obtained regarding the textural properties of these materials, an LPG was coated with this film to see if any optical response could be observed. However, calibration of this coated LPG yielded strange and undecipherable attenuation behaviour consistent with what we had previously encountered with films of RI exceeding that of the fibre cladding (see Section 2.3.2).

VASE was used to estimate the RIs of the coatings as the RI of these films was predicted to be higher than any of the other surfactant-templated materials previously synthesized over the course of this project due to the presence of the nanoparticulate titania. The RI of the 9 mol% **BTESPTS** (Si basis) / 91 mol% TTBO material was measured to be ~ 1.6 at 1550 nm. In addition to the exceedingly high RI of this film, the film thickness was not optimized for a coating of this RI value, either. Not surprisingly, therefore, no meaningful optical response data was obtained using this nanoparticulate film–LPG system.

Although our initial attempts to prepare porous and hydrolytically stable, organically-functionalized titania-based films for use as chemically-selective coatings on LPG-inscribed fibre-optic waveguides have been met with limited success to date, this approach continues to remain promising. We plan to continue working with these transition metal oxide-based materials with the objective of better controlling their mesostructuring and phase stability, and subsequently exploiting their unique properties in evanescent wave and related optical sensing applications.

2.3.7 Organically-Modified Mesoporous Films as Functional Coatings for Silicon-on-Insulator (SOI) Microchip Sensing Devices

Given the relative ease with which parameters such as porosity and organic functionality in these surfactant-templated, metal oxide sol-gel-type materials may theoretically be tuned, one can easily envision extending the application of such functional materials to other types of sensing devices. Specifically, in staying with the theme of evanescent wave sensors, silicon-on-insulator (SOI) microchip devices are of particular interest.[100]

In this embodiment, high-index silicon waveguides supported on a lower index silicon dioxide layer (i.e. the 'lower cladding' layer) are patterned onto a silicon wafer 'base substrate' (see Scheme 2-7). Amazingly, a very large number of individual, miniaturized devices may be patterned onto a given chip (e.g. more than 46 devices on a < 2 cm^2-sized chip) to construct sensor arrays, which easily allow for multiplexed sensing

in conjunction with a microfluidic platform (see Figure 2-37). Here, the high RI contrast between the silicon nanowire waveguides and the underlying silicon dioxide layer allows for the existence of a very strong and highly concentrated evanescent field surrounding the waveguiding structures (see Figure 2-38). Advantageously, this results in high sensitivity to RI changes without the necessity for RI matching between the waveguiding substrate and a given functionalized overlay, which is in direct contrast to the one of the main criteria of LPG-based RI sensing and one of the main difficulties we encountered with that platform. Therefore, potential for the successful application of the materials developed in the preceding sections to these types of devices is of significant interest to us.

A few different device configurations were patterned onto the microchips provided by our collaborators at the National Research Council (NRC) (Ottawa, ON) (see Appendix 2), but our brief foray into this work (in collaboration with the research group of Prof. Hans-Peter Loock at Queen's University) began with tests on the balanced, spiral path Mach-Zehnder interferometers (MZIs) (see Figure 2-37). In particular, the MZIs were designed such that one arm of the interferometer was protected from the external environment by a dense silica upper cladding (i.e. the 'isolation layer') to serve as the reference arm. Meanwhile the second arm of the interferometer was open to the external environment (see Scheme 2-7 and Figure 2-37). Furthermore, in this particular chip design by NRC, each arm of the device follows a spiraled / coiled path in order to increase the sensitivity of the device through an elongated effective path length for light

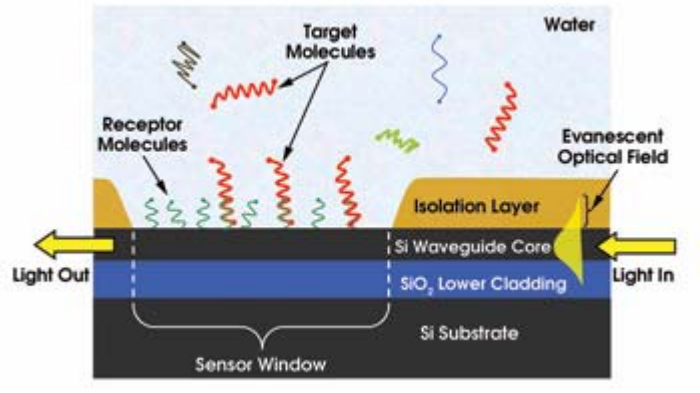

Scheme 2-7. Schematic representation of a cross-sectional view of the sensing window of a silicon photonic wire waveguide device (image taken from reference 100c). The isolation layer may be composed of SU-8 photoresist or dense silica.

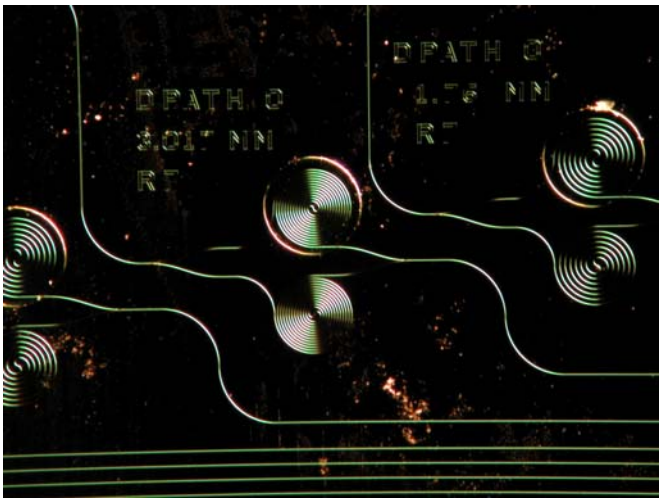

Figure 2-37. Optical micrograph of three different pairs of spiral path MZIs (note the open windows for the sensing arms) on a SOI microchip. The image was taken at 10 × magnification (objective) with dark-field differential interference contrast.

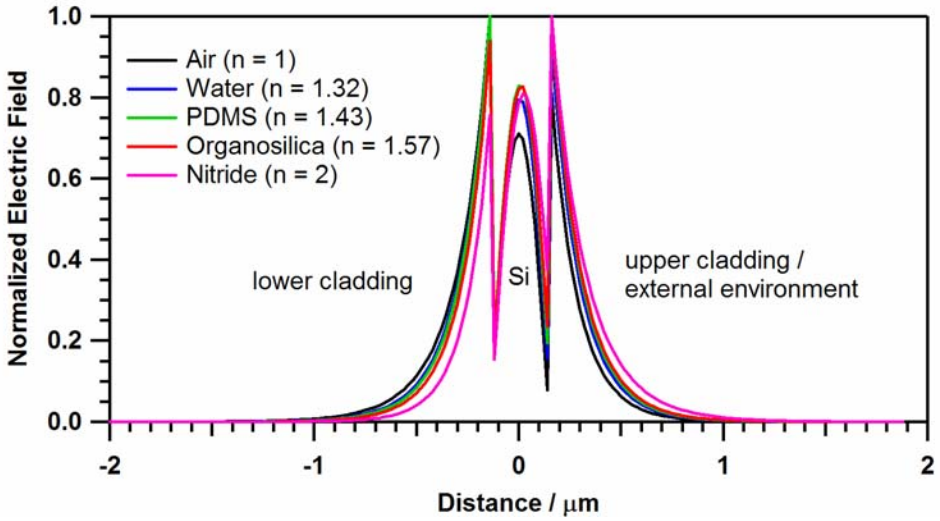

Figure 2-38. Normalized electric field distribution profile for the transverse magnetic (TM) mode at λ = 1550 nm for a 0.26 μm × 0.45 μm SOI photonic wire waveguide with a SiO_2 lower cladding and various upper cladding media. Data modeled and provided by Dr. Dan-Xia Xu (NRC, Ottawa).

passing through the sample of interest. In this fashion, a change in the RI surrounding the exposed 'sensing' arm of the MZI would result in a change in the optical path of the light traveling along the sensing arm relative to the reference arm, which would result in a particular interference pattern. With accurate pre-calibration of the device (see Figure 2-39 for an example), the phase shift deduced from the interference pattern can then be related to the concentration of a given target analyte. The long term goal of this aspect of our sensing project is, therefore, to demonstrate the extension of heavy metal detection in purely aqueous systems using hybrid organosilica films as functional coatings for the sensing arm of these 'lab-on-a-chip' SOI MZI evanescent wave microchip devices.

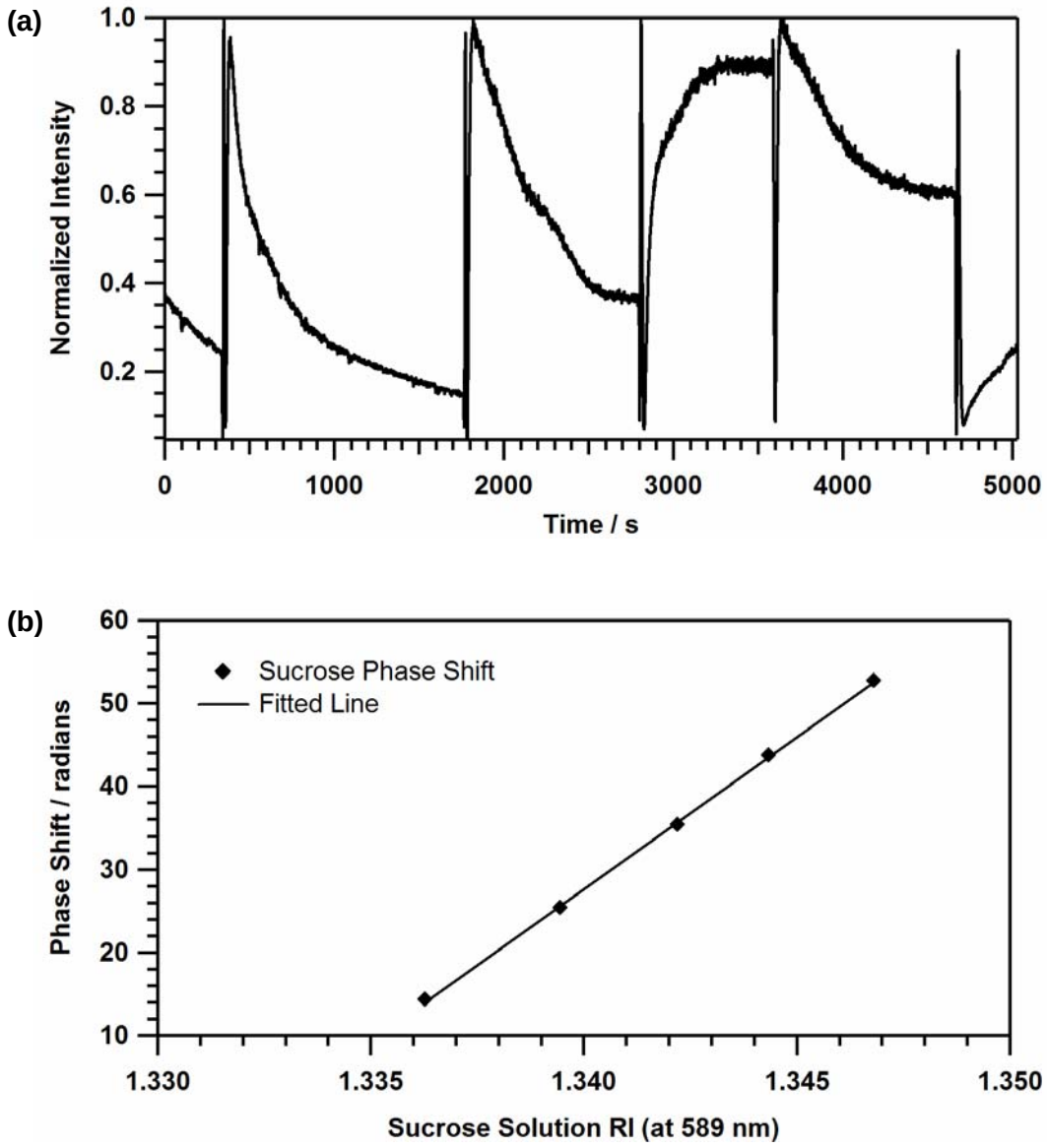

Figure 2-39. (a) Plot of transmitted intensity (normalized) for an unmodified SOI spiral path MZI exposed to water and sucrose solutions of increasing concentration (and RI) showing the interference fringes that arise due to changes in the RI of the ambient environment. (b) Plot of the phase shift measured from 'fringe counting' of the interference fringes in (a) as a function of the RI of the surrounding solution.

Given that RI-matching for these SOI devices is less critical than in the case of LPGs, we first attempted the preparation of thin (~ 400 nm in thickness), 100% **BTESPTS** films for Pb(II) sensing following the same formulation and layer-by-layer coating process used in Section 2.3.2. Unfortunately, no significant optical response in the presence of aqueous Pb(II) solutions of 5 ppb to 50 ppm concentration was observed.

As these non-templated films likely possessed little to no accessible porosity, the **TEOS**-based, mesoporous, tetrasulfide-functionalized films described in Section 2.3.4 were next proposed for Pb(II) sensing on the SOI MZI devices given their success on LPGs in mixed solution media. This time around, thin films were prepared (~ 400 nm in thickness) using the formulation described in Reference 38 and tested for Pb(II) uptake in water. Unfortunately, the effective RI of these silica-based coatings was now *too close* to that of the protective SiO_2 cladding covering the reference arm of the MZI. This led to much smaller differences in the effective RIs surrounding each of the MZI arms, resulting in extremely broad and slow phase shifting behaviour of the device upon exposure to solutions of the target analyte.

The broadness of the interference pattern was not a major setback in and of itself. Certainly, there remain several options with respect to the exploration of other analyte-binding materials. However, when coupled with the large degree of drift observed in the intensity of the transmitted signal, the lack of a well-defined baseline / reference signal makes interpretation of the phase shifts and the collection of reliable and reproducible data incredibly challenging.

An additional technical challenge was the coupling of light in and out of the SOI microchip devices. A nanotaper coupler[100a,101] (i.e. a single-mode fibre-optic waveguide with a finely tapered tip) was used to couple light into the silicon photonic nanowire waveguides, while a multimode fibre was used to collect the light at the waveguide exit. Maximization of the intensity of the transmitted signal depended very strongly on the alignment between the tapered fibre, the nanowire on the chip, and the multimode fibre. However, given the small dimensions (e.g. 9 μm for the diameter of the core of the tapered fibre) and the small overlapping cross-sections between the ends of each of those components as well as the relatively low degree of precision with which each of the components could be positioned using the translating stages,[102] optimization / maximization of the alignment proved to be quite difficult. Any small degree of mechanical creep in the positioning of the various components (which was always eventually an issue) was enough to contribute to drifting of the intensity of the transmitted signal.

For these reasons, the pursuit of an optimal functional overlay material for solution-based heavy metal detection using these SOI devices has been suspended until these important technical and instrumental difficulties are largely rectified.

2.4 MZ (Mach–Zehnder)-Type Tapered Fibre Interferometers

Lastly, in yet another variation of an evanescent wave sensing device, MZ (Mach–Zehnder)-type tapered fibre interferometers[103] (generously provided by Prof.

Scott S.-H. Yam Queen's University, Electrical and Computer Engineering) were also briefly explored in this relation to this project involving mesoporous organosilica films as functional coatings for heavy metal sensors.[104]

These MZ-type tapered fibre interferometers were produced by creating two tapers of controlled size (using a fusion splicer) separated by a distance (L) varying between ~ 25–55 mm along the central region of a length of silica-based, single-mode fibre-optic cable (see Scheme 2-8).[103] To measure the optical response of this device, the fibre-optic waveguide is maintained under constant tension (in similar fashion to the LPG devices, as described in Section 2.7.12) and subjected to water / DMSO solutions of varying RI. In contrast to the LPG devices where the optical response is expressed as shift in the position of a given resonant peak, the optical response for the tapered fibre interferometers manifests itself as a shift in an interference pattern recorded by an OSA.[105]

Although a handful of trials were conducted to in an attempt to calibrate and coat the tapered fibre devices in addition to testing them as heavy metal solution sensors, interpretation and analysis of the attenuation spectra was often unclear (see Figure 2-40). Specifically, there was significant ambiguity in determining the direction in which the interferometric patterns were shifting using our instrumental set-up. Given a different method for data tracking and recording, investigations using this type of evanescent wave sensing device may potentially be revisited. However, in our experience, as this type of device was not yielding results that out-performed our results with LPGs, experimentation on these MZ-type tapered fibre interferometers was suspended.

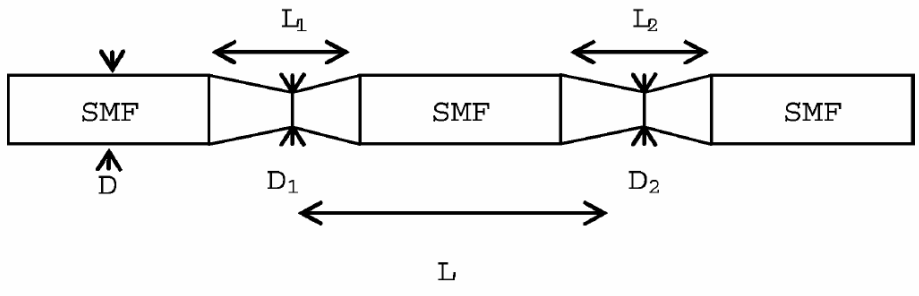

Scheme 2-8. Schematic representation of a MZ-type tapered fibre interferometer, showing two tapers of specific length and diameter separated by a distance, *L*, along a single-mode fibre-optic waveguide (SMF). (Image taken from reference 103.)

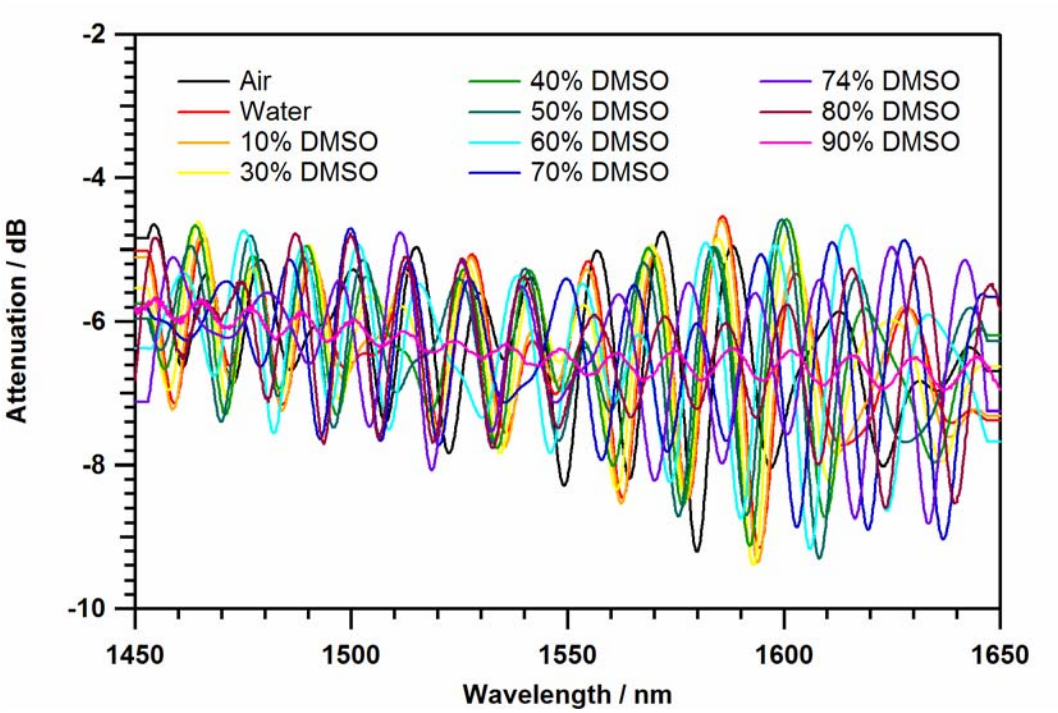

Figure 2-40. Attenuation spectra for a bare, uncoated tapered fibre interferometer in water / DMSO solutions of varying composition. (Data courtesy of Dr. Judy Cipot-Wechsler, Queen's University.)

2.5 Future Work

With respect to the overarching objective of demonstrating the utility of surfactant-templated, organically-modified mesporous metal oxide materials as functional coatings for heavy metal optical sensors, a few important 'proof-of-concept' milestones have been achieved to-date. However, several facets of this work remain to be explored in order to gain a better understanding of the materials design and synthesis, and the interactions at the interface between the materials and the devices – as well as the optimization of the final devices themselves – and are addressed and summarized in the paragraphs that follow.

Firstly, sensitive and reproducible heavy metal detection in purely aqueous solutions remains to be seen. Efforts towards realizing this aim may be focused on further exploring the use of higher-index transition metal oxide-based films as alternatives to the silica-based films predominantly explored in this project to date. Although such an endeavour will likely be made difficult due to the higher reactivity (and hence the decreased stability) of transition metal oxide precursors,[30] several strategies may be explored in order to obtain materials bearing dense metal oxide frameworks with concomitant preservation of a high degree of uniform and interconnected mesoporosity, as well as improved hydrolytic stability.

For example, the synthesis of nanoparticulate titania-based films (as introduced in Section 2.3.6) may be explored in greater depth to recover porosity in these materials. Also, silica films doped with Zr or Al may be an interesting alternative for the preparation of hydrolytically stable coatings.[106]

Furthermore, a variety of other silica and organosilica precursors may prove to be useful for both boosting the RI of these coatings for evanescent wave sensing devices and increasing their hydrolytic stability. For instance, organically-modified zeolitic films, as well as the use of a majority fraction of silsesquioxane-type precursors such as **BTESE** in the surfactant-templated sols could be of interest.[107] Also, phosphate-functionalized ligand moieties may be better incorporated into a titania-based framework than the analogous alkoxysilane derivatives.[30]

In addition, a large variety of templates are available – the breadth of which has been largely under-explored in this project thus far. It has been purported that films prepared from CTAB (cetyltrimethylammonium bromide or hexadecyltrimethylammonium bromide) as a template are more stable than films prepared from nonionic block copolymers (such as F127) as a result of a decreased fraction of microporosity in the CTAB-templated films.[30] On a related note, films prepared using KLE-type surfactants (i.e. poly(ethylene-*co*-butylene)-*b*-poly(ethylene oxide) polymers) have been reported to be more robust that their Pluronic®-templated counterparts.[30] Consequently, experimentation with film syntheses that make use of such templating agents may be expected to yield some intriguing materials for the development of solution-based, optical heavy metal sensors.

In yet another possible avenue, silylated Pluronic®-type surfactants could be explored as a dopant for tuning the RIs of the coatings.[108] Here, a mixture of both non-silylated and silylated Pluronic® block copolymer could be used in a starting sol to serve as a template for mesostructure formation, however, the amount of block copolymer

removed during the solvent-extraction process could be reliably varied over a wide range. This would be particularly interesting as the residual surfactant would be expected to affect the film RI, but – as shown in our studies (see Table 2-2) – not impair heavy metal absorption by the films.

Once heavy metal detection is realized in purely aqueous systems, further explorations in the realm of the characterization and quantification of analyte specificity and selectivity may then proceed. Factors such as solution pH may prove to be important.[109] Additionally, more specialized ligand species may have to be introduced into the films in order to achieve improved heavy metal selectivity.

Surfactant-templated, organically-functionalized mesoporous silica and transition metal oxide films that prove to be effective coatings for LPG-based optical heavy metal sensors will then be expected to translate over to a wide array of other evanescent wave-based detection schemes. Some variations (e.g. SOI microchip MZIs and MZ-type tapered fibre interferometers) were explored, here, in unoptimized configurations, but merit further development. In particular, alternative nanowire waveguide devices on the SOI microchips (single interferometers, multiplexed interferometers, as well as microring resonators, and so forth) could prove promising.

2.6 Conclusions

In summary, we have explored the design, synthesis, and application of thick, sol-gel derived, surfactant-templated, organically-functionalized mesoporous silica–titania

films as functional coatings for the refractive index-based detection of heavy metal species in solution. Notably, this work provides evidence in support of the ease of processing surfactant-templated mesoporous films in comparison to non-templated xerogel films, and eventually we were able to the demonstration of sub-ppm level Pb(II) sensing in mixed aqueous–organic solutions using LPG-inscribed fibre-optic waveguides.[38,39]

Despite the rich variety of materials that may be accessed via surfactant-templated sol-gel chemistry and the versatility of the methodology, this work has emphasized the true complexity of the film synthesis process – the greatest effect being the significant interplay and interdependence of a variety of processing parameters that influence the synthesis of a kinetically-frozen framework.

Furthermore, different types of surfactant-templated materials (i.e. titania-based materials) have also been recently explored in an effort to realize LPG-based heavy metal detection in purely aqueous media. Although these pursuits are still in their infancy, the synthesis of a suitable LPG overlay seems highly plausible, and efforts to continue along this research objective will certainly be maintained.

Finally, with steady improvements in the design of our functional, hybrid films, we anticipate that these materials may be extended to a variety of evanescent wave-based heavy metal sensing schemes – all of which may contribute to significant and much-needed advancements in fields such as on-site, on-line, and remote environmental detection and monitoring.

2.7 Experimental Procedures

2.7.1 General and Materials

Pluronic® F127 (**F127**, poly(ethylene oxide)$_{106}$–poly(propylene oxide)$_{70}$–poly(ethylene oxide)$_{106}$), Brij® 56 (**B56**, poly(ethylene oxide)$_{10}$–hexadecyl ether), Pluronic® P123 (**P123**, poly(ethylene oxide)$_{20}$–poly(propylene oxide)$_{70}$–poly(ethylene oxide)$_{20}$), **TEOS** (tetraethoxysilane), **MPTMS** (3-mercaptopropyltrimethoxysilane), **APTES** (3-aminopropyltriethoxysilane), **BTESB** (1,4-bis(triethoxysilyl)benzene), **BTESE** (1,2-bis(triethoxysilyl)ethane), **TTIP** (titanium(IV) tetraisopropoxide), TTBO (Ti(O^{n}Bu)$_4$, titanium(IV) tetrabutoxide), $TiCl_4$ (titanium(IV) tetrachloride), *n*-BuOH, *t*-BuOH, $Pb(NO_3)_{2(s)}$, $NaNO_{3(s)}$, $K_2CO_{3(s)}$, and $(NH_4)HF_{2(s)}$ (ammonium hydrogen difluoride) were purchased from Sigma-Aldrich. **MPTES** (3-mercaptopropyltriethoxysilane), **BTESPTS** (bis[3-(triethoxysilyl)propyl]tetrasulfide), $Hg(NO_3)_2{\cdot}H_2O_{(s)}$, and $LiCl_{(s)}$ were purchased from Alfa Aesar. **BTESO** (1,8-bis(triethoxysilyl)octane) was purchased from Gelest. $Cd(NO_3)_2{\cdot}4H_2O_{(s)}$, $Co(NO_3)_2{\cdot}6H_2O_{(s)}$, $Fe(NO_3)_3{\cdot}9H_2O_{(s)}$, $Ni(NO_3)_2{\cdot}6H_2O_{(s)}$, $Zn(NO_3)_2{\cdot}6H_2O_{(s)}$, $KCl_{(s)}$, $KNO_{3(s)}$, in addition to concentrated $HCl_{(aq)}$, $H_2SO_{4(aq)}$, $H_2O_{2(aq)}$, $NH_4OH_{(aq)}$, and Optima®-grade concentrated $HNO_{3(aq)}$, as well as $KOH_{(s)}$, acetone, DMSO (dimethylsulfoxide), hexanes, toluene, plain glass microscope slides, and syringe filters (with either 0.45 μm Nylon® or Teflon® membranes) were purchased from Thermo Fisher Scientific. Both 95% ethanol and anhydrous ethanol were purchased from Commercial Alcohols. Certified RI-matching fluid (1.7250 ± 0.0005) was purchased from Cargille Labs. All of the aforementioned reagents and solvents were used as

received without further purification. Millipore® water was used in all reaction mixtures and LPG test solutions.

Corning® standard telecommunication fibre-optic waveguides (SMF-28) inscribed with an LPG (grating length = 25 mm, periodicity = 548 μm and 320 μm) were generously provided by ITF Labs (Montréal, Canada). Single-mode, tapered MZ-type fibre interferometers were generously provided by Prof. Scott S. H. Yam (Queen's University, Electrical and Computer Engineering). Single-mode fibre (SMF-28) was purchased from Corning. High-index SF10 glass wafers were purchased from Volume Precision Glass, Inc. Crystalline, single-side polished Si wafers (boron-doped, <111> orientation, 500 μm wafer thickness) were purchased from Virginia Semiconductor. SOI microchips were generously provided by NRC (Ottawa, Canada).

Spin-coated films were prepared using a Laurell WS-400-6NPP / LITE spin-coater (typical conditions included spinning at a rate of 3000 rpm for 10 s). Dip-coated films were prepared using a dip-coater built in-house ('Automated Dip Coater, Software Version 1.0', 18 / 11 / 2005, written by Mr. Robert Hobden) (typically at a withdrawal rate of 10 $mm \cdot s^{-1}$). LPGs were dip-coated and submerged in the test solutions using Teflon®-based sample holders built in-house (designed by Dr. Jack Barnes, Queen's University).

2.7.2 Substrate Preparation / Activation

Base Etching. Glass or crystalline Si substrates were first immersed in a 1 M $KOH_{(aq)}$ solution and sonicated for 10 minutes, and then immersed and sonicated in DI H_2O two more times for 10 minutes each time. The substrates were subsequently allowed to air-dry overnight prior to use.

Piranha Etching. Glass or crystalline Si substrates were first immersed in Piranha solution (prepared using a 3 : 1 volumetric ratio of concentrated $H_2SO_{4(aq)}$ and concentrated $H_2O_{2(aq)}$, respectively) for 10–20 minutes (***CAUTION: Piranha solution is an extremely energetic and potentially explosive mixture! The preparation of this solution and its reaction with substrate surfaces and organics results in a significant release of heat! DO NOT store this solution! Prepare it just prior to use, and discard the solution immediately afterwards by flushing it down the drain with copious amounts of water!)***. The substrates were then generously rinsed with DI H_2O and subsequently allowed to air-dry overnight prior to use. This Piranha etching solution was also occasionally used to remove silica- and organosilica-based sol-gel coatings from glass and Si substrates as well as LPGs in order to recover and re-use the substrates.

LPG Etching. The LPG was first connected to a light source and an Agilent 86142B optical spectrum analyzer (OSA) to locate the highest order (i.e. longest wavelength) resonant peak within a 1200–1700 nm window. The LPG-containing section of the fibre was then suspended across a Teflon® well and was anchored at both ends by magnetic fibre clamps to maintain constant tension across the LPG during all of the spectral measurements. The Teflon® well was then filled with a concentrated aqueous solution of

$(NH_4)HF_{2(aq)}$ (25 g of $(NH_4)HF_2$ in 100 mL of DI H_2O, or 20 wt% $(NH_4)HF_{2(aq)}$) and the LPG was exposed to this etching solution either for a prescribed length of time (on the order of a few minutes) or until the resonant peak shifted to a desired position while in solution. The etching solution was then carefully pulled out of the well with a syringe or pipette, and the LPG was subsequently generously flushed with DI H_2O while fixed inside the well. The LPG was then allowed to dry ambiently for at least 4 hours prior to use. This $(NH_4)HF_{2(aq)}$ etching solution was also frequently used to remove silica- and organosilica-based sol-gel coatings from glass and Si substrates as well as LPGs in order to recover and re-use the substrates.

2.7.3 MPTMS Monolayers and Thin Multilayers

Base- or Piranha-etched glass substrates and LPGs were immersed in either **MPTMS** / hexanes or **MPTMS** / toluene solutions of 0.2–20 mol% **MPTMS** for 24 h at room temperature. The silylated substrates were then rinsed with copious amounts of fresh hexanes or toluene (as appropriate) and allowed to dry at T = 25–80 °C for 4–16 hours prior to use.

2.7.4 TEOS–MPTMS Xerogel Films

Xerogel Film Synthesis. A two-step acid- and base-catalyzed procedure previously published in the literature[45] was modified to incorporate **MPTMS** in the starting sol to yield organosilica xerogel films. In the first step, **TEOS**, **MPTMS**, H_2O, anhydrous

EtOH and HCl (present in a molar ratio of $1 - x : x : 2.0 : 3.8 : 7.3 \times 10^{-4}$, respectively, where x assumed fractional values between '0' and '1') were added to an RBF and allowed to react at 60 °C for 1.5 h under stirring (typical scale = 25 mmol of total Si species). Next, an aliquot of 50 mM $NH_4OH_{(aq)}$ was added under stirring such that the molar ratio of NH_4OH / Si species = 2.05×10^{-3}. Immediately following the addition of the base, the sol was passed through a syringe filter and then used to coat the designated substrates either by spin-coating, dip-coating, or drop-casting. Alternatively, the sol was left to condense for 15–20 minutes (as t_{gel} ~ 30 minutes) before using it to coat the designated substrates in order to yield thick, xerogel films.

***Post-Synthetic Treatments*:** *Oven Drying / Curing*. In the simplest case, the as-synthesized films were immediately dried and cured at a temperature between 25 °C and 120 °C for a time span lasting anywhere from 4 h to 16 h prior to further characterization and testing. It should also be noted that following any series of aging steps, the last step always involved drying and curing of the films under the conditions listed above prior to further characterization and testing.

Solvent-Saturated Atmosphere. To create a solvent-saturated atmosphere for the aging of spin-coated films, the aging solution / solvent of interest (e.g. an EtOH (95%) / water / $NH_4OH_{(aq)}$ mixture, or hexanes)[45], was introduced into the spin-coating chamber, bell jar, or dessicator, which was then sealed off to allow for the accumulation of solvent vapours within the vessel. Films were subsequently exposed to the solvent-saturated atmosphere for 1–2 h.

Immersion in an Aging Solution. In an alternative aging procedure, as-synthesized spin- or dip-coated films were directly immersed in a given aging solution[48b,c] (e.g. $NH_4OH_{(aq)}$ in 95% ethanol, or a non-polar solvent system such as hexanes) at temperatures between 25 °C and 60 °C for anywhere between 0.5 h and 24 h.

Freeze-Drying. For the freeze-drying of films,[48d] film synthesis procedures were modified to include *t*-BuOH as a substitute for ethanol as the solvent in the coating sols. After coating, the as-synthesized films were then chilled in container immersed in an ice bath at 0 °C to freeze the films prior to transferring the films to a Labconco Freezone 4.5 freeze-dryer where they were left under vacuum (< 0.1 mbar) at -48 °C for 24 h.

2.7.5 Polysilsesquioxane Xerogel Films

Polysilsesquioxane xerogel films were synthesized from either **BTESE**, **BTESO**, or **BTESB** alone, or in combination with either **MPTMS** or **MPTES**. Based on recommendations provided by Prof. Kenneth J. Shea and co-workers,[49a] the general sol composition consisted of a total monomer concentration of 0.4 M in alcoholic solvent (e.g. anhydrous ethanol), a molar ratio of water : total monomers = 6 : 1, and a catalyst (e.g. NaOH or HCl) loading of 10.8 mol% with respect to the total moles of monomer present (typical scale = 2 mmol of total Si species). The reagents were added to each other and manually shaken at room temperature. The sol was then used to coat substrates immediately thereafter, or was left to stand and condense for $t \sim 0.8t_{gel}$ (where t_{gel} ranged from 4–12 h depending on the sol) before using it to coat the designated substrates in

order to yield thick, xerogel films. Lastly, the as-synthesized films were oven-dried / cured at 95 °C for 16 h prior to further characterization and testing.

2.7.6 First-Generation Pluronic® F127-Templated Materials

Using a procedure provided by Prof. Galen Stucky and co-workers,[57] a sol was prepared at room temperature using the following reagents in the molar ratios of **TEOS** : **MPTMS** : **F127** : EtOH : H_2O : HCl = $1 - x : x : 8.0 \times 10^{-3} : 34 : 6.0 : 0.10$ (where $x = 0$–0.4). **F127** was weighed out into a small glass jar and dissolved under stirring (~ 20 minutes) with anhydrous EtOH. Next, $HCl_{(aq)}$ and the silanes were added to the solution of **F127** and the sol was capped and left to stir at room temperature for an additional 30 minutes (typical scale = 10 mmol of total Si species). Thin films were prepared by spin-coating or dip-coating with this sol after the 30 minutes had elapsed. Alternatively, the sol was left stirring and open to atmosphere at room temperature or at 60 °C to allow the sol to age and thicken in order to prepare thicker films. It should be noted that – depending on temperature used – this aging and thickening step took anywhere from ~ 3 h to 5 days. The remaining, unused sol was subsequently poured into a Petri dish and left to gel under ambient conditions before being subjected to the same post-synthetic treatment conditions as the corresponding films.

In the following step, the films were cured at 90–120 °C for 8–24 h. Template removal was attempted by Soxhlet extraction with a mixture of 95% EtOH and 6 M $HCl_{(aq)}$ (at a loading of 1 mL of 6 M $HCl_{(aq)}$ per 200 mL of EtOH) for 24–72 h. Finally,

the films were dried once more either ambiently or at 90–120 °C for 8–24 h prior to further characterization and testing.

2.7.7 Brij® 56-Templated Functionalized Films

A procedure published by Brinker and co-workers was modified for our purposes.[58] A starting sol with a molar ratio **TEOS** : **APTES** or **MPTMS** or **BTESPTS** : **B56** : anhydrous EtOH : H_2O : HCl = 1.0 : *x* : 0.082 : 24 : 5.2 : 0.28 was prepared (where *x* = 0–0.25) by first dissolving **B56** in EtOH under stirring at room temperature. Next, the silanes, acid, and additional water were added to the ethanolic solution (typical scale = 11 mmol of total Si species), and the sol was capped and left to stir at room temperature for an additional 0.5–1 h. Thin films were prepared by spin-coating or dip-coating with this sol after the 0.5–1 h had elapsed. Alternatively, the sol was left stirring and open to atmosphere at room temperature or at 60 °C to allow the sol to age and thicken in order to prepare thicker films. It should be noted that depending on temperature used, this aging and thickening step took anywhere from ~ 3 h to 3 days. The remaining, unused sol was subsequently poured into a Petri dish and left to gel under ambient conditions before being subjected to the same post-synthetic treatment conditions as the corresponding films.

In the following step, the as-synthesized films were dried ambiently for 8–24 h, and then exposed to a saturated ammonia atmosphere[63,64,65] for 2 h at room temperature. Specifically, the saturated ammonia atmosphere was established by placing ~ 5 mL of

concentrated $NH_4OH_{(aq)}$ at the bottom of a sealed dessicator chamber and allowing the environment within the chamber to equilibrate over at least 2 h prior to introducing the as-synthesized silica and organosilica samples into the chamber. After ammonia treatment, the films were cured at 80 °C for 16–24 h. Template removal was facilitated by solvent extraction in an RBF with a mixture of 95% EtOH (80 mL) and 9 M $HCl_{(aq)}$ (10 mL) under reflux for 16–24 h. Finally, the films were dried once more either ambiently or at 90–120 °C for 8–24 h prior to further characterization and testing.

2.7.8 High-Index Tetrasulfide Films

Using a previously published procedure as a starting point,[69] a 5 vol% solution of **BTESPTS** in anhydrous EtOH was prepared (typical scale = 0.4 mmol of **BTESPTS**). To this solution, acidic water (in the form of 0.1 M $HCl_{(aq)}$) was added such that the molar ratio of **BTESPTS** : H_2O = 1 : 8. The reaction mixture was then sonicated for 15 minutes, and then capped and left to stand for 16 h at room temperature.

A layer-by-layer spin-coating process was used to build up films on 2 cm × 2 cm crystalline Si substrates. For the first layer, a 0.05 mL aliquot of the coating sol was deposited onto the substrate, and the substrate was then spun at 3000 rpm for 10 s. The coated substrate was left to dry ambiently for 24 h before depositing the next layer. This process was repeated such that a film consisting of 4 total organosilane layers was obtained. An analogous procedure was followed for the multilayered dip-coating of crystalline Si wafers as well as LPGs (at withdrawal rates between 10 and 20 $mm \cdot s^{-1}$).

2.7.9 Second-Generation Pluronic® F127-Templated Materials

A procedure previously published by Stucky and co-workers was used as a starting point for the preparation of these films.[81] **BTESPTS** was prehydrolyzed along with **TEOS** using deionized water, $HCl_{(aq)}$, and anhydrous ethanol at 60 °C for 1.5 h. After this, a solution of **TTIP** dispersed in ethanol and $HCl_{(aq)}$ was added to the silica sol. The resulting mixture was then added to a solution of **F127** dissolved in anhydrous ethanol. The reagents in the final sol were present in molar ratios of **TEOS** : **BTESPTS** : **TTIP** : **F127** : EtOH : H_2O : HCl = 1.0 : 0.050 : 0.010 : 6.0×10^{-3} : 35 : 8.0 : 0.11 (typical scale = 10 mmol of total Si species). After stirring at room temperature (capped) for up to 24 h, thin films were prepared by spin-coating or dip-coating with this sol. To prepare thick films, the sol was further aged at 60 °C while open to the atmosphere until its density had increased to 0.95 $g \cdot mL^{-1}$, at which point it was used to either spin-coat and / or dip-coat designated substrates in a humidity-controlled chamber (RH = 45%, controlled with a saturated solution of $K_2CO_{3(aq)}$).[78] The films were then left to stand and dry inside the humidity-controlled chamber for 16–24 h. In order to promote silanol condensation and reinforce the framework of the thick films, the as-synthesized films were exposed to a saturated atmosphere of ammonia vapour[63,64,65] for 2 h and a trimethylethoxysilane atmosphere[82] at 80 °C for 5 h. After a final oven curing at 80 °C for 16 h, removal of the surfactant was accomplished by solvent extraction in acetone followed by rinsing with hot acetone to yield the thick, porous films. A similar procedure was followed to prepare a large number of films on glass microscope slides, which were

later scraped to collect a sufficient amount of material to conduct nitrogen physisorption analysis as well as TEM, HAADF-STEM, and EDX-STEM characterization.

2.7.10 Titania-Based Films

Amorphous Organotitania–Silica Films. This procedure was adapted from a procedure previously reported in the literature.[94] **F127** was first dissolved in anyhydrous EtOH under stirring. In a separate vial, **TEOS** and **BTESPTS** were solubilized in a bit of EtOH, and this mixture of silanes was then added to the solution of **F127**. Finally, $TiCl_4$ and H_2O were added to the reaction mixture. The reagents in the final sol were present in molar ratios of $TiCl_4$: **TEOS** : **BTESPTS** : **F127** : EtOH : H_2O = 1.0 : 0.33 : 0.066 : 0.73 : 59 : 7.3 (typical scale = 11 mmol of total Ti and Si species). After stirring at room temperature (capped) for up to 24 h, thin films were prepared by spin-coating or dip-coating with this sol. To prepare thick films, the sol was further aged at 60 °C while open to the atmosphere until its density had increased to 1.0 $g \cdot mL^{-1}$, at which point it was used to either spin-coat and / or dip-coat designated substrates in a humidity-controlled chamber (RH = 45%, controlled with a saturated solution of $K_2CO_{3(aq)}$).[78] The films were then left to stand and dry inside the humidity-controlled chamber for 16–24 h. In order to promote silanol condensation and reinforce the framework of the thick films, the as-synthesized films were exposed to a saturated atmosphere of ammonia vapour[63,64,65] for 2 h. After a final oven curing at 80 °C for 16 h, removal of the surfactant was accomplished by solvent extraction in acetone to yield the thick, porous films. A similar

procedure was followed to prepare a large number of films on glass microscope slides, which were later scraped to collect a sufficient amount of material to conduct nitrogen physisorption analysis, as well as TEM and metal uptake characterization.

Nanoparticulate Organotitania–Silica Films. This procedure was adapted from a procedure previously reported in the literature.[97] **P123** was first dissolved in *n*-BuOH and concentrated $HCl_{(aq)}$ under stirring for ~ 1.5 h before adding TTBO. Next, **BTESPTS** was added slowly and the reaction mixture was capped and left to stir for 3 h at room temperature. The reagents in the resulting sol were present in molar ratios of TTBO : **BTESPTS** : **P123** : *n*-BuOH : concentrated $HCl_{(aq)}$ = 1.0 : 0.050 : 0.037 : 8.6 : 1.7 : (typical scale = 7 mmol of total Ti and Si species). The sol was then heated at 100 °C for 1 h to hydrothermally produce the anatase nanocrystallites in solution. Thereafter, the sol was used to either spin-coat and / or dip-coat designated substrates in a humidity-controlled chamber (RH = 45%, controlled with a saturated solution of $K_2CO_{3(aq)}$).[78] The remaining, unused sol was subsequently poured into a Petri dish and left to gel and age under ambient conditions for 2 days before being subjected to the same post-synthetic treatment conditions as the corresponding films.

The films were then aged for 2 days in an atmosphere with an RH of 84% (controlled with a saturated solution of $KCl_{(aq)}$). Occasionally, the as-synthesized films were exposed to a saturated atmosphere of ammonia vapour[63,64,65] for 2 h before proceeding to cure the films at 80 ° C for 24 h. Removal of the surfactant was accomplished by solvent extraction in a mixture of diethyl ether and acetone (in a 1 : 1

volumetric ratio). The films and bulk gel underwent solvent extraction for 1 day and 3 days, respectively.

2.7.11 Determination of Heavy Metal Concentration in Test Solutions Using Standard Analytical Techniques

The Hg(II) content of a solution was measured both before and after exposure to the porous, organically-functionalized bulk materials or films using cold-vapour atomic absorption spectrometry (CV-AAS). The Pb(II) content of a solution was measured both before and after exposure to the porous, organically-functionalized bulk materials or films using inductively-coupled plasma optical emission spectrometry (ICP-OES).

As a starting point, experiments were usually set up with the assumption of metal-to-ligand binding occurring in a 1 : 1 mole ratio in solution. Furthermore, the total volume of solution was typically set to ~20–50 mL with the use of 10–50 mg of bulk organosilica material as heavy metal adsorbent. In some cases, films (intact on their corresponding substrates) were directly immersed into heavy metal solution. The starting concentration of the heavy metal solution depended on the EA data for a given organosilica sample (from which a value for the loading of the ligand in such a material was obtained), and could thus vary anywhere from 1–100 ppm. Importantly, all metal-containing solutions and related serial dilutions were prepared gravimetrically. In addition, Hg(II) solutions were acidified with high-purity Optima®-grade concentrated nitric acid (1 $\mu L \cdot mL^{-1}$ of solution), while Pb(II) solutions were left neutral.

2.7.12 LPG Calibration and Metal Sensing

The LPG-containing section of the fibre was suspended across a Teflon® well and was anchored at both ends by magnetic fibre clamps to maintain constant tension across the LPG during all of the spectral measurements. The PTFE well was then filled with a given test solution. Importantly, the well was designed to ensure that the entire LPG and organosilica coating remained completely immersed in the test solutions. The both bare LPGs and PMO-coated LPGs were exposed to each water / DMSO calibration solution for 3 minutes and each metal(II) solution for 20 minutes prior to noting the resonant peak position, recording the corresponding attenuation spectrum, and moving on to the next test solution. In general, the LPG was exposed to either calibration or metal-containing solutions of progressively increasing concentration without any sort of LPG 'washing' step in between exposures. All attenuation spectra were recorded on an Agilent 86142B optical spectrum analyzer (OSA). An Ocean Optics LS-1 broadband (360–2000 nm) tungsten halogen lamp was used as the light source. All water / DMSO solutions were prepared volumetrically, and all metal-containing solutions and related serial dilutions were prepared gravimetrically. To re-use a given coating on a particular LPG, the film was soaked in aqueous acid (typically 1 M $HCl_{(aq)}$, but occasionally 6 M $HCl_{(aq)}$ solutions were used) for 5–20 minutes, followed by rinsing with copious amounts of DI H_2O and drying under ambient conditions.

Due to the inherent variability between batches of received LPG-inscribed fibre-optic waveguides and slight differences in the physical and chemical properties in the PMO coatings, each LPG and PMO–LPG pairing must be calibrated individually by

exposure to water / DMSO solutions of varying RI to generate a plot exemplified by Figure 2-23. Once the calibration is complete and the steepest section of the response curve identified for the PMO–LPG system, the RI of the metal sensing medium can then be determined.

An analogous procedure was followed for the calibration and testing of both bare and coated MZ-type tapered fibre interferometers.

2.7.13 SOI Microchip Calibration and Metal Sensing

Microchip Alignment and Solution Exposure. Using an apparatus built in-house (by Dr. Jack Barnes, Queen's University), the microchip was fixed in place within a laminar flow hood. Light was coupled into the microchip by aligning a tapered, single-mode fibre (Oz Optics; core diameter = 9 μm, and cladding diameter = 125 μm) (connected to an ANDO AQ432OD tunable diode laser source with a 1520–1620 nm wavelength range and an operating power of 1 mW, and a Stanford Research Systems SR844RF lock-in amplifier) against the appropriate photonic wire / facet exposed at one edge of the microchip. Light was collected at the other edge of the microchip (with a THOR Labs D400FC InGaAS photodiode detector) by aligning a Corning® multimode fibre against the appropriate exposed wire / facet. The positions of the tapered fibre and the collection fibre were adjusted using fibre-optic alignment stages that were moveable in all three dimensions to maximize the intensity of transmitted light at a set wavelength (usually ~ 1550 nm). Furthermore, the polarization of the incoming light was adjusted and fixed using a set of

three polarization control paddles to also maximize the intensity of transmitted light at a set wavelength.

Once the tapered fibre and multimode fibre were aligned against the microchip, a testing chamber was carefully lowered onto the microchip and pressure-sealed against the microchip. The testing chamber included both capillary inlet and outlet ports. The testing chamber (i.e. an inverted well) allowed for the introduction of a test solution, its accumulation within the exposed windows of the spiral MZIs (thus ensuring contact between the test solution and the sensing arm of the MZIs), and a means of exit for the test solution from the chamber / well. Once more, the alignment of the tapered fibre and multimode fibre with respect to the microchip was verified and re-optimized in case the microchip had moved from its previously optimized position as a result of mounting the test chamber on top of the microchip.

DI H_2O was introduced into the test chamber (usually at a flow rate of ~ 10–20 $\mu L \cdot min^{-1}$) via a fused silica capillary that was connected to a Harvard Apparatus 11plus syringe pump. Using a data logging program (TracerDAQ or LabView), the intensity of the transmitted light was allowed to stabilize before changing the test solution. To calibrate the device, calibration solutions (e.g. aqueous sucrose solutions of known RI) were introduced one after another into the chamber (being careful not to introduce any air bubbles into the chamber upon changing the solution). For each calibration solution, the oscillations (i.e. the interference pattern) in the transmitted signal were monitored. Once the transmitted signal intensity stabilized, a new solution was pumped across the microchip. This data was then collected and used to generate a calibration curve to

determine the RI-sensitivity of the device. Once the sensing arm of the MZI was coated with a functional coating of interest, the microchip was exposed to the designated test solutions using a procedure analogous to that described above.

Coating of the SOI Microchips. The microchips were thinly coated with the sols described in Sections 2.6.8 and 2.6.9 by spin-coating. The surface of the chip was first briefly cleaned and activated using Piranha solution (as described in Section 2.6.2). Once dry, the microchip was fixed to the rotor of the spin-coater and then flooded with the desired coating sol, which was left to stand on the microchip for 1 minute prior to spinning the sample. The film was then treated as described previously prior to testing.

2.7.14 Characterization Techniques

Scraped film samples or bulk powder samples were degassed under reduced pressure at 80 °C prior to nitrogen physisorption analysis on a Micromeritics ASAP 2010 analyzer at 77 K. The thickness of films prepared on flat substrates (e.g. microscope slides, high-index SF-10 wafers, and Si wafers) was measured on a Dektak 8 Stylus Surface Profiler (with a diamond stylus of radius = 12.5 μm). Refractive index determination was conducted on an instrument built in-house by Mr. Nicholas Trefiak (formerly of Queen's University), as well as on a J. A. Woollam Co., Inc. WVASE32® ellipsometer at incident angles of 65°, 70°, and 75° over a wavelength range of 370–1700 nm. Optical micrograph images were obtained on a Nikon Eclipse ME600L microscope. Field-emission scanning electron images were obtained on a LEO / Zeiss 1530 FE-SEM.

Additionally, a 200 keV JEOL 2010 STEM was operated in both transmission and STEM modes. In STEM mode, a Gatan High Angle Annular Dark Field (HAADF) detector was used to image the sample. Elemental maps and spectra were generated using an EDAX (Genesis) Energy Dispersive X-ray system. The sample was prepared by placing a small amount of the scraped film in ethanol and sonicating for 5 minutes, then 20 μL of the solution was dispersed onto a carbon-coated, 200-mesh copper grid.

2.8 References

1. Fifield, F. W.; Haines, P. J. *Environmental Analytical Chemistry*, 1st ed.; Blackie Academic and Professional: London, 1995.
2. Canadian Environmental Protection Act, 1999; Government of Canada: 1999.
3. Pollution Probe Publications Page, 'Mercury Primer' (June 2003): http://www.pollutionprobe.org/Publications/Mercury.htm (accessed June 15, 2007)
4. Skoog, D. A.; West, D. M.; Holler, F. J. *Fundamentals of Analytical Chemistry*, 7th ed.; Saunders College Publishing: Orlando, 1996.
5. Nolan, E. M.; Lippard, S. J. *Chem. Rev.* **2008**, *108*, 3443–3480.
6. Health Canada. *Effects of Lead on Human Health*; Catalogue # H50-3/127-2003E-PDF; Government of Canada (Ministry of Health), 2008.
7. Zhang, L; Fang, M. *Nano Today* **2010**, *5*, 128–142.

8. Bhalla, V.; Tejpal, R.; Kumar, M.; Sethi, A. *Inorg. Chem.* **2009**, *48*, 11677–11684.

9. Métivier, R.; Leray, I.; Valeur, B. *Chem. Eur. J.* **2004**, *10*, 4480–4490.

10. Descalzo, A. B.; Martínez-Máñez, R.; Radeglia, R.; Rurack, K.; Soto, J. *J. Am. Chem. Soc.* **2003**, *125*, 3418–3419.

11. For reviews, see: (a) Wallace, K. J. *Supramol. Chem.* **2009**, *21*, 89–102; (b) Quang, D. T.; Kim, J. S. *Chem. Rev.* **2010**, *110*, 6280–6301; (c) Aragay,G.; Pons, J.; Merkoçi, A. *Chem. Rev.* **2011**, DOI: 10.1021/cr100383r.

12. Scully, P. *Optical Techniques for Water Monitoring*, Proceedings of the European Workshop on Standards, Measurements and Testing for the Monitoring of Water Quality: The Contribution of Advanced Technologies, Nancy, France, May 29–31, 1997; Elsevier: Oxford, 1998; pp. 15–35.

13. Clark, P.; Boriniski, J.; Gunther, M.; Poland, S. *Smart Mater. Bull.* **2001**, (6), 8–11.

14. Culshaw, B. *J. Phys. E: Sci. Instrum.* **1983**, *16*, 798–806.

15. James, S. W.; Tatam, R. P. *Meas. Sci. Technol.* **2003**, *14*, R49–R61.

16. Barnes, J.; Dreher, M.; Plett, K.; Brown, R. S.; Crudden, C. M.; Loock, H.-P. *Analyst* **2008**, *133*, 1541–1549.

17. Based on our experience and observations across different batches of received LPGs, the depth to which the grating is inscribed into the waveguides also appears to affect both the resonant peak position as well as the peak intensity. However,

this dependence on the depth of LPG inscription is neither well understood nor well documented in the literature.

18. Gauglitz, G. *Anal. Bioanal. Chem.* **2005**, *381*, 141–155.

19. Hochreiner, H. *Modelling of Long-Period Fibre Gratings in Chemical Sensing Applications*, Ph. D. Thesis, Dalhousie University, Halifax, Canada, January 2008.

20. Hochreiner, H.; Cada, M.; Wentzell, P. D. *J. Lightwave Technol.* **2008**, *26*, 1968–1992.

21. Jagiellonian University Institute of Physics, Atomic Optics Department, Evanescent Wave Spectroscopy Group, Evanescent Wave Properties Page: http://users.uj.edu.pl/~tkawalec/?dir=21&lang=en (accessed May 14, 2007).

22. (a) Oehme, I.; Wolfbeis, O. S. *Mikrochim. Acta.* **1997**, *126*, 177–192; (b) Freeman, J. E.; Childers, A. G.; Steele, A. W.; Hieftje, G. M. *Anal. Chim. Acta* **1985**, *177*, 121–128; (c) Ueberfeld, J.; Parthasarathy, N.; Zbinden, H.; Gisin, N.; Buffle, J. *Anal. Chem.* **2002**, *74*, 664–670; (d) Vaughan, A. A.; Narayanaswamy, R. *Sens. Actuators, B* **1998**, *51*, 368–376; (d) Zhujun, Z.; Seitz, W. R. *Anal. Chim. Acta* **1985**, *171*, 251–258.

23. (a) Zhang, J.; Tang, X.; Dong, J.; Wei, T.; Xiao, H. *Sens. Actuators B* **2009**, *135*, 420–425; (b) Zhang, J.; Tang, X.; Dong, J.; Wei, T.; Xiao, H. *Opt. Express* 2008,

16, 8317–8323; (c) Wei, T.; Montoya, J.; Xiao, H.; Zhang, J.; Dong, H. *Proc. SPIE Int. Soc. Opt. Eng.* **2007**, *6556*, 655617-1–655617-8.

24. Kumar, P. S.; Vallabhan, C. P. G.; Nampoori, V. P. N.; Radhakrishnan, P. *Proc. SPIE Int. Soc. Opt. Eng.* **2003**, *5116*, 348–352.

25. Falciai, R.; Mignani, A. G.; Vannini, A. *Sens. Actuators B* **2001**, *74*, 74–77.

26. Ogawa, M. *J. Am. Chem. Soc.* **1994**, *116*, 7941–7942.

27. Although the discussion centers on the synthesis of silica-based films, the principles may also be extended to the synthesis of other metal oxide films (e.g. titania films).

28. Edler, K. J.; Roser, S. J. *Int. Rev. Phys. Chem.* **2001**, *20*, 387–466.

29. Soler-Illia, G. J. A. A.; Sanchez, C.; Lebeau, B.; Patarin, J. *Chem. Rev.* **2002**, *102*, 4093–4138.

30. Sanchez, C.; Boissière, C.; Grosso, D.; Laberty, C.; Nicole, L. *Chem. Mater.* **2008**, *20*, 682–737.

31. Lu, Y.; Ganguli, R.; Drewien, C. A.; Anderson, M. T.; Brinker, C. J.; Gong, W.; Guo, Y.; Soyez, H.; Dunn, B.; Huang, M. H.; Zink, J. I. *Nature* **1997**, *389*, 364–368.

32. Brinker, C. J.; Lu, Y.; Sellinger, A.; Fan, H. *Adv. Mater.* **1999**, *11*, 579–585.

33. Grosso, D.; Cagnol, F.; Soler-Illia, G. J. A. A.; Crepaldi, E. L.; Amenitsch, H.; Brunet-Bruneau, A.; Bourgeois, A.; Sanchez, C. *Adv. Funct. Mater.* **2004**, *14*, 309–322.

34. Cagnol, F.; Grosso, D.; Soler-Illia, G. J. A. A.; Crepaldi, E. L.; Babonneau, F.; Amenitsch, H.; Sanchez, C. *J. Mater. Chem.* **2003**, *13*, 61–66.

35. Athens, G. L.; Ein-Eli, Y.; Chmelka, B. F. *Adv. Mater.* **2007**, *19*, 2580–2587.

36. Miyata, H.; Suzuki, T.; Fukuoka, A.; Sawada, T.; Watanabe, M.; Noma, T.; Takada, K.; Mukaide, T.; Kuroda, K. *Nature Mater.* **2004**, *3*, 651–656.

37. Barnes, J. A.; Brown, R. S.; Cipot-Wechsler, J.; Crudden, C. M.; Du, J.; Loock, H.-P.; Plett, K. *Proc. SPIE Int. Soc. Opt. Eng.* **2008**, *7099*, 70992C-1–70992C-8.

38. Du, J.; Cipot-Wechsler, J.; Lobez, J. M.; Loock, H.-P.; Crudden, C. M. *Small* **2010**, *6*, 1168–1172.

39. Crudden, C. M.; Loock, H.-P.; Dickson, S. E.; Du, J.; Benhabib, L. M. S.; Brown, R. S. *Optical Sensor Using Functionalized Composite Materials*. US7776611(B2), August 17, 2010.

40. Iler, R. K. *Chemistry of Silica – Solubility, Polymerization, Colloid and Surface Properties and Biochemistry*; John Wiley & Sons: New York, 1979.

41. (a) Feng, X.; Fryxell, G. E.; Wang, L.-Q.; Kim, A. Y.; Liu, J.; Kemner, K. M. *Science* **1997**, *276*, 923–926; (b) Liu, J.; Feng, X.; Fryxell, G. E.; Wang, L.-Q.; Kim, A. Y.; Gong, M. *Adv. Mater.* **1998**, *10*, 161–165.

42. (a) Walcarius, A.; Etienne, M.; Bessière, J. *Chem. Mater.* **2002**, *14*, 2757–2766; (b) Walcarius, A.; Etienne, M.; Lebeau, B. *Chem. Mater.* **2003**, *15*, 2161–2173; (c) Walcarius, A.; Delacôte, C. *Chem. Mater.* **2003**, *15*, 4181–4192.

43. (a) Mercier, L.; Pinnavaia, T. J. *Adv. Mater.* **1997**, *6*, 500–503; (b) Mercier, L.; Pinnavaia, T. J. *Environ. Sci. Technol.* **1998**, *32*, 2749–2754; (c) Brown, J.; Mercier, L.; Pinnavaia, T. J. *Chem. Commun.* **1999**, 69–70.

44. Refractive indices for all precursors obtained from the Sigma-Aldrich website (http://www.sigmaaldrich.com/canada-english.html (accessed March 12, 2011)), with the exception of **BTESO** and **APTES**, which were obtained from the Gelest website (http://www.gelest.com/index.asp (also accessed March 12, 2011)).

45. Nitta, S.V.; Pisupatti, V.; Jain, A.; Wayner, P. C., Jr.; Gill, W. N.; Plawsky, J. L. *J. Vac. Sci. Technol. B* **1999**, *17*, 205–212.

46. The position of the interface relates to the critical angle at the prism–sample interface (i.e. the incident angle above which total internal reflection of the incoming light occurs), which is influenced by the sample RI. For more details, see: (a) Zhang, J. *Development of LPG Sensor for Monitoring Contaminants in Ground Water*, M. Sc. Thesis, Queen's University, Kingston, Canada, January

2008; and (b) Plett, K. L. *Development and Characterization of Polysiloxane Polymer Films for Use in Optical Sensor Technology*, Ph. D. Thesis, Queen's University, Kingston, Canada, September 2008.

47. Brinker, C. J.; Scherer, G. W. *Sol-Gel Science: The Physics and Chemistry of Sol-Gel Processing*, Academic Press: New York, 1990.

48. (a) Film processing in a solvent-saturated atmosphere and aging in an ammonia-and-solvent-saturated atmosphere were adapted from reference 45; (b) Solvent exchange of wet films in non-polar solvent was adapted from reference 45; (c) Aging in alkaline solution was adapted from reference 47; (d) Freeze-drying of films was adapted from Hyun, S. H.; Kim, T. Y.; Kim, G. S.; Park, H. H. *J. Mater. Sci. Lett.* **2000**, *19*, 1863–1866.

49. (a) Zhao, L.; Shea, K. J. University of California, Irvine, Irvine, CA, USA. Personal communication, June 21, 2005; (b) Shea, K. J.; Loy, D. A.; Webster, O. *J. Am. Chem. Soc.* **1992**, *114*, 6700–6710; (c) Loy, D. A.; Shea, K. J. *Chem. Rev.* **1995**, *95*, 1431–1442; (d) Shea, K. J.; Loy, D. A. *Acc. Chem. Res.* **2001**, *34*, 707–716.

50. (a) Kresge, C. T.; Leonowicz, M. E.; Roth, W. J.; Vartuli, J. C.; Beck, J. S. *Nature* **1992**, *359*, 710–712; (b) Beck, J. S.; Vartuli, J. C.; Roth, W. J.; Leonowicz, M. E.; Kresge, C. T.; et al. *J. Am. Chem. Soc.* **1992**, *114*, 10834–10843.

51. (a) Zhao, D.; Feng, J.; Huo, Q.; Melosh, N.; Fredrickson, G. H.; Chmelka, B. F.; Stucky, G. D. *Science* **1998**, *279*, 548–522; (b) Zhao, D.; Huo, Q.; Feng, J.; Chmelka, B. F.; Stucky, G. D. *J. Am. Chem. Soc.* **1998**, *120*, 6024–6036.

52. Yang, H.; Kuperman, A.; Coombs, N.; Mamiche-Afara, S.; Ozin, G. A. *Nature* **1996**, *379*, 703–705.

53. Zhao, D.; Yang, P.; Melosh, N.; Feng, J.; Chmelka, B. F.; Stucky, G. D. *Adv. Mater.* **1998**, *10*, 1380–1385.

54. For more regarding double-gyroid (i.e. bicontinuous cubic) mesostructured silica films, see: (a) Bollmann, L.; Urade, V. N.; Hillhouse, H. W. *Langmuir* **2007**, *23*, 4257–4267; (b) Urade, V. N.; Bollmann, L.; Kowalski, J. D.; Tate, M. P.; Hillhouse, H. W. *Langmuir* **2007**, *23*, 4268–4278; (c) Wei, T.-C.; Hillhouse, H. W. *Langmuir* **2007**, *23*, 5689–5699; (d) Urade, V. N.; Wei, T.-C.; Tate, M. P.; Kowalski, J. D.; Hillhouse, H. W. *Chem. Mater.* **2007**, *19*, 768–777.

55. For a review, see: Innocenzi, P.; Malfatti, L.; Kidchob, T.; Falcaro, P. *Chem. Mater.* **2009**, *21*, 2555–2564, and references therein.

56. Wanka, G.; Hoffmann, H.; Ulbricht, W. *Macromolecules* **1994**, *27*, 4145–4159.

57. Fan, J.; Stucky, G. D. University of California, Santa Barbara, Santa Barbara, CA, USA. Personal communication, July 01, 2005.

58. Liu, N.; Assink, A.; Smarsly, B.; Brinker, C. J. *Chem. Commun.* **2003**, 1146–1147.

59. Mesoporous organosilica materials (bulk and films) were also prepared using Brij® 76 ($C_{18}H_{37}(EO)_{10}$) as a templating agent and yielded materials with similar physical and chemical properties to those prepared by us using **B56** as a templating agent.

60. Although a value was not reported in reference 58 for the loading of amino groups in this condensed material, a value for the amino group surface coverage was calculated by Brinker and co-workers to be ~ 2 $–NH_2$ groups · nm^{-2}. Using the values obtained by us from nitrogen porosimetry and EA, the functional group surface coverage for our materials was calculated to be ~ 3 $–NH_2$ groups · nm^2, which is within reasonable agreement with the value reported in reference 58.

61. Wan, Y.; Zhao, D. *Chem. Rev.* **2007**, *107*, 2821–2860.

62. Ting, C.-Y.; Sheu, S.-H.; Wu, W.-F.; Wan, B.-Z. *J. Electrochem. Soc.* **2007**, *154*, G1–G5.

63. Grosso, D.; Balkenende, A. R.; Albouy, P. A.; Ayral, A.; Amenitsch, H.; Babonneau, F. *Chem. Mater.* **2001**, *13*, 1848–1856.

64. Lin, H.-P.; Mou, C.-Y.; Liu, S.-B.; Tang, C.-Y.; Lin, C.-Y. *Microporous Mesoporous Mater.* **2001**, *44–45*, 129–137.

65. Bardeau, J.-F.; Gourbil, A.; Dutreilh-Colas, M.; Dourdain, S.; Mehdi, A.; Gibaud, A. *Thin Solid Films* **2006**, *495*, 191–196.

66. In fact, it has been shown in the literature that the poly(alkylene oxide) blocks of Brij®- and Pluronic®-type surfactants may chelate certain metal species. For more details, see: Soler-Illia, G. J. de A. A.; Sanchez, C. *New J. Chem.* **2000**, *7*, 493–499.

67. Del Villar, I.; Matías, I. R.; Arregui, F. J.; Lalanne, P. *Opt. Express* **2005**, *13*, 56–69.

68. Wang, Z.; Heflin, J. R.; Stolen, R. H.; Ramachandran, S. *Opt. Express* **2005**, *13*, 2808–2813.

69. Guo, Y.; Guadalupe, A. R. *J. Pharm. Biomed. Anal.* **1999**, *19*, 175–181.

70. Zhang, L.; Zhang, W.; Shi, J.; Hua, Z.; Li, Y.; Yan, J. *Chem. Commun.* **2003**, 210–211.

71. n_D^{20} obtained from: *The Merck Index*, 14th ed. [electronic edition]; Merck: Whitehouse Station, NJ, 2006 (accessed December 13, 2010). The values for the RI of water and DMSO at 1550 nm were provided by the Loock Group (Queen's University).

72. (a) Zhou, K.; Liu, H.; Hu, X. *Opt. Commun.* **2001**, *197*, 295–299; (b) Vasiliev, S. A.; Dianov, E. M.; Varelas, D.; Limberger, H. G.; Salathé, R. P. *Opt. Lett.* **1996**, *21*, 1830–1832.

73. With the OSA instrument error being ± 0.2 nm, the measured peak shift was deemed to be significant and a reliable value.

74. Loock, H.-P. Queen's University, Kingston, ON, Canada. Personal communication, June 06, 2007.

75. Note that **BTESPTS** is a bis-silylated condensable precursor. Consequently, the loading of the **BTESPTS** monomer into these organosilica materials was determined on the basis of Si content to keep the total number of condensable moieties consistent across sols composed of different organosilanes.

76. Nicole, L.; Boissière, C.; Grosso, D.; Quach, A.; Sanchez, C. *J. Mater. Chem.* **2005**, *15*, 3598–3627.

77. Huang, L. C.; Richman, E. K.; Kirsch, B. L.; Tolbert, S. H. *Microporous Mesoporous Mater.* **2006**, *96*, 341–349.

78. The table of saturated salt solutions and their corresponding equilibrium RHs was obtained from the Omega Engineering, Inc. website: http://www.omega.com/temperature/z/pdf/z103.pdf (accessed June 28, 2010).

79. Vercaemst, C.; Ide, M.; Allaert, B.; Ledoux, N,; Verpoort F.; Van Der Voort, P. *Chem. Commun.* **2007**, 2261–2263.

80. Alvarez-Herrero, A.; Ramos, G.; del Monte, F.; Bernabeu, E.; Levy, D. *Thin Solid Films* **2004**, *455 –456*, 356–360.

81. **F127**-templated film synthesis adapted from: Zhao, D.; Yang, P.; Melosh, N.; Feng, J.; Chmelka, B. F.; Stucky, G. D. *Adv. Mater.* **1998**, *10*, 1380–1385.

82. Maruo, T.; Tanaka, S.; Hillhouse, H. W.; Nishiyama, N.; Egashira, Y.; Ueyama, K. *Thin Solid Films* **2008**, *516*, 4771–4776.

83. (a) Tanev, P. T.; Pinnavaia, T. J. *Science*, **1995**, *267*, 865–867; (b) Bagshaw, S. A.; Prouzet, E.; Pinnavaia, T. J. *Science* **1995**, *269*, 1242–1244; (c) Prouzet, E.; Pinnavaia, T. J. *Angew. Chem., Int. Ed.* **1997**, *36*, 516–518; (d) Kim, S.-S.; Pauly, T. R.; Pinnavaia, T. J. *Chem. Commun.* **2000**, 835–836.

84. Films prepared on flat substrates displayed the same textural properties by TEM as films prepared on fibre-optic waveguides (i.e. curved substrates).

85. In the ideal scenario where the templating agent is completely removed, the material is fully condensed, and S and Ti are 100% incorporated, the theoretical S and Ti loadings are 2.6 and 0.13 $mmol \cdot g^{-1}$, respectively. Therefore, we have a minimum of ~ 58% incorporation of these functionalities in our materials.

86. This particular set of experiments with the 9 mol% **BTESPTS** (Si basis) / 5 mol% **TTIP** / 86 mol% **TEOS** films on LPGs was conducted by Dr. Judy Cipot-Wechsler (formerly at Queen's University).

87. Interestingly, this film–LPG system only blue-shifted by a total of ~ 3 nm when exposed to acidified aqueous solutions of up to 100 ppm Hg(II).

88. Although it is unclear why this result could not be replicated, we hypothesize that the issue is closely tied to factors that would affect the RI of the coating. In all

subsequent attempts to reproduce this film–LPG system and its corresponding optical response to Pb(II) solutions, the RI of the film always appeared to be slightly lower than what would be ideal for metal detection in purely aqueous solution (as determined by the water / DMSO calibration of the film–LPG system conducted prior to the metal sensing trials). It, therefore, may be possible that this material coincidentally had an excessive amount of residual surfactant trapped within the film matrix in comparison to all other films prepared. Based on our previous studies (see Table 2-2), the presence of the surfactant within the films would not affect metal uptake by the films, but could significantly alter the film RI so as to allow for such high RI sensitivity in aqueous solution.

89. This extrapolation was carried out by Dr. Hans-Peter Loock (Queen's University).

90. USA: *National Primary Drinking Water Regulations*; Title 40 CFR: Protection of the Environment, Chapter 1 Part 141, EPA; Canada: *Guidelines for Canadian Drinking Water Quality*, 6th ed., Health Canada, 1996; Germany: *Verordnung über die Qualität von Wasser für den menschlichen Gebrauch*, Anlage 2 zu § 6 Abs. 2, 2001.

91. Due to the inherent variability between batches of received LPG-inscribed fibre-optic waveguides and slight differences in the physical and chemical properties in the PMO coatings, each PMO–LPG pairing must be calibrated individually by exposure to water / DMSO solutions of varying RI to generate a plot exemplified

by Figure 2-23. Once the calibration is complete and the steepest section of the response curve identified, the RI of the metal sensing medium can then be determined. For these reasons, the RI of the solutions used for Figure 2-24, Figure 2-26, Figure 2-27, and Figure 2-28 differ slightly from each other. However, these curves are very representative of the metal sensing behavior consistently observed for this PMO–LPG fibre-optic detection scheme.

92. After soaking in a 1 M $HCl_{(aq)}$ solution for ~ 20 minutes, the coating on the LPG could be 'regenerated' and used for a second round of Pb(II) sensing. Although the data in Figure 2-25 (black triangles, Trial #2) shows an increase in the total accumulative resonant peak shift, the sensitivity at low Pb(II) concentrations was decreased in comparison to the initial run (open circles, Trial #1).

93. At this point, this particular film–LPG combination had been used for multiple, consecutive metal sensing trials and had been thus repeatedly exposed to solution-based acid treatment. Consequently, further metal sensing investigations with this specific system were limited by the degradation in the integrity of the PMO film.

94. Soler-Illia, G. J. A. A.; Angelomé, P. C.; Bozzano, P. *Chem. Commun.* **2004**, 2854–2855.

95. Recall that a large blue-shift in the resonant peak position for moving a coated LPG from an 'air' environment to 'water' environment was previously noted (Section 2.3.4) as a prerequisite for the realization of metal sensing in purely aqueous media.

96. A new film was prepared using the same formulation on a new LPG by Mr. Marian Dreher (formerly of Queen's University) and the same optical response behaviour was observed. Recall that sensing in purely aqueous systems could not – in contrast – previously be reproduced using our organosilica-based films for the detection of Pb(II) in purely aqueous media (see Section 2.3.4).

97. Haseloh, S.; Choi, S. Y.; Mamak, M.; Coombs, N.; Petrov, S.; Chopra, N.; Ozin, G. A. *Chem. Commun.* **2004**, 1460–1461.

98. These films are not as transparent as any of the films previously prepared that were composed of amorphous matrices. These nanoparticulate titania-based films are, in fact, somewhat heterogeneous in appearance.

99. In our hands, porosity was also not observed for 100% TTBO films prepared according to the procedure published in reference 97.

100. (a) Densmore, A.; Xu, D.-X.; Waldron, P.; Janz, S.; Cheben, P.; Lapointe, J.; Delâge, A.; Lamontagne, B.; Schmid, J. H.; Post, E. *IEEE Photon. Technol. Lett.* **2006**, *18*, 2520–2522; (b) Densmore, A.; Xu, D.-X.; Janz, S.; Waldron, P.; Mischki, T.; Lopinski, G.; Delâge, A.; Lapointe, J.; Cheben, P.; Lamontagne, B.; Schmid, J. H. *Opt. Lett.* **2008**, *33*, 596–598; (c) Janz, S. "Food and Water Safety: Silicon Photonic Wire Waveguide Sensors Detect the Presence of Pathogens and Chemicals." *Photonics Spectra*, **2008** (*March*), Feature Article:

http://www.photonics.com/Article.aspx?AID=32594 (accessed September 16, 2009).

101. Almeida, V.R.; Panepucci, R. R.; Lipson, M. *Opt. Lett.* **2003**, *28*, 1302–1304.

102. The stages can adjust position to a precision on the order of micrometers, which is quite impressive. However, it is described, here, as a 'low precision' instrument because the degree of precision technically required for this particular set up is on the order of fractions of micrometers.

103. Tian Z.;, Yam, S. S.-H.; Barnes, J.; Bock, W.; Greig, P.; Fraser, J. M.; Loock, H.-P.; Oleschuk, R. D. *IEEE Photon. Technol. Lett.* **2008**, *20*, 626–628.

104. This work with the tapered fibre interferometers was conducted by Dr. Judy Cipot-Wechsler (formerly at Queen's University), and has been included, here, for the sake of providing a comprehensive and complete picture of the scope of this particular project. This work was carried out in parallel with some of the LPG-related experiments.

105. For both of these scenarios, a broadband laser (i.e. a 360–2000 nm tungsten halogen lamp) was used as the light source.

106. Bass, J. D.; Grosso, D.; Boissière, C.; Belamie, E.; Coradin, T.; Sanchez, C. *Chem. Mater.* **2007**, *19*, 4349–4356.

107. Hunks, W. J.; Ozin, G. A. *J. Mater. Chem.* **2005**, *15*, 3716–3724.

108. Urata, C.; Yamauchi, Y.; Mochizuki, D.; Kuroda, K. *Chem. Lett.* **2007**, *36*, 850–851.

109. Walcarius, A.; Etienne, M.; Delacôte, C. *Anal. Chim. Acta* **2004**, *508*, 87–98.

Chapter 3

Uniaxially-Aligned, Mesostructured Films from the Self-Assembly of Amphiphilic, Oligomeric Organosiloxane Precursors

3.1 Introduction

Since the discovery of periodically ordered, surfactant-templated mesostructured silica,[1,2,3] there has been significant interest in utilizing the unique physical and chemical properties of these and related materials in areas such as catalysis, optics, and sensing, to name a few.[4] As mentioned in Chapter 1, many of these applications[5,6,7] require convenient access to well-defined, mesostructured thin films,[8] as well as films possessing tailored organic functionality.[9,10,11] Such films can be easily produced by the evaporation-induced self-assembly (EISA) process[12,13,14,15] or, alternatively, by spontaneous growth and deposition under hydrothermal conditions onto appropriate substrates (see Chapter 2).[16] Although the mesostructural features in the film are oriented with respect to the substrate surface, the in-plane orientation (i.e. in the direction normal to the surface of the substrate) is generally not fully controlled (see Scheme 3-1).[17] Additionally, a high degree of loading of organofunctional silanes in the starting solution (i.e. > 25 mol%) generally causes a dramatic decrease in the structural order and uniformity.[18] To maximize the efficacy of these mesostructured materials in advanced applications, control of their in-plane structures over large length scales is essential.

A few different strategies have been explored in the literature to direct the growth and alignment of the 2D and 3D mesostructures of surfactant-templated metal oxide films.[17,19] These include epitaxial growth on single-crystalline[16,20,21] or polymer-coated

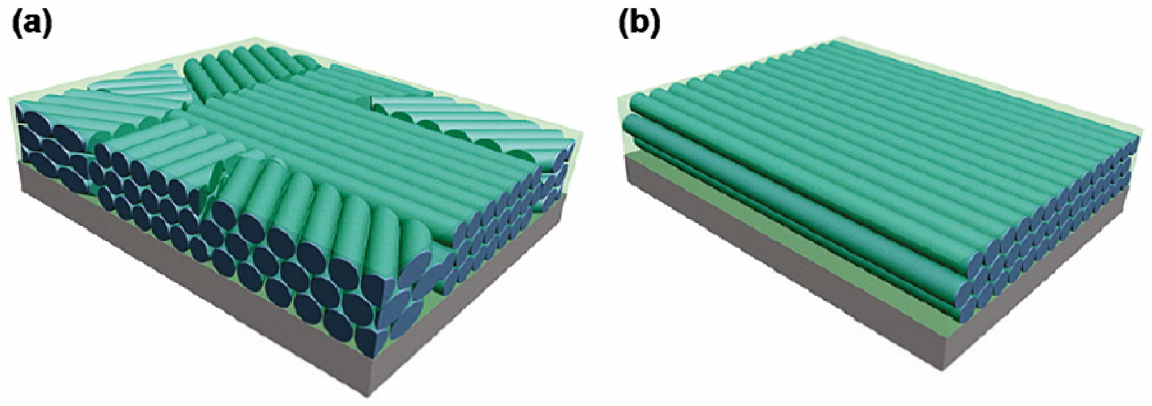

Scheme 3-1. Schematic representation of 2D hexagonally-ordered films bearing (a) poor in-plane alignment (i.e. 'polycrystalline-like') and (b) coherent in-plane alignment (i.e. 'single crystalline-like'). (Scheme taken from reference 17.)

substrates,[22,23] alignment under reactant flow[24] or shear stress,[25] alignment with magnetic fields,[26] and impregnation into a pre-aligned block copolymer or colloidal template.[27]

For example, Ozin and co-workers demonstrated[16] that a freshly cleaved, atomically-flat mica substrate could be used for the nucleation and growth of elongated and aligned, micrometer-sized silica 'islands' from a tetraethoxysilane-based, surfactant-containing sol under hydrothermal conditions. With extended reaction times (of up to one week), the elongated silica islands increased in number and density such that they eventually coalesced into a continuous silica film with macroscopically-sized domains that displayed co-aligned 2D hexagonal mesostructures.

By pre-coating a substrate with a photo-cross-linkable, polymeric liquid crystalline species, Seki and co-workers could prepare an anisotropically ordered film on top of which an aligned, surfactant-templated silica film with 2D hexagonal order could

be synthesized.[22b] The polymeric precursor consisted of biphenylene moieties that could first be aligned upon exposure to linearly polarized UV light and subsequent thermal annealing. Next, under further irradiation by UV light, the side chains of the polymer underwent photocatalyzed cross-linking to effectively 'lock in' the polymeric chain alignment. Surfactant-templated, silica films with co-aligned 2D hexagonal mesostructures were then subsequently prepared via hydrothermal growth initiated from the polymer–sol interface over 48 h.

In another example, Tsapatsis and co-workers prepared surfactant-templated, 2D hexagonally ordered silica films on the internal surfaces of glass capillaries (internal diameter = 1 mm) under conditions of continuous flow of the sol along the substrate over the course of 1 h to 1 day.[24a] At short reaction times (< 2 h), evidence for the preferential alignment of silica tubules along the direction of reagent flow was observed by FE-SEM.

Although these selected examples from the literature are only a brief survey of the work concerning the preparation of uniformly aligned hybrid and porous silica films (bearing, of course, alignment over extended length scales) reported to date, it is at least suffice to say that this issue continues to be of significant interest to the scientific community, and that a lot of room remains to contribute to this area.

Along the same lines as using pre-coated / pre-treated substrates to induce mesostructural alignment, Kuroda et al. have previously reported the preparation of continuous, surfactant-templated silica films with macroscopically oriented 2D and 3D

hexagonal mesostructures on substrates bearing anisotropic polymer coatings such as Langmuir–Blodgett films[28] and rubbing-treated polyimide-functionalized surfaces.[29]

Although obtaining mesostructured films using amphiphiles such as surfactants or block copolymers as structure-directing agents is relatively facile, the process involves a complex and sensitive interplay between numerous parameters including the composition of the precursors, as well as external conditions such as temperature and humidity during film formation.[30] In recent years, Kuroda and co-workers have reported a new approach for the preparation of films with highly ordered mesostructures through the use of organosiloxane nanohybrid molecular building blocks.[31,32] Oligomeric siloxane-based precursors (as exemplified by **C*n*** in Scheme 3-2), which are comprised of hydrophobic alkyl chains and condensable alkoxysilyl groups, were specially designed for this purpose. The hydrolysis of such precursors thus generates amphiphilic molecules having both self-assembling and cross-linking abilities. Interestingly, the materials obtained from precursors bearing short alkyl chains (n = 6–10) demonstrated uniform 2D hexagonal order, while those obtained from precursors bearing longer alkyl chains (n = 14–18) had lamellar structure.[31] This dual-function precursor architecture eliminates the need to employ separate templating agents and polymerizable matrix precursors, in contrast to the conventional surfactant-templated sol-gel methodologies (see Chapters 1 and 2). As the Kuroda group has demonstrated, the reproducible formation of a uniform structure at the molecular scale is achieved using this strategy.[31,32]

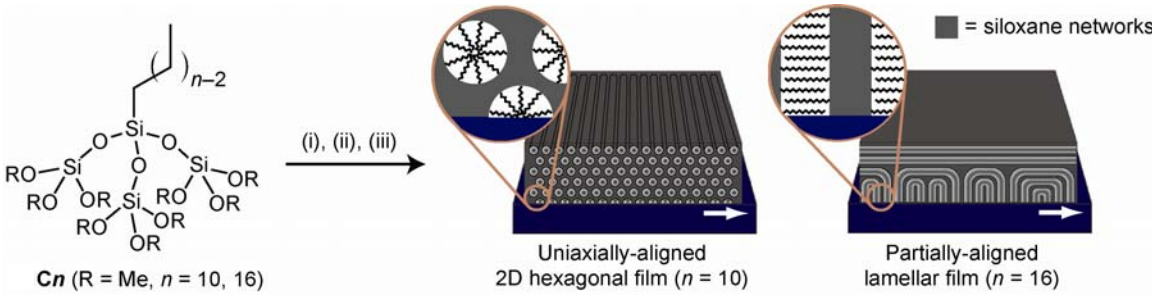

Scheme 3-2. Preparation of macroscopically oriented, mesostructured films by: (i) hydrolysis of the precursor, **C*n***; (ii) dip-coating of the hydrolyzed solution onto a rubbing-treated substrate; and (iii) self-assembly and polycondensation of the amphiphilic hydrolyzed species. The white arrow on the substrate indicates the rubbing direction.

In these hybrid materials devised by Kuroda et al., the molecular scale positions of the organic moiety with respect to the inorganic one, as well as the ratio of organic-to-inorganic components, are precisely controlled through the design of the starting molecules. This approach holds promise for the preparation of advanced and highly functional nanoscale hybrid materials by introducing appropriate functional groups into the starting molecules. For example, ester groups incorporated into the organic moiety have been shown to undergo post-synthetic cleavage under acidic conditions to generate a hybrid mesoporous material with well-defined –COOH group distribution and loading within the pores.[33]

To further exploit these advanced materials, control of the resultant hybrid mesostructure at macroscopic scales is of substantial importance.[34,35] This chapter will hereafter detail my work conducted during a three-month stay as a visiting student researcher in the research group of Prof. Kazuyuki Kuroda at Waseda University (Tokyo,

Japan) focusing on the preparation of continuous organosiloxane films displaying structural control over extended length scales using molecular precursors **C*n*** as building units. In brief, these films were formed on substrates bearing a rubbing-treated polyimide layer[29] (**PI**) (see Section 3.8.3) by a dip-coating method. The in-plane orientation of the 2D hexagonal and lamellar mesostructures of these films is controlled as a result of the initial interfacial interactions between the hydrolyzed **C*10*** and **C*16*** precursors, respectively, with the anisotropic polymeric film.[36] Furthermore, a reproducible and mild method for the elimination of the alkyl chains from the 2D hexagonally-ordered films using UV / ozone treatment was developed. This method was critical for the preparation of porous films with concomitant retention of the continuous uniaxial mesostructure, since the conventional method of calcination resulted in a complete loss of order and porosity.[31]

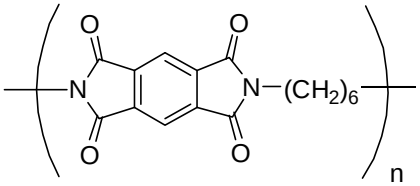

PI

3.2 Alignment Control of Self-Assembled Nanohybrid Films

As mentioned above, Kuroda et al. have previously established that bifunctional **C*10*** oligomers yield materials with 2D hexagonal order, while materials with alternating organic and siloxane layers in a lamellar arrangement are formed when the **C*16*** oligomers are employed.[31] The objective of my research was thus to see if materials with

uniaxially-aligned mesostructures could be prepared on rubbing-treated substrates in similar fashion to what has been previously observed with traditional surfactant-templated silica and organosilica systems.[29,37]

The synthesis of the ***C10*** and ***C16*** precursors is outlined in Section 3.8.22 and Scheme 3-3. Hybrid films were prepared from a sol of the oligomers by dip-coating onto rubbing-treated quartz or silicon substrates with the substrates oriented such that the rubbing direction was positioned perpendicular to the dip-coating direction.[38] Specifically, the coating sol was left to stir for 12 h prior to film formation as Kuroda and co-workers had previously determined that it was only after this length of elapsed time that acid-catalyzed pre-hydrolysis and pre-condensation of the oligomeric siloxane headgroup was complete.[31b] Furthermore, after dip-coating, the films were left to dry under ambient conditions for 2 days, as it was only after this length of elapsed time that the framework siloxane condensation was judged to be complete and the resultant mesostructures were deemed to be stable.[39] Once dry, characterization of the mesophase, degree of long range order, and orientation of the mesostructure in the resulting films was then facilitated by a combination of microscopy and X-ray diffraction (XRD) techniques.

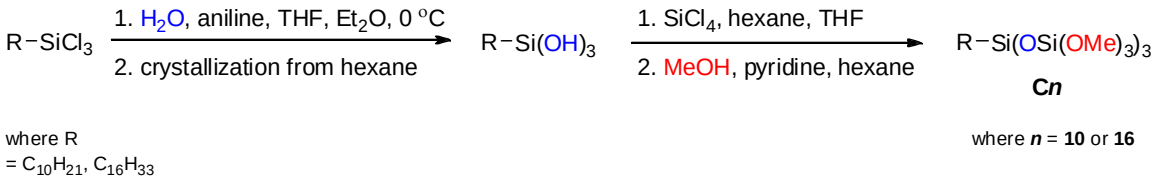

Scheme 3-3. Synthesis of **C*n*** precursors from the corresponding alkyltrichlorosilane.

The two main X-ray techniques utilized in this work were: (i) conventional, out-of-plane (Bragg–Brentano geometry, θ–2θ) XRD; and (ii) in-plane, grazing-incidence XRD (GIXRD). A schematic of the experimental set-ups is depicted in Scheme 3-4. In brief, 1_i and 1_d represent the incident and diffracted X-ray paths for the out-of-plane experiments, respectively, while 2_i and 2_d represent the incident and diffracted X-ray paths for the in-plane experiments, respectively. Additionally, ω and 2θ are the rotation axes for the sample and the detector, respectively, for the out-of-plane XRD measurements, while φ and $2\theta\chi$ are the rotation axes for the sample and detector, respectively, for the in-plane XRD measurements. Therefore, with such an arrangement, out-of-plane XRD probes the diffraction planes that predominantly lie parallel to the substrate plane (Scheme 3-5a). In contrast, the incident X-ray beam hits the sample at a very shallow angle with respect to the substrate surface (α) in the case of in-plane XRD, and allows for the detection of diffraction planes that predominantly lie perpendicular with respect to the substrate plane (Scheme 3-5b). With both of these techniques in hand, a comprehensive picture of the orientation and uniformity of mesoscopic ordering within unaxially-aligned **C*n***-derived films may be obtained – particularly when used in combination with imaging techniques such as optical and electron microscopy.

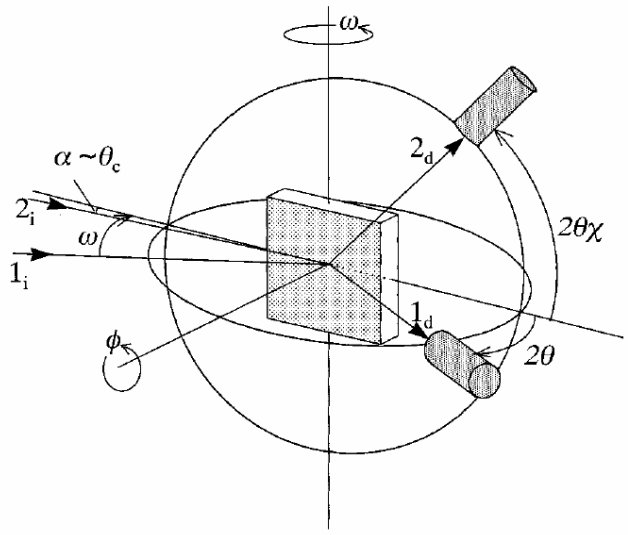

Scheme 3-4. Schematic representation of the various axes manipulated in out-of-plane and in-plane XRD experiments (taken from reference 29b).

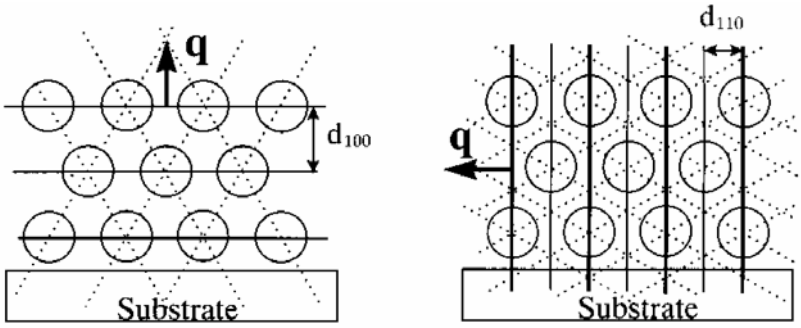

Scheme 3-5. Schematic representation of the 2D hexagonal mesostructure and the diffraction information obtained in the case of (a) out-of-plane XRD, and (b) in-plane XRD (where **q** = diffraction vector). (Scheme taken from reference 29a)

Figure 3-1 shows the conventional XRD pattern for the **C*10***-derived film measured in Bragg–Brentano (out-of-plane, *θ–2θ*) geometry with the rubbing direction of the substrate oriented parallel to the projection of the incident X-ray beam. The XRD pattern shows three peaks assigned to the (10), (20), and (30) lattice planes (d = 2.81 nm, 1.41 nm, and 0.93 nm, respectively), which closely correspond to the XRD pattern previously observed for the unaligned 2D hexagonally-ordered film prepared from **C*10***.[31] The out-of-plane XRD data did not conclusively demonstrate the presence of uniaxial alignment in these films. However, the film texture (observed in the optical micrographs in Figure 3-2a) – showing features aligned perpendicularly to the rubbing direction – is similar to that previously reported for uniaxially-aligned surfactant–silica composite films prepared on rubbing-treated polyimide-coated substrates (Figure 3-2b).[29,37] These results encouragingly suggested alignment of the **C*10***-derived 2D hexagonal structure in the direction perpendicular to the rubbing direction.

It should be noted that the intensity of the out-of-plane XRD peaks and the quality of the alignment texture obtained for these films are dependent on the dip-coating rate (Figure 3-3 and Figure 3-4). From Figure 3-3, it can be seen that the out-of-plane XRD peak intensities improve as the dip-coating rate is increased from 0.5 $mm \cdot s^{-1}$ to 2.0 $mm \cdot s^{-1}$. Correspondingly, the improvement in the alignment texture observed by optical microscopy follows the same trend (Figure 3-4). Thus, it appears that a fine balance between the rate of solvent evaporation and structure formation exists, which controls the quality of the final mesophase obtained.

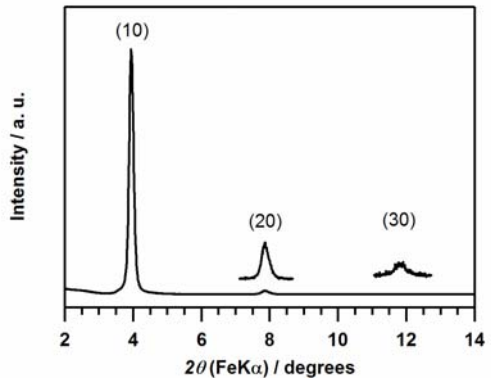

Figure 3-1. Out-of-plane XRD pattern for the **C*10***-derived film measured with the rubbing direction oriented parallel to the projection of the incident X-ray beam. The (20) peak has been magnified by a factor of 10 and the (30) peak has been magnified by a factor of 40.

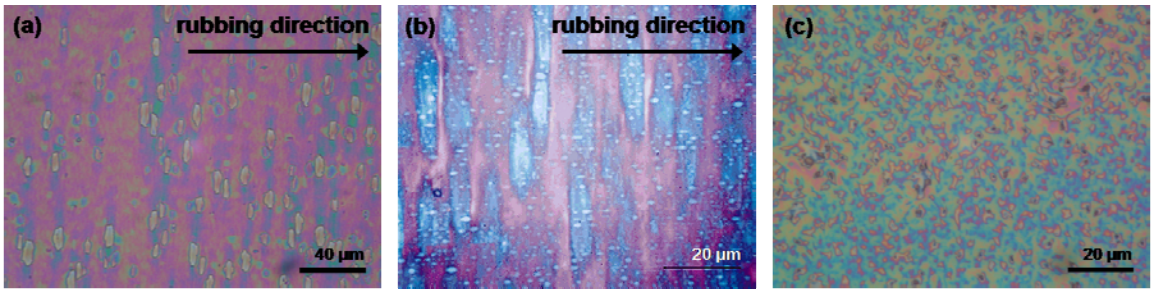

Figure 3-2. Optical micrographs of: (a) a **C*10***-derived film prepared on a rubbing-treated substrate; (b) a TEOS-derived film prepared on a rubbing-treated substrate (image taken from reference 29a); and (c) a **C*10***-derived film on a non-rubbing-treated substrate.

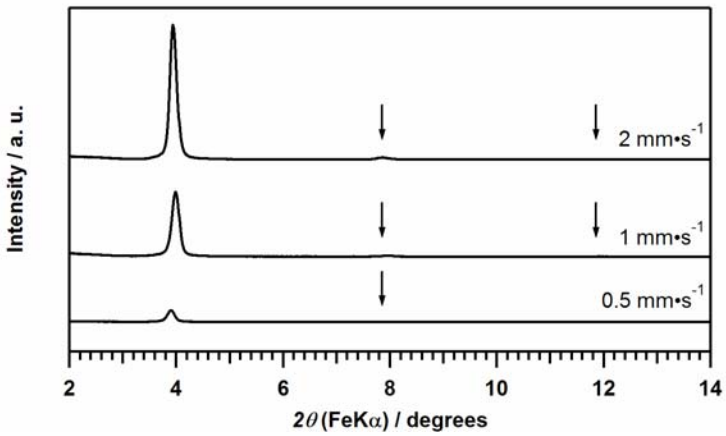

Figure 3-3. Out-of-plane XRD patterns for **C*10*** films dip-coated onto rubbing-treated substrates at rates of 0.5 mm·s^{-1}, 1.0 mm·s^{-1} and 2.0 mm·s^{-1}. The arrows indicate the positions of higher-order peaks.

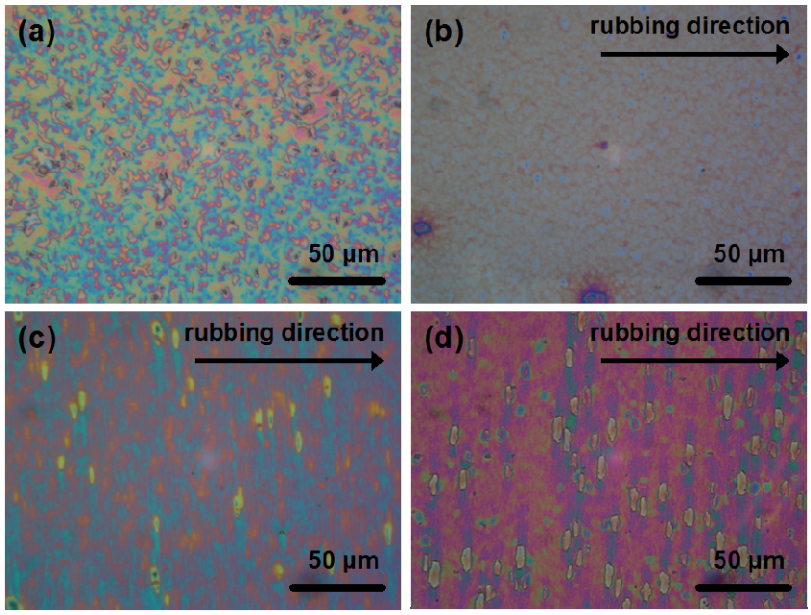

Figure 3-4. Optical micrographs of ***C10***-derived films coated onto (a) a non-rubbing-treated substrate at 2.0 mm·s^{-1}, and rubbing-treated substrates at rates of (b) 0.5 mm·s^{-1}, (c) 1.0 mm·s^{-1} and (d) 2.0 mm·s^{-1}.

The alignment of the cylindrical assemblies was further probed using grazing incidence in-plane XRD (GIXRD).[29,40] The in-plane radial (φ–$2\theta\chi$) scanning profile clearly shows the anisotropic nature of the film. No peak is observed in the profile when the rubbing direction is set parallel to the projection of the incident beam (Figure 3-5a, red trace), whereas two diffraction peaks assigned to the $(\bar{1}\,1)$ and $(2\,\bar{1})$ lattice planes are observed at $2\theta\chi$ = 2.50 ° and 4.76 °, respectively, when the rubbing direction is set perpendicular to the incident X-rays (Figure 3-5a, black trace). The observed anisotropy in the in-plane XRD patterns provides convincing evidence for the presence of strong anisotropy in the 2D hexagonal mesostructure over the whole volume of these **C*10***-derived films.[29]

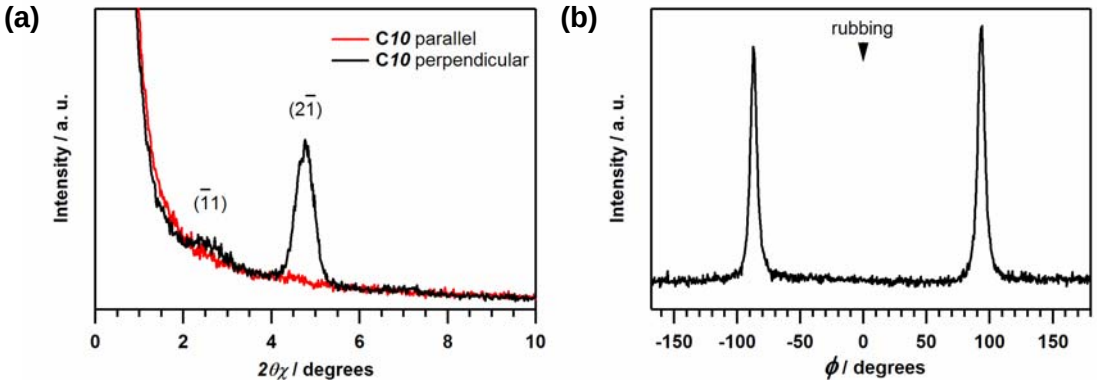

Figure 3-5. (a) In-plane φ–$2\theta\chi$ scanning profiles for the **C*10***-derived film with the rubbing direction oriented parallel (red trace) and perpendicular (black trace) to the projection of the incident X-ray beam at φ = 0 °; and (b) the corresponding φ-scanning profile at $2\theta\chi$ = 4.76 °.

The distribution of the in-plane alignment of the cylindrical assemblies can be quantitatively estimated by measuring the in-plane φ-scanning profile (in-plane rocking curve) with the detector fixed at the $(2\,\bar{1})$ peak position. The profile in Figure 3-5b shows two strong, sharp peaks separated by an interval of 180 °, which supports the formation of a 2D hexagonal mesostructure uniaxially aligned perpendicularly to the rubbing direction.

The uniaxial alignment of the cylindrical assemblies is also demonstrated by cross-sectional TEM. Figure 3-6a shows the cross-sectional view of the **C*10***-derived film when the film is cut parallel to the rubbing direction. The film is about 400 nm thick, and complete alignment of the structure is achieved over the entire thickness of the film from the substrate–film interface (lower right) to the film–air interface (upper left). The alignment of the long axis of the cylinders is also observed when the film is cut perpendicular to the rubbing direction (Figure 3-6b).

After successfully demonstrating the formation of uniaxially-aligned 2D hexagonal mesostructures using amphiphilic **C*10*** precursors on rubbing-treated substrates, we next explored the effect of the rubbing-treated substrate on the formation of hybrid materials prepared using longer chain precursors and their resultant structures. Again, as reported previously, oligosiloxane precursors with relatively long alkyl chains (n = 14–18) yield materials with lamellar structures bearing interdigitated alkyl chains.[31]

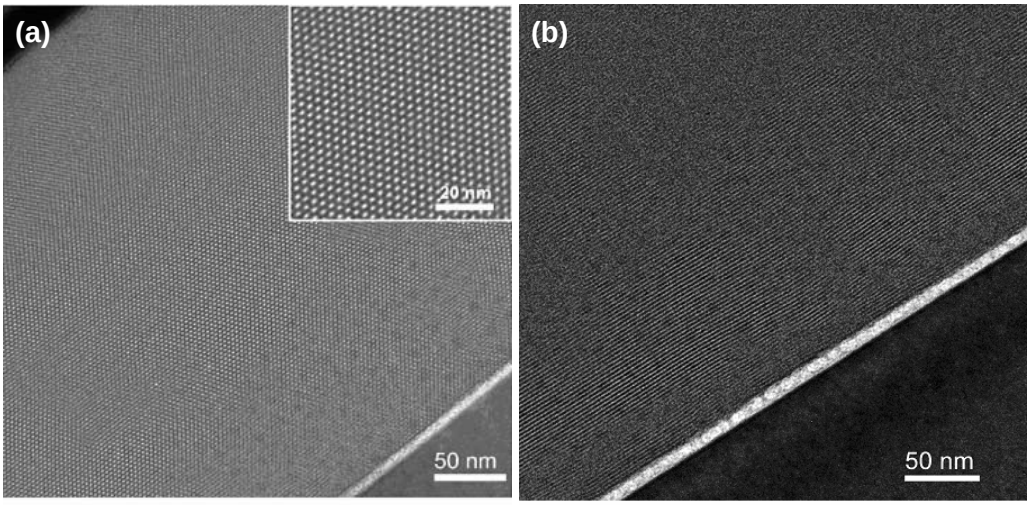

Figure 3-6. Cross-sectional TEM image of our **C*10***-derived film sliced (a) parallel (inset shows an enlarged image (× 2) of the central region of the film), and (b) perpendicular to the rubbing direction. The polyimide layer is about 10 nm thick.

This can be explained using simple geometric arguments. A longer alkyl chain (when paired with the same oligosiloxane head group as used for **C*10***) results in a decreased interfacial curvature of the micelles, favoring the formation of a lamellar structure (see Chapter 1, Scheme 1-5).[41] Here, films were prepared using the **C*16*** oligomer on the same rubbing-treated polyimide-coated substrates to compare the resultant structure to that obtained with the **C*10*** oligomer.

The XRD profile measured under the Bragg–Brentano geometry (Figure 3-7) is consistent with the formation of a conventional lamellar structure where the lamellar planes lie parallel to the substrate surface. However, surprisingly, the optical micrograph image of this film shows some alignment texture (Figure 3-8). Further investigation by in-plane XRD revealed the presence of lamellae that did not lie parallel to the substrate

surface (Figure 3-9a), and the in-plane radial (φ–$2\theta\chi$) scanning profile (Figure 3-9b) shows definite in-plane structural anisotropy of the film.

The lattice spacing estimated from the Bragg–Brentano geometry (d_{01} = 3.35 nm, Figure 3-7) is slightly different from that estimated from the in-plane geometry (d_{01} = 3.53 nm, Figure 3-9a, black trace). This inconsistency may be attributed to the shrinkage

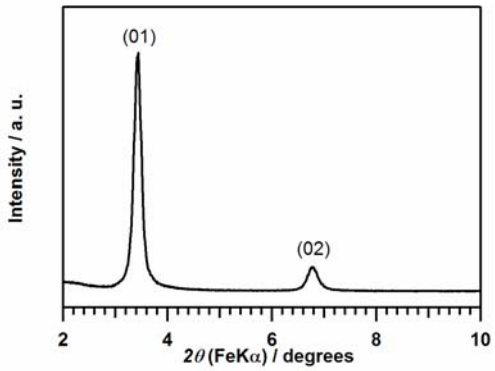

Figure 3-7. Out-of-plane XRD pattern of a **C*16***-derived film measured with the rubbing direction oriented parallel to the projection of the incident beam.

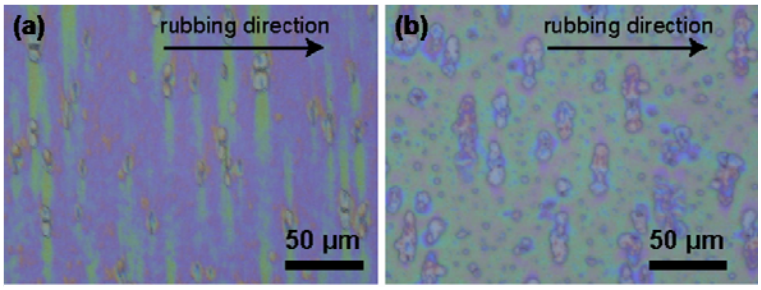

Figure 3-8. Comparison of the optical micrograph images for (a) a **C*10***-derived film and (b) a **C*16***-derived film, both prepared on rubbing-treated substrates.

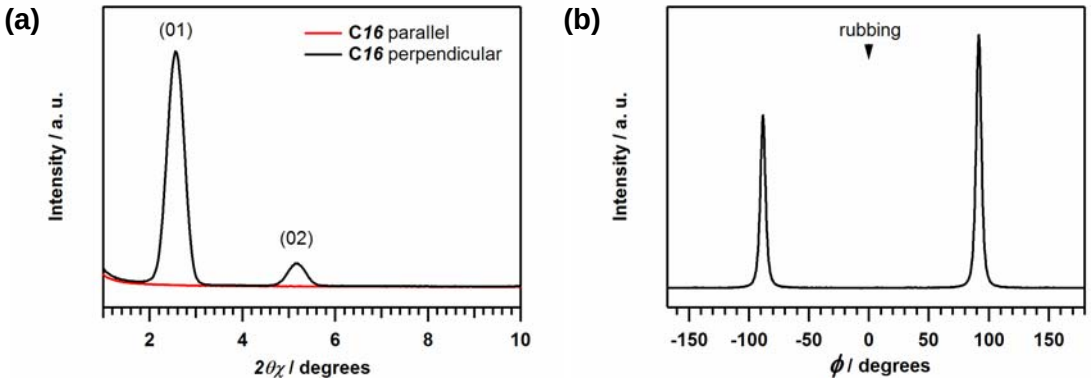

Figure 3-9. (a) In-plane φ–$2\theta\chi$ scanning profiles for the **C*16***-derived film with the rubbing direction oriented parallel (red trace) and perpendicular (black trace) to the projection of the incident X-ray beam at φ = 0 °; and (b) the corresponding φ-scanning profile at $2\theta\chi$ = 2.56 °.

of the film in the direction normal to the substrate surface during the drying process. Such anisotropic shrinkage only affects the lattice spacing measured under the Bragg–Brentano geometry and has been observed for many mesostructured films.[19,29]

The in-plane φ-scanning profile of this ***C16*** film (Figure 3-9b) shows two sharp peaks separated by an interval of approximately 180 °, indicating that the lamellae that contribute to the in-plane diffraction are aligned perpendicularly with respect to the rubbing direction in the plane of the film (see Scheme 3-2, n = 16, for a possible structural model).

Figure 3-10a shows the TEM image of the film (cross-sectioned along the rubbing direction) near the substrate–film interface. The perpendicular alignment of lamellae extending from the substrate surface (bottom right) is evident. However, near the film–air interface, complete alignment of the lamellae parallel to the interface is observed

(Figure 3-10b). Thus the in-plane alignment of the lamellae observed near the substrate surface is not maintained through the entire thickness of the film. A transition region is observed where the orientation of the lamellae changes between the two different orientations so as to minimize the formation of structural defects, which is evidenced by the curved stripes in Figure 3-10a between the two interfaces.

The overall lamellar structure of the film is, therefore, influenced by the two interfaces (substrate–film and film–air) – each of which gives rise to a different orientation of the lamellae. The lamellae should lie parallel to the film–air interface as shown in Scheme 3-6b (top), as the air phase is considered to be hydrophobic in nature.[42] In contrast, the lamellae can be formed perpendicularly to the anisotropic rubbing-treated polyimide surface because the hydrolyzed **C*16*** molecules adsorb parallel to the surface to

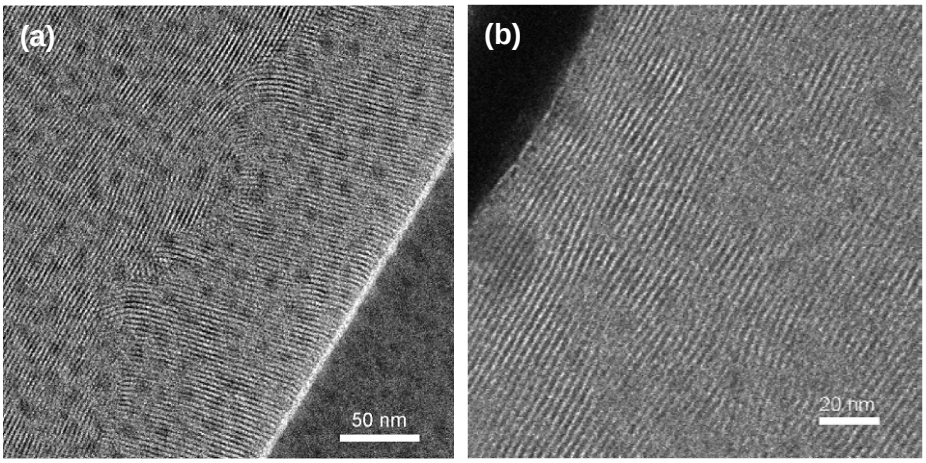

Figure 3-10. Cross-sectional TEM images of the **C*16***-derived film sliced parallel to the rubbing direction with (a) the substrate–film interface located at the bottom right corner of the image, and (b) the film–air interface located at the top left corner of the image.

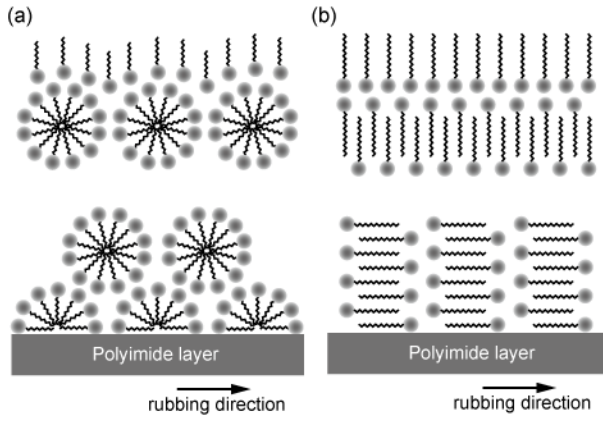

Scheme 3-6. Illustration of the arrangements of hydrolyzed C***n*** molecules in the (a) C***10*** and (b) C***16*** systems near the film–air interface (top) and substrate–film interface (bottom) viewed from the direction normal to the rubbing direction.

maximize their hydrophobic interactions with the elongated alkyl moieties of the polyimide (Scheme 3-6b, bottom). It should be noted that a similar perpendicular orientation of the lamellae near the substrate surface was not achieved when the film was coated onto a plain substrate (i.e. no polyimide layer present). Although the XRD profile measured under the Bragg–Brentano geometry is quite similar to that for the film prepared on a rubbing-treated substrate, no obvious peak is observed in the in-plane radial (φ–$2\theta\chi$) scanning profile for this unaligned film (Figure 3-11b), suggesting that the lamellae are oriented parallel to the substrate over the whole thickness.

In contrast to the partial alignment of the lamellar film, the 2D hexagonal film prepared from C***10*** has a highly aligned cylindrical mesostructure over the whole film, presumably because the parallel orientation of the 2D hexagonal structure satisfies the boundary conditions for both interfaces. At the substrate surface, we postulate that

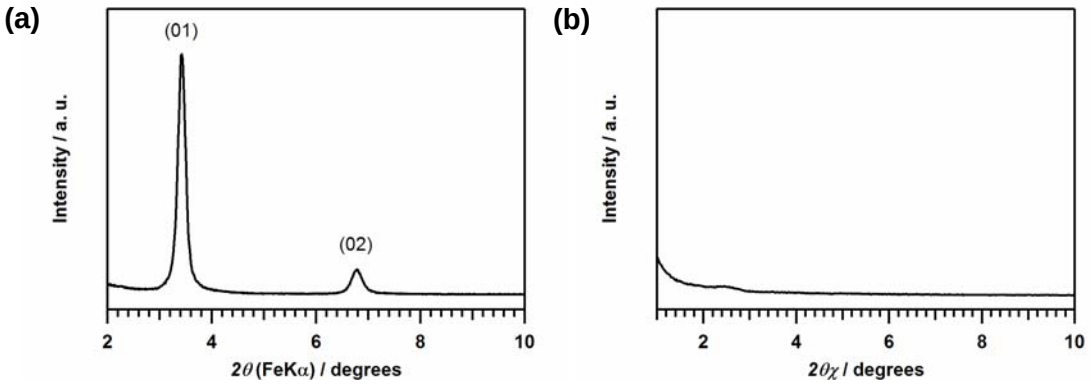

Figure 3-11. (a) Out-of-plane XRD pattern and (b) in-plane φ–$2\theta\chi$ scanning profile of **C*16***-derived film prepared on a non-rubbing-treated substrate.

hydrolyzed **C*10*** molecules adsorb parallel to the elongated polyimide chains by hydrophobic interactions to form aligned hemi-cylindrical surface micelles, from which total uniaxial alignment is initiated (Scheme 3-6a).[29b] It is thus plausible that since a change in the alignment between the substrate–film and film–air interfaces is unnecessary in the case of **C*10***-derived films, uniform alignment control throughout the entire film thickness by the rubbing-treated polyimide layer through anisotropic hydrophobic interactions with the **C*10*** oligomers can be facilitated.

3.3 Introduction of Porosity Using UV / Ozone Treatment

As described in Section 3.2, 2D hexagonally-ordered hybrid films with uniaxial cylindrical alignment were easily prepared via the dip-coating of specially-designed, amphiphilic, oligomeric, alkylsiloxane precursors onto rubbing-treated polyimide-coated

substrates. Removal of the alkyl moieties to yield uniaxially-aligned, porous channels is desirable, but unfortunately the 2D hexagonal mesostructure of thin film samples collapses under the thermal stress of high-temperature calcination.[31] To preserve the structural order of the film, UV / ozone treatment was explored as a potentially milder method of alkyl chain elimination.

Brinker et al. and Takai et al. have previously demonstrated that nonionic[43] and cationic[44] surfactants, respectively, can be removed from the pores of templated mesoporous silica films using UV / ozone treatment, where ozone is photogenerated *in situ* using ambient air as the oxygen source. Given the apparent mildness of the UV treatment, we employed a similar strategy to try and eliminate the alkyl moieties covalently bonded to the silica walls from the as-synthesized, uniaxially-aligned films since thermal calcination did not prove to be a viable strategy for these materials.[31] Thus, as-synthesized ***C10*** films were exposed to UV irradiation with variations in the distance from the UV lamp, chamber pressure, and exposure time in an attempt to find a combination of effective conditions.

For example, Figure 3-12b shows the optical micrograph for the UV-exposed, uniaxially-aligned film (UV-exposed at a separation of 2 mm[45] for 20 minutes at 50 Pa). Again, the characteristic alignment texture is still evident for this film (compare to Figure 3-12a), and the film has remained continuous and crack-free after UV treatment. In contrast, the optical micrograph for a calcined, unaligned film (Figure 3-12c) shows extensive cracking and deterioration of the quality of the silica film, suggesting that this film underwent significant thermal shrinkage.

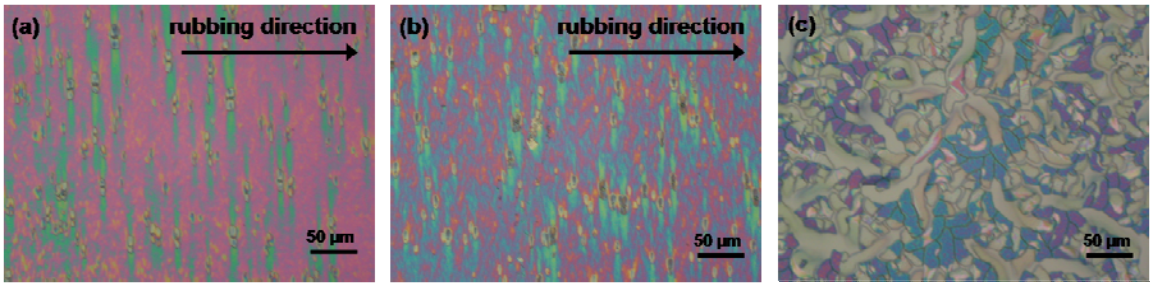

Figure 3-12. Optical micrographs of **C*10*-**derived films: (a) as-synthesized on a rubbing-treated substrate; (b) UV-exposed on a rubbing-treated substrate (UV exposure at a 2 mm-separation for 20 minutes at 50 Pa); and (c) calcined on a non-rubbing-treated substrate.

The effectiveness of alkyl chain elimination from the as-synthesized organosilica films was evaluated by FT-IR spectroscopy. Using this technique, we were able to evaluate alkyl chain removal by the disappearance of the peaks centered at 2856 cm^{-1} and 2926 cm^{-1}, which are assigned to overlapping $–CH_2–$ and $–CH_3$ symmetric and anti-symmetric stretching modes, respectively. From Figure 3-13, the reduction in the intensities of the alkyl IR stretching bands after exposing the uniaxially-aligned film at a distance of 2 mm from the UV lamp at 50 Pa for 20 minutes is notable. However, under such conditions, alkyl chain removal is incomplete. Therefore, other exposure conditions were explored to try and improve upon the degree of alkyl chain elimination (for example, see Figure 3-14). The best conditions appeared to be UV exposure at a separation of 1 cm for 30 minutes at 25 Pa. Therefore, as determined via FT-IR characterization, UV / ozone treatment can be as effective as thermal calcination for eliminating organic moieties from these materials as long as appropriate exposure

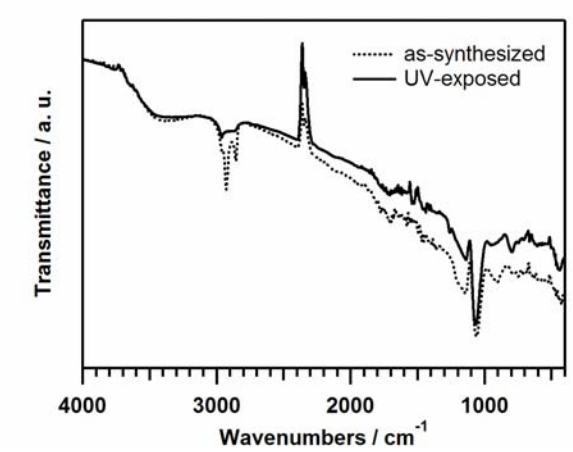

Figure 3-13. FT-IR spectra for as-synthesized and UV-exposed (2 mm-separation for 20 minutes at 50 Pa) **C*10***-derived films.

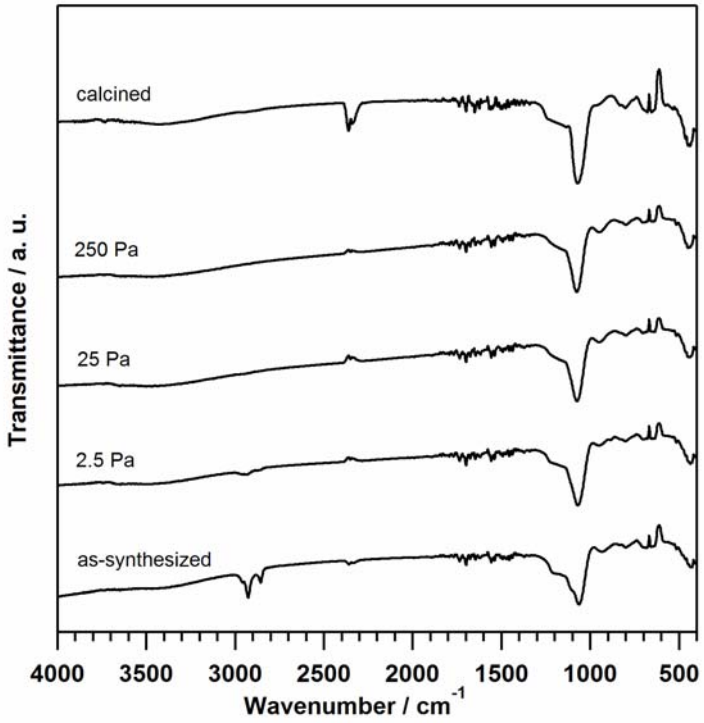

Figure 3-14. FT-IR spectra for the UV-exposure of a **C*10***-derived film at various oxygen pressures at a separation of 1 cm for 30 minutes each.

conditions are employed (i.e. separation distance between the sample and UV source, exposure time, and residual pressure).

Interestingly, however, there appears to be a depth-dependence of the effectiveness of alkyl chain removal from the as-synthesized **C*10*** films. From the cross-sectional TEM images in Figure 3-15, it is clear that the rubbing-treated polyimide layer is still visible. Therefore, it is plausible that alkyl chain elimination may be incomplete under the given UV / ozone exposure conditions near the film–polyimide interface, while alkyl chain elimination near the air-film interface may be complete. Therefore, the as-synthesized film thickness may need to be optimized in addition to the other treatment parameters.[46]

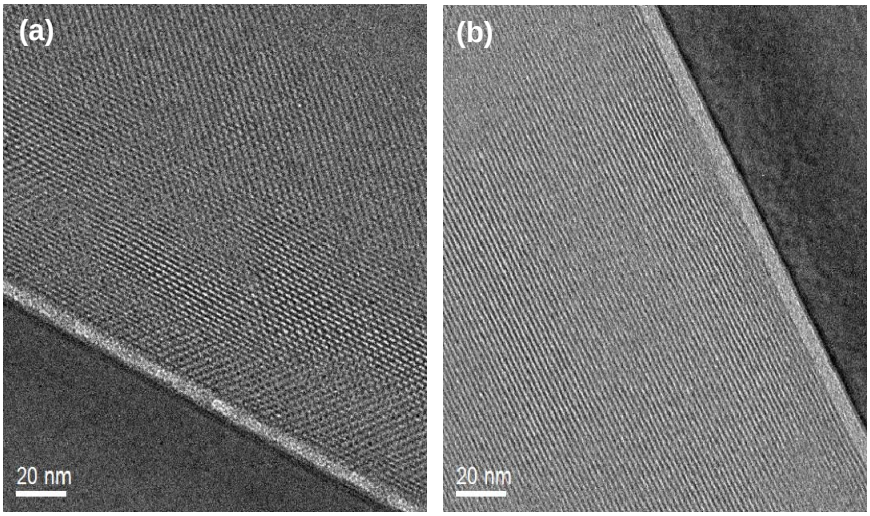

Figure 3-15. Cross-sectional TEM images for an aligned, UV-exposed, **C*10***-derived film sliced (a) parallel and (b) perpendicular to the rubbing direction.

After UV exposure, the films were characterized by out-of-plane and in-plane XRD to verify the retention of the uniaxially-aligned structure. Indeed, by out-of-plane XRD, as shown in Figure 3-16 ('UV-exposed' trace), diffraction peaks and higher order peaks are still visible, although slight shifts to higher angles indicate that some vertical shrinkage occurred in the films. For UV-treated, uniaxially-aligned films, the *d*-spacings changed from 2.81 nm, 1.41 nm, and 0.93 nm to 2.10 nm, 1.04 nm, and loss of the highest angle peak, respectively. Nevertheless, the intensities of the observed peaks are notably greater than what is obtained by calcination of the films (Figure 3-16, 'calcined' trace). In addition, the anisotropic nature of the mesostructural ordering is still very strongly evident from the in plane φ–$2\theta\chi$ scanning profiles (Figure 3-17a), and the φ-scan shows two peaks symmetrically centered about $\varphi = 0$ ° (specifically, at -85.0 ° and +94.5 °) of comparable intensity and width to the as-synthesized peaks (Figure 3-17b). All of these results confirm retention of the uniaxial alignment of the 2D hexagonally-ordered silica films prepared from the **C*10*** precursor after removal of the alkyl moieties.

Finally, cross-sectional TEM images of the UV-treated aligned films show preservation of the uniaxial channel alignment over large length scales (Figure 3-15). However, shrinkage of the mesostructure (as previously evidenced by out-of-plane XRD) is confirmed in Figure 3-15a where vertical contraction of the film resulted in distortion of the channel cross-section to yield rectangular-shaped pore openings. Nonetheless, this is the first example of the application of UV / ozone treatment for the successful elimination of covalently-bound organics from this type of nanostructured, hybrid organosilica films.

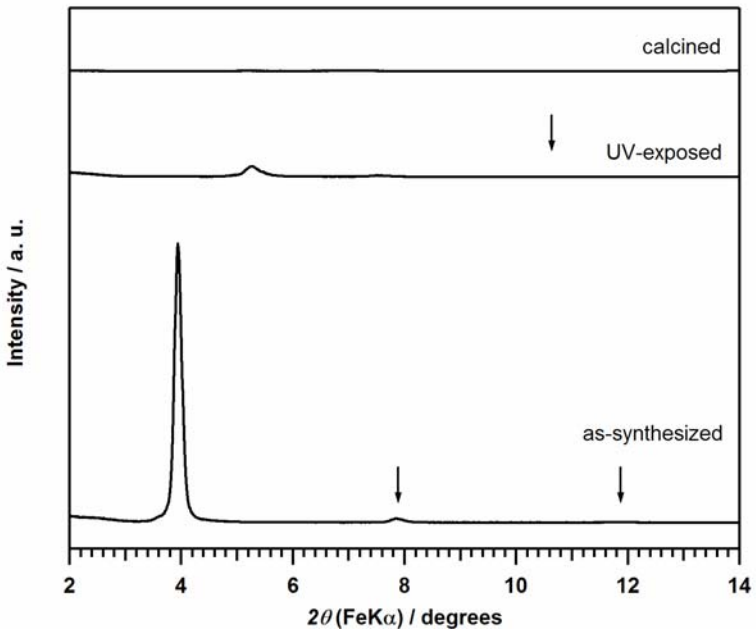

Figure 3-16. Out-of-plane XRD patterns for as-synthesized, UV-exposed (2 mm-separation for 20 minutes at 50 Pa), and calcined **C*10***-derived films.

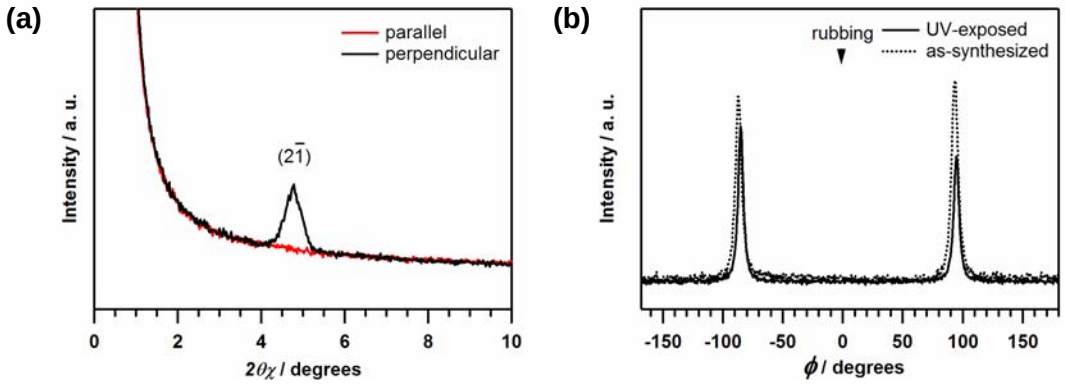

Figure 3-17. (a) In-plane φ–$2\theta\chi$ scanning profiles for the **C*10***-derived film with the rubbing direction oriented parallel (red trace) and perpendicular (black trace) to the projection of the incident X-ray beam at $\varphi = 0$ ° after UV-exposure (2 mm-separation for 20 minutes at 50 Pa); and (b) the corresponding φ-scanning profile for the UV-exposed film in comparison to the as-synthesized film.

It should be noted that more aggressive UV treatment conditions (i.e. exposure times of up to ~ 2 h, compared to the 2 mm separation at 50 Pa for 20 minutes) were more effective for complete alkyl chain elimination, but were accompanied by more dramatic degradation of the film mesostructure as evidenced by out-of-plane XRD. The high degree of retention of the uniaxially-aligned 2D hexagonal mesostructure observed under optimized conditions as described above may be a result of the presence of residual organic moieties trapped in the channels, which could provide some structural support. With the shorter exposure time (i.e. 20 minutes in comparison to 30 minutes), there is less time over which shrinkage of the framework can occur. Given the very thin siloxane walls of these oligomeric materials (1.0 nm in thickness, as estimated from reference 31 in comparison to ~1.5 nm and ~3 nm for MCM-41[2] and SBA-15,[3] respectively), the siloxane layer is expected to be very sensitive to mechanical stresses such as those resulting from oxidation of the alkyl moieties and rearrangement of the siloxane network on a microscopic scale during UV / ozone treatment and / or thermal calcination. Further investigation into the effectiveness of UV / ozone treatment on these uniaxially-aligned, as-synthesized films may be explored in the future under different conditions, and possibly with different UV sources.

3.4 Improving the Efficacy of Alkyl Chain Removal

In an attempt to improve the efficacy of alkyl chain removal from the as-synthesized hybrid organic–inorganic films by high-temperature calcination as well as

UV / ozone irradiation, a few alternative strategies were investigated. Firstly, we tried co-condensing TEOS (tetraethoxysilane, $Si(OEt)_4$) with the **C*10*** oligomeric precursor at a 1 : 1 mole ratio, respectively, with the intention of creating a thicker siloxane layer in the walls of the condensed films to potentially improve the mechanical and chemical stability of the film – preserving porosity and mesostructural ordering to a larger extent. However, upon incorporation of TEOS into the sol under the conditions typically used for 100% **C*10*** films, the diffraction peaks in the out-of-plane XRD patterns for the as-synthesized, spin-coated TEOS–**C*10*** films remained essentially unchanged with respect to the as-synthesized, spin-coated **C*10***-only films. Presumably, if the siloxane layer was indeed thicker in the case of the TEOS–**C*10*** films, the peak positions should have shifted to slightly lower 2θ angles to reflect an increase in the *d*-spacing of the mesostructure. Therefore, at this point, it was difficult to determine whether TEOS was successfully incorporated into the films to any degree at all.[47] Furthermore, subjecting these TEOS–**C*10*** films to each of calcination and UV / ozone treatment did not yield any improvements in comparison to what was previously obtained for the **C*10***-only films. It is plausible that the film synthesis conditions and corresponding sol composition may need to be re-optimized for this **TEOS-C*10*** system in order to see any signs indicating significant **TEOS** incorporation into the film matrix before evaluating the effect of this **TEOS** incorporation on the mechanical and chemical reinforcement of the film's mesostructure.

We also attempted to incorporate titania into the film matrix. As titania (in both its anatase form and as single-site, isolated species) is known to act as a photocatalyst for

the oxidative degradation of organic species,[48] it was thought that the presence of catalytic amounts of titania in these nanohybrid films would assist in the elimination of the alkyl moieties from the films during UV / ozone treatment. If the UV / ozone exposure conditions could be shortened in time or lessened in intensity, it was postulated that the uniaxial 2D hexagonal channel structure could be preserved to a greater extent.

Thus, titanium tetraisopropoxide ($Ti(O^iPr)_4$, **TTIP**) was used as the condensable titania precursor and was first subjected to substoichiometric alkoxy group exchange with acetylacetone (**acac**) in order to generate a less reactive titanium species (see Scheme 3-7). Unaligned films with a molar composition of **TTIP** : **C*10*** = 0.5 : 1.0 were then prepared by spin-coating a sol of similar formulation to that used for the 100% ***C10*** films. Unfortunately, with this composition, the resulting films were relatively opaque in appearance – suggesting a certain degree of macrophase separation within the films.

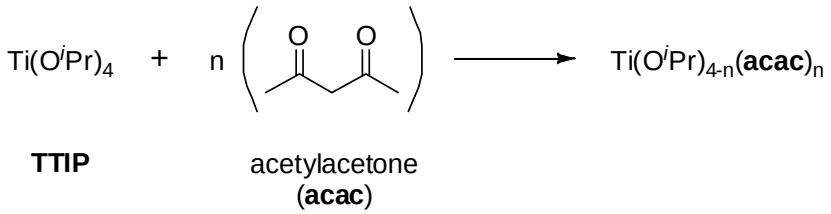

Scheme 3-7. In-situ ligand exchange to generate a less-reactive titania precursor.

The **TTIP** loading was then decreased to 0.2 mol% (again, after first exchanging alkoxy groups with acetylacetone) and a new batch of **TTIP-C*10*** films were spin-coated. This time, although the majority of the resultant coatings were transparent, small

particulate clusters were observed by eye and by optical microscopy to be embedded within the films, suggesting inhomogeneous incorporation of titania once more. Additionally, as could be expected, these heterogeneously dispersed titania clusters did little to improve alkyl chain removal during UV / ozone exposure.

Although these trials were subsequently discontinued, we suspect that successful, homogeneous dispersion and incorporation of single-site titania into these organosiloxane-based nanohybrid films would be possible if the sol forming conditions could be optimized to mitigate the rapid, self-condensation of the titania precursors.

3.5 The Accommodation of Guest Molecules within the Aligned Films

Upon the successful demonstration of the formation of uniaxially aligned, 2D hexagonally-ordered films from **C*10*** precursors, we were curious to see: (i) if the organic cores of the as-synthesized films could be swelled to generate 2D hexagonally-ordered cylinders of larger diameter, which could then yield porous channels also of larger diameter upon alkyl chain elimination; and (ii) if small, photoactive molecules could be entrapped and aligned within either the organic cores of as-synthesized films or the channels of the porous films to produce materials displaying enhanced non-linear optical behaviour. The results from this brief series of investigations are summarized in Table 3-1.

Table 3-1. Summary of experimental trials conducted to incorporate various dopants into **C*10***-based films.

Dopant	Molar Ratio (Dopant **: C*10***)	Doping Method	General Outcome and Comments
TEOS	1.0 : 1.0	in situ (unaligned, spin-coated)	inconclusive TEOS incorporation
TTIP	0.5 : 1.0 0.002 : 1.0	in situ (unaligned, spin-coated)	inhomogeneous films / phase separation (titania crystallite formation)
TIPB	0.2 : 1.0 0.5 : 1.0 1.0 : 1.0	in situ (aligned, dip-coated)	inhomogeneous films / phase separation (oil droplet formation)
DO3	2×10^{-4} : 1.0	in situ (unaligned, spin-coated)	inhomogeneous films / phase separation (oil droplet formation)
	N/A	passive diffusion of **DO3** (from a saturated solution of **DO3**) into aligned, UV-exposed, **C*10*** film	inconclusive **DO3** incorporation

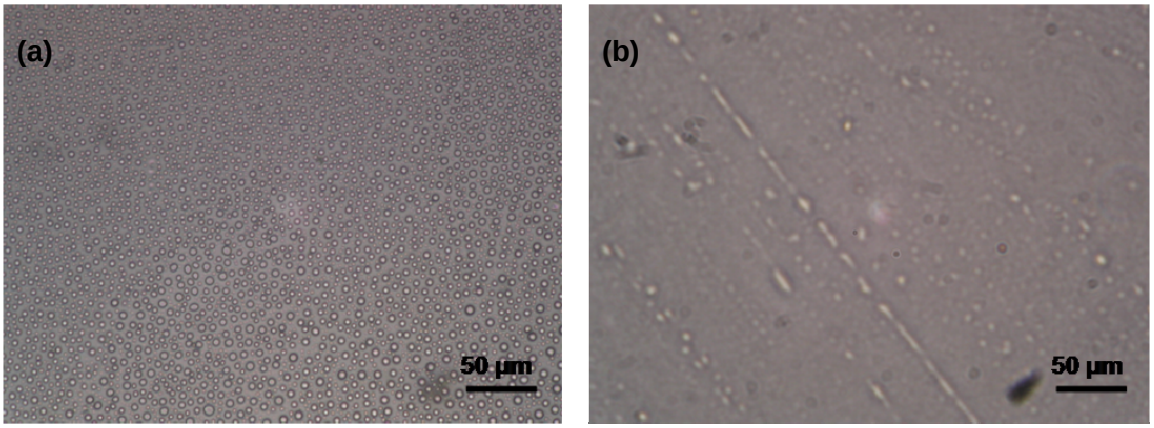

Figure 3-18. Optical micrograph images showing phase separation in (a) a TIPB-doped **C*10***-derived film, and (b) a **DO3**-doped **C*10***-derived film.

Overall, the difficulty of solubilizing the dopants within the organic portions of the as-synthesized nanohybrid structures was commonly encountered. The formation of 'oil-like' droplets or streaks at the expense of as-synthesized film homogeneity and uniformity, as well as a notable absence of the typical 'alignment texture' for the **C*10***-based films prepared on rubbing-treated substrates were evident by optical microscopy (see Figure 3-18). Additionally, by out-of-plane XRD, the diffraction patterns obtained for these 1,3,5-triisopropylbenzene (TIPB)- and Disperse Orange 3 (**DO3**)-doped samples showed dramatically reduced peak intensities and only very minor shifts in the peak positions to slightly lower 2θ angles relative to the XRD data obtained for **C*10***-only films. Moreover, no diagnostic peaks indicating the presence of **DO3** dye molecules in the films were observed by FT-IR or UV-VIS spectroscopy.[49] If any TIPB or **DO3** was indeed incorporated in the as-synthesized and / or UV / ozone-treated films, it was not to any significant degree that was quantifiable using the particular techniques applied here.

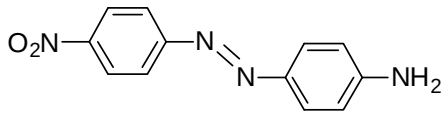

Disperse Orange 3 (**DO3**)

Although dopant incorporation was not explored further in any greater depth, we postulated that (at the loadings applied in these few experiments) the dopant molecules (in particular, **TIPB**) could be disrupting the interactions between the **C*10*** precursors and

the polyimide chains at the organosilica film–polyimide interface during the formation of the as-synthesized films on rubbing-treated substrates, which would in turn detrimentally affect the achievement of uniaxial alignment across the entire film in all three dimensions. However, despite the apparent incompatibility of the various dopant species with this particular **C*10***-based sol system, it is certainly possible that a different set of conditions (e.g. a change of the solvent system and / or dopant loading) could be established that would allow for both uniaxial structure formation as well as dopant entrapment within both the nanohybrid and porous mesostructures.[50] Alternatively, other, more compatible swelling agents and photoactive dyes could also be explored for the purposes of creating modified, functional variants of these **C*10***-based oligomeric, organosiloxane films.

3.6 Chiral, Oligomeric Organosiloxanes

In yet another attempt to extend the scope of these designer, amphiphilic, oligomeric, organosiloxane precursors, we briefly explored the synthesis of chiral variants of the precursors. A summary of the proposed routes used to address this aspect of the project are depicted in Scheme 3-8. In general, we hoped to prepare precursors bearing a molecular scaffold reminiscent of the **C*n*** precursors described above (i.e. precursors comprised of a condensable, oligomeric siloxane-based head group coupled with a relatively long, hydrophobic, organic moiety), coupled with the presence of a chiral center in various positions relative to the head group in order to see its effect on

subsequent uniaxial structure formation. The main challenge, then, was to obtain a chiral, organotrichlorosilane that could be subjected to further silylation in order to build up the oligomeric siloxane-based head group. The reactions also needed to yield each of the products at large enough scale that purification by distillation was viable.

Route A involved an asymmetric hydrosilylation of terminal alkenes to generate branched, 2-substituted alkyltrichlorosilanes by a method reported by Hayashi and co-workers.[51] The preliminary investigative work was conducted using 1-octene (**1**), with the idea that if this route proved successful for 1-octene, both terminal and internal alkenes of varying length could be subjected to similar hydrosilylation conditions to generate other chiral, alkyltrichlorosilane derivatives. Unfortunately, this reaction was not very reproducible nor scalable (generally poor conversion, and the best yield was only 25% at a 5 mmol scale of **1**). However, more significantly, the desired branched isomer was obtained as ~ a 9 : 1 mixture (molar ratio) with the linear isomer,[51] from which it was inseparable.

We then decided to try synthesizing a different monomer in which the center of chirality was significantly removed from the targeted position of siloxane condensation (depicted in Scheme 3-8, Route B). The olefinic, branched benzyl ether (**7**) was first prepared by an S_N2 reaction between a racemate of α-methylbenzyl alcohol (**5**) and allyl bromide (**6**) in the presence of NaH and dry THF.[52,53] Once purified by column chromatography, **7** was subjected to chloroplatinic acid (H_2PtCl_6)-catalyzed hydrosilylation with $HSiCl_3$ to produce **8**.[54] Although the first step proceeded with reasonable results (90% yield for a 25 mmol scale of **5**), the hydrosilylation step suffered

Route A

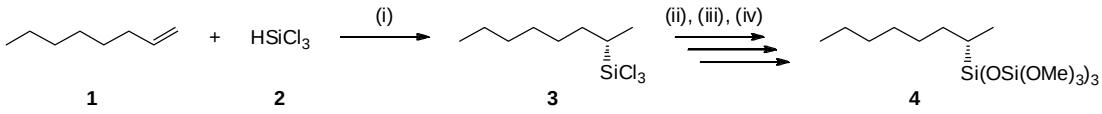

Route B

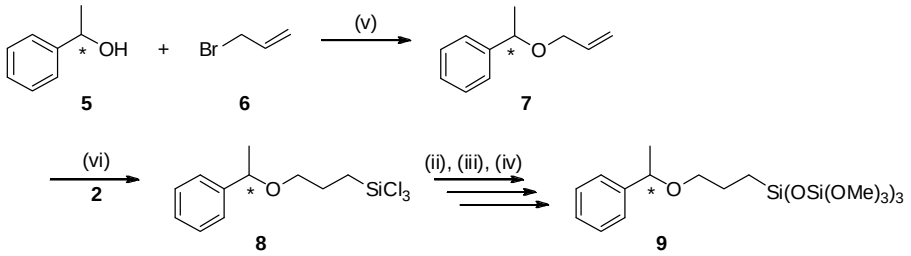

Route C

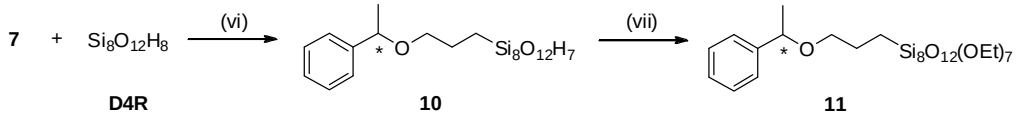

where,

(*R*)-MeO-MOP (**L***) =

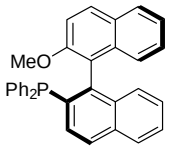

$Si_8O_{12}H_8$ (**D4R**) =

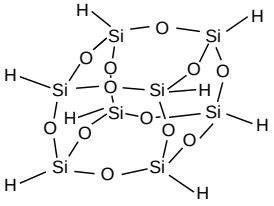

Scheme 3-8. Synthesis of chiral, oligomeric organosiloxanes. Reaction conditions are summarized as follows: (i) $[PdCl(\eta^3\text{-}C_3H_5)]_2$, **L***, neat, 40 °C, 2 h; (ii) H_2O, aniline, THF / Et_2O, 0 °C, 2 h, then crystallization in hexane; (iii) $SiCl_4$, hexane / THF; (iv) MeOH, pyridine, hexane; (v) NaH, THF, 45 °C, 48 h; (vi) $H_2PtCl_6{\cdot}6H_2O$ in ACN, and neat at 70 °C for 2 h (Route B), or in toluene at 50 °C for 18 h (Route C); (viii) $(C_2H_5)_2NOH$, EtOH, toluene, room temperature, 16 h.

from poor yields (< 60%). Since **8** was not obtained in an amount that would be suitable for purification by distillation, crude **8** was subjected to the conditions for transformation of the organotrichlorosilane to the silanetriol, nonetheless. Not surprisingly, however, this reaction did not proceed as desired, and gelation of the reaction mixture (presumably due to self-condensation of the monomer under these 'wet' conditions) was observed.

As a last resort, we explored the hydrosilylation of **7** with double-four-ring ($Si_8O_{12}H_8$, **D4R**) cubic polyhedral oligosilsesquioxane units (Scheme 3-8, Route C).[33,55] The advantage of this route was that the **D4R** unit could itself serve as a condensable, oligomeric head group once the residual hydride groups on the **D4R** unit were converted to ethoxy substituents. This would allow us to eliminate the additional silylation steps that would otherwise be required to build up the oligomeric head group present on the **C*n***-based precursors. However, the hydrosilylation reaction proceeded with poor conversion. Furthermore, given that the equipment necessary to purify the substituted **D4R** units was not available for our use and the relatively high cost of the **D4R** oligomer (~ $200 per gram), it was decided that this was also not a scalable option.

Although we were disappointed to discontinue this project at this stage in favour of more intensely pursuing the work described in the proceeding chapter (Chapter 4), we believe that given more focused time and effort, designer, chiral, amphiphilic, oligomeric organosiloxane-based monomers (based on the scaffolds suggested above or otherwise) could be truly realized and investigated for their potentially novel materials-forming properties.

3.7 Conclusions and Future Work

Amphiphilic, oligomeric alkyl siloxane precursors **C*10*** and **C*16*** easily form mesostructured films with uniaxially-aligned 2D hexagonal mesostructures and partially aligned lamellar structures, respectively, by dip-coating a pre-hydrolyzed sol of **C*n*** onto a substrate bearing a rubbing-treated polyimide layer.[36] In addition, UV / ozone irradiation under nominally room temperature conditions was shown to be a reasonable method for removing the majority of the alkyl moieties from the **C*10*** hybrid films to reveal porous structures with retention of the 2D hexagonal structure and its uniaxial alignment. The ease and high reproducibility of this methodology are promising for the preparation of inorganic–organic hybrid films with improved functionality as a direct result of the control over the structural order on both microscopic and macroscopic scales.

In these films, the position of the organic moiety can be precisely defined on the substrate and in relation to the siloxane matrix. Consequently, the introduction of more complex functional groups in the organic fraction in future investigations would be of noteworthy interest. For example, the direct incorporation of photoactive molecules into the chemical structure of the precursors themselves could be envisioned, from which molecular packing and alignment might be tuned on the microscale and then transmitted throughout the macroscale. This bottom-up approach to synthesizing new and novel materials could, therefore, prove to be quite powerful. Moreover, in their as-synthesized forms, an improvement in the chemical stability of these nanohybrid materials in comparison to conventional silica–surfactant composites could also be anticipated due to

the covalent nature of the interface between the silyloxy and organic moieties, which could also impact their usefulness in advanced applications.

Lastly, as described above, the formation of a uniformly anisotropic film depends on the two boundary conditions at the air–film and the film–substrate interfaces.[17] If the conditions of the two interfaces are consistent, anisotropic structure formation can be achieved over the whole film. Future work could also thus explore strategies to design and optimize the chemical functionality and geometry of these molecular building blocks to achieve total structural alignment and uniformity of more complex and demanding mesostructures.

3.8 Experimental Procedures

3.8.1 General and Materials

Decyltrichlorosilane, hexadecyltrichlorosilane, and tetrachlorosilane were purchased from Tokyo Kasei Kogyo Co., Ltd. and used as received. Anhydrous THF (tetrahydrofuran) (without stabilizer), anhydrous methanol, hexane, diethyl ether, aniline, and anhydrous pyridine used for the synthesis of **C*10*** and **C*16***, in addition to 0.01 M $HCl_{(aq)}$ were purchased from Wako Pure Chemical Industries and used as received. TEOS (tetraethoxysilane), **TTIP** (titanium(IV) tetraisopropoxide), acetylacetone, TIPB (1,3,5-triisopropylbenzene), and **DO3** (Disperse Orange 3, 4-(4-nitrophenylazo)aniline) were purchased from Sigma-Aldrich and used as received. Millipore® deionized water (DI H_2O) was also used for the synthesis of the **C*n*** precursors and the corresponding

films. Non-alkaline glass slides (#7059) were purchased from Corning. Crystalline, single-side polished Si wafers (<100> orientation, 525 μm wafer thickness) were purchased from Shin-etsu Chemical Co., Ltd. Rubbing-treated crystalline silicon and quartz substrates were generously provided by Dr. Hirokatsu Miyata (Canon, Inc.).

For the synthesis of the chiral oligosiloxanes, allylpalladium(II) chloride dimer ($[PdCl(\eta^3\text{-}C_3H_5)]_2$), hexachloroplatinic acid ($H_2PtCl_6 \cdot 6H_2O$), and (*R*)-MeO-MOP ((*R*)-2-(diphenylphosphino)-2'-methoxy-1,1'-binaphthyl) were purchased from Strem Chemicals Inc. and used as received. 1-Octene, sodium hydride (60% dispersion in mineral oil), α-methylbenzyl alcohol, allyl bromide, and trichlorosilane were purchased from Sigma-Aldrich. THF (without stabilizer), toluene, and acetonitrile were purchased from Fisher Scientific. With the exception of 1-octene and THF, which were freshly distilled prior to use, all of the other reagents and solvents were used as received. Lastly, **D4R** (cubic, octasilane POSS®) was generously provided by Dr. Atsushi Shimojima (University of Tokyo, Japan) and used as received.

Spin-coated films were prepared using a Oshigane Inc. SC-300 spin-coater. Dip-coated films were prepared using a dip-coater built in-house (constructed by Dr. Atsushi Shimojima, formerly at Waseda University, Japan).

3.8.2 Alkyl Organosiloxane Precursor Synthesis

The precursors (tris(trimethoxysilyloxy)(decyl)silane (**C*10***) and tris(trimethoxysilyloxy)(hexadecyl)silane (**C*16***)) were prepared according to previously

published procedures[31] under nitrogen atmosphere using standard Schlenk techniques. In a typical procedure for the synthesis of **C*10***, decyltrichlorosilane (12.5 g, 48.5 mmol) in diethyl ether (120 mL) was slowly added to a mixture of anhydrous THF (180 mL), diethyl ether (180 mL), deionized water (2.7 mL, 150 mmol), and aniline (13.7 mL, 150 mmol) under vigorous stirring for 2 h at 0 °C. Under these optimized conditions, the alkyltrichlorosilane, water, and aniline are present in molar ratios of $RSiCl_3$: H_2O : aniline = 1.0 : 3.1 : 3.1. The resultant aniline hydrochloride precipitate was removed from the reaction mixture by vacuum filtration to give a transparent solution. Solvent exchange with hexane was conducted under vacuum and repeated three times to afford the crystallization of decylsilanetriol, which was the collected by vacuum filtration and dried *in vacuo*. Decylsilanetriol was then dissolved in anhydrous THF (300 mL) and added to a solution of tetrachlorosilane (50 mL) and hexane (60 mL). The solvent volume was reduced under vacuum, followed by the addition of anhydrous MeOH, hexane, and anhydrous pyridine for the methanolysis of $C_{10}H_{21}Si(OSiCl_3)_3$. Removal of excess solvent and reagents under vacuum yielded the crude product. Finally, pure **C*10*** was isolated as a clear, colorless liquid by vacuum distillation and characterized by ^{1}H, ^{13}C, and ^{29}Si solution-state NMR (spectra data were compared to those previously published in reference 31). Analogous conditions were used for the synthesis of **C*16*** using hexadecyltrichlorosilane as the starting precursor.

3.8.3 Preparation of Rubbing-Treated Substrates

Rubbing-treated polyimide coated substrates were prepared according to a previously published procedure.[29] The polyimide (poly(hexamethylenepyromellitimide), **PI**) film is prepared by spin-coating the polyamic acid onto clean silicon or quartz substrates, followed by heating at 200 °C for 1 h in air to allow for the formation of the polyimide layer (approximately 10 nm in thickness) via thermal imidization. The polyimide-coated substrates are then subjected to a rubbing treatment by fixing the substrates to a height-controllable stage and contacting the polyimide layer with a Nylon®-covered cylindrical roller of 24 mm radius rotating at a rate of 1000 rpm.

3.8.4 Nanohybrid Film Synthesis

The coating solution was prepared according to previously published procedures[31] with hydrolysis of **C*n*** in a starting sol with the reagents respectively present in the following molar ratios: **C*n*** : THF : H_2O : HCl = 1.0 : 50 : 18 : 0.002. In a typical procedure for synthesizing **C*10***-based films, the **C*10*** precursor (0.47 g, 0.8 mmol) was weighed out into a Teflon® flask. After charging the flask with a stir bar, anhydrous THF (3.3 mL, 40 mmol), DI H_2O (0.10 mL, 5.6 mmol), and 0.01 M $HCl_{(aq)}$ (0.16 mL, 1.6×10^{-3} mmol of acid) were added. The resulting sol was allowed to stir at 25 °C for 12 h before adding additional H_2O (0.47 mL, 26 mmol) at a molar ratio of H_2O / **C*n*** = 32. Rubbing-treated polyimide-coated substrates and plain substrates were then coated with the solution by dip-coating (with the withdrawal direction set perpendicular to the rubbing direction in the case of the rubbing-treated substrates) at a rate of 2 $mm\cdot s^{-1}$. Spin-coated

films were prepared by spinning at a rate of 3000 rpm for 10 s. All of the film processing was carried out in air at a relative humidity of approximately 50%, and the films were then dried under ambient conditions for 2 days.

3.8.5 Removal of Alkyl Moieties from 2D Hexagonally-Ordered Films

Alkyl groups were removed from the as-synthesized materials either by calcination in air at 500 °C for 8 h (with both a ramp rate and cooling rate of 1 °C·min^{-1}) or by UV irradiation using a Xe_2 excimer lamp (Ushio Electric UER20-172V, λ = 173 nm, 10 mW·cm^{-2}) at a various distances from the UV source and at various O_2 pressures to yield porous films. For example, several of the aligned films were UV-exposed at a separation of 2 mm under a pressure of 50 Pa for 20 minutes. It should also be noted that the UV / ozone treatments were conducted by Dr. Atsushi Shimojima at the University of Tokyo (Japan).

3.8.6 Incorporation of TEOS, TTIP, and Organic Guest Molecules

Unaligned, Spin-Coated, TEOS–C10 Films. The coating solution was prepared by hydrolysis of **C*10*** and TEOS in a starting sol with the reagents respectively present in the following molar ratios: **C*10*** : TEOS : THF : H_2O : HCl = 1.0 : 1.0 : 23 : 7.4 : 7.5×10^{-4}. The sol was allowed to stir at 25 °C for 12 h before adding additional H_2O in a molar ratio of H_2O / **C*10*** = 15. Crystalline Si wafer substrates were then spin-coated with the

solution at a rate of 3000 rpm for 10 s in air at a relative humidity of approximately 50%. The films were then dried under ambient conditions for 2 days.

Unaligned, Spin-Coated, TTIP–C10 Films. The coating solution was prepared by hydrolysis of **C*10*** in a starting sol with the reagents respectively present in the following molar ratios: **C*10*** : THF : H_2O : HCl = 1.0 : 50 : 18 : 0.002. The sol was allowed to stir at 25 °C for 12 h. Meanwhile, **TTIP** was separately pre-mixed with acetylacetone in a molar ratio of **TTIP** : acetylacetone = 1.0 : 1.2 to generate a partially ligand-exchanged and less hydrolytically reactive Ti-based precursor. This **TTIP**–acetylacetone mixture was then added to the silane mixture such that the **TTIP** was present at a loading of 0.2 mol%. Crystalline Si wafer substrates were then spin-coated with the solution at a rate of 3000 rpm for 10 s in air at a relative humidity of approximately 50%. The films were then dried under ambient conditions for 2 days.

Incorporation of TIPB into Aligned, Dip-Coated C10 Films. The coating solution was prepared firstly by hydrolysis of **C*10*** in a starting sol with the reagents respectively present in the following molar ratios: **C*10*** : THF : H_2O : HCl = 1.0 : 50 : 18 : 0.002. The resulting sol was allowed to stir at 25 °C for 12 h before adding additional H_2O at a molar ratio of H_2O / **C*10*** = 32. Thereafter, TIPB was added at a molar ratio of TIPB / **C*10*** = x (where x = 0.2, 0.5, or 1.0) under stirring. Rubbing-treated polyimide-coated substrates were then coated with the solution by dip-coating (with the withdrawal direction set perpendicular to the rubbing direction) at a rate of 2 $mm \cdot s^{-1}$ at a relative humidity of approximately 50%, and the films were subsequently dried under ambient conditions for 2 days.

In-Situ Incorporation of DO3 into Unaligned, Spin-Coated C10 Films. The coating solution was prepared firstly by hydrolysis of **C*10*** in a starting sol with the reagents respectively present in the following molar ratios: **C*10*** : THF : H_2O : HCl = 1.0 : 50 : 18 : 0.002. The resulting sol was allowed to stir at 25 °C for 12 h. Meanwhile, a 3 mM solution of **DO3** in THF was prepared. Thereafter, an aliquot of the **DO3** solution was added to the silane solution such that **DO3** was added at a molar ratio of **DO3** / **C*10*** = 2×10^{-4} under stirring. Corning® glass substrates were then spin-coated with the solution at a rate of 3000 rpm for 10 s in air at a relative humidity of approximately 50%. The films were then dried under ambient conditions for 2 days.

Incorporation of DO3 into Uligned, Spin-Coated and UV-Exposed C10 Films. Unaligned, as-synthesized **C*10*** films were first prepared by spin-coating onto crystalline Si substrates using the standard protocol described in Experimental Section 3.8.4. Alkyl chain elimination by UV / ozone exposure was then conducted using the conditions specified in Experimental Section 3.8.5 to yield porous, 2D-hexagonally ordered films. Thereafter, the UV-treated films were soaked for in closed vessel containing a 10 mM solution of **DO3** in ethanol for 24 h. The films were then pulled out of the **DO3** solution and dried under ambient conditions for 1 day prior to further analysis.

3.8.7 Chiral Organosiloxane Precursor Synthesis

Route A: Asymmetric Hydrosilylation of Terminal Alkenes. **3** was prepared according to a previously published procedure.[51] In a typical procedure, allylpalladium(II) chloride

dimer ($[PdCl(\eta^3\text{-}C_3H_5)]_2$) (0.92 mg, 0.0025 mmol), (*R*)-2-(diphenylphosphino)-2'-methoxy-1,1'-binaphthyl ((*R*)-MeO-MOP) (4.68 mg, 0.010 mmol), and 1-octene (560 mg, 5 mmol) were weighed out into a Schlenk flask in a nitrogen atmosphere glove box. The flask was then charged with a stir bar, taken out of the glove box, and cooled to 0 °C with an ice bath. Thereafter, using standard Schlenk techniques, trichlorosilane (745 mg, 5.5 mmol) was added to the mixture. The reaction mixture was allowed to stir 40 °C for 24 h. The product was obtained in 25 % yield (as a mixture with the linear regioisomer) after vacuum distillation as determined by ^1H NMR in $CDCl_3$ (spectra data were compared to those previously published in reference 51).

***Route B*: Synthesis of Racemic, Allyl 1-Phenylethyl Ether.** The synthesis of **7** was adapted from previously published procedures.[52,53] In a typical procedure, sodium hydride (60% dispersion in mineral oil, 2.0 g, 50 mmol) was weighed out into a 100 mL round-bottomed flask charged with a stir bar and sealed with a rubber septum. Under argon flow, freshly distilled THF (25 mL) was then added and the suspension was allowed to stir. Thereafter, racemic α-methylbenzyl alcohol (3 mL, 25 mmol) was added dropwise to the suspension. Once bubbling of the mixture (i.e. hydrogen gas evolution) was complete, allyl bromide (4.3 mL, 50 mmol) was added dropwise and then the reaction mixture was stirred for 48 h at 45 °C. The reaction mixture was next transferred into a separating funnel and repeatedly extracted with diethyl ether. The organic fractions were combined and washed with a saturated brine solution, and subsequently dried with $MgSO_{4(s)}$. After evaporation of the solvent, the resulting pale yellow oil was purified by silica gel chromatography (volumetric ratio of hexane : diethyl ether = 20 : 1)

to give **7** as a colorless oil in 90% isolated yield (3.7 g), which was characterized by ^{1}H NMR in $CDCl_3$ (spectra data were compared to those previously published in references 52 and 53).

Pt-Catalyzed Hydrosilylation of Racemic, Allyl 1-Phenylethyl Ether (7) with $HSiCl_3$. The synthesis of **8** was adapted from previously published procedures.[54] In a typical procedure, **7** (0.5 g, 3 mmol) was weighed into a threaded test tube (10-mL capacity). After charging the test tube with a stir bar, trichlorosilane (0.9 mL, 9 mmol) and a 0.02 M solution of hexachloroplatinic acid ($H_2PtCl_6 \cdot 6H_2O$, 0.012 mL of solution, 2.4×10^{-4} mmol of catalyst) in acetonitrile were added. The test tube was briefly purged with dry argon gas prior to capping the tube and stirring the reaction mixture at 70 °C for 48 h. Evidence for the formation of the desired product was obtained with ~ 60% conversion of the starting olefin (**7**) as determined by ^{1}H NMR of the crude reaction mixture in $CDCl_3$, but pure product was never isolated.

<u>Route C</u>: Pt-Catalyzed Hydrosilylation of Racemic, Allyl 1-Phenylethyl Ether (7) with D4R. The synthesis of **10** was adapted from previously published procedures.[33,55] In a typical procedure, **D4R** (0.1 g, 0.24 mmol) was weighed into a 10-mL threaded test tube. After charging the test tube with a stir bar, **7** (0.038 g, 0.24 mmol), toluene (2 mL), and a 0.02 M solution of hexachloroplatinic acid ($H_2PtCl_6 \cdot 6H_2O$, 0.010 mL of solution, 2×10^{-4} mmol of catalyst) in acetonitrile were added. The test tube was briefly purged with dry argon gas prior to capping the tube with a Teflon®-lined lid and stirring the reaction mixture at 50 °C for 18 h. Some crude product was obtained as determined by ^{1}H (in $CDCl_3$), but pure product could not be isolated.

3.8.8 Characterization Methods

The surface texture of the films was observed by optical microscopy (Olympus BX50). The X-ray diffraction (XRD) in Bragg–Brentano geometry was performed with a MAC Science M03XHP22 diffractometer using Mn-filtered Fe Kα radiation at 40 kV and 20 mA. In-plane XRD patterns were recorded with a Rigaku ATX-G diffractometer with a 4-axis goniometer using Cu Kα radiation at 50 kV and 300 mA. A soller slit with a vertical divergence of 0.48 ° was used to obtain a parallel beam. The incident angle of the X-ray in the in-plane geometry was 0.2 °. Samples were prepared for cross-sectional TEM using focused ion beam (FIB) etching (SEIKO EG&G SMI2050), and cross-sectional TEM images were recorded with a JEOL JEM-2010 microscope operated at 200 kV. Fourier transform infrared (FT-IR) spectra of the films were recorded in transmission mode on a Perkin-Elmer Spectrum One spectrometer with a nominal resolution of 0.5 cm^{-1}. Solution state NMR spectra were collected at Waseda University (Japan) on a JEOL Lambda 500 MHz spectrometer, and at Queen's University on Bruker Avance 300 MHz and 400 MHz spectrometers.

3.9 References

1. Yanagisawa, T; Shimizu, T; Kuroda, K.; Kato, C. *Bull. Chem. Soc. Jpn.* **1990**, *63*, 988–992.

2. (a) Kresge, C. T.; Leonowicz, M. E.; Roth, W. J.; Vartuli, J. C.; Beck, J. S. *Nature* **1992**, *359*, 710–712; (b) Beck, J. S.; Vartuli, J. C.; Roth, W. J.; Leonowicz, M. E.; Kresge, C. T.; et al. *J. Am. Chem. Soc.* **1992**, *114*, 10834–10843.

3. (a) Zhao, D.; Feng, J.; Huo, Q.; Melosh, N.; Fredrickson, G. H.; Chmelka, B. F.; Stucky, G. D. *Science* **1998**, *279*, 548–522; (b) Zhao, D.; Huo, Q.; Feng, J.; Chmelka, B. F.; Stucky, G. D. *J. Am. Chem. Soc.* **1998**, *120*, 6024–6036.

4. For a review, see: Sanchez, C.; Julián, B; Belleville, P.; Popall, M. *J. Mater. Chem.* **2005**, *15*, 3559–3592.

5. Cortial, G.; Siutkowski, M.; Goettmann, F.; Moores, A.; Boissière,, C.; Grosso, D.; Le Floch, P.; Sanchez, C. *Small* **2006**, *2*, 1042–1045.

6. Scott, B. J.; Wirnsberger, G.; Stucky, G. D. *Chem. Mater.* **2001**, *13*, 3140–3150.

7. Nguyen, T.-Q.; Wu, J.; Doan, V.; Schwartz, B. J.; Tolbert, S. H. *Science* **2000**, *288*, 652–656.

8. Etienne, M.; Quach, A.; Grosso, D.; Nicole, L.; Sanchez, C.; Walcarius, A. *Chem. Mater.* **2007**, *19*, 844–856.

9. Nicole, L.; Boissière, C.; Grosso, D.; Quach, A.; Sanchez, C. *J. Mater. Chem.* **2005**, *15*, 3598–3627.

10. Soler-Illia, G. J. A. A.; Innocenzi, P. *Chem. Eur. J.* **2006**, *12*, 4478–4494.

11. (a) Hoffmann, F.; Cornelius, M.; Morell, J.; Fröba, M. *Angew. Chem. Int. Ed.* **2006**, *45*, 3216–3251; (b) Hoffmann, F.; Fröba, M. *Chem. Soc. Rev.* **2011**, *40*, 608–620.

12. Ogawa, M. *J. Am. Chem. Soc.* **1994**, *116*, 7941–7942.

13. Ogawa, M. *Chem. Commun.* **1996**, 1149–1150.

14. Lu, Y.; Ganguli, R.; Drewien, C. A.; Anderson, M. T.; Brinker, C. J.; Gong, W.; Guo, Y.; Soyez, H.; Dunn, B.; Huang, M. H.; Zink, J. I. *Nature* **1997**, *389*, 364–370.

15. Brinker, C. J.; Lu, Y.; Sellinger, A.; Fan, H. *Adv. Mater.* **1999**, *11*, 579–585.

16. Yang, H.; Kuperman, A.; Coombs, N.; Mamiche-Afara, S.; Ozin, G. A. *Nature* **1996**, *379*, 703–705.

17. Innocenzi, P.; Malfatti, L.; Kidchob, T.; Falcaro, P. *Chem. Mater.* **2009**, *21*, 2555–2564.

18. Hatton, B.; Landskron, K.; Whitnall, W.; Perovic, D.; Ozin, G. A. *Acc. Chem. Res.* **2005**, *38*, 305–312.

19. Sanchez, C.; Boissière, C.; Grosso, D.; Laberty, C.; Nicole, L. *Chem. Mater.* **2008**, *20*, 682–737.

20. Suzuki, T.; Kanno, Y.; Morioka, Y.; Kuroda, K. *Chem. Commun.* **2008**, 3284–3286.

21. Miyata, H.; Kuroda, K. *J. Am. Chem. Soc.* **1999**, *121*, 7618–7624.

22. (a) Fukumoto, H.; Nagano, S.; Kawatsuki, N.; Seki, T. *Adv. Mater.* **2005**, *17*, 1035–1039; (b) Fukumoto, H.; Nagano, S.; Kawatsuki, N.; Seki, T. *Colloids Surf., A* **2006**, 309–314.

23. Seki, T.; Nagano, S.; Kawashima, Y.; Zettsu, N.; Ubukata, T. *Mol. Cryst. Liq. Cryst.* **2005**, *430*, 107–114.

24. (a) Hillhouse, H. W.; Okubo, T.; van Egmond, J. W.; Tsapatsis, M. *Chem. Mater.* **1997**, *9*, 1505–1507; (b) Hillhouse, H. W.; van Egmond, J. W.; Tsapatsis, M. *Langmuir* **1999**, *15*, 4544–4550; (c) Trau, M.; Yao, N.; Kim, E.; Xia, Y.; Whitesides, G. M.; Aksay, I. A. *Nature* **1997**, *390*, 674–676.

25. Melosh, N. A.; Davidson, P.; Feng, P.; Pine, D. J.; Chmelka, B. F. *J. Am. Chem. Soc.* **2001**, *123*, 1240–1241.

26. (a) Yamauchi, Y.; Sawada, M.; Noma, T.; Ito, H.; Furumi, S.; Sakka, Y.; Kuroda, K. *J. Mater. Chem.* **2005**, *15*, 1137–1140; (b) Yamauchi, Y.; Sawada, M.; Sugiyama, A.; Osaka, T.; Sakka, Y.; Kuroda, K. *J. Mater. Chem.* **2006**, *16*, 3693–3700.

27. Freer, E. M.; Krupp, L. E.; Hinsberg, W. D.; Rice, P. M.; Hedrick, J. L.; Cha, J. N.; Miller, R. D.; Kim, H. C. *Nano Lett.* **2005**, *5*, 2014–2018.

28. Miyata, H.; Kuroda, K. *Adv. Mater*. **1999**, *11*, 1448–1452.

29. (a) Miyata, H.; Kuroda, K. *Chem. Mater.* **1999**, *11*, 1609–1614; (b) Miyata, H.; Kuroda, K. *Chem. Mater.* **2000**, *12*, 49–54; (c) Miyata, H.; Kuroda, K. *Adv. Mater.* **2001**, *13*, 558–561; (d) Miyata, H.; Noma, T.; Watanabe, M.; Kuroda, K. *Chem. Mater.* **2002**, *14*, 766–722; (e) Miyata H.; Suzuki, T.; Fukuoka, A.; Sawada, T.; Watanabe, M.; Noma, T.; Takada, K.; Mukaide, T.; Kuroda, K. *Nature Mater.* **2004**, *3*, 651–656; (f) Miyata, H.; Kawashima, Y.; Itoh, M.; Watanabe, M. *Chem. Mater.* **2005**, *17*, 5323–5327; (g) Suzuki, T.; Miyata, H.; Watanabe, M.; Kuroda, K. *Chem. Mater.* **2006**, *18*, 4888–4893; (h) for a review, see: Miyata, H. *Microporous Mesoporous Mater.* **2007**, *101*, 296–302.

30. Grosso, D.; Cagnol, F.; Soler-Illia, G. J. de A. A.; Crepaldi, E. L.; Amenitsch H.; Brunet-Bruneau, A.; Bourgeois, A.; Sanchez, C. *Adv. Funct. Mater.* **2004**, *14*, 309–322.

31. (a) Shimojima, A.; Kuroda, K. *Angew. Chem., Int. Ed.* **2003**, *42*, 4057–4060; (b) Shimojima, A.; Liu, Z.; Ohsuna, T.; Terasaki, O.; Kuroda, K. *J. Am. Chem. Soc.* **2005**, *127*, 14108–14116.

32. Shimojima, A.; Kuroda, K. *Chem. Rec.* **2006**, *6*, 53–63.

33. Goto, R.; Shimojima, A.; Kuge, H.; Kuroda, K. *Chem. Commun.* **2009**, 6152–6154.

34. Fukuoka, A.; Miyata, H.; Kuroda, K. *Chem. Commun.* **2003**, 284–285.

35. Molenkamp, W. C.; Watanabe, M.; Miyata, H.; Tolbert, S. H. *J. Am. Chem. Soc.* **2004**, *126*, 4476–4477.

36. Du, J.; Fukushima, M.; Sakamoto, S.; Sakurai, M.; Suzuki, T.; Shimojima, A.; Miyata, H.; Crudden, C. M.; Kuroda, K. *Langmuir* **2009**, *25*, 13614–13618.

37. Suzuki, T.; Miyata, H.; Kuroda, K. *J. Mater. Chem.* **2008**, *18*, 1239–1244.

38. A hydrothermal synthesis of **C*n***-derived films (as opposed to film synthesis via evaporation-induced self-assembly (EISA)) was briefly pursued using conditions adapted from reference 29g. However, in combination with the strongly aqueous sol composition of this procedure, a homogeneous solution was not obtained with the **C*n*** precursors. Consequently, continuous and homogenous films were not obtained with this method. Soon thereafter, the more time-consuming and laborious hydrothermal synthesis method was abandoned in favour of the EISA method given the ease with which ordered films could be prepared by dip-coating.

39. Kuroda and co-workers had previously recorded the out-of-plane XRD patterns of both bulk materials and films prepared using **C*n*** precursors after various drying time intervals. It was only after 2 days of ambient drying that the diffraction peak positions were identified to be stable, implying complete consolidation of the siloxane framework and the corresponding mesostructural order. (Shimojima, Atsushi. Waseda University, Tokyo, Japan. Personal communication, October 20, 2007.)

40. (a) Tarey, R. D.; Rastogi, R. S.; Chopra, K. L. *The Rigaku Journal* **1987**, *4*, 11–15; (b) Matsuno, S. Y.; Kuba, M.; Nayuki, T.; Soga, S.; Yuen, P. W. T. *The Rigaku Journal* **2000**, *17*, 36–44.

41. Conversely, Kuroda et al. demonstrated that by enlarging the size of the oligomeric siloxane headgroup relative to the hydrophobic alkyl moiety in this type of precursor, 3D mesostructures (i.e. structures with higher interfacial curvature) could be formed. See: Sakamoto, S.; Shimojima, A.; Miyasaka, K.; Ruan, J.; Terasaki, O.; Kuroda, K. *J. Am. Chem. Soc.* **2009**, *131*, 9634–9635.

42. To get a better idea of this concept, picture, for example: (i) the self-assembly of a monolayer of amphiphilic molecules at a water–air interface (i.e. the hydrophilic groups associate with the water phase while the hydrophobic groups extend towards the air phase); or (ii) the formation of a 'film' of oil at the surface of a puddle of water (i.e. concentration of the oil phase at the water–air interface). The molecules assemble in this fashion to minimize the interfacial energy between the water and the air phases.

43. Clark, T., Jr.; Ruiz, J. D.; Fan, H.; Brinker, C. J.; Swanson, B. I.; Parikh, A. N. *Chem. Mater.* **2000**, *12*, 3879–3884.

44. Hozumi, A.; Yokogawa, Y.; Kameyama, T.; Hiraku, K.; Sugimura, H.; Takai, O.; Okido, M. *Adv. Mater.* **2000**, *12*, 985–987.

45. All separation distances quoted in this work must also take into account an additional 3 cm of separation (i.e. the minimum distance allowed between the sample mount and the UV lamp in the instrument) in order to obtain the 'absolute' separation distance.

46. Alternatively, the dense, cross-linked, aromatic polyimide layer may be more difficult to remove from the films by UV / ozone treatment under these conditions and relatively short exposure timeframes in comparison to the alkyl moieties of the as-synthesized materials. In this case, removal of the alkyl moieties may actually be complete while the polyimide layer remains largely intact.

47. It should be noted that the characterization of films by other strategies such as solid state NMR is not always viable given the extremely low sample quantities obtained with film syntheses.

48. Yamashita, H.; Mori, K. *Chem. Lett.* **2007**, *36*, 348–353.

49. We also tried to incorporate **DO3** into the uniaxially-aligned ***C10***-based films after exposing them to UV / ozone (see Section 3.8.6), but without any conclusive success. The affinity of **DO3** molecules to occupy the internal pore volume may be relatively low. Furthermore, steric constraints may also be an issue in this passive, diffusion-based loading procedure.

50. Kuroda and co-workers have very recently reported the swelling of **C*6***, **C*10***, and **C*16*** bulk materials with 1,3,5-trialkylbenzenes such as TIPB, as well as *n*-alkanes

and *n*-alkyl alcohols. Interestingly, in their report, the addition of TIPB to the **C*6***-derived sol (which typically yields a 2D hexagonally-ordered material) led to the formation of a disordered material, while the addition of TIPB to the **C*10***-derived sol led to swollen 2D hexagonal mesostructures. On the other hand, upon adding *n*-alkyl alcohol swelling agents to the sols, the resulting **C*10***-derived products displayed lamellar mesostructures. Furthermore, in all cases, the **C*16*** materials remained lamellar in structure. For more details, see: Shimojima, A.; Sakurai, M.; Kuroda, K.; Okubo, T. *J. Colloid Interface Sci.* **2010**, *350*, 155–160.

51. (a) Uozumi, Y.; Hayashi, T. *J. Am. Chem. Soc.* **1991**, *131*, 9887–9888; (b) Uozumi, Y.; Kitayama, K.; Hayashi, T.; Fukuyo, E. *Bull. Chem. Soc. Jpn.* **1995**, *68*, 713–722.

52. Murakami, H.; Minami, T.; Ozawa, F. *J. Org. Chem.* **2004**, *69*, 4482–4486.

53. Motoyama, Y.; Abe, M.; Kamo, K.; Kosakoa Y.; Nagashima, H. *Chem. Commun.* **2008**, 5321–5323.

54. Shimojima, A.; Atsumi, N.; Umeda, N.; Fujimoto, Y; Kuroda, K. *J. Ceram. Soc. Jpn.* **2006**, *114*, 819–822.

55. Shimojima, A.; Goto, R.; Atsumi, N.; Kuroda, K. *Chem. Eur. J.* **2008**, *14*, 8500–8506.

Chapter 4

Probing Chiral Recognition in Chiral Binaphthalene-Based Periodic Mesoporous Organosilica Powders and Monoliths

4.1 Introduction

4.1.1 Periodic Mesoporous Organosilicas (PMOs)

From the preceding chapters, it may be appreciated that surfactant-templated and self-templating methodologies for synthesizing porous, ordered silica-based materials are incredibly versatile and may be readily modulated to allow access to a wide variety of different types of materials. However, it is not only the purely inorganic variants that are of great utility. Arguably, it is their tailored, organically-functionalized counterparts that more dramatically expand the range of materials that may be synthesized and implemented in advanced applications.[1,2,3,4]

As described previously, there are three main routes for introducing organic functionality into silica-based sol-gel materials: (i) post-synthetic grafting of organosilanes onto a pre-formed, solid support; (ii) co-condensation of polymerizable organosilane(s) with the inorganic precursor directly in the starting sol; and (iii) condensation of hybrid organic–inorganic precursors such as bridge-bonded silsesquioxanes in the starting sol.[1,2,3,4] It should be noted, of course, that these three routes may be used in various combinations (for example, condensation of bridge-bonded silanes alone or with an inorganic precursor to first form a periodic mesoporous organosilica (PMO) material that may then be further modified through the post-synthetic grafting of an additional functional group in a subsequent step) in order to arrive at a

material of targeted composition and applicability for a chosen task. In this chapter, these PMO-type materials are of particular interest.[1,3,4]

The syntheses of porous, hybrid organic–inorganic materials by a surfactant-templated sol-gel process to yield PMOs were first reported in 1999 by three independent research groups.[5,6,7] In these instances, the silsesquioxane monomers were either ethane-[5,6] or ethene-bridged[6,7] (see 1,2-bis(trimethoxysilyl)ethane (**BTMSE**), 1,2-bis(triethoxysilyl)ethane (**BTESE**), and 1,2-bis(triethoxysilyl)ethylene (**BTESEY**) in Scheme 4-1). However, it was really the reports by Inagaki and co-workers released in 2002 pertaining to the preparation of benzene- and biphenylene-bridged PMOs bearing molecular scale crystallinity in the walls of the materials[8] that fascinated us (1,4-bis(triethoxysilyl)benzene (**BTESB**) and 4,4'-bis(triethoxysilyl)-1,1'-biphenyl (**BTESBP**) in Scheme 4-1 and Figure 4-1).

These particular examples of benzene- and biphenylene-bridged materials were of heightened interest because, up until this point, surfactant-templated silica-based sol-gel materials had not been prepared with any significant degree of crystallinity in the framework. The periodicity and order present in the hitherto reported templated materials really only pertained to the pore-to-pore relationships. With these crystalline PMOs synthesized by Inagaki et al., the possibility of generating materials that could take advantage of this manifestation of close-range, intermolecular interactions – which were appealingly 'locked' in the solid state – in order to exploit or reveal additional physical and chemical properties on the bulk scale was now within closer reach. Furthermore, the idea of creating PMOs based on rigid chiral monomers was also an attractive venture.

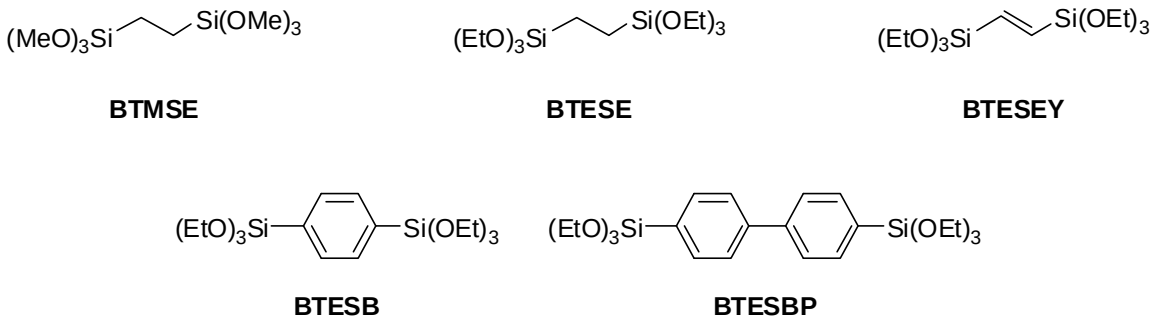

Scheme 4-1. Bis-silylated silsesquioxane monomers used in some of the first reported syntheses of PMO materials.

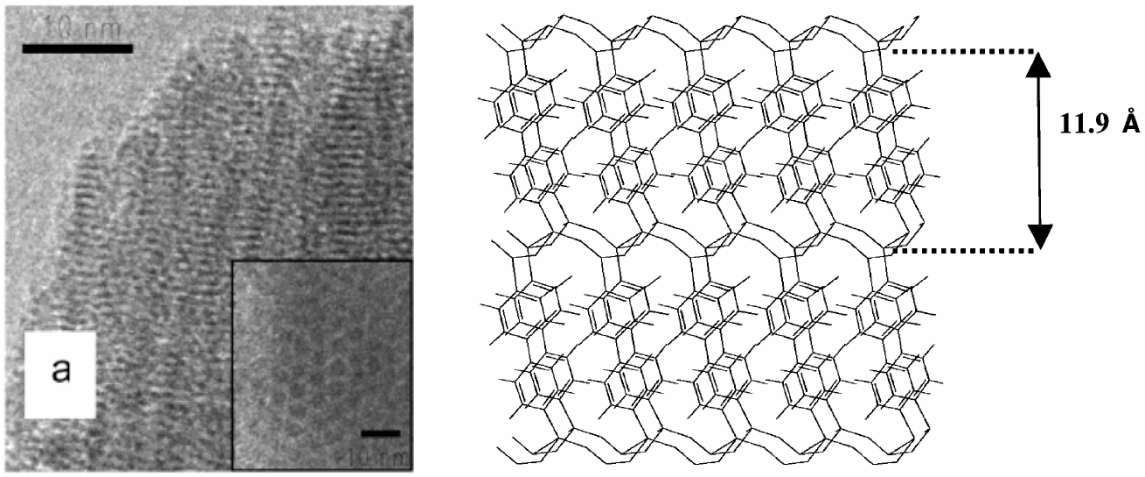

Figure 4-1. (a) TEM image of the porous, solvent-extracted biphenylene-bridged crystalline PMO material showing lattice fringes in the pore walls with a spacing of 11.6 Å, as well as a 2D hexagonal mesopore arrangement (inset). Scale bars = 10 nm. (b) COMPASS (Condensed-Phase Optimized Molecular Potentials for Atomistic Simulation Studies) force field-optimized structural model of the crystallinity within the walls of the mesoporous biphenylene-bridged PMO. (Both images taken from reference 8b.)

4.1.2 Chirality Transfer in PMOs

In the literature pertaining to the field of liquid crystals (LCs), it has been well-documented that the addition of a chiral dopant (i.e. a guest species), for example, into an achiral, nematic host LC induces the formation of a bulk, chiral mesophase in the host medium.[9,10,11,12] Importantly, therefore, under the appropriate conditions, a highly valuable or unique guest species may be used to impart selected properties to a host material that itself does not possess such characteristics.

Thus, we envisioned that silylated, axially chiral biarylene-derived dopants could be synthesized and condensed alone or with the biphenylene monomer (4,4'-bis(triethoxysilyl)-1,1'-biphenyl, **BTESBP**). The main goal of such a venture would be to try and establish a set of conditions whereby transfer of the chiral conformation of a given biarylene atropisomer to the dynamically racemic, unsubstituted biphenyl core of **BTESBP** might be possible in the solid state and also appropriately observed. If the bulk material could then be synthesized with molecular-scale crystallinity, the chiral conformation of the dopant monomer may potentially be translated through accumulative guest–host and host–host interactions to span throughout the entire framework over extended length scales.

Enabling the encoding of chiral information and / or chirality transfer in the solid-state would have important implications in fields such as heterogeneous asymmetric catalysis and chiral chromatography. As biaryl and binaphthyl motifs are frequently encountered in the backbones of many highly effective chiral ligands (for the most common examples, see **BINAP**, **QUINAP**, **BINOL**, and **BIPHEP** in Scheme 4-2,

below),[13,14] silylated versions of these axially chiral ligands could be employed as the dopants in a biphenylene-based host system to form functional PMO materials. In addition to providing heterogenized ligands for asymmetric chemical transformations, it was our hope that the chiral biaryl unit would interact with the biphenyl monomer that forms the bulk material. This interaction would then result in an enhanced and extended homochiral topography along the pore walls that could lead to dramatic improvements in the efficacy of these transformations in comparison to typical supported chiral ligands, where the microenvironment of the chiral ligand is disordered (for example, in the case of regular amorphous silica). Furthermore, the occurrence of significant chirality transfer within this type of a support material may perhaps then facilitate the use of only minor quantities of these typically costly chiral ligands without having to sacrifice asymmetric catalytic performance.

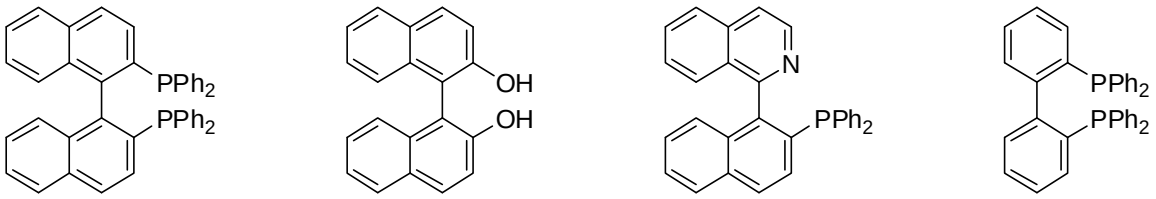

BINAP **BINOL** **QUINAP** **BIPHEP**

Scheme 4-2. Examples of binaphthyl-based ligands commonly used in metal-catalyzed asymmetric transformations.

A similar influence could also be postulated in the synthesis of materials as supports for chiral chromatography. Here, the separation and resolution of a pair of enantiomers depends on the formation of transient diastereomeric complexes between the analyte molecules of interest and a given chiral stationary phase (CSP).[15] Additionally, chiral cavities may also induce steric interactions of an enantioselective nature.[15,16] In the end, the summation of these diastereomeric interactions of relatively small differential energy over the total time spent by the analytes in the presence of the CSP leads to the separation of enantiomeric molecules. Therefore, the development of novel, chiral PMOs may not only contribute to the domain of chiral chromatography by providing new types of CSPs for use, but may also result in improvements in chiral chromatographic performance in light of their unique properties and potential for exhibiting enhanced functionality.

Our research group thus set out to explore the consequences of incorporating axially chiral biarylene monomers into biphenylene-based PMO materials. For a model compound, the tetra-*ortho*-substituted species **1** (Scheme 4-3) was chosen as the target chiral monomer and synthetic routes for preparing this monomer were painstakingly established and reported by us in 2006.[17] In the years that followed, a significant amount of effort was dedicated the synthesis of PMO-type materials composed of **1** and **BTESBP** as the 'guest' and 'host' components, respectively, and in 2008, the major findings from this work were reported. [18] Importantly, convincing evidence for the formation of chiral aggregates between **1** and **BTESBP** species in the condensed materials were

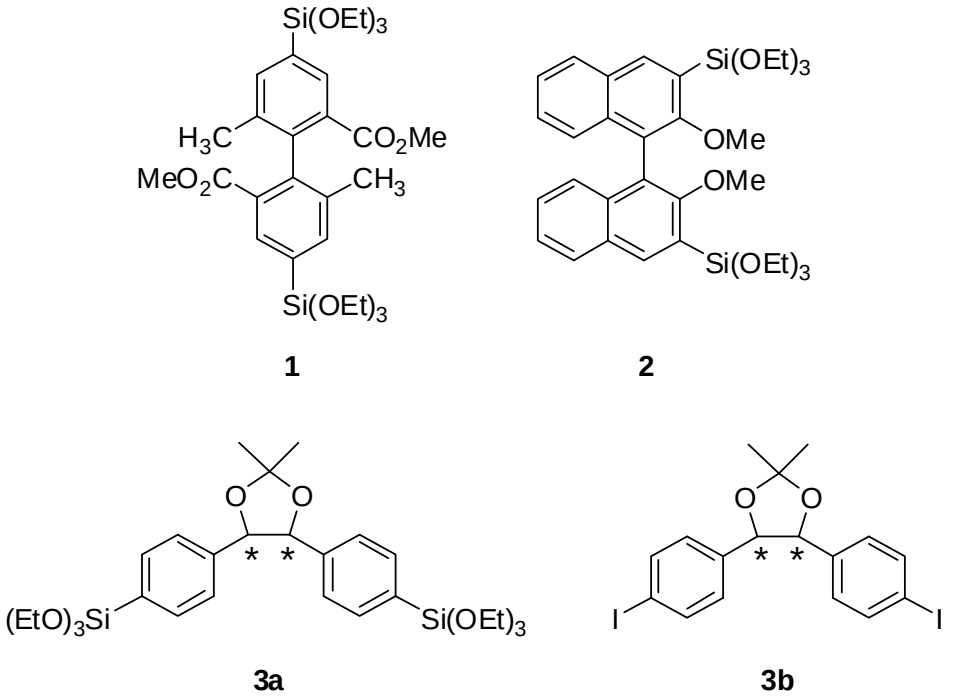

Scheme 4-3. Axially chiral, bis-silylated monomers designed by the Crudden research group (**1**, **2**, and **3a**). The chiral precursor to **3a** (**3b**) was used in this work as a test analyte for chiral capillary chromatography (chiral centers marked by *).

demonstrated via solid-state circular dichroism (CD) and further corroborated by computational models.[18]

From this success, the research in our laboratory has since taken off in a few different directions as we continue exploring alternative motifs for axially chiral monomers – in particular, those that more closely replicate ligands of interest to asymmetric catalysis. One of these motifs is based on the binaphthylene framework, which is considered to be a 'privileged' structure for chiral ligands (as can be seen above with **BINAP**, **BINOL**, and **QUINAP**, which are just a few select examples).[9b,9d,13a,19] In

addition to their well-documented ability to affect chirality transfer in various fashions,[9,13a,19] binaphthyl structures are typically much more easily prepared than related biphenyl monomers.[20]

Binaphthalene-based derivative **2** was designed by Crudden / Snieckus student, Tom Blackburn, using directed *ortho*-metalation (D*o*M) methodology to introduce the key silicon units for hydrolysis and condensation.[21] As published by Blackburn in his Master's thesis, after preparing enantiomerically pure chiral monomer **2**, he succeeded in preparing powdered, PMO materials incorporating monomer either the *rac*- (*R*)- or (*S*)-**2** monomer in varying amounts as a chiral dopant alongside **BTESBP** as the dynamically racemic host species. As in our previous report of employing chiral biphenyl derivative **1** as a guest species,[18] chirality transfer from the chiral monomer to the biphenylene host was observed by solid-state CD and supported by computational models.[21]

To take these materials beyond simply demonstrating yet another example of chirality transfer and to instead provide evidence for chiral recognition, we began an evaluation of these chiral PMO materials as chiral stationary phases for reverse phase nano-HPLC in collaboration with the research group of Prof. Richard D. Oleschuk (Queen's University). In the first instance, a bulk sol-gel material prepared using 100% *S*-**2** was packed into a fused silica capillary (internal diameter ($\emptyset_{ID}$) = 75 μm and length (L) ~ 9 cm) to affect the enantiomeric separation of a racemic mixture of **3b** (yet another chiral monomer motif explored by our group, which was synthesized by Dr. Steven Dickson).[22] It should be noted that a material synthesized using only the chiral silane was employed in these preliminary chromatography trials since it was believed that this would

provide maximum interaction with the chiral analyte. After optimizing the conditions with this material, we planned to proceed to chiral materials prepared from dopant / host mixtures.

Encouragingly, some separation of the racemate of **3b** was detected.[23,24] Unfortunately, however, the resolution of the two corresponding enantiomeric peaks was far from complete (see Figure 4-2).[25]

The main goal of chromatography is to achieve the highest possible resolution in the shortest possible time.[26] Specifically, column resolution (R_S) is related to the separation of two analytes (*A* and *B*), and may be quantitatively defined as:

$$R_S = \frac{2[(t_R)_B - (t_R)_A]}{W_A + W_B} \qquad \textbf{(4-1)}$$

where t_R is the retention time (i.e. time elapsed before reaching the detector at the exit of the column) for a given species (e.g. *A* or *B*, where species *A* elutes ahead of species *B*) and *W* is the width of the base of the peak (in units of time) corresponding to a given species. A resolution of 1.5 gives essentially gives complete separation of species *A* and *B* (i.e. peak overlap is ~ 0.3%), while smaller values of R_S imply worse peak separation (see Scheme 4-4).[26]

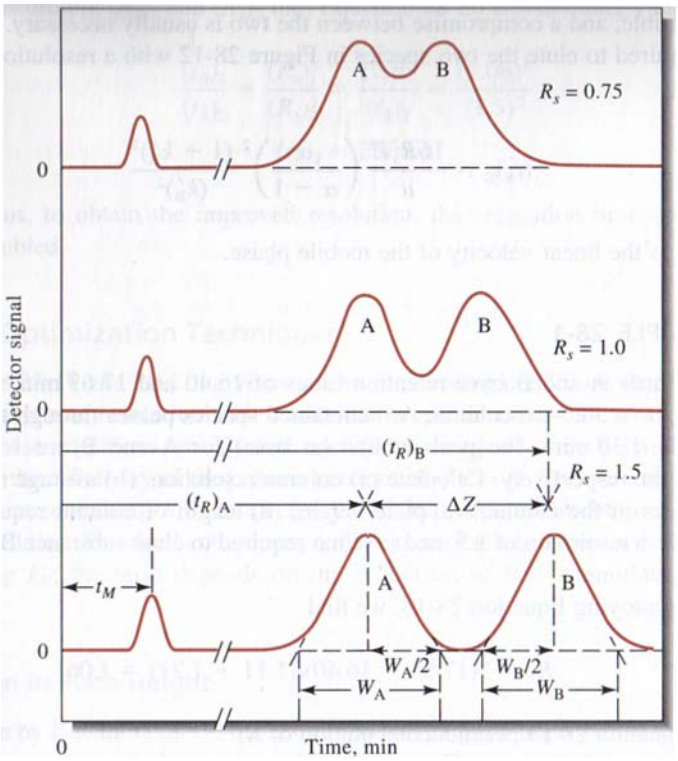

Scheme 4-4. Schematic representation of the separation of two peaks (species A and B) at three different resolutions (R_S) and the corresponding chromatographic parameters included in the calculation of R_S. (Scheme taken from reference 26.)

Column resolution may also be related to other parameters that are commonly used to describe column efficiency – namely, the number of theoretical plates (N) and plate height (H) – by the following relationships:[26]

$$R_S = \frac{\sqrt{N}}{4}\left(\frac{\alpha - 1}{\alpha}\right)\left(\frac{k'_B}{1 + k'_B}\right) \qquad \textbf{(4-2)}$$

where α is the selectivity factor and is defined as a ratio of the partition coefficients (K) for species A and B:

$$\alpha = \frac{K_B}{K_A} = \frac{(t_R)_B - t_M}{(t_R)_A - t_M} \qquad \textbf{(4-3)} \text{ and } \textbf{(4-4)}$$

and t_M is the elution time for a species that is not retained on the column (i.e. 'dead time') (which provides a measure of the average rate of migration of the mobile phase). Also, k'_B is the capacity factor for species B (i.e. indicative of the migrate rate of the solute along the column), which is defined as:

$$k'_B = \frac{(t_R)_B - t_M}{t_M} \qquad \textbf{(4-5)}$$

Finally, the plate height, H, and the number of theoretical plates, N, are related by:

$$N = \frac{L}{H} \qquad \textbf{(4-6)}$$

where L is the length of the column. Alternatively, N may be obtained by the following relationship:

$$N = 8\ln(2)\left(\frac{t_R}{W_{FWHM}}\right)^2 \quad \text{or} \quad = 16\left(\frac{t_R}{W}\right)^2 \qquad \textbf{(4-7)} \text{ and } \textbf{(4-8)}$$

where W_{FWHM} is the peak width at half-maximum. In summary, to achieve high resolution, the column and operating conditions of interest will correspondingly have a high value for the number of theoretical plates per unit length of the column and a small plate height.[26]

Additionally, column efficiency may be related to the flow processes within the column by the van Deemter equation, which is expressed as:

$$H = A + \frac{B}{u} + C \cdot u \qquad \textbf{(4-9)}$$

where A, B, and C are constants relating to eddy diffusion, longitudinal diffusion, and resistance to mass transfer, respectively, and u is the linear velocity of the mobile phase:[26]

$$u = \frac{L}{t_M} \qquad \textbf{(4-10)}$$

Importantly, the A term of the van Deemter equation relates to the multiple flow paths through the column bed, and is affected by:[27]

- particle size
- particle shape and uniformity
- particle pore shape / structure
- quality of the packing
- wall effects (e.g. material, roughness, and column diameter)

The objective, then, is to minimize the number of errant paths through the column so as to minimize band broadening at the exit of the column.

For our materials tested to this point (i.e. bulk, chiral PMO powders packed into capillary columns), the factors listed above are of greatest influence on our column efficiency and chromatographic performance. Upon examination of the 100% *S*-**2** material by FE-SEM, it became glaringly apparent that the morphology of this bulk

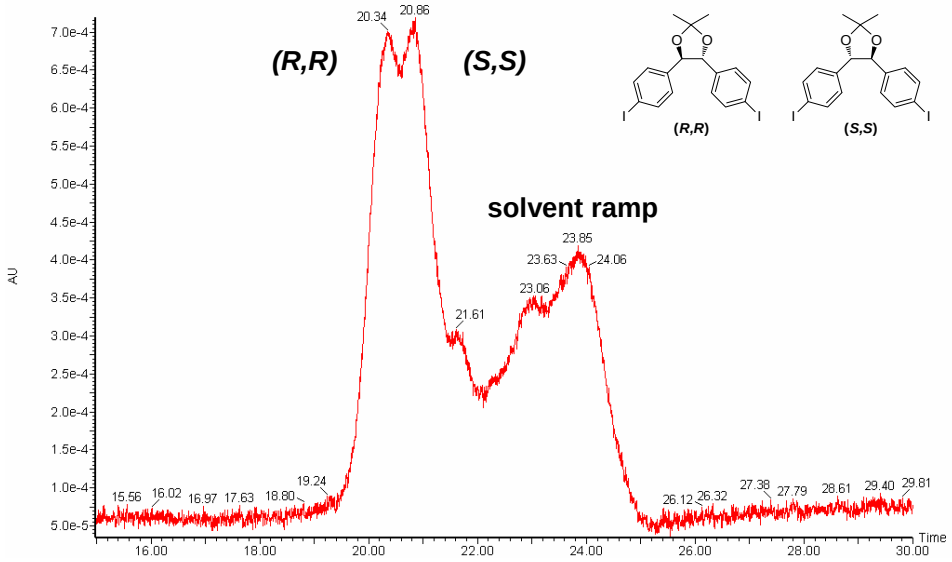

Figure 4-2. Reverse phase nano-HPLC chromatograph for the gradient elution of *R,R*- and *S,S*-**3b** on a capillary column packed with 100% *S*-**2** PMO powder (data provided by Dr. Graham Gibson, Queen's University).

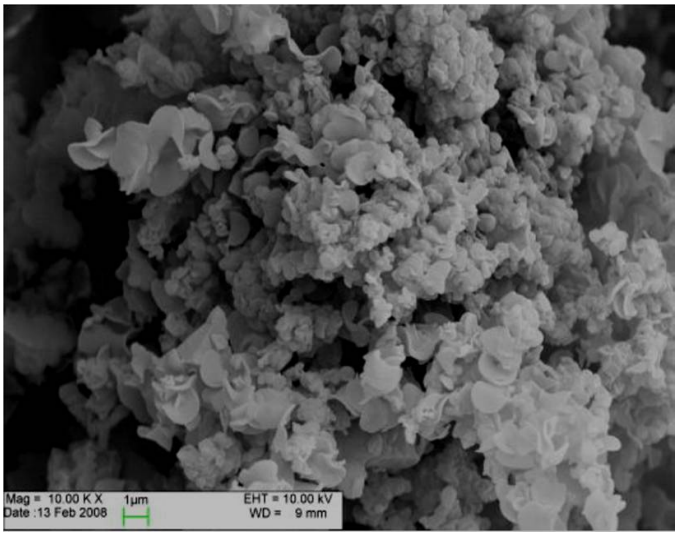

Figure 4-3. FE-SEM image showing the morphology of the 100% *S*-**2** PMO material (image taken from reference 21).

material was not suitable for packing into column form (see Figure 4-3), and that a different morphology would have to be explored for future demonstrations of chiral separations.

Dr. Xiaowei Wu (Queen's University) had explored the possibility of synthesizing chiral PMO powders (incorporating **2** as the chiral monomer) with spherical morphology. Although she was successful in synthesizing spherical materials, the particles that she obtained were too small (particle diameter ~ 1 μm) and upon packing the materials into a capillary, the resulting back pressure was too high to allow for any flow to be established along the column bed.

In related work, Dr. Steven Dickson (Queen's University) had tried to silylate the surface of commercially-available, monodisperse silica spheres with his chiral monomer (**3a**) to prepare CSPs that would be suitable for the separation of other chiral analytes. However, upon packing that material into a capillary column and conducting nano-HPLC trials, it appeared as though significant leaching of his chiral monomer was occurring off the column bed – making it difficult to evaluate the chromatographic performance of this material.[28]

A few other parameters such as column length, mobile phase flow rate, and isocratic versus gradient elution protocols were also adjusted to improve upon the nano-HPLC performance with Blackburn's original chiral PMO-packed columns. However, each modification came with a given cost (e.g. increased run times, decreased peak separation, and so forth) and, in the end, the modifications were not enough to overcome

the deficiencies posed by the material morphology.[29] Thus, monolithic morphologies were considered as interesting and promising options.

4.1.3 Monoliths and Capillary Chromatography

As reported extensively by Nakanishi and others, silica and organosilica monoliths characterized by both macro- and mesoporosity have significant promise in the field of chromatography.[30] Under carefully controlled conditions, monoliths can be prepared that exhibit excellent flow-through properties, which improve the performance and efficiency of chromatographic separations in comparison to conventional, packed particle beds.[30,31] Specifically, these monolithic columns resolve analytes as well as standard columns packed with 5 μm-diameter silica particles, but can do so in half the time with half the column back pressure.[30c,32] In fact, these silica-based monoliths have been developed, optimized, and proven to such an extent that they have been commercially available since 2001 under the name Chromolith® (Merck).[31,32] Furthermore, these monoliths may also be prepared within fused silica capillaries (see the example of a typical cross-sectional SEM image shown in Figure 4-4),[30c,33] and thus may be applied to small-scale separations as well, which is of particular interest to a growing number of chemists since it minimizes the amount of analyte that needs to be employed.

These monoliths are prepared by sol-gel chemistry. The characteristic co-continuous structure consisting of interpenetrating porous and skeletal networks is achieved through uniform phase separation of the solid and solvent phases via spinodal

decomposition with concomitant gelation of the solid phase.[30,34] Subsequent drying of the monolithic structures reveals the integral porous network. As we have seen with other materials prepared in this thesis, a templating agent such as a nonionic polymer or block copolymer is added to the sol. However, this species is not added solely as a mesostructuring agent, but rather as a component that modulates the solubility of the developing silica-based matrix with respect to the solvent media and arrests premature gel formation to allow for progressive coarsening of the silica phase prior to phase separation.[30,33,34]

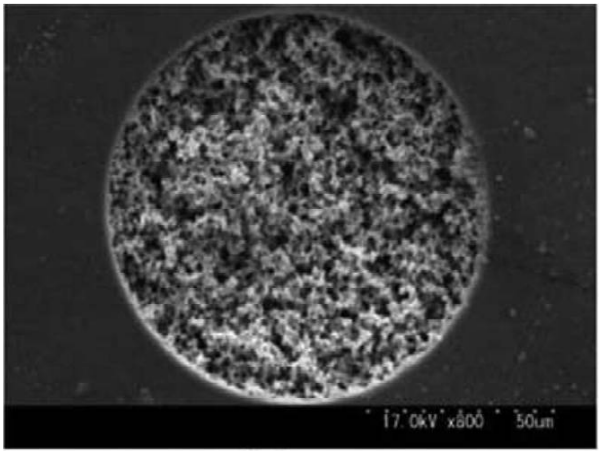

Figure 4-4. Cross-sectional SEM image of a monolith prepared from a equimolar mixture of methytrimethoxysilane and tetramethoxysilane inside of a 100 μm-diameter fused silica capillary. (Image taken from reference 33.)

For the most part, monoliths and capillary monoliths have largely been explored using TMOS (tetramethoxysilane, $Si(OMe)_4$) or TEOS (tetraethoxysilane, $Si(OEt)_4$) as the condensable silica precursors with functionalization of these silica monoliths to provide organically-modified derivatives achieved by post-synthetic grafting of the desired organic moieties onto the pre-formed silica columns. Only in more recent years have reports describing the use of organotrialkoxysilanes and silsesquioxane precursors to form such co-continuous monoliths appeared. The first examples involved monomers such as methyltrimethoxysilane (**MTMS**), vinyltrimethoxysilane (**VTMS**), allyltrimethoxysilane (**ATMS**), 1,1-bis(trimethoxysilyl) methane (**BTMSM**), 1,2-bis(trimethoxysilyl)ethane (**BTMSE**), 1,3-bis(trimethoxysilyl)propane (**BTMSP**), and 1,6-bis(trimethoxysilyl)hexane (**BTMSH**) (Scheme 4-5).[33,35]

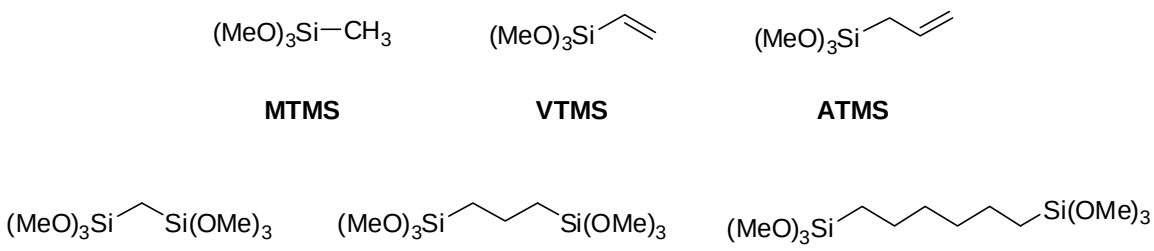

Scheme 4-5. Organosilane precursors used in some of the first examples of monolithic organosilica materials prepared by spinodal decomposition (i.e. polymerization-induced phase separation).

Notably, in 2009 and 2010, the syntheses of porous, co-continuous monoliths from 1,4-bis(triethoxysilyl)benzene (**BTESB**)[36] and 4,4'-bis(triethoxysilyl)-1,1'-biphenyl (**BTESBP**)[37] monomers were demonstrated, respectively, which are of significant interest to us. In these reports, Nakanishi and co-workers prepared bulk organosilica monoliths that were later converted to porous silicon carbide (SiC) ceramics by carbothermal reduction. Our objective was instead to adapt the synthesis of the biphenylene-bridged PMO monolith to yield the corresponding PMO capillary monoliths, and then extend the capillary monolith synthesis to incorporate the chiral binaphthyl monomer, **2**. We hypothesized that these PMO capillary monoliths would be a more appropriate alternative to the powdered PMO materials of the previous section for the demonstration of chiral separation. In addition to possessing more favourable flow-through characteristics typical of such co-continuous materials, the synthesis of capillary monoliths would require only very small amounts of our precious chiral monomers and would simultaneously open the doors to the exploration of interesting aspects of device miniaturization for microfluidic applications of chromatography and flow catalysis.

4.2 Biphenylene-Based PMO Capillary Monoliths

Before preparing chiral variants of the PMO capillary monoliths, we first prepared capillary monoliths using 100% of the biphenylene precursor in order to better understand the sensitivity of the system to various synthetic parameters. In parallel to the procedures previously reported by Nakanishi and co-workers,[37] the PMO-type capillary

monolith system of interest, here, was composed of **BTESBP** as the condensable silane, Pluronic® F127 as the templating agent, dimethylacetamide (DMA) as the solvent, and 1 M aqueous nitric acid as the catalyst for hydrolysis and siloxane condensation. As this system has previously been reported to be quite sensitive to the amount of water present, the molar ratio of water to silane was maintained at H_2O : **BTESBP** = 6.3 : 1.0.[37] We henceforth chose to initiate our investigations with the exploration of the effects of changing the template-to-silane ratio and the solvent fraction for reactions conducted on a 0.22 mmol **BTESBP** scale (which corresponds to 105 mg or 0.10 mL **BTESBP** and 0.025 mL of 1 M $HNO_{3(aq)}$) at a gelation temperature of 60 °C. It should also be noted that all of the starting sols are homogeneous and transparent in appearance prior injection of the sols into fused silica capillaries of 100 μm-internal diameter (ID) and subsequent phase separation / gelation of the organosilica species.

Importantly, though, prior to our systematic studies regarding F127 and solvent content, it was discovered that sol composition alone was not sufficient to guarantee the formation of a co-continuous structure with the targeted textural properties (a desirable combination of skeleton thickness and pore diameter[38] may be see in Figure 4-5, bottom left) (pore size = 3.8 μm; skeleton thickness = 2.2 μm). As illustrated by the composite image of cross-sectional SEM images for four different capillary PMO monoliths formed using the same starting sol composition in Figure 4-5, the structural evolution of the co-continuous monoliths is sensitive to the timing of the pre-mixing steps, as well as the precision and uniformity of the temperature control within a convection oven in comparison to a conventional oven or water bath.[39] In response to this finding, we

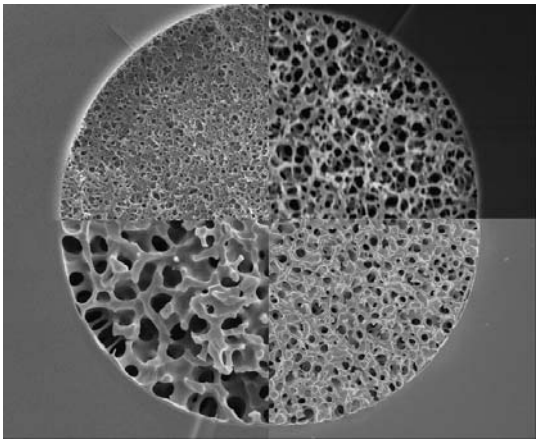

Figure 4-5. Composite cross-sectional SEM images of four different capillary monoliths bearing co-continuous structures prepared with the same sol composition, but with different reaction times. The desired skeletal structure for this work is shown in the bottom left quadrant. All monoliths were prepared in capillaries that were 100 μm in diameter.

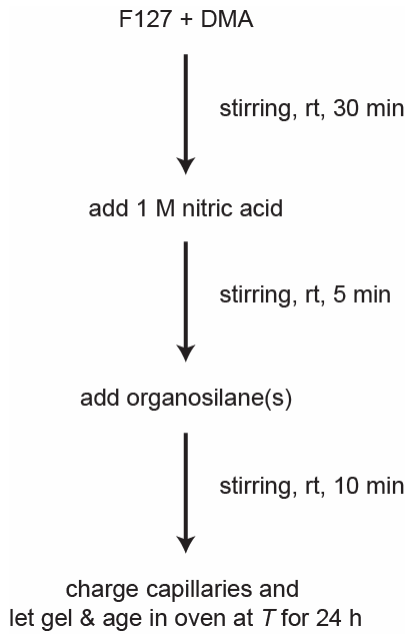

Scheme 4-6. Protocol and timing of individual steps in the synthesis of PMO capillary monoliths.

established a standardized procedure for capillary PMO monolith synthesis (outlined in Scheme 4-6), which was followed for all proceeding experiments.

Specifically, F127 is solubilized in DMA with short burst of heat from a heat gun and gentle shaking,[40] and then left to stir at room temperature at ~ 600 rpm for 30 minutes.[41] 1 M $HNO_{3(aq)}$ is next added to the mixture and stirred for 5 minutes at room temperature prior to adding the condensable silane(s). The resulting sol is then left to stir at room temperature for an additional 10 minutes before charging a fused silica capillary[42] and placing the sample into a digitally-controlled convection oven[43] (T = 60 °C) where the sol is left to gel and age for a total of 24 h.[44]

For our first study, the mass ratio of F127 : **BTESBP** was varied from 0.48–0.67 : 1.0, respectively, and the effect of the F127 content on the resulting structure of the capillary monoliths was evaluated by SEM. The final sol compositions are summarized in Table 4-1 (entries 1–5) and depicted in the ternary phase diagram of Scheme 4-7. As can be seen by the SEM images in Figure 4-6 and the corresponding phase diagram (Scheme 4-7), the skeletal structure of the capillary monoliths is extremely sensitive to F127 content. At the lower end of the range of F127 mass fractions explored, the formation of a porous, co-continuous structure with small pores and a fine skeleton is observed (Figure 4-6a). Notably, the thickness of the organosilica skeleton increases with progressively increasing F127 content, and is accompanied by the formation of relatively larger diameter macropores (Figure 4-6, b and c). With an even greater amount of F127 in the starting sol, the formation of a particulate aggregate occurs (Figure 4-6d).

Table 4-1. Summary of sol compositions and resultant structures of 100% **BTESBP**-based capillary PMO monoliths (prepared inside 100 μm-ID fused silica capillaries at T_{gel} = 60 °C).

Entry	Volume of BTESBP [mL][a]	Mass of F127 [g][a]	Volume of DMA [mL][a]	Avg. Macropore Diameter [μm][b]	Avg. Skeleton Thickness [μm][b]	Ratio of Pore Size / Skeleton Size	Resultant Structure
1	0.10	0.050	0.40	1.1	0.38	2.9	co-continuous
2	0.10	0.055	0.40	3.9	1.5	2.6	co-continuous
3	0.10	0.060	0.40	12.4	5.2	2.4	co-continuous
4	0.10	0.065	0.40	N / A	4.8[c]	N / A	nanoparticulate aggregate
5	0.10	0.070	0.40	N / A	5.0[c]	N / A	nanoparticulate aggregate
6	0.10	0.055	0.20	N / A	N / A	N / A	non-porous / nanoporous gel
7	0.10	0.055	0.30	2.3	1.0	2.3	co-continuous
8	0.10	0.055	0.40	3.0	1.1	2.7	co-continuous
9	0.10	0.055	0.50	1.2	0.51	2.4	co-continuous
10	0.10	0.055	0.70	N / A	N / A	N / A	non-porous / nanoporous gel

[a] – Quantity of a given reagent used in a sol containing 0.025 mL of 1 M $HNO_{3(aq)}$ as the catalyst for silane hydrolysis and condensation. [b] – Macropore diameter and skeleton thickness each determined as an average of measurements at 6 different points within a cross-sectional SEM image of a given sample. [c] – Average diameter of nanoparticle.

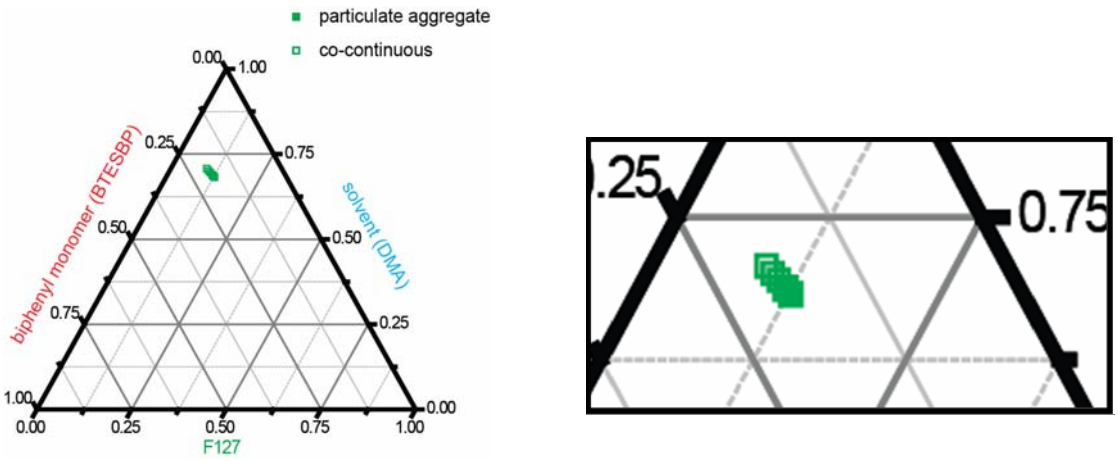

Scheme 4-7. Ternary phase diagram (left) (with 0.025 mL of 1 M $HNO_{3(aq)}$ as a constant across all sols) showing the variation in the F127 content. An enlarged image of the data points is also shown (right).

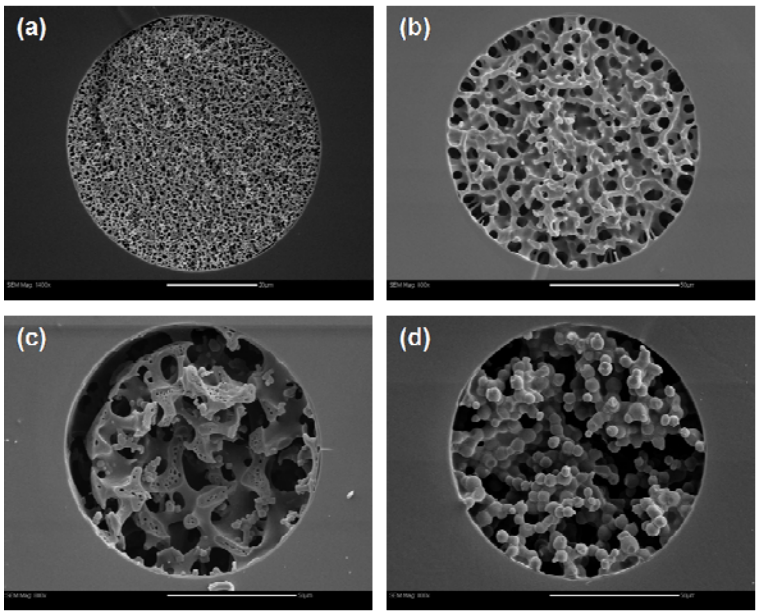

Figure 4-6. Cross-sectional SEM images showing the structural variations of 100% **BTESBP**-based PMO capillary monoliths with 0.10 mL of **BTESBP**, 0.40 mL of DMA, 0.025 mL of 1 $HNO_{3(aq)}$, and (a) 0.050 g, (b) 0.055 g, (c) 0.060 g, and (d) 0.070 g of F127 (all capillaries are 100 μm in diameter).

Finally, if the F127 content is augmented further, a non-porous / nanoporous phase is obtained once more, and eventually gelation is suppressed altogether.

As briefly mentioned before, this trend may be attributed to the role of F127 as an agent that modulates the solubility of the growing solid, organosilica phase in the sol. In the absence of any F127 in the reacting sol, only a transparent organosilica gel is produced, which is due to the lack of formation of a coarse and phase-separated skeleton. By associating with the hydrolyzed organosilane monomers and the growing siloxane network through hydrogen bonding, the F127 modulates the interfacial interactions between the organosilica and the solvent phase such that the rate of formation of an extended spanning cluster (i.e. the requisite condition for the formation of a gel) is suppressed. Consequently, this prolongs the time period within which coarsening of the organosilica skeleton may occur to successfully yield a uniform, co-continuous structure once phase separation and concomitant gelation eventually occur. It may thus be reasoned that at low F127 mass fractions, there is insufficient F127 in the sol to overcome the tendency for gelation of a dense organosilica phase.[45] In contrast, at high F127 mass fractions, only a weakly gelled monolith is formed. At more elevated F127 mass fractions, the organosilane monomers are now so well-solubilized in sol that even gelation is completely repressed. Therefore, under the conditions explored by us, there exists a relatively narrow range of ideal compositions within which the desired co-continuous structure may be obtained (i.e. F127 = 5–6 wt% of the total sol consisting of organosilane, solvent, and aqueous acid for spinodal decomposition at 60 °C).

The next parameter studied was the solvent fraction of the starting sols. The corresponding sol compositions are summarized in Table 4-1 (entries 6–10) and Scheme 4-8. Not surprisingly, there is an optimal solvent fraction wherein a co-continuous structure may be formed (see the cross-sectional SEM images in Figure 4-7). With the amount of 1 M $HNO_{3(aq)}$ constant from one formulation to the next, condensation of the organosilanes may be expected to proceed quickly to yield a non-porous / nanoporous monolith at low solvent fractions (Figure 4-7a). Under dilute conditions the solvent phase dominates in volumetric occupancy over the forming solid phase, which again prevents the formation of a uniform and phase-balanced co-continuous structure (Figure 4-7d). At intermediate solvent content, however, a co-continuous structure may be

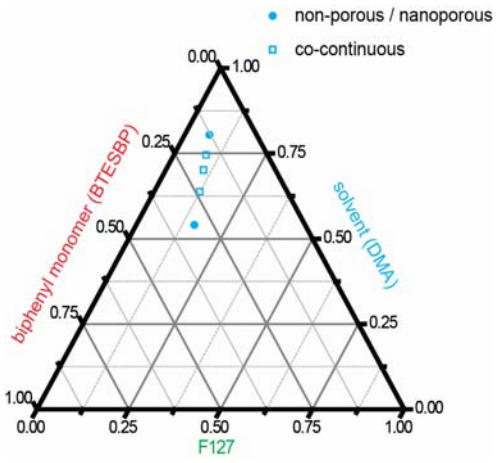

Scheme 4-8. Ternary phase diagram (with 0.025 mL of 1 M $HNO_{3(aq)}$ as a constant across all sols) showing the variation in the solvent (i.e. DMA) content.

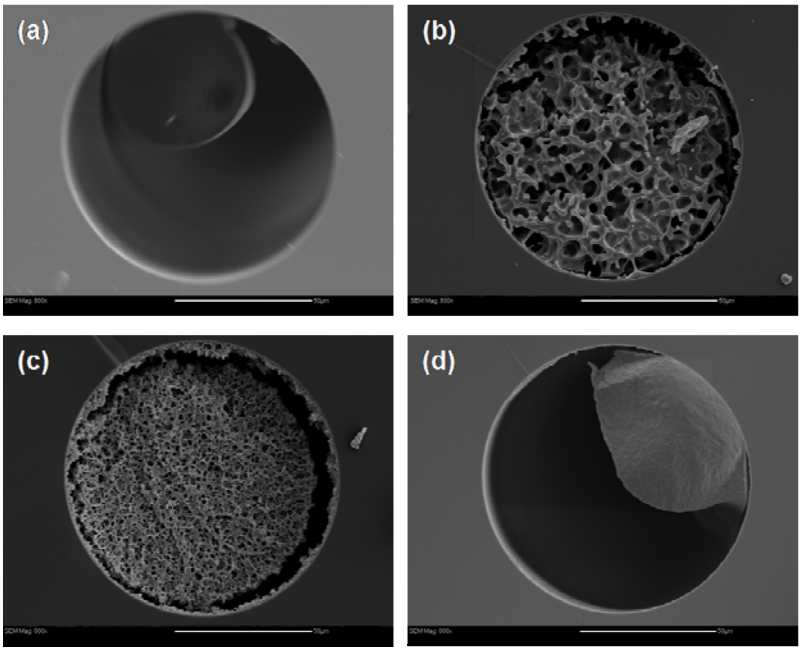

Figure 4-7. Cross-sectional SEM images showing the structural variations of 100% **BTESBP**-based PMO capillary monoliths with 0.10 mL of **BTESBP**, 0.055 g of F127, 0.025 mL of 1 $HNO_{3(aq)}$, and (a) 0.20 mL, (b) 0.30 mL, (c) 0.50 mL, and (d) 0.70 mL of DMA (all capillaries are 100 μm in diameter).

obtained, and the size and volumetric fraction of the resultant pores may be somewhat tuned by varying the amount of solvent present in the starting sol (Figure 4-7, b and c).

In addition to the trends identified above, a particularly interesting finding from our SEM observations was that the degree of drying-induced shrinkage of the as-synthesized capillary monolith appeared to correlate with the structure formed. In general, capillary PMO monoliths that possessed a co-continuous porous structure were better able to resist the interfacial stresses induced by drying of the monolith. This resulted in monoliths that exhibited dramatically reduced shrinkage in comparison to

their non-porous / nanoporous counterparts (for example, see Figure 4-7 'b' and 'c' in comparison to 'a' and 'd', respectively). Furthermore, to a certain extent, co-continuous structures bearing a thicker organosilica skeleton and larger diameter pores withstood monolith shrinkage to an even greater degree than those with finer skeletons and smaller pore openings.

Having gained a handle on the sensitivity of this system to various parameters, co-continuous, biphenylene-bridged, capillary organosilica monoliths with the desired textural characteristics could be reliably produced. The next step was then to introduce the chiral monomer, **2**, into this **BTESBP**-based system so as to obtain porous, chiral, organosilica capillary monoliths that could be applied to chiral chromatography.

4.3 Chiral Binaphthylene-Doped PMO Capillary Monoliths

Using our optimized sol composition and procedure from Section 4.2 for synthesizing 100% biphenylene-based capillary monoliths as a starting point, we tried to prepare a **BTESBP**-based capillary monolith constituting 13 wt% of a racemic mixture of our chiral binaphthyl monomer, **2** (i.e. *rac*-**2**).[46] Unfortunately, no co-continuous structure was observed under these conditions – only a non-porous / nanoporous monolith was obtained. Based on the previous experience of Blackburn in his syntheses of chiral, powdered PMO materials, this chiral monomer hydrolyzes and condenses even more quickly than **BTESBP**. With this in mind, one may comprehend the formation of a non-porous / nanoporous structure upon co-condensation of **2** and **BTESBP** under conditions

that have been optimized for obtaining co-continuous capillary monoliths using **BTESBP** alone.

In an attempt to more strongly favour co-continuous network formation, the F127 content was increased relative to **2** content to decrease the rate of sol gelation and promote increased coarsening of the siloxane phase (as experienced from our trials involving the 100% **BTESBP** systems previously discussed in Section 4.2).[47] As evidenced by the series of SEM images in Figure 4-8, the amount of F127 incorporated in the starting sol could indeed be increased to a point where co-continuous structure formation could be re-established.

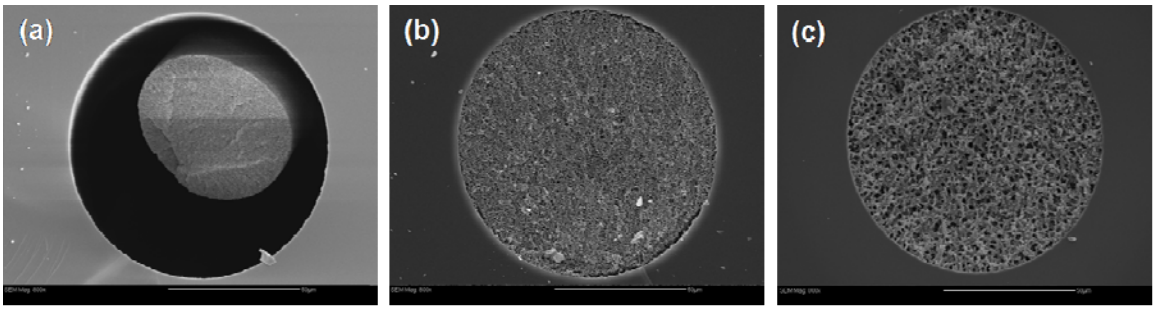

Figure 4-8. Cross-sectional SEM images showing the structural variations of PMO capillary monoliths containing 13 wt% chiral binaphthyl monomer (**2**) with F127 : **2** mass ratios of (a) 3.9 : 1.0, (b) 6.3 : 1.0, and (c) 7.9 : 1.0 (in 0.40 mL of DMA and 0.025 mL of 1 $HNO_{3(aq)}$) (all capillaries are 100 μm in diameter).

4.4 Problems with Capillary PMO Monolith Stability in Solution

Given that the F127 block copolymer was still present in these seemingly porous materials, a handful of co-continuous capillary monoliths (both of 100% **BTESBP** and *rac*-, *R*-, or *S*-**2**–**BTESBP** compositions) were subjected to solvent extraction with either water, acetone, or ethanol under conditions of flow (realized with an HPLC pump).[48] Unfortunately, the monolithic structures did not withstand exposure to any of these solvents. Often, solvent flow with a reasonable back pressure (up to ~ 1000 psig) could be established for a short time (< 1–2 h). However, with prolonged exposure times, the back pressure would slowly decrease. Examination of various segments of these solvent-exposed capillary PMO monoliths by SEM showed that the original co-continuous structures were maintained to a certain degree, but critically, the monoliths had shrunk / collapsed to a significant degree (see Figure 4-9). Not surprisingly, then, this catastrophic 'pull-away' of the monolith from the internal capillaries walls would be expected to compromise the ability of such materials to allow for the build-up of any fluid pressure.

A few other extreme cases have also been encountered. Occasionally, after an extreme build-up of initial column back pressure (up to ~ 5000 psig), an apparent break-through of the flowing solution would occur in concert with a sudden and dramatic decrease in the measured column back pressure to negligible levels (i.e. only tens of psig). On the other hand, we have also experienced a few select occurrences whereby no back pressure could be measured with the columns at all. Upon inspection of the exit of

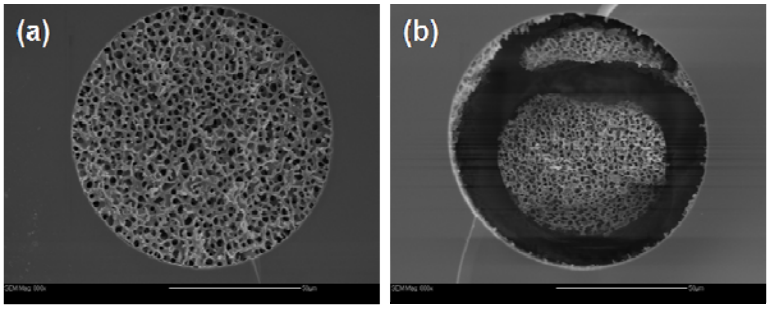

Figure 4-9. Cross-sectional SEM images showing the structural variations of 100% **BTESBP**-based PMO capillary monoliths (a) before (i.e. as-synthesized) and (b) after exposure to ethanol (both capillaries are 100 μm in diameter).

those columns, a thread-like portion of the capillary monolith could sometimes be seen essentially extruded from the capillaries. Regardless of the mode of failure, in all of these cases there was no doubt that the integrity of the capillary monolith columns was completely compromised, making these particular samples inappropriate for further testing.

It was hypothesized that exposure of these as-synthesized monoliths to aqueous solvent systems employed during both solvent extraction of the F127 template as well as during chromatographic trials could cause the monolith to shrink by promoting further silanol condensation within the organosilica phase. This is especially true given the notoriety of acid-catalyzed silica sol-gel systems to generally exhibit low degrees of siloxane condensation (particularly in the as-synthesized state).[49] This was corroborated by solid state ^{29}Si CP MAS NMR characterization of the corresponding bulk, as-synthesized, co-continuous 100% **BTESBP** monoliths obtained from phase separation and gelation of the sols that remained after charging the capillaries, which demonstrated

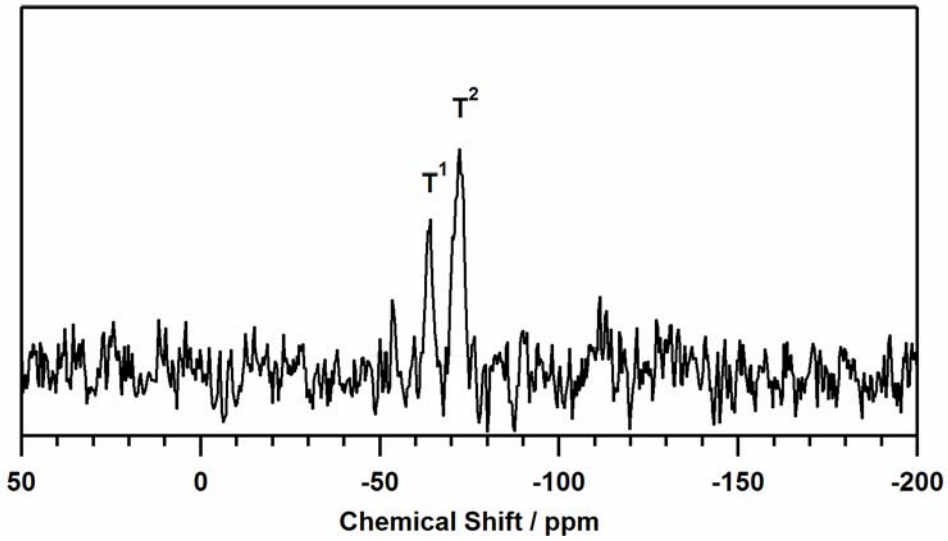

Figure 4-10. ^{29}Si CP MAS (solid-state) NMR of a 100% **BTESBP**-based bulk PMO monolith obtained from the leftover sol of a corresponding capillary monolith – prepared and treated under equivalent conditions.

the presence of mainly incompletely condensed T^1 and T^2 siloxane species (δ = –64.4 and –72.3 ppm, respectively) (see Figure 4-10). Further efforts to improve the integrity of the organosilica skeleton were necessarily pursued. Those strategies and corresponding outcomes are discussed in greater detail in Section 4.6, below.

Despite the unsuccessful attempts to reliably remove the F127 from these materials, it was at least possible that mobile phase and analyte retention could be realized with an as-synthesized PMO capillary monolith. Importantly, the as-synthesized PMO capillary monolith would have to be subjected to the nano-HPLC conditions (i.e. conditioning with the mobile phase solvent system and subsequent analyte injection and elution) in a short timeframe to minimize catastrophic 'pull-away' of the monolith from

the capillary walls during a given HPLC trial. Therefore, with as-synthesized chiral binaphthyl-modified capillary PMO monoliths in hand, we nonetheless proceeded to investigate the application of these materials in chiral chromatography.

4.5 Nano-HPLC and Continued Problems with Capillary Monolith Shrinkage

To compare our monolithic materials to the packed columns prepared previously using powdered, chiral PMOs, we returned to reverse phase nano-HPLC as the chromatographic testing platform for the separation of our chiral acetals, **3b** (see Section 4.10.9 for details regarding the experimental conditions).

Using a chiral, PMO capillary monolith column (11 wt% *R*-**2**, with 1 μm-diameter pores and a 0.29 μm-thick skeleton) that had a co-continuous structure but which had also exhibited drying-induced shrinkage in our first nano-HPLC attempt (see Figure 4-11), an extremely broad peak (with no discernible enantiomeric resolution) was observed in the chromatographic trace (Figure 4-11, black trace) when a racemic mixture of **3b** was individually passed through the capillary column. This experiment was characterized by low back pressure ($< \sim 100$ psig), but this was expected given that the capillary monolith did not span the full diameter of the fused silica capillary tubing. However, upon injecting *R,R*-**3b** and *S,S*-**3b** separately into the capillary column in two separate subsequent runs, it appeared as though each of the enantiomers may have been retained differently on the column (with a separation of 0.5 minutes), indicative of chiral recognition (Figure 4-11, red and blue traces, respectively). These results suggested that

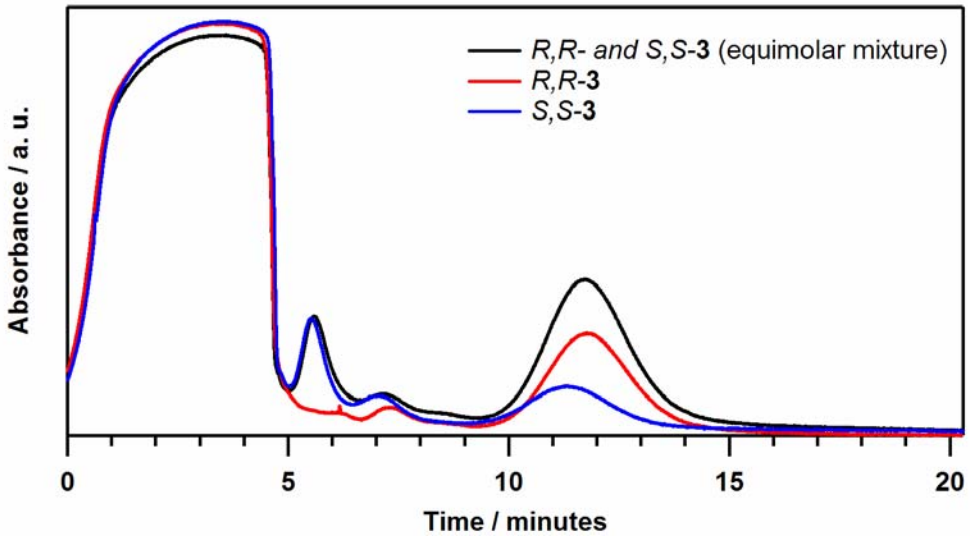

Figure 4-11. Reverse phase nano-HPLC chromatograph for the isocratic elution of *R,R*- and *S,S*-**3b** on a shrunken 11 wt% *R*-**2** PMO capillary monolith (data provided by Dr. Graham Gibson, Queen's University).

the enantiomeric separation of **3b** could be realized so long as the column efficiency could be increased to such a point that satisfactory peak resolution could be observed.[50] This would involve using a monolithic column that did not exhibit excessive sections of void space that would otherwise allow analytes to freely pass through the column without intimately interacting with the stationary phase.

Moreover, a comparison of Figure 4-2 and Figure 4-11 shows that chiral recognition is certainly expressed with this system involving species **2** and **3b** as switching from the *S*-**2** PMO to the *R*-**2**-functionalized PMO materials resulted in a reversal of the order of elution of *R,R*- and *S,S*-**3b**. Notably, the capillary monolith

showed chiral recognition by nano-HPLC using only an 11 wt% loading of the chiral binaphthyl monomer in the stationary phase, while no chiral recognition was observed using bulk powdered PMO materials prepared by Blackburn with 15 wt% of the chiral monomer. Interestingly, the challenge was not thus related to a lack of enantioselective interaction between the analytes and the chiral stationary phase, but rather one of morphological control and stabilization.

Another chiral, co-continuous, capillary PMO monolith (13 wt% *R*-**2**, with 1.7-μm diameter pores and a 0.51 μm-thick skeleton) was then subjected to nano-HPLC evaluation. Despite this capillary monolith demonstrating reasonably open porosity in the SEM images, including monolithic structures that completely spanned the diameter of the fused silica capillaries, the complications of an excessive build-up of back pressure followed by a sudden and relatively dramatic decrease in the measured column back pressure (as seen previously in Section 4.4) plagued us once more. In similar fashion to our previous experience involving solvent extraction of the as-synthesized capillary monoliths under conditions of flow, these capillary PMO monoliths, again, showed significant structural shrinkage and 'pull-away' from the internal capillary walls by SEM after solvent exposure. Without reinforcement of the condensed, organosiloxane phase to prevent such 'pull-away', chiral separation of any analytes would most likely not be possible by nano-HPLC.

4.6 Improving the Hydrolytic Stability of Capillary PMO Monoliths

A variety of different strategies were thus explored in an attempt to improve the hydrolytic stability of the capillary PMO monoliths with the goal of mitigating catastrophic monolith shrinkage and 'pull-away', which compromised the use of such materials in chromatographic applications. All of these strategies aimed to increase the degree of condensation of the organosiloxane phase – either after formation of the as-synthesized, co-continuous capillary monoliths or in-situ during monolith phase separation and gelation. Given the precious nature of the chiral monomer, **2**, these investigations were first pursued using 100% **BTESBP** systems to demonstrate the concepts.

Reports by Nakanishi and others have shown that the stiffness of TEOS-based bulk monoliths and capillary monoliths may be improved by either aging / hydrothermally treating the monoliths in a basic, aqueous solution of 1 M $NH_4OH_{(aq)}$[51] or 1 M urea[33,52] at 80–100 °C, or by dissolving urea into the starting sol[33,48,53] and then heating the resultant monoliths to 120 °C to create $NH_{3(aq)}$ from within the wet monoliths. In each of these instances, the condensed phase is exposed to a medium of elevated pH, which promotes further silanol condensation and coarsening of the siloxane network. However, given the incredible sensitivity of our capillary PMO monoliths to aqueous exposure, aging / hydrothermal treatment of the materials in basic solution did not result any improvements in the organosilica structure. In fact, only capillary monolith shrinkage and 'pull-away' were observed.

In terms of incorporating urea into the starting sol, we unfortunately could not succeed in obtaining any capillary monoliths that displayed a co-continuous structure in their as-synthesized state. Instead, non-porous / nanoporous structures were consistently obtained despite experimenting with different F127 mass fractions in these particular systems.

We postulated that presence of all of the sol reagents at a gelation temperature of 60 °C may cause even partial, premature decomposition of the urea into ammonia, which would then cause the pH to shift from its intended range and consequently change the structural evolution of the monoliths. The synthesis of 100% **BTESBP** capillary PMO monoliths was subsequently re-optimized for a gelation temperature of 40 °C in the absence of added urea, and a reagent composition was established that reliably allowed for the formation of a co-continuous monolith. However, upon re-introduction of urea into the newly optimized starting sol, only non-porous / nanoporous structures were, once more, obtained. By modifying the F127 content in these systems, a co-continuous structure was recovered. However, upon heating to 120 °C to decompose the urea and then subjecting the capillary monoliths to solvent exposure, no improvements in the hydrolytic stability were noted.

Next, we tried aging as-synthesized, co-continuous, 100% **BTESBP** capillary PMO monoliths in ethanolic solvents of progressively increasing aqueous content.[54] Starting from anhydrous ethanol and stepping down by 10 vol% increments in ethanol fraction to eventually reach 100% H_2O, a given aging solution was introduced into a particular capillary monolith by an HPLC pump and the monolith was left to 'soak' in the

aging solution for 2–12 h at 60 °C. The purpose of such a sequence of treatments was to progressively expose the capillary monoliths to increasingly aqueous conditions. In this way, the skeletal structure of the monoliths would be able to age more gradually and thus potentially better withstand the stresses on exerted on the organosilica framework due to unavoidable siloxane condensation, which would result in decreased monolith shrinkage. Unfortunately, this methodology did not prove to be effective for our materials as, once more, only capillary monolith shrinkage and 'pull-away' were observed.

Although these aforementioned treatment conditions have previously been shown to be successful in mitigating monolith shrinkage by others groups,[33,48,53] it should be noted that at least some degree of monolith shrinkage was *always* observed by these groups.[33,55] Furthermore, the majority of the successful cases have involved the minimization of monolith shrinkage in *bulk* systems. A workaround employed by many of these groups is the construction of HPLC instrumentation around a bulk monolith after it has been removed from its original mould and subjected to extensive aging and drying treatments.[30,31,56,57,58,59] This approach is obviously not an option with capillary monoliths systems. In fact, in order to render the original Chromolith® columns commercially viable, a specially-designed PEEK (polyether-ether-ketone) cladding had to be engineered that encased and protected the dry, bulk silica rods, which had been removed from their original mould.[30,31,56,57] Notably, this cladding layer was designed fit the monoliths, specifically accounting for the fact that the monoliths underwent post-synthetic shrinkage after monolith aging and drying. It was finally decided, then, that our

issues with capillary monolith shrinkage could not be overcome by any treatment process that would require post-synthetic solvent / solution exposure.

In a different route, we wanted to find a means of more strongly anchoring the body of the monolith to the internal walls of the capillary with the objective of minimizing capillary PMO monolith 'pull-away'. We first grafted the internal walls of the fused silica capillary with **γ-MAPS** (γ-methacryloxypropyltrimethoxysilane) – a monomer that self-crosslinks via thermally-induced radical polymerization.[60] Following surface activation of the capillary wall, a sol comprised of both **BTESBP** and **γ-MAPS** along with a radical initiator, VAZO® 88 (**V88**, 1,1′-azobis(cyclohexanecarbonitrile)) (see Scheme 4-9), was then charged into the capillary. Upon heating the sol, the ensuing thermal decomposition of **V88** was expected to initiate the radical polymerization of the methacrylate moieties of the **γ-MAPS** groups present in the mixture. Not only would crosslinking then occur across the body of the monolith itself, but presumably covalent

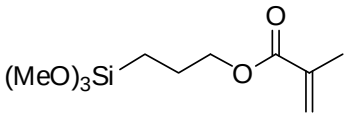

γ-MAPS

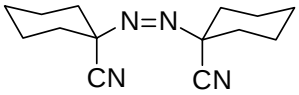

V88

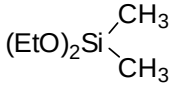

DMDES

Scheme 4-9. Auxiliary reagents added to the **BTESBP**-based PMO capillary monolith sols with the aim of minimizing monolith shrinkage (where **V88** is the radical initiator for the thermally-induced free radical polymerization of the methacrylate groups of **γ-MAPS**).

bonds between the monolith body and the **γ-MAPS**-functionalized capillary walls would also be formed.

Direct incorporation of **γ-MAPS** into our standard protocol for capillary monolith synthesis was conducted using 5, 10, and 20 mol% **γ-MAPS** (Si basis). At 5 mol% loading, a fine co-continuous structure was obtained (1.2 μm-diameter pores and a 0.39 μm-thick skeleton), but at 10 and 20 mol% loadings only non-porous / nanoporous materials were produced. Despite re-optimization the **BTESBP**–**γ-MAPS** sol composition at a **γ-MAPS** loading of 10 mol% to yield materials bearing co-continuous structures, no improvements to the degree of monolith adherence to the capillary walls were observed.

The failure of this strategy may be attributed to a variety of different factors. To begin, **V88** is generally intended for use in reactions that proceed at temperatures between ~100–120 °C,[61] but we decided to keep the gelation temperature unchanged from our standard synthetic conditions (i.e. T_{gel} = 60 °C) so as to minimize the extent to which the synthetic protocol would be modified. Although 60 °C is certainly not ideal for initiating the decomposition of **V88**, the formation of a non-negligible population of radical species was still plausible.[62] However, it is also likely that radical initiation proceed to an insufficient extent and that polymerization of the constituent methacrylate groups did not, in fact, proceed to any significant degree to make any difference in the adherence of the monolith to the capillary walls.

Also, in contrast to **BTESBP** (a bridge-bonded bis-silane), **γ-MAPS** is a mono-silylated monomer with a pendant organic functional group. Consequently, the degree of siloxane condensation and crosslinking in this system may be compromised in comparison to the 100% **BTESBP** systems. As our experimentation with **γ-MAPS** incorporation into the capillary PMO monolith synthesis did not lead to dramatic improvements in our materials, this course of action was abandoned for the sake of not wanting to introduce more chemical components (i.e. both **γ-MAPS** and **V88**) into our already complex and sensitive reaction system.[63]

Next, the incorporation of dimethyldiethoxysilane (**DMDES**) (see Scheme 4-9) into the **BTESBP**-based sol was briefly explored as organosilica xerogel materials previously synthesized using **DMDES** have exhibited a certain degree of 'springback' after drying / curing.[64] This ability of the condensed materials to 'springback' to their original, as-synthesized dimensions after drying (while xerogels synthesized from, for example, TEOS shrink irreversibly) is attributed to the flexibility imparted by **DMDES** to the siloxane framework.[64,65] Moreover, the dimethyl substitution of the monomer's central silane adds steric bulk, which prevents the formation of an overly dense and compact siloxane network and allows drying of the xerogel without dramatic collapse of the material.

Similarly to what was previously observed in the case of elevated **γ-MAPS** incorporation, direct incorporation of **DMDES** at 10 and 30 mol% (Si basis) into our standard **BTESBP**-based sol recipe lead to the formation of non-porous / nanoporous capillary monoliths. Encouragingly, this **DMDES-BTESBP** system could be re-

optimized with the addition of a greater amount of F127 to yield capillary monoliths bearing co-continuous structures. Unfortunately, however, the presence of **DMDES** alongside **BTESBP** did not yield materials with improved resistance to monolith shrinkage upon re-exposure to solvent after re-optimization of the sol composition to yield capillary PMO monoliths bearing intact co-continuous structures. To our disappointment, this course of action was also eventually put to an end.[63]

In our final attempts to improve the adherence of the monoliths to the internal capillary walls and increase the degree of siloxane condensation within the organosilica monolith matrix, we decided to: (a) increase the gelation temperature; and (b) use fused silica capillaries with smaller internal diameters. By increasing the gelation temperature, it was expected that siloxane condensation would proceed to a greater extent in the resulting capillary monoliths in comparison to those synthesized at lower temperatures, which could improve the hydrolytic and mechanical stability of the materials. In addition, by decreasing the size of the capillaries used (which essentially act as moulds for monolith formation), it was hypothesized that the tendency for monolith 'pull-away' from the internal capillary walls could be somewhat mitigated because the surface-area-to-volume ratio of this smaller monolith would be slightly higher than that of a larger monolith and would thus allow for a proportionately greater contact area between the as-synthesized monolith and the capillary walls. This would improve monolith adherence to the capillary walls and potentially prevent catastrophic monolith shrinkage. Consequently, the gelation temperature was increased from 60 °C to 80 °C,[66] and fused silica capillaries with 100 μm-ID capillaries were replaced with 50 μm-ID capillaries.

The synthesis of capillary monoliths at 80 °C required yet another re-optimization of the sol composition in order to yield materials with co-continuous structures bearing large pores and a thick organosiloxane skeleton. This was first pursued for 100% **BTESBP** materials. At higher temperatures, the expected increase in the rate of gelation may have been the cause for the observation of only non-porous / nanoporous monoliths produced from sols compositionally optimized for gelation at 60 °C. In the end, more F127 was then added to obtain capillary PMO monoliths with the desired co-continuous structures.

A series of capillaries of different internal diameters (namely 100 μm-, 75 μm-, and 50 μm-ID) were then each charged with a given batch of sol to see if the size of the capillary opening would affect the skeletal structure obtained. Fortunately, within this range of IDs, no significant differences in the structures of the as-synthesized capillary PMO monoliths were identified.

Regrettably, despite all of the above efforts and their apparent promise, these capillary monoliths still did not sufficiently resist monolith shrinkage so as to remain useful for the demonstration of chiral separation by nano-HPLC. It was then decided that an alternative analytical technique for demonstrating chiral recognition and authenticating the application of these capillary PMO monolith materials as effective chromatographic stationary phases was needed.

4.7 Capillary Electrochromatography

An alternative to nano-HPLC for achieving analyte separation is capillary electrochromatography (CEC) – a technique that has increasingly gained popularity in recent years.[67,68] While HPLC requires pressure to drive the flow of the mobile phase through the stationary phase, flow of the mobile phase is driven by a gradient in the electric field present along the length of the column in EC.[67] Since the flow of the mobile phase is no longer pressure-dependent, small particle sizes and long column lengths are theoretically no longer an impediment to achieving both high-efficiency and high-resolution analyte separation in EC. In addition, under conditions of electroosmotic flow (EOF), the analyte is more likely to travel along the length of the column with a plug flow velocity profile, which should, in principle, reduce band broadening of a given solute as it travels along the column and thus improve resolution.[67]

With nano-HPLC, the shrinkage of the capillary monoliths and their associated 'pull-away' from the internal capillary walls introduces a significant amount of void space along the monolith–capillary interface – opening up a path for unrestricted fluid flow that compromises both the ability of these columns to hold any fluid pressure as well as the separation efficiency of the columns. However, with CEC, the presence of such a gap between the monolith body and the capillary walls would be less problematic as the flow of analytes along the column is governed more so by differences in their electrophoretic mobility along the surface of the stationary phase.[67]

Chiral CEC also continues to be an increasingly important tool in chemical, pharmaceutical, clinical, environmental, and agrochemical research and analysis, and we

envision that our chiral organosilica capillary monoliths can potentially serve as effective CSPs for chiral CEC. Notably, there is a high availability of both ionizable silanols on the surface of the PMO monoliths that would allow for EOF of the mobile phase and the analytes along the column. As well, the carbon content within the chiral PMO stationary phase itself is relatively high, which may prove useful for the separation of neutral molecules.[67] Furthermore, in general, most chiral organosilica stationary phases for chromatography have consisted of pendant chiral functionalities that have typically been attached through post-synthetic grafting or co-condensation of the chiral organosilane. However, our materials would be more unique in terms of having chirality embedded within and along the walls of the siloxane framework.

As a preliminary evaluation of chromatographic performance under CEC conditions, a co-continuous, 100% **BTESBP**-based achiral capillary PMO monolith (with 1.8 μm-diameter pores and 0.72 μm-thick skeleton), was synthesized at T_{gel} = 80 °C inside of a 50 μm-ID fused silica capillary (final L ~ 22cm) and fitted into the CEC instrumentation. After a brief conditioning of the monolith with the buffered mobile phase, an equimolar mixture of each of *R,R*- and *S,S*-**3b** (along with thiourea as an EOF marker) was injected into the achiral column. The resulting electrograph may be seen in Figure 4-12 with the data summarized in Table 4-3.

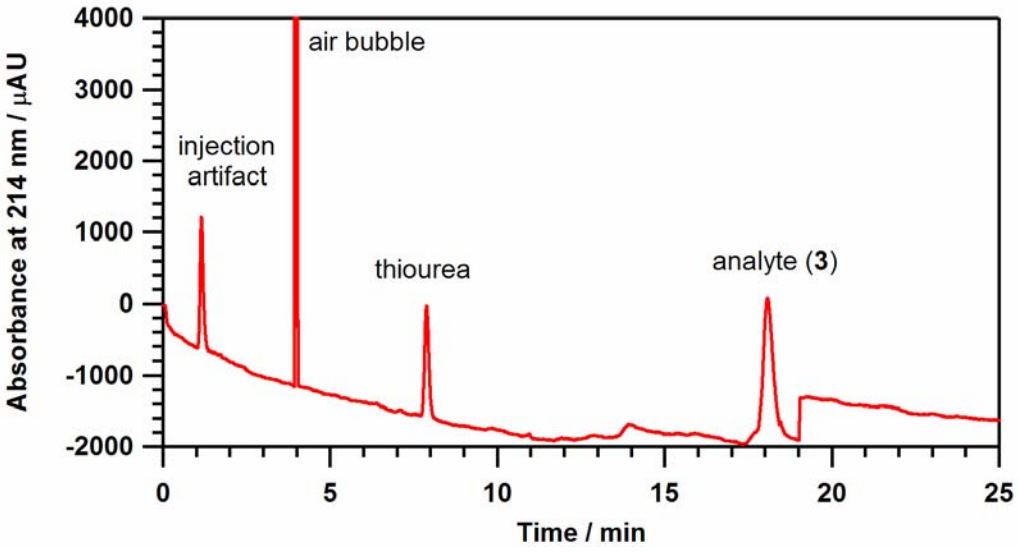

Figure 4-12. CEC electrograph for injection of a racemic mixture of **3b** into a 100% **BTESBP**-based achiral capillary monolith column (thiourea is an EOF marker). (Data courtesy of Dr. Graham Gibson, Queen's University.)

Table 4-2. Summary of CEC data from Figure 4-12 for a 100% **BTESBP**-based achiral monolithic column.

Compound	Elution Time [minutes]	FWHM [minutes]
thiourea (*EOF marker*)	7.9	0.13
rac-**3b**	18.1	0.33

It is evident from the electrograph that both the thiourea (EOF marker) peak and the analyte peak are both very narrow. It is also impressive that the analyte peak width for species **3b** remains very narrow even at extended elution time. Given this data, we

are confident that application of our chiral binaphthyl-functionalized PMO capillary monoliths in CEC will lead to the enantiomeric separation of **3b** with excellent resolution. Optimization of our chiral PMO capillary monoliths for CEC is presently underway.

4.8 Probing Chiral Recognition by Isothermal Titration Microcalorimetry

Chiral chromatography is one method of evaluating chiral interactions between a support and a set of analytes. However, in a different variation, microcalorimetry was briefly pursued in our lab as a means of quantifying the energetic differences in the interactions between chiral analytes and the bulk, powdered, chiral binapthyl-based PMOs originally prepared by Blackburn.

This investigation was inspired by the report of Avnir and co-workers[69] whereby a selection of chiral aluminosilicate zeolites[70] demonstrated enantioselective recognition of D- and L-histidine by isothermal titration microcalorimetry (ITC) as judged by a difference in the magnitude of the heat flow measured following injection of a solution of each of the amino acids into a suspension of the chiral zeolite in buffered aqueous solution (see Figure 4-13) (for a picture and brief description of the experimental set-up, see Scheme 4-10[71] and the accompanying caption). Notably, the authors did not observe any differences in the heat flows for the interaction of D- and L-histidine with MCM-41 (i.e. achiral, ordered mesoporous silica). It was then postulated that a similar study could be conducted using Blackburn's chiral binaphthyl PMOs.

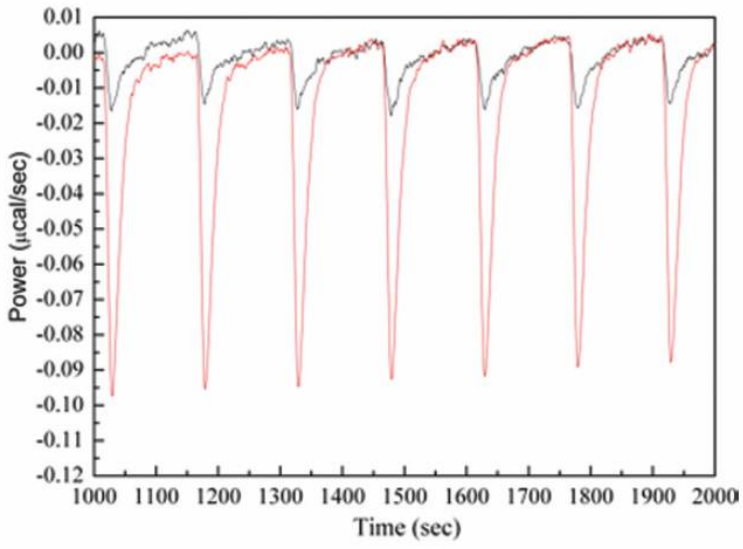

Figure 4-13. VP-ITC traces for adsorption of D- and L-histidine (red and black traces, respectively) onto the chiral zeolite, Goosecreekite, in buffered aqueous media (figure taken from reference 69).

It should be noted that our studies (outlined below) and those of Avnir and co-workers are not analyzed in the way that microcalorimetry studies are typically analyzed. As mentioned previously, we are looking for a difference in the magnitude of the heat flow upon adsorption of an analyte onto a given heterogeneous support. However, microcalorimetry is customarily used in the biological / biochemical sciences to study protein (or enzyme)–analyte binding events.[72] In those instances, significantly larger magnitude energy changes are observed due to the occurrence of higher specificity binding events, as well as additional energy contributions associated with conformational changes undergone by the protein. Furthermore, the 'heat flow (or differential power) versus time' curves (similar in nature to those shown in Figure 4-13) tend to have a

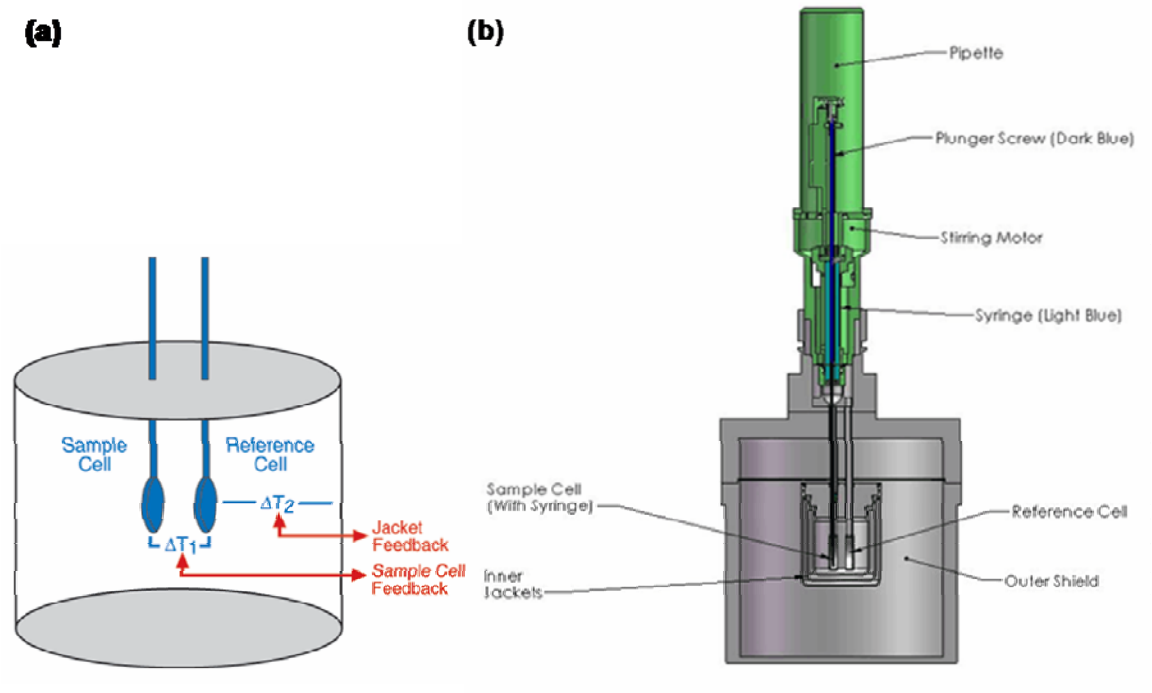

Scheme 4-10. Schematic representation of the MicroCal® VP-ITC instrumental set-up. (a) The system monitors the difference in temperature between the sample cell and the reference cell, as well as the difference in temperature between the reference cell and the surroundings. Power is delivered to or retracted from the sample cell in response to the addition of the syringe reactant (which is usually a solution of the analyte of interest) in order to maintain both the sample cell and the reference cell at the same temperature. (b) The syringe reactant (i.e. a solution of the analyte of interest) is injected into the sample via the action of a stepper motor, and a propeller-style stirrer extends from the syringe into the sample cell medium to promote continuous mixing of the contents of the sample cell. (Both images taken from reference 71.)

distinctive profile[73] from which more information may be gleaned in order to accurately calculate a value for a thermodynamic protein–analyte binding constant. In contrast, the interactions between our chiral organosilica supports and a given analyte are expected to be much weaker. As such, only the magnitude of the heat flow curves may be compared

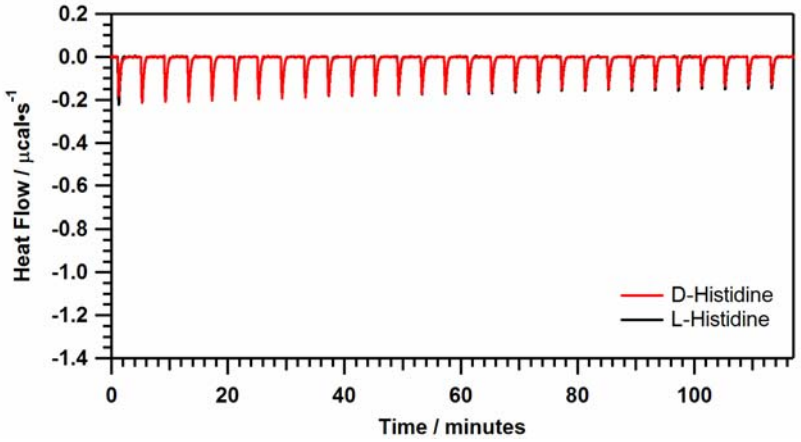

Figure 4-14. VP-ITC control traces for the dilution of D-histidine (red trace) and L-histidine (black trace) (each at an initial concentration of 8 mM in buffered water (pH 7)) into buffered water.

as the occurrence of a distinctive titration curve profile is not anticipated, and thus no binding constants can be genuinely calculated with our materials.

In parallel to the work of Avnir and co-workers,[69] our initial studies were initiated with D- and L-histidine (**HIS**, Scheme 4-11) as the enantiomeric analyte pair. Firstly, the heat flow curves for the dilution of each of D- and L-histidine (8 mM solutions prepared in buffered water (pH 7)) into buffered water were recorded as a control (Figure 4-14). Fittingly, the D- and L-histidine heat flow curves showed exothermic peaks of equal magnitude.[74]

Next, the solutions of D- and L-histidine were individually added to a suspension of 15 wt% *S*-**2** PMO in buffered water (see Table 4-3 for a summary of all of the chiral recognition experiments). Interestingly, the peaks in the VP-ITC trace for L-histidine

appeared to be six times more exothermic than the D-histidine trace (Figure 4-15a, black and red traces, respectively). An analogous pair of experiments was subsequently run involving the addition of solutions of D- and L-histidine to a suspension of 15 wt% *R*-**2** PMO in buffered water. However, to our dismay, the L-histidine interaction still appeared to be more exothermic (also by a factor of six) than the D-histidine interaction (Figure 4-15b, black and red traces, respectively). Presumably, if chiral recognition was to have been observed in these instances, an equal but opposite result[75] would have been anticipated between the two sets of experiments.

Table 4-3. Summary of the isothermal titration microcalorimetry experiments.

Syringe Reactant / Analyte	Cell Reactant	Solvent System
8 mM D-**HIS**	blank	20 mM phosphate buffer (pH = 7)
8 mM L-**HIS**	blank	20 mM phosphate buffer (pH = 7)
8 mM D-**HIS**	15 wt% *R*-**2** PMO	20 mM phosphate buffer (pH = 7)
8 mM L-**HIS**	15 wt% *R*-**2** PMO	20 mM phosphate buffer (pH = 7)
8 mM D-**HIS**	15 wt% *S*-**2** PMO	20 mM phosphate buffer (pH = 7)
8 mM L-**HIS**	15 wt% *S*-**2** PMO	20 mM phosphate buffer (pH = 7)
8 mM D-**HIS**	MCM-41	20 mM phosphate buffer (pH = 7)
8 mM L-**HIS**	MCM-41	20 mM phosphate buffer (pH = 7)
8 mM D-**HIS**	100% **BTESBP** PMO	20 mM phosphate buffer (pH = 7)
8 mM L-**HIS**	100% **BTESBP** PMO	20 mM phosphate buffer (pH = 7)
1.5 mM D-**TYR**	blank	20 mM phosphate buffer (pH = 7)
1.5 mM L-**TYR**	blank	20 mM phosphate buffer (pH = 7)

Table 4-3 (continued). Summary of the isothermal titration microcalorimetry experiments.

Syringe Reactant / Analyte	Cell Reactant	Solvent System
1.5 mM D-**TYR**	MCM-41	20 mM phosphate buffer (pH = 7)
1.5 mM L-**TYR**	MCM-41	20 mM phosphate buffer (pH = 7)
1.5 mM D-**TYR**	100% **BTESBP** PMO	20 mM phosphate buffer (pH = 7)
1.5 mM L-**TYR**	100% **BTESBP** PMO	20 mM phosphate buffer (pH = 7)
1.5 mM D-**TYR**	15 wt% *R*-**2** PMO	20 mM phosphate buffer (pH = 7)
1.5 mM L-**TYR**	15 wt% *R*-**2** PMO	20 mM phosphate buffer (pH = 7)
1.5 mM D-**TYR**	15 wt% *S*-**2** PMO	20 mM phosphate buffer (pH = 7)
1.5 mM L-**TYR**	15 wt% *S*-**2** PMO	20 mM phosphate buffer (pH = 7)
8 mM D-**PHE**	15 wt% *S*-**2** PMO	20 mM phosphate buffer (pH = 7)
8 mM L-**PHE**	15 wt% *S*-**2** PMO	20 mM phosphate buffer (pH = 7)
8 mM D-**TRP**	15 wt% *R*-**2** PMO	20 mM phosphate buffer (pH = 7)
8 mM L-**TRP**	15 wt% *R*-**2** PMO	20 mM phosphate buffer (pH = 7)
2.5 mM (*R,R*)-**3b**	blank	pesticide grade acetonitrile
2.5 mM (*S,S*)-**3b**	blank	pesticide grade acetonitrile
2.5 mM (*R,R*)-**3b**	100% **BTESBP** PMO	pesticide grade acetonitrile
2.5 mM (*S,S*)-**3b**	100% **BTESBP** PMO	pesticide grade acetonitrile
2.5 mM (*R,R*)-**3b**	15 wt% *R*-**2** PMO	pesticide grade acetonitrile
2.5 mM (*S,S*)-**3b**	15 wt% *R*-**2** PMO	pesticide grade acetonitrile
2.5 mM (*R,R*)-**3b**	15 wt% *S*-**2** PMO	pesticide grade acetonitrile
2.5 mM (*S,S*)-**3b**	15 wt% *S*-**2** PMO	pesticide grade acetonitrile
2.5 mM (*R,R*)-**3b**, recryst.	blank	pesticide grade acetonitrile
2.5 mM (*S,S*)-**3b**, recryst.	blank	pesticide grade acetonitrile
2.5 mM (*R,R*)-**3b**, recryst.	15 wt% *R*-**2** PMO	pesticide grade acetonitrile
2.5 mM (*S,S*)-**3b**, recryst.	15 wt% *R*-**2** PMO	pesticide grade acetonitrile
2.5 mM (*R,R*)-**3b**, recryst.	15 wt% *S*-**2** PMO	pesticide grade acetonitrile
2.5 mM (*S,S*)-**3b**, recryst.	15 wt% *S*-**2** PMO	pesticide grade acetonitrile
2.5 mM (*R,R*)-**8**, recryst.	blank	pesticide grade acetonitrile
2.5 mM (*S,S*)-**8**, recryst.	blank	pesticide grade acetonitrile
2.5 mM (*R,R*)-**8**, recryst.	15 wt% *R*-**2** PMO	pesticide grade acetonitrile
2.5 mM (*S,S*)-**8**, recryst.	15 wt% *R*-**2** PMO	pesticide grade acetonitrile
2.5 mM (*R,R*)-**8**, recryst.	15 wt% *S*-**2** PMO	pesticide grade acetonitrile
2.5 mM (*S,S*)-**8**, recryst.	15 wt% *S*-**2** PMO	pesticide grade acetonitrile

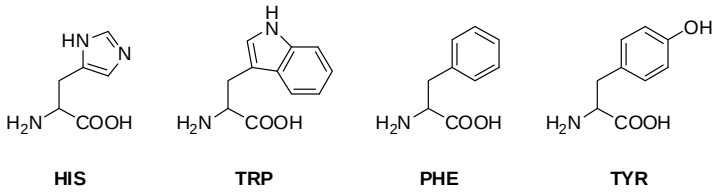

Scheme 4-11. Amino acids used as analytes in the isothermal titration microcalorimetry experiments.

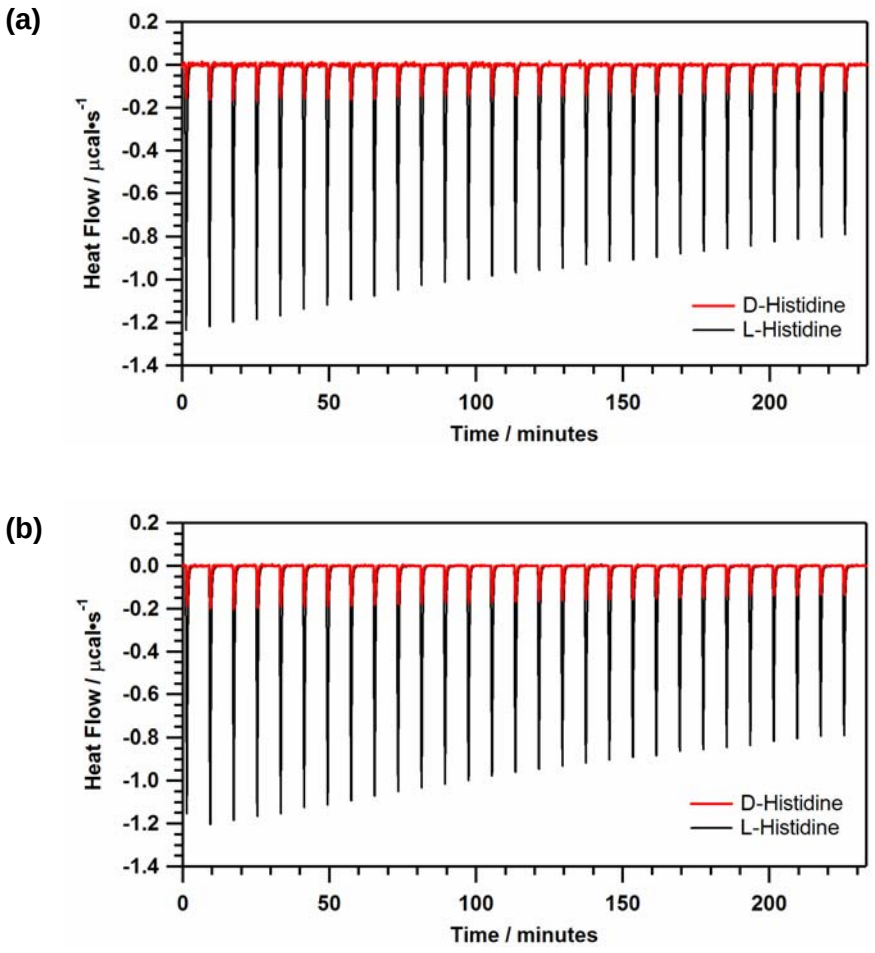

Figure 4-15. VP-ITC traces for the interaction of D- and L-histidine (each at an initial concentration of 8 mM in buffered water (pH 7)) with (a) 15 wt% *S*-**2** PMO, and (b) 15 wt% *R*-**2** PMO (both as solid suspensions in buffered water).

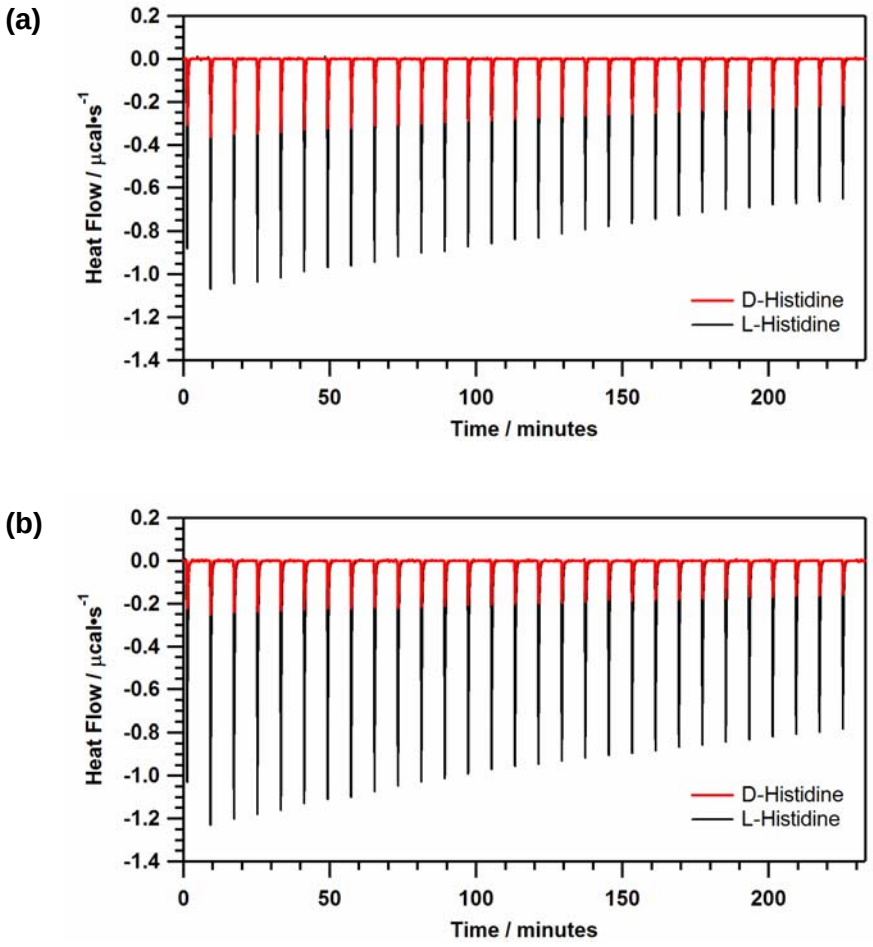

Figure 4-16. VP-ITC traces for the interaction of D- and L-histidine (each at an initial concentration of 8 mM in buffered water (pH 7)) with (a) MCM-41 (mesoporous inorganic silica), and (b) 100% **BTESBP**-based PMO (both as solid suspensions in buffered water).

In an attempt to get a better picture of our amino acid–chiral PMO system, control experiments for the adsorption of D- and L- histidine onto MCM-41 support were conducted. Also, given the more organic and hydrophobic nature of our PMO materials in comparison to a totally inorganic support such as MCM-41, another control experiment was added to our study to see to what degree the nature of our support

materials affected the magnitude of the observed heat flows. Consequently, a 100% biphenylene-based PMO material was synthesized under the same conditions used for the preparation of the related chiral binaphthylene variants and then subjected to microcalorimetry experiments with D- and L-histidine, as well. Surprisingly, differences in the heat flows for that pair of experiments were observed with L-histidine interacting more exothermically than D-histidine with both the MCM-41 and 100% **BTESBP** supports (Figure 4-16, a and b, respectively). At this point, it was evident that something was amiss.

As microcalorimetry is an exceptionally sensitive technique, we postulated that the amino acid samples may not have been pure enough to use in these experiments, and that the presence of a minor amounts of an impurity that had a greater affinity for the silica- and organosilica-based materials relative to the target amino acid would be enough to affect the results. Although these samples appeared pure by NMR spectroscopy, elemental analysis of the solid D- and L-histidine showed that the analytes were indeed impure.[76]

A new set of experiments were then conducted using analytical grade samples of both the D- and L-enantiomers of a new set of amino acids (ones we thought may also interact more strongly with our organosilica supports) (see Table 4-3): (i) tryptophan (**TRP**); (ii) tyrosine (**TYR**); and (iii) phenylalanine (**PHE**). All of the corresponding amino acid solutions (prepared in buffered water (pH 7)) demonstrated nice dilution behaviour. However, disappointingly, upon introduction of the chiral PMOs into the

sample cell, no enantioselectivity was displayed at all (i.e. both D- and L-amino acids interacted with the same energetic magnitude with both *R*- and *S*-**2** PMOs).

Given that the *S*- and *R*-**2** powdered PMOs and PMO capillary monoliths, respectively, had previously displayed a certain degree of chiral recognition with chiral acetal **3b** via the nano-HPLC experiments (Figure 4-2 and Figure 4-11, respectively) *R,R*- and *S,S*-**3b** were subsequently explored as targets for analysis (see Table 4-3). However, the switch to **3b** as the target analyte introduced some new challenges as the aqueous solubility of **3b** was quite poor. Acetonitrile was consequently tested as the solvent for the microcalorimetry experiments as the chromatographic trials were conducted with acetonitrile as the mobile phase modifier.

With the initial experiments using acetonitrile, the VP-ITC traces showed totally erratic and irreproducible behaviour. Over the course of the dilution control experiments for each of *R,R*- and *S,S*-**3b** (each at an initial concentration of 2.5 mM in acetonitrile), the intensities of the heat flow peaks did not trend in any systematic fashion, the peak shapes were constantly changing, and the peaks often did not return to baseline in between injections of the analyte (even despite changing the delay time between injections).

A few hypotheses were developed to account for such anomalous behaviour. Firstly, as titration microcalorimetry is predominantly used for biological / biochemical analyses, which by and large use aqueous solutions as the solvent medium, the instrumentation is not particularly suited for conducting experiments in organic media.

For instance, the differential power feedback[77] that controls the temperature of the sample cell relative to the reference cell may be intimately tuned to, for example, the specific heat capacity of water – which differs significantly from that of acetonitrile (e.g. 4.18 $J \cdot g^{-1} \cdot K^{-1}$ and 2.23 $J \cdot g^{-1} \cdot K^{-1}$, respectively).[78] Adjustments were made to the instrumental settings such that the chosen feedback mode provided a reasonable compromise between response time and sensitivity.

Another potential source for complications in the recording of microcalorimetry data for this acetonitrile-based system was related to the absorption of water by the polar organic solvent. As residual water was likely adsorbed onto the walls of the metal sample cell and reference cell as a result of the manufacturer's prescribed aqueous-based instrument cleaning and pre-equilibration protocols, we speculated that the system could be responding to a 'heat of hydration' of the acetonitrile. A second pre-equilibration step was, therefore, added to the experimental protocol (to essentially 'dehydrate' the sample and reference cells) whereby acetonitrile was injected into a sample cell containing only acetonitrile (alongside an acetonitrile-only reference cell, as well). This pre-equilibration step was repeated until the heat flow peaks appeared to have stabilized, after which point water was deemed to have been removed from the system to an acceptable degree, and the experimental runs could finally start.

With these new procedures in place, reliable and reproducible heat flow curves (now endothermic in nature) were eventually obtained. Upon testing *R,R*- and *S,S*-**3b** with 15 wt% *R*-**2** PMO, it appeared that the *R,R*-**3b** showed a stronger interaction with the chiral PMO support. However, problems with analyte purity plagued us once more as

the testing of *R,R*- and *S,S*-**3b** with 15 wt% *S*-**2** PMO did not reveal the 'switch' in enantioselectivity we were hoping for (i.e. once again, *R,R*-**3b** showed a stronger interaction – even with the PMO of opposite handedness).

We tried to purify our samples of **3b** by recrystallization in methanol, however, analytical purity was never quite obtained. Nonetheless, microcalorimetry experiments were pursued yet again with these new samples to see what might be ascertained from the resulting heat flow curves. With the recrystallized samples of *R,R*- and *S,S*-**3b**, the corresponding dilution curves showed peaks of significantly decreased magnitude (i.e. only slightly endothermic). Furthermore, when subjected to experiments with the chiral PMO supports, no 'switching' in the responses was observed under the conditions of our experiments.

There was a possibility, again, that the minor impurity in the original samples of *R,R*- and *S,S*-**3b** exerted a greater influence on the heat flows observed in our experiments with the chiral supports.[79] It was then decided that the impurity could instead be used as the analyte in the microcalorimetry experiments. If the impurity did indeed interact more strongly with the solid supports – even when present in minor amounts – then experiments that employed the impurity as the target analyte should yield VP-ITC traces of greater heat flow intensities. An added advantage of having greater heat flow peak magnitudes was that a differential interaction between the analyte and the chiral support could be determined with greater confidence.

To obtain **3b** on route to the synthesis of **3a** (see Scheme 4-12), *R,R*- and *S,S*-**7** are derived from the dihydroxylated intermediate, **6**, which may be present in trace amounts in **3b**. Furthermore, **3b** may undergo hydrolysis of its acetal group to again yield a dihydroxylated intermediate. Therefore, we postulated that hydrobenzoin (**8**, Scheme 4-13) could act as possible 'model suspect' as an impurity in the samples of **3b**.

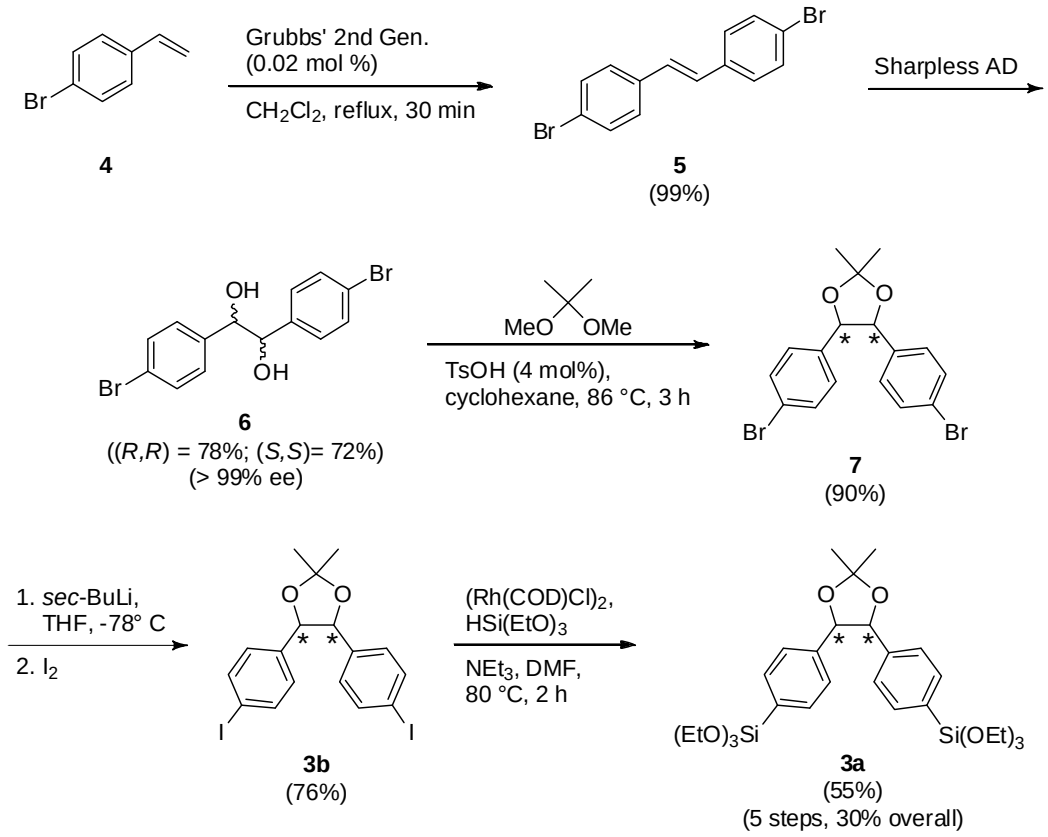

Scheme 4-12. Synthetic route for the preparation of chiral monomer **3a**. (Scheme courtesy of Dr. Steven Dickson, Queen's University.)

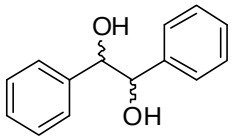

8

Scheme 4-13. Schematic representation of hydrobenzoin.

R,R- and *S,S*-**8** were purchased from a commercial supplier and purified by recystallization with methanol.[80] Solutions of *R,R*- and *S,S*-**8** were then prepared in acetonitrile and subjected to dilution control experiments as well as exposure to both 15 wt% *R*-**2** and 15 wt% *S*-**2** PMO materials (Table 4-3). Once more, the dilution experiments showed nice behaviour, but no enantioselectivity was observed when the analytes were added to a suspension of the chiral supports (i.e. no difference in the magnitudes of the heat flow peaks among any of the combinations of enantiopure **8** and chiral PMOs).

It is certainly possible that the chiral interaction is too weak to be observed under the present conditions of our experimental set-up. However, given the evidence obtained through the chromatography experiments conducted in Section 4.1.2, Section 4.5, and Section 4.7, the manifestation of genuine chiral recognition in these binaphthyl-functionalized PMO materials cannot be ignored. We postulate that although no chiral recognition was observed by microcalorimetry, accumulation of a very small differential interaction between a given analyte and a chiral stationary phase can occur over the

course of a chromatographic run such that macroscopic evidence of chiral recognition may be observed as enantiomeric separation in the case of chromatography.

Despite the disappointing results obtained from this compilation of microcalorimetry experiments conducted to date, we still believe that the experimental conditions may be eventually be optimized (e.g. via choice of analyte, concentrations of the analyte and support in solution, instrumental tuning, and so forth) such that chiral recognition could be observed with surfactant-templated PMO-type systems by this technique. However, careful consideration will have to be given in future experiments to account for the extremely high degree of sensitivity of this technique, and protocols will have to be established that would allow one to collect reliable and meaningful data from such experiments.

4.9 Conclusions and Future Work

In summary, this chapter has explored the synthesis of surfactant-templated periodic mesoporous organosilica materials bearing axially-chiral binaphthylene building blocks. Notably, this work has demonstrated evidence for the manifestation of chiral recognition in the cases of both bulk and monolithic chiral PMO materials.

In an attempt to prepare materials with improved morphology for application to chiral chromatography, chiral PMO capillary monoliths were synthesized and encouragingly showed improvements in chromatographic performance over their bulk, powdered PMO counterparts. In particular, evidence for chiral separation was observed

at 11 wt% loading of the chiral binaphthyl monomer (**2**) in a non-optimized capillary monolith system, whereas chiral separation was only observed at 100% loading of the chiral monomer in the particle-packed capillary columns. Furthermore, we demonstrated the order of elution of the *R,R*- and *S,S*-enantiomers of chiral acetal **3b** switched upon changing the handedness of the chiral stationary phase, which further supports our demonstration of genuine chiral recognition with our materials.

In the case of the application of the PMO capillary monoliths to nano-HPLC, the low hydrolytic stability of the monoliths is still a weak point with these materials. It therefore remains a challenge to optimize these systems for application to chiral nano-HPLC, but such work is ongoing. However, achiral PMO capillary monoliths have been shown to perform exceptionally well under CEC conditions. With the excellent chromatographic performance of the achiral, 100% **BTESBP**-based PMO capillary monolith by CEC (as demonstrated in Section 4.7), we are confident that – with the preparation a chiral PMO capillary monolith bearing co-continuous frameworks of large pore diameters and relatively thick organosiloxane skeletons – chiral separation with full enantiomeric peak resolution can be achieved.

Lastly, although our brief attempts to demonstrate chiral recognition by isothermal titration microcalorimetry have been unsuccessful to date, we are still convinced that the experimental conditions may continue to be modified and optimized such that this phenomenon may be quantified in chiral, surfactant-templated, sol-gel-derived, periodic mesoporous organosilicas.

4.10 Experimental Procedures

4.10.1 Materials

Pluronic® F127 (poly(ethylene oxide)$_{106}$–poly(propylene oxide)$_{70}$–poly(ethylene oxide)$_{106}$), **BTESBP** (4,4'-bis(triethoxysilyl)-1,1'-biphenyl), **γ-MAPS** (γ-methacryloxypropyltrimethoxysilane), **DMDES** (dimethyldiethoxysilane), urea, and Vazo® 88 (**V88**, 1,1′-azobis(cyclohexanecarbonitrile)) (all 'reagent grade') were purchased from Sigma-Aldrich. D-Tyrosine, L-tyrosine, D-phenylalanine, L-phenylalanine, D-tryptophan, and L-tryptophan (all 'BioUltra grade') were also purchased from Sigma-Aldrich. D-Histidine and L-histidine (both 'reagent grade') were purchased from Alfa Aesar. Concentrated $HCl_{(aq)}$, $HNO_{3(aq)}$, and $NH_4OH_{(aq)}$, formic acid, as well as glacial acetic acid, $NaOH_{(s)}$, $KH_2PO_{4(s)}$ (potassium dihydrogen phosphate), $K_2HPO_{4(s)}$ (dipotassium hydrogen phosphate), DMA (dimethylacetamide), acetone, methanol, and acetonitrile (both HPLC grade and pesticide grade) were purchased from Thermo Fisher Scientific. Both 95% ethanol and anhydrous ethanol were purchased from Commercial Alcohols. All of the aforementioned reagents and solvents were used as received without further purification. *R*,*R*-hydrobenzoin and *S*,*S*-hydrobenzoin (both 99% ee) were purchased from Sigma-Aldrich and recrystallized from methanol[80] prior to use. Millipore® deionized water (DI H_2O) was used in all solutions and reaction mixtures. Fused silica capillaries coated with a protective polyimide layer were purchased from Polymicro (with an outer diameter of 363 μm, and an internal diameter of 50, 75, or 100 μm). Thermogreen LB-1 GC Septa (9.5 mm) used to seal the capillary ends were purchased from Supelco.

4.10.2 Synthesis of Chiral Binaphthyl Monomer, 2

The preparation of *rac*-, *R*-, and *S*-**2** followed the procedures previously reported by Tom Blackburn (Queen's University)[21]. Notably, the desired racemate or enantiomer was obtained by starting the series of synthetic steps with the methylation of the corresponding commercially-available racemic or optically pure 2,2'-binaphthol to yield the final, silylated product, **2**, as a viscous, transparent oil.

4.10.3 Synthesis of Chiral Acetal Analyte, 3b

The preparation of *R*,*R*- and *S*,*S*-**3b** (used in both the nano-HPLC and CEC trials) was conducted by Dr. Steve Dickson (Queen's University) and is reported in reference 22.

4.10.4 Fused Silica Capillary Activation

This capillary activation procedure was adapted and optimized from conditions previously reported in the literature,[33] and includes details learned during a one-week stay with the research group of Prof. Kazuki Nakanishi (Kyoto University, Japan) in March 2010. This sequence of treatments is carried out to expose 'fresh' silanol sites on the internal walls of the fused silica capillaries in order to improve monolith attachment to the capillary walls (**NOTE:** *The although the following steps have been conducted with manual introduction of the given solutions into the capillaries, syringe pumps* (Harvard

Apparatus 11plus) *were also occasionally used to execute these steps with equal effectiveness*).

Using a 3 mL-syringe fitted with a syringe-to-capillary adapter, a 1 M $NaOH_{(aq)}$ solution was manually introduced into the capillary (L ~ 40 cm required for CEC columns). Sufficient solution was pushed through so as to allow ~ 3–5 drops of fluid to exit from the other end of the capillary. The capillary was next detached from the syringe and each end of the capillary was pierced partway through a segment of rubber septa to seal / cap the ends. The capillary was then heated at 40 °C for 3 h to etch the internal capillary walls.

After etching with base, the ends of the capillary were freshly cleaved and a 1 M $HCl_{(aq)}$ solution was manually introduced into the capillary. This acidic solution was pushed through the capillary until the droplets exiting the far of the capillary were acidic in nature (pH ~ 1–2) (as verified with pH paper). Thereafter, the ends of that capillary were, again, sealed with rubber septa and then heated at 40 °C for 1 h.

After acid treatment and freshly cleaving the ends of the capillary once more, the capillary was manually flushed with DI H_2O until the droplets of solution exiting the far end of the capillary were of neutral pH (as verified using pH paper).

Finally, the capillary was attached to a $He_{(g)}$ cylinder using the appropriately sized capillary adapter, and the $He_{(g)}$ flow was slowly increased to 80 psig and held for 1–2 minutes to dry the interior of the fused silica capillary.

4.10.5 100% BTESBP Capillary PMO Monolith Preparation (T_{gel} = 60 °C)

This procedure was used to prepare the 'standard', co-continuous 100% **BTESBP** capillary PMO monoliths (i.e. no extra additives such as urea, **γ-MAPS**, or **DMDES** included), and was adapted and optimized from conditions reported by Nakanishi and co-workers.[37]

Pluronic® F127 (0.055 g) was weighed out into a 1-dram (5-mL) vial (**NOTE:** *the mass of F127 was never more than ± 0.5 mg off from the targeted mass as monolith preparation was incredibly sensitive to the F127 content in the starting sol*). DMA (0.40 mL) was then added to the F127. To solubilize the F127, the mixture was briefly heated with a heat gun and then gently, manually swirled to obtain a transparent and homogeneous solution. Next, the mixture was left to stir (at ~ 600 rpm) at room temperature for 30 minutes. 1 M $HNO_{3(aq)}$ (0.025 mL) was then added and the reaction mixture was left to stir for an additional 5 minutes at room temperature. Finally, **BTESBP** (0.100 mL) was added at room temperature and the sol was stirred for 10 more minutes.

To charge the above sol into the activated capillaries (see Appendix 3 for photos of the procedure and set-up), the sol was first transferred into a small GC vial and capped. An unfilled / unactivated capillary (L ~ 10–15 cm) was next attached to a $He_{(g)}$ cylinder (with the appropriate capillary adapter) at one end and pierced into the sol-containing GC vial through the septum of the vial's cap at the other end. One end of the activated capillary was then pierced into the same sol-containing GC vial while the opposite end of the activated capillary was left open to the surrounding atmosphere. The cap was

subsequently unscrewed off of the GC vial and ~ 1 cm of length was trimmed off from the ends of the capillaries that were pushed through the cap of the GC vial to remove any rubber that might have been otherwise trapped in the ends of the capillaries, causing a blockage of fluid flow. The cap was then replaced onto the GC vial and both capillary tips were pushed farther into the vial so as to completely submerge them in the sol.

The pressure of the incoming $He_{(g)}$ was slowly increased to 60 psig and the pressure within the GC vial was allowed to build up – resulting in flow of the sol into the activated capillary. After the appearance / formation of ~ 5 drops of sol at the free end of the activated capillary, the free tip of the capillary was also pierced into the sol-containing GC vial and submerged into the sol. The unactivated capillary that connected the GC vial and the constituent sol to the He(g) cylinder was then pulled out of the cap of GC vial. The GC vial holding the organosilica sol and charged capillary was finally transferred to a Sun Systems EC10 Environmental Chamber (digitally-controlled convection oven) set to 60 °C and left to stand for 24 h (**NOTE:** *the sol gelled within < 15 minutes, but was left in the oven at the prescribed temperature for the full 24 h to age the wet gel and increase the degree of siloxane condensation within the newly formed organosilica network*).

Lastly, the last ~ 1 cm of each end of the filled capillaries was cleaved off to remove any blockages that might be present, and the capillary monoliths were dried at T_{gel} for 24–72 h.

To prepare capillary PMO monoliths at either T_{gel} = 40 °C or 80 °C, the required reagents were used in the quantities outlined in Appendix 4 and the procedural steps followed were the same as outlined above.

4.10.6 Chiral Capillary PMO Monolith Preparation

To obtain a desired mass of chiral (*rac*-, *R*-, or *S*-) monomer, **2**, a given batch of the liquid chiral monomer was solubilized in CH_2Cl_2 and an appropriate aliquot of this solution was transferred to a pre-weighed 1-dram vial. The solvent was removed under reduced pressure (firstly by rotoevaporator, followed by dynamic high-vacuum) and the mass of the transferred monomer was determined and then used to calculate the volume of **BTESBP** required to account for the balance of condensable Si groups present in the reacting sol (**NOTE:** *total moles of 'Si' in any given sol was held constant at* 4.37×10^{-4} *mol*).

Meanwhile, a mixture of F127, DMA and 1 M $HNO_{3(aq)}$ was prepared as outlined above (see Appendix 5 for the desired reagent quantities). However, for the chiral variant of the capillary PMO monoliths, **BTESBP** was first added to the vial of chiral monomer, and the F127-based solution was then transferred to the vial containing the mixture of organosilanes. After 10 minutes of stirring, the sol was finally used to charge the activated capillaries via the aforementioned techniques and allowed to gel, age, and dry at the prescribed temperature.

4.10.7 Post-Synthetic Solution Exposure

In order to introduce either water, acetone, ethanol, a 1 M aqueous urea solution, 1 M $NH_4OH_{(aq)}$ solution, or mixed EtOH / H_2O solutions into an as-synthesized capillary PMO monolith, the capillary of interest was attached to an Upstream nano-HPLC pump with the fluid flow set to a constant rate of 200 $nL \cdot min^{-1}$. As there was usually a significant lag time prior to seeing the appearance of fluid droplets at the exit of the capillary (~ 30–45 minutes), the pump was operated for a total of ~ 2 h to ensure sufficient time for solution exchange to occur within the capillary monolith.

The capillary was then detached from the nano-HPLC pump and sealed at both ends of the capillary with rubber septa (as described in Section 4.9.3) before heating at 80–100 °C for 3–16 h for 1 M $urea_{(aq)}$ or 1 M $NH_4OH_{(aq)}$ exposure, or heating at 60 °C for 12 h for ethanolic solution exposure.

4.10.8 Incorporation of Sol Additives

To incorporate urea in to the starting sol, F127 and DMA were firstly added to a 1-dram vial as described above. Urea was then added to this mixture of F127 and DMA prior to heating and stirring of the mixture (see Appendix 4 for the desired reagent quantities). Afterwards, $HNO_{3(aq)}$ addition, silane addition, capillary charging, and subsequent monolith gelation, and aging proceeded as outlined above. Lastly, urea decomposition to ammonia was conducted by heating the as-synthesized capillary

monolith to 120 °C at a ramp rate of 1 °C·min^{-1} (using a Lindberg / Blue BF51848A programmable oven) and holding at 120 °C for 4 h.

For **γ-MAPS** incorporation, an activated capillary was first silylated with **γ-MAPS** using a procedure based on that previously reported by Oleschuk and co-workers.[60] A 1-mL **γ-MAPS** solution was freshly prepared with each component present in the following volumetric proportion: 20% **γ-MAPS** / 30% glacial acetic acid / 50% DI H_2O. Thereafter, an activated capillary was filled with the **γ-MAPS** solution using $He_{(g)}$ pressure (as described above) and allowed to stand at room temperature for 18 h (with both ends of the capillary pierced into a GC vial and immersed into ~ 0.3 mL of excess **γ-MAPS** solution). Once exposure to the **γ-MAPS** solution was complete, ~ 0.5 cm of length was cleaved off the ends of the capillary to remove any potential blockages, and DI H_2O was manually flushed through the silylated capillary until the liquid droplets exiting the far end of capillary were of neutral pH. Lastly, the silylated capillary was flushed with $He_{(g)}$ (as described above).

Next, to prepare a **γ-MAPS**-containing sol, F127 and **V88** were first solubilized in DMA in a 1-dram vial and subsequently acidified with $HNO_{3(aq)}$ as described above. This F127-based solution was then later added to a mixture of **γ-MAPS** and **BTESBP** prepared in a separate 1-dram vial (see Appendix 5 for the desired reagent quantities). Capillary charging as well as monolith gelation, aging, and drying proceeded as outlined above.

Lastly, to incorporate **DMDES** into the monolith-forming sol, F127 was first solubilized in DMA in a 1-dram vial and subsequently acidified with $HNO_{3(aq)}$ as described above. This F127-based solution was then later added to a mixture of **DMDES** and **BTESBP** prepared in a separate 1-dram vial (see Appendix 5 for the desired reagent quantities). Capillary charging as well as monolith gelation, aging, and drying proceeded as outlined above.

4.10.9 Nano-HPLC and CEC Trials

All of the instrument operation and maintenance, capillary monolith loading and conditioning, analyte loading, as well as cleaning and preparation of the instrument before, during, and after individual runs was carried out by Dr. Graham Gibson of the Oleschuk research group at Queen's University.

Nano-HPLC. Capillary monoliths were conditioned on a Waters NanoAcquity UPLC system to wet and establish flow through the monoliths. Specifically, flow was achieved using a solvent system consisting of 50 vol% HPLC-grade acetonitrile in DI H_2O with 0.1 vol% formic acid at a flow rate of 100 $nL \cdot min^{-1}$.

Typically, the analytes were individually stored as 2 mM stock solutions in HPLC-grade acetonitrile. For sample injection, the analyte solutions were diluted to 20 μM using as much water as possible and injected in 2-μL aliquots. In the case of an injection of a mixture of analytes, each analyte / enantiomer was present at a concentration of 20 μM.

Chromatographic trials were also performed on the same UPLC system without the use of a column heater or trapping column. This UPLC system was coupled via a Teflon® tube union to an Acquity TUV detector with a 10 nL-flowcell, which was set to 214 nm and 254 nm for the chiral acetals (**3b**) and **BINOL**. The flow rate was 600 $nL \cdot min^{-1}$ unless otherwise noted, and the mobile phase consisted of (A) 0.1% formic acid in water and (B) 0.1% formic acid in acetonitrile.

CEC. The capillary monoliths were not directly inserted to the CE cartridge because they were not compatible with the UV absorbance detector. Therefore, the capillary monoliths were cut to ~ 22 cm in length and coupled with a UV-transparent capillary (50 μm-ID) using a Teflon® tube union (i.e. a ~2 cm-long tube with an ID that matches the OD (outer diameter) of the fused silica capillary). The junction was then positioned as close to the detector window of the CE cartridge as possible. The ends of each capillary were then cut to fit the system, leaving the monolith to be ~ 18.3 cm in length.

The capillary monoliths were conditioned on a NanoAcquity UHPLC pump to wet and establish flow through the monoliths. Specifically, flow was achieved using a solvent system consisting of 50 vol% HPLC-grade acetonitrile in DI H_2O with 0.1 vol% formic acid at a flow rate of 100 $nL \cdot min^{-1}$. A buffered solvent mixture (70 vol% ACN / 30 % 1 mM pH 7.2 aqueous potassium phosphate buffer) was then pumped into the capillary assembly using a separate HPLC pump (Lab Alliance Series 1500) with a 500-μL reservoir loop at 1000 psig (controlled pressure) until a droplet formed at the opposite end and no bubbles were observed within the capillary.

Electrochromatographic experiments were performed on a Beckman P / ACE MDQ capillary electrophoresis system with a UV-absorbance diode array detector. Data was acquired and processed with 32 Karat software. The mobile phases, composed of ACN with varying concentrations of phosphate buffer, were filtered before use. Typically, the analytes were individually stored as 2 mM stock solutions in HPLC-grade acetonitrile. For sample injection, the analyte solutions were diluted to 0.4 mM. Sample injection was done electrokinetically (i.e. by EOF with an applied voltage) (usually at 5 kV for 5 s), and separation was obtained with an applied voltage of 10 kV. The non-interacting EOF marker was thiourea at a concentration of 1 mM. All CEC runs were conducted at 25 °C with the aid of coolant in the cartridge.

4.10.10 Microcalorimetry Trials

All of the instrument operation and maintenance, sample loading, cleaning and preparation of the instrument before, during, and after individual runs were carried out by Mr. Kim Munro (Queen's University, Protein Function and Discovery Facility). Moreover, the experimental procedure used in our investigations was adapted from the work of Avnir et al.[69]

Each run on the MicroCal® VP-ITC (isothermal titration calorimeter) required three different components: (i) a 'syringe reactant' (2 mL); (ii) a 'cell reactant' (2 mL); and (iii) a 'blank' solution medium in the reference cell (2 mL). The sequence of experiments and the corresponding conditions used to collect our data are outlined in

Table 4-3. Importantly, each of the amino acid, chiral acetal (**3b**), and hydrobenzoin (**8**) solutions used as the 'syringe reactants' were prepared as stock solutions (in buffered water for the amino acids and pesticide grade acetonitrile for the aromatics) to minimize variability from one run to the next. In addition, when required, the organosilica and silica dispersions used as the 'cell reactants' were prepared by mixing a given support (5.5 mg) with the solution medium of interest (e.g. buffered water or pesticide grade acetonitrile) (4.4 mL). This heterogeneous mixture was then sonicated for 10 minutes before dividing the mixture into two 2-mL portions – one of which would be titrated with, for example, the D-enantiomer of a given amino acid, while the other portion would be reserved for titration with the L-enantiomer of the same amino acid in a subsequent run. Lastly, for the trials involving amino acid analytes, the aqueous solutions were buffered at pH = 7 using a mixture of KH_2PO_4 and K_2HPO_4 at a mass ratio of 1 : 1.77, respectively.

4.10.11 Characterization Methods

Optical micrograph images were obtained on a Nikon Eclipse ME600L microscope. SEM images of gold-coated samples were obtained on a JEOL JSM-840 scanning microscope operated at an accelerating voltage of 20 kV. Solid-state CP MAS NMR spectra were collected on a Bruker Avance 600 MHz spectrometer.

4.11 References

1. (a) Hoffmann, F.; Cornelius, M.; Morell, J.; Fröba, M. *Angew. Chem. Int. Ed.* **2006**, *45*, 3216–3251; (b) Hoffmann, F.; Fröba, M. *Chem. Soc. Rev.* **2011**, *40*, 608–620.

2. Sanchez, C.; Julián, B.; Belleville, P.; Popall, M. *J. Mater. Chem.* **2005**, *15*, 3559–3592.

3. Stein, A.; Melde, B. J.; Schroden, R. C. *Adv. Mater.* **2000**, *12*, 1403–1419.

4. (a) Hatton, B.; Landskron, K.; Whitnall, W.; Perovic, D.; Ozin, G. A. *Acc. Chem. Res.* **2005**, *38*, 305–312; (b) Hunks, W. J.; Ozin, G. A. *J. Mater. Chem.* **2005**, *15*, 3716–3724.

5. Inagaki, S.; Guan, S.; Fukushima, Y.; Ohsuna, T.; Terasaki, O. *J. Am. Chem. Soc.* **1999**, *121*, 9611–9614.

6. Melde, B. J.; Holland, B. T.; Blanford, C. F.; Stein, A. *Chem. Mater.* **1999**, *11*, 3302–3308.

7. Asefa, T.; MacLachlan, M. J.; Coombs, N.; Ozin, G. A. *Nature* **1999**, *402*, 867–871.

8. (a) S. Inagaki, S.; Guan, S.; Ohsuna, T.; Terasaki, O. *Nature* **2002**, *416*, 304–307; (b) Kapoor, M. P.; Yang, Q.; Inagaki, S. *J. Am. Chem. Soc.* **2002**, *124*, 15176–15177.

9. Lemieux, R. P. *Acc. Chem. Res.* **2001**, *34*, 845–853.

10. Eelkema, R.; Feringa, B. L. *Org. Biol. Chem.* **2006**, *4*, 3729–3745.

11. Lemieux, R. P. *Chem. Soc. Rev.* **2007**, *36*, 2033–2045.

12. Pieraccini, S.; Ferrarini, A.; Spada, G. P. *Chirality* **2008**, *20*, 749–759.

13. Noyori, R. *Angew. Chem. Int. Ed.* **2002**, *41*, 2008–2022.

14. Bringmann, G.; Price Mortimer, A. J.; Keller, P. A.; Gresser, M. J.; Garner, J.; Breuning, M. *Angew. Chem. Int. Ed.* **2005**, *44*, 5384–5427.

15. Lämmerhofer, M. *J. Chromatogr. A* **2010**, *1217*, 814–856.

16. Take, for example, the case of cyclodextrins: (a) Takahashi, Keiko. *Chem. Rev.* **1998**, *98*, 2013–2033; (b) Bellia, F.; La Mendola, D.; Pedone, C.; Rizzarelli, E.; Savianoc, M.; Vecchioa, G. *Chem. Soc. Rev.* **2009**, *38*, 2756–2781.

17. Montoya-Pelaez, P. J.; Uh, Y.-S.; Lata, C.; Thompson, M. P.; Lemieux, R. P.; Crudden, C. M. *J. Org. Chem.* **2006**, *71*, 5921–5929.

18. MacQuarrie, S.; Thompson, M. P.; Blanc, A.; Mosey, N. J.; Lemieux, R. P.; Crudden, C. M. *J. Am. Chem. Soc.* **2008**, *130*, 14099–14101.

19. Hayashi, T. *Acc. Chem. Res.* **2000**, *33*, 354–362.

20. Clayden, J.; Greeves, N.; Warren, S.; Wothers, P. *Organic Chemistry*, 1st ed.; Oxford University Press: Oxford, 2001.

21. Blackburn, T. *I. Progress in Directed ortho-Metalation, and II. Generating Chirality in Periodic Mesoporous Organosilica.* M. Sc., Queen's University, Kingston, Canada, September 2009.

22. Dickson, S. E. *Periodic Mesoporous Organosilica: Preparation, Characterization, and Applications of Novel Materials*. Ph. D., Queen's University, Kingston, Canada, March 2011.

23. Three separate trials were conducted involving the injection of: (i) *R,R*-**3b** alone; (ii) *S,S*-**3b** alone; and (iii) an equimolar mixture of *R,R*- and *S,S*-**3b** as the test analyte(s). The reversed phase nano-HPLC trials were run with water as the mobile phase and acetonitrile as the modifier (each with 0.1 vol% formic acid added).

24. *Rac*-ibuprofen and *rac*-**BINOL** were also tested as chiral analytes for Blackburn's packed, 100% *S*-**2** PMO capillary columns. However, no enantiomeric resolution was observed under the nano-HPLC conditions explored.

25. Under isocratic conditions, the *R,R*-**3b** and *S,S*-**3b** peaks (for each species injected individually in two independent runs) were separated by ~ 3.7 minutes, but the peaks were incredibly broad.

26. Skoog, D. A.; West, D. M.; Holler, F. J. *Fundamentals of Analytical Chemistry*, 7th ed.; Saunders College Publishing: Orlando, 1996.

27. Chromedia (Chromatography Knowledge Base) website: http://www.chromedia.org/chromedia?waxtrapp=xqegzCsHqnOxmOlIEcCbC&subNav=wnjedDsHqnOxmOlIEcCzBaF (accessed March 30, 2011)

28. Dr. Kevin McEleney (Queen's University) and Mr. Tom Blackburn had also attempted silylation of these commercial silica beads with their respective chiral silanes, but – in both cases – experienced the same problems as reported by Dr. Steven Dickson.

29. Gibson, G. T. T. Queen's University, Kingston, Canada. Personal communication, May 18, 2010.

30. For reviews, see: (a) Tanaka, N.; Kobayashi, H.; Nakanishi, K.; Minakuchi, H.; Ishizuka, N. *Anal. Chem.* **2001**, *73*, 420A–429A; (b) Cabrera, K. *J. Sep. Sci.* **2004**, *27*, 843–852; (c) Nakanishi, K.; Tanaka, Nobuo. *Acc. Chem. Res.* **2007**, *40*, 863–873.

31. Lubda, D.; Cabrera, K.; Nakanishi, K.; Minakuchi, H. *J. Sol-Gel Sci. Technol.* **2002**, *23*, 185–189.

32. EMD Chemicals Canada website: http://www.emd-chemicals.ca/food-analytics/chromolith-hplc-columns/c_29Sb.s1OGNEAAAEWk39ZAh62?PortalCatalogID=merck4food&CountryName=Canada (accessed February 07, 2011).

33. Motokawa, M.; Kobayashi, H.; Ishizuka, N.; Minakuchi, H.; Nakanishi, K.; Jinnai, H.; Hosoya, K.; Ikegamia, T.; Tanaka, N. *J. Chromatogr. A* **2002**, *961,* 53–63.

34. Nakanishi, K. *J. Porous Mater.* **1997**, *4*, 67–112.

35. (a) Nakanishi, K.; Yamato, T.; Hirao, K. *Mater. Res. Soc. Symp. Proc.* **2002**, *726*, Q9.7.1–6; (b) Nakanishi, K.; Kobayashi, Y.; Amatani, T.; Hirao, K.; Kodaira, T. *Chem. Mater.* **2004**, *16*, 3652–3658; (c) Nakanishi, K.; Kanamori, K. *J. Mater. Chem.* **2005**, *15*, 3776–3786.

36. Hasegawa, G.; Kanamori, K.; Nakanishi, K.; Hanada, T. *J. Mater. Chem.* **2009**, *19*, 7716–7720.

37. Hasegawa, G.; Kanamori, K.; Nakanishi, K.; Hanada, T. *Chem. Mater.* **2010**, *22*, 2541–2547.

38. Through our experience gained in subsequent experiments that involving pumping fluid through the as-synthesized capillary monoliths, monoliths with small pore openings and fine skeletons lead often caused a dramatic build-up of back pressure, and often complete blockage of flow through such monoliths (i.e. no fluid flow even at elevated pressures, P > 4000 psig). On the other hand, flow could be achieved through more open structures at more reasonable pressures (~ 800–2000 psig).

39. Furthermore, increasing the scale of the reaction also lead to irreproducibility in obtaining materials with a co-continuous structure.

40. F127 is not immediately solubilized upon adding DMA. However, with a quick blast of heat while simultaneously swirling the mixture, the F127 dissolves into solution and the mixture remains homogeneous and transparent for the duration of the monolith synthesis.

41. 30 minutes was chosen as the stirring time to allow for the F127 / DMA mixture to equilibrate at room temperature before adding any of the subsequent reagents to the sol.

42. It should be noted that – since hydrolysis and condensation of the organosilane is initiated upon mixing with the aqueous acid present in the sol – the charging of the capillaries is done within a window of 15–20 minutes to minimize variability in the extent of reaction prior to heating the sols in the oven.

43. According to the manufacturer's published specifications with respect to temperature control, the "absolute error (not including the probe error) = ±0.25 °C." See Sun Electronic Systems, Inc. website: http://www.sunelectronics.com/docs/SUMTBL1.pdf (accessed March 21, 2011).

44. With the preparation of a bulk monolith under the same conditions, the corresponding sol-to-gel transition occurs in less than 15 minutes, so the additional

time is allotted for the gelation and aging is specifically to encourage further solidification of the skeletal network through continued siloxane condensation.

45. As reported by Nakanishi and co-workers, **BTESBP**-based bulk monoliths prepared with no or little F127 added to that starting sol yielded only transparent and colorless gels, indicating that macroscopic phase separation had not occurred to any significant extent.

46. 13 wt% **2** corresponds to 10 mol% **2** on a 'Si basis'.

47. Each of *rac*-, *R*-, and *S*-**2** were employed for the various trials.

48. Puy et al. (see: Puy, G.; Demesmay, C.; Rocca, J.-L.; Iapichella, J.; Galarneau, A.; Brunel, D. *Electrophoresis* **2006**, *27*, 3971–3980) reported that water, methanol, and ethanol could be used at room temperature under HPLC flow to remove ~70% of the PEG polymer from capillary monoliths synthesized from TMOS, and that the residual polymer did not appear hamper the subsequent chromatographic performance of the materials. Furthermore, from Chapter 2, acetone was established as a suitable solvent for F127 extraction from surfactant-templated materials (albeit at ~ 80 °C). Thus, these solvents were explored as possible extraction solvents in this PMO capillary monolith work.

49. Brinker, C. J.; Scherer, G. W. *Sol-Gel Science: The Physics and Chemistry of Sol-Gel Processing*, Academic Press: New York, 1990.

50. It should be noted that chiral recognition was observed for Blackburn's bulk 100% *S*-PMO packed into a capillary column, but was never observed for his bulk **BTESBP**-based PMO materials prepared using 15 wt% of **2**. However, despite the poor column efficiencies obtained with our initial chiral PMO capillary monoliths, chiral recognition is encouragingly observed – even at low chiral monomer loading.

51. (a) Minakuchi, H.; Nakanishi, K.; Soga, N.; Ishizuka, N.; Tanaka, N. *J. Chromatogr. A* **1998**, *797*, 121–131; (b) Ishizuka, N.; Minakuchi, H.; Nakanishi, K.; Soga, N.; Nagayama, H.; Hosoya, K.; Tanaka, N. *Anal. Chem.* **2000**, *72*, 1275–1280.

52. Saito, H.; Nakanishi, K.; Hirao, K.; Jinnai, H. *J. Chromatogr. A* **2006**, *1119*, 95–104.

53. Hara, T.; Kobayashi, H.; Ikegami, T.; Nakanishi, K.; Tanaka, N. *Anal. Chem.* **2006**, *78*, 7632–7642.

54. Hasegawa, G. Kyoto University, Kyoto, Japan. Personal communication, October 21, 2009.

55. Colón, L. A.; Li, L. Organo-Silica Hybrid Monolithic Columns for Liquid Chromatography. In *Advances in Chromatography*; Grushka, E.; Grinberg, N. Eds.; M. Dekker: New York, 2008; 46, 391–421.

56. Lubda, D.; Lindner, W.; Quaglia, M.; du Fresne von Hohenesche, C.; Unger, K. K. *J. Chromatogr. A* **2005**, *1083*, 14–22.

57. Cabrera; K.; Kraus, A.; Neuroth, W.; Lubda, D. *Monolithic Sorbents with Fibre-Reinforced Plastic Coating*. US6863820, March 08, 2005.

58. Minakuchi, H.; Nakanishi, K.; Soga, N.; Ishizuka, N.; Tanaka, N. *J. Chromatogr. A*. **1997**, *762*, 135–146.

59. Galarneau, A.; Iapichella, J.; Brunel, D.; Fajula, F.; Bayram-Hahn, Z; Unger, K.; Puy, G.; Demesmay, C.; Rocca, J.-L. *J. Sep. Sci.* **2006**, *29*, 844–855.

60. (a) Gibson, G. T. T.; Koerner, T. B.; Xie, R.; Shah, K.; de Korompay, N.; Oleschuk, R. D. *J. Colloid Interface Sci.* **2008**, *320*, 82–90; (b) Gibson, G. T. T.; Mugo, S. M.; Oleschuk,, R. D. *Polymer* **2008**, *49*, 3084–3090.

61. DuPont website:
http://www2.dupont.com/Vazo/en_US/products/grades/grade_selector.html
(accessed October 13, 2010).

62. From reference 61, the **V88** half-life may be calculated at various temperatures. For $T = 60$ °C, $t_{1/2} = 684$ h and at $T = 80$ °C, $t_{1/2} = 34$ h.

63. To quote from reference 55, page 399:
"One single set of experimental processing conditions does not necessarily apply to the fabrication of two different systems; therefore, it is difficult to have one single

recipe [ ] be applicable to the fabrication of organo-silica monoliths in which the only change would be the alkyl[-substituted] silane. Each particular organo-silica system must be optimized individually in order to obtain desired structures and characteristics that are suitable for LC[. T]his can be a time-consuming task that must be outweighed by the potential benefits of the hybrid system."

64. Constantin, S.; Freitag, R. *J. Sol-Gel Sci. Technol.* **2003**, *28*, 71–80.

65. Kanamori, K.; Aizawa, M.; Nakanishi, K.; Hanada, T. *Adv. Mater.* **2007**, *19*, 1589–1593.

66. By ^{29}Si CP MAS NMR, the T^2 to T^1 peak ratio appeared to have qualitatively increased for the 100% **BTESBP** bulk monolith prepared at 80 °C compared to equivalent monoliths prepared at 60 °C.

67. Cikaloa, M. G.; Bartle, K. D.; Robson, M. M.; Myers, P.; Euerby, M. R. *Analyst* **1998**, *123*, 87R–102R.

68. (a) Preinerstorfer, B.; Lämmerhofer, M. *Electrophoresis* **2007**, *28*, 2527–2565; (b) Lämmerhofer, M.; Gargano, A. *J. Pharm. Biomed. Anal.* **2010**, *53*, 1091–1123.

69. Dryzun, C.; Mastai, Y.; Shvalb, A.; Avnir, D. *J. Mater. Chem.* **2009**, *19*, 2062–2069.

70. The zeolites investigated in reference 70 were chiral in a geometrical sense as opposed to possessing, for example, atom-centered chirality due to non-equivalent

tetra-substitution at a carbon center. The chirality in the zeolites was reported to arise from non-equivalent distortions in the molecular-scale tetrahedral TT'_4 building blocks building blocks of the zeolites (i.e. a $T(–O–T')_4$ unit, where T = Si and T' = Al, and O is omitted from the notation).

71. MicroCal (the manufacturer of the VP-ITC instrument used in these experiments) website: http://www.microcal.com/technology/itc.asp (accessed March 22, 2011).

72. Doyle, M. L. Chapter 20: Quantification of Protein Interactions; Unit 20.4: Titration Microcalorimetry. In *Current Protocols in Protein Science*; John Wiley & Sons, Inc., 1999.

73. The protein-based profiles reflect the gradual saturation of the protein's binding site(s). However, given the fact that our chiral binaphthyl organosilica materials do not have distinct binding sites and that the support–analyte interactions are weak in nature, a 'saturation point' cannot be reliably determined from our data.

74. Dilution curves for a pair of enantiomers (each prepared as solutions of equal concentration) should theoretically show the same behaviour. In the event that the curves are not equivalent, these control runs would then potentially reveal a difference in concentration of each of the analyte solutions or evidence of significant contamination of the sample.

75. For example, if L-histidine interacted more exothermically with the *S*-**2** PMO, then D-histidine would have been expected to interact more exothermically with the *R*-**2**

PMO. However, this was not observed to be the case in this particular set of experiments.

76. For example, by elemental analysis, the theoretical C, H, and N values for **HIS** are 46.4, 5.9, and 27.1 wt%, respectively. The actual values measured for D-**HIS** were 45.3, 5.8, and 27.2 wt%, while the actual values measured for L-**HIS** were 46.4, 6.0, and 27.5 wt%, respectively.

77. VP-ITC MicroCalorimeter User's Manual, MAU130030 Rev. A (Update March 12, 2002), viewed at: http://www.med.yale.edu/wmkeck/biophysics/VP_ITC_MANUAL_11_20_02a.pdf (accessed October 29, 2010).

78. Specific heat capacities converted from the corresponding values for molar heat capacities, which were taken from: *CRC Handbook of Chemistry and Physics,* 91st ed. [electronic edition]; CRC Press: Cleveland, 2011 (accessed February 02, 2011).

79. This was also supported by the fact that upon exposing the 'non-recrystallized' samples of *R,R*- and *S,S*-**3b** to a 100% **BTESBP**-based, unfunctionalized, achiral support, no differences in the heat flow peak magnitudes were observed in the VP-ITC traces.

80. Ikariya, T.; Hashiguchi, S.; Murata, K.; Noyori, R. *Org. Synth.* **2005**, *82*, 10–17; *Org. Synth.* **2009**, *Coll. Vol. 11*, 17–24.

Chapter 5
Conclusions

Over the past two decades, research related to the synthesis and applications of sol-gel-based, ordered silica materials has experienced explosive growth and development. In particular, the versatility of the surfactant-templating strategy has proved to be very powerful as it has allowed scientists to access a rich variety of materials with unique morphologies, as well as structural periodicity at both nano- and macroscopic length scales. Furthermore, the ease with which such a methodology may be modified to form not only silica-based materials – but to also include more exotic metal oxides and a diverse array of organic functionalities – has expanded the tailorability of these types of materials and their extension to applications that are broad in scope.

Although a large proportion of the materials synthesized to date are in powdered or particulate form, film- and monolith-based morphologies are also of important interest to advanced applications in areas such as optical device fabrication, sensing, photovoltaics, and catalysis. This thesis has, therefore, endeavoured to contribute to aspects concerning both the synthesis and applications of films and monoliths on a few different fronts.

In Chapter 2, we examined the synthesis and application of thick, mesoporous organosilica films to a fibre-optic sensing platform for the detection of heavy metal contaminants in solution. The challenges associated with synthesizing thick films by sol-

gel processing and interfacing the materials with the evanescent wave-based sensing element were addressed, and eventually a proof-of-concept sensor was demonstrated whereby sub-ppm level detection of Pb(II) was realized in mixed aqueous–organic solutions. This work also extended to the exploration of hybrid titania-based materials high-index coatings to effectuate heavy metal detection in purely aqueous systems, the study of which is ongoing. In addition, the extension of surfactant-templated organosilica films to other evanescent wave-based devices was initiated. Although presently in their early stages, these investigations will certainly carry on as our understanding of these new device architectures deepens and optimization of both the composition and structure of hybrid sol-gel films is achieved to suit the sensing criteria.

This thesis also addressed the concept of controlling nanostructural order within sol-gel-derived films. In Chapter 3, a bottom-up approach to synthesizing hybrid organosilica-based films with uniaxial alignment of the nanostructure across macroscopic length scales was achieved. Specifically, the interactions between novel, amphiphilic, alkyl-functionalized oligosiloxane precursors and a rubbing-treated polyimide layer were exploited to prepare such films. Furthermore, these films bearing tightly-controlled and highly uniform nanostructures were processed by a simple dip-coating process. As this project continues to evolve, the synthesis of novel amphiphilic, chiral oligosiloxanes should be pursued to a greater degree, as fundamentally interesting structure–property relationships should arise through the self-assembly of such precursors and characterization of their resulting bulk properties. Additionally, given the unique ability to control both the proportion and distribution / placement of inorganic and organic

groups within such materials, oligosiloxanes incorporating unique functionality (e.g. photoactive moieties) and uniform, 'single-crystalline-like' alignment should be designed to create advanced materials for demanding applications.

Finally, Chapter 4 probed the demonstration of chiral recognition in sol-gel derived hybrid organosilica materials that incorporated binaphthylene-based monomers bearing axial chirality. Although our initial attempts at probing such chiral interactions in powdered materials by isothermal titration microcalorimetry were not fruitful, the search for optimized experimental conditions should continue in the future as this technique would provide a very powerful means of quantifying chiral recognition in related sol-gel derived systems.

In related investigations, chiral organosilica capillary monoliths with co-continuous, interconnected pore structures were synthesized and demonstrated chiral recognition via nano-HPLC while requiring less of the chiral dopant in comparison to their powdered counterparts. While the hydrolytic stability of the monolithic materials must be improved to a greater extent in order to improve the chromatographic performance of these materials in nano-HPLC applications, CEC looks to be a very promising avenue for effecting chiral separations using our materials. In this work, CEC has only been demonstrated so far with achiral variants of our capillary monoliths. Extension of this CEC work to the chiral systems is the next step. Once enantiomeric resolution is demonstrated by chiral CEC, future studies should explore the effect of loading of the axially chiral monomer within these monolithic materials to see if chirality transfer within the framework of such materials may be at play, which may then allow for

the achievement of increased enantiomeric separation efficiency using minimal incorporation of the precious chiral dopant. Moreover, the combination of structural chirality and favourable pore networks could also result in interesting advances to fields such as chiral chromatography as well as heterogeneous asymmetric catalysis.

In general, despite all of the advancements that have been made in the field of materials synthesis via surfactant-templated, sol-gel-based strategies, it is evident that several opportunities remain to explore and discover new hybrid, multifunctional, hierarchically-structured materials that would exhibit interesting and useful properties in a variety of different configurations to address many of the evolving needs of our society.

Appendix A

Appendix 1. Table of saturated salt solutions used to control atmospheric relative humidity at various temperatures. (Tables obtained from Chapter 2, reference 75.)

Relative Humidity (%RH)			
Temperature °C	Lithium Chloride	Potassium Acetate	Magnesium Chloride
0	11.23 ± 0.54		33.66 ± 0.33
5	11.26 ± 0.47		33.60 ± 0.28
10	11.29 ± 0.41	23.28 ± 0.53	33.47 ± 0.24
15	11.30 ± 0.35	23.40 ± 0.32	33.30 ± 0.21
20	11.31 ± 0.31	23.11 ± 0.25	33.07 ± 0.18
25	11.30 ± 0.27	22.51 ± 0.32	32.78 ± 0.16
30	11.28 ± 0.24	21.61 ± 0.53	32.44 ± 0.14
35	11.25 ± 0.22		32.05 ± 0.13
40	11.21 ± 0.21		31.60 ± 0.13
45	11.16 ± 0.21		31.10 ± 0.13
50	11.10 ± 0.22		30.54 ± 0.13
55	11.03 ± 0.23		29.93 ± 0.16
60	10.95 ± 0.26		29.26 ± 0.18
65	10.86 ± 0.29		28.54 ± 0.21
70	10.75 ± 0.33		27.77 ± 0.25
75	10.64 ± 0.38		26.94 ± 0.29
80	10.51 ± 0.44		26.05 ± 0.34
85	10.38 ± 0.51		25.11 ± 0.39
90	10.23 ± 0.59		24.12 ± 0.46
95	10.07 ± 0.67		23.07 ± 0.52
100	9.90 ± 0.77		21.97 ± 0.60

Relative Humidity (%RH)						
Temperature °C	Potassium Carbonate	Magnesium Nitrate	Sodium Chloride	Potassium Chloride	Potassium Nitrate	Potassium Sulfate
0	43.13 ± 0.66	60.35 ± 0.55	75.51 ± 0.34	88.61 ± 0.53	96.33 ± 2.9	98.77 ± 1.1
5	43.13 ± 0.50	58.86 ± 0.43	75.65 ± 0.27	87.67 ± 0.45	96.27 ± 2.1	98.48 ± 0.91
10	43.14 ± 0.39	57.36 ± 0.33	75.67 ± 0.22	86.77 ± 0.39	95.96 ± 1.4	98.18 ± 0.76
15	43.15 ± 0.33	55.87 ± 0.27	75.61 ± 0.18	85.92 ± 0.33	95.41 ± 0.96	97.89 ± 0.63
20	43.16 ± 0.33	54.38 ± 0.23	75.47 ± 0.14	85.11 ± 0.29	94.62 ± 0.66	97.59 ± 0.53
25	43.16 ± 0.39	52.89 ± 0.22	75.29 ± 0.12	84.34 ± 0.26	93.58 ± 0.55	97.30 ± 0.45
30	43.17 ± 0.50	51.40 ± 0.24	75.09 ± 0.11	83.62 ± 0.25	92.31 ± 0.60	97.00 ± 0.40
35		49.91 ± 0.29	74.87 ± 0.12	82.95 ± 0.25	90.79 ± 0.83	96.71 ± 0.38
40		48.42 ± 0.37	74.68 ± 0.13	82.32 ± 0.25	89.03 ± 1.2	96.41 ± 0.38
45		46.93 ± 0.47	74.52 ± 0.16	81.74 ± 0.28	87.03 ± 1.8	96.12 ± 0.40
50		45.44 ± 0.60	74.43 ± 0.19	81.20 ± 0.31	84.78 ± 2.5	95.82 ± 0.45
55			74.41 ± 0.24	80.70 ± 0.35		
60			74.50 ± 0.30	80.25 ± 0.41		
65			74.71 ± 0.37	79.85 ± 0.48		
70			75.06 ± 0.45	79.49 ± 0.57		
75			75.58 ± 0.55	79.17 ± 0.66		
80			76.29 ± 0.65	78.90 ± 0.77		
85				78.68 ± 0.89		
90				78.50 ± 1.0		
95						
100						

Appendix 2. Device map for half of a SOI microchip designed and fabricated by NRC, Ottawa. (Figure courtesy of Dr. Dan-Xia Xu, NRC, Ottawa.)

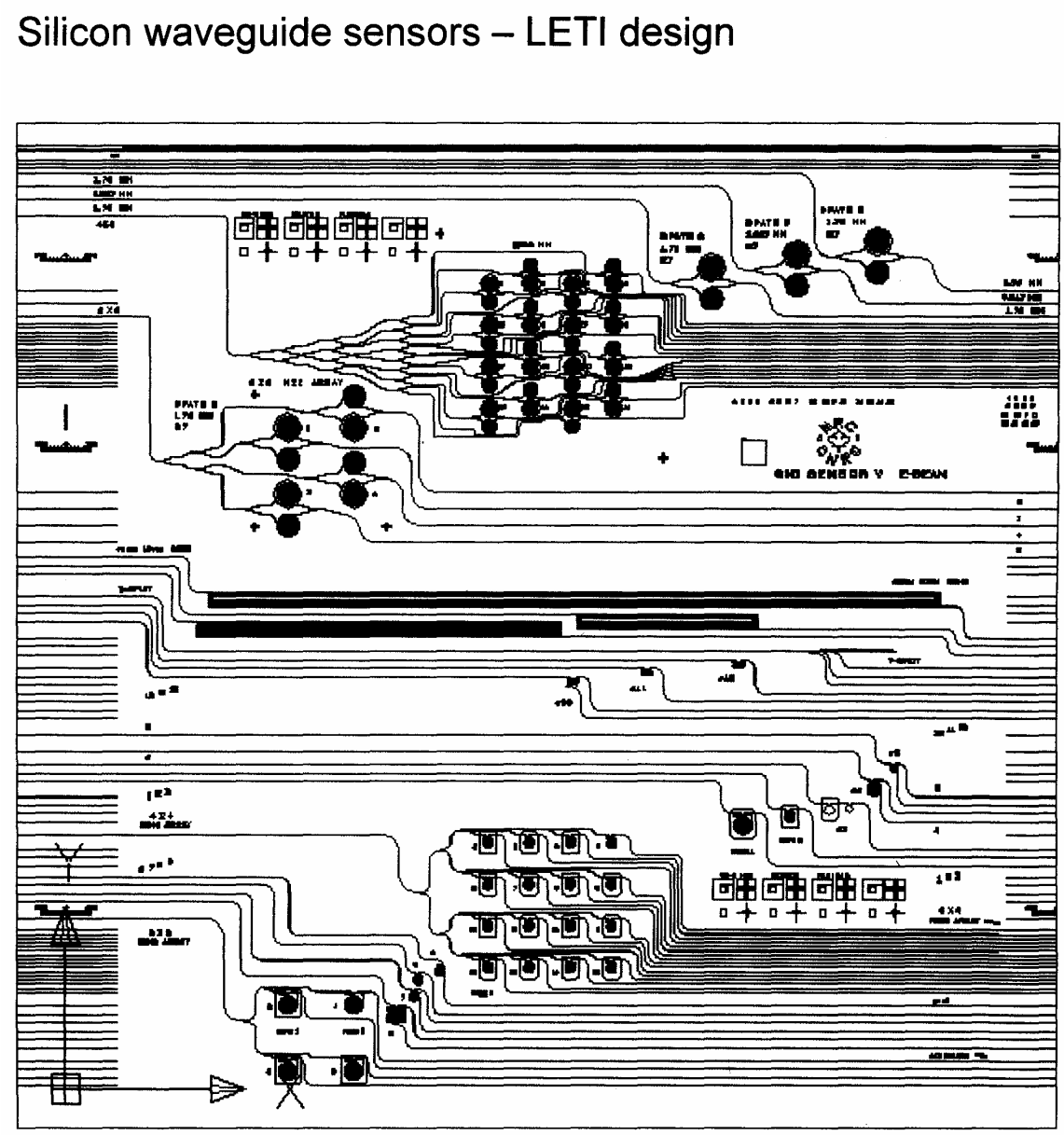

Appendix 3. Photo of the experimental set-up for the charging of activated, fused silica capillaries with monolith-forming sols.

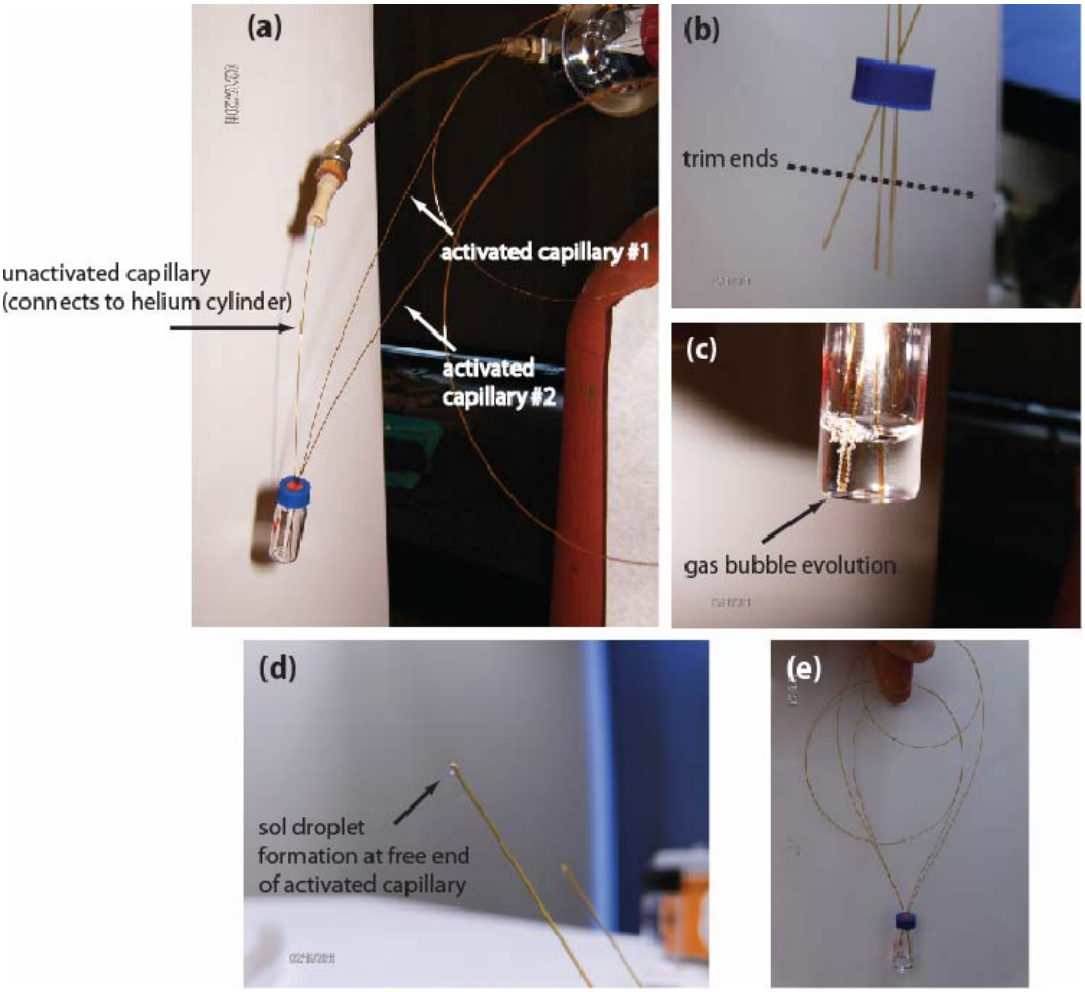

Details:
(a) The unactivated capillary connects the helium cylinder to a GC vial. Two other activated capillaries are also connected (each by only one end) to the same GC vial. (b) The ends of the capillaries that are pierced through the lid of the GC vial are trimmed off to remove any potential blockages. (c) The GC vial is filled with the sol of interest, and the lid is reattached to the vial. All capillary ends are immersed into the sol, and the helium flow to the GC vial is increased. Gas flow is confirmed by the evolution of bubbles in the sol. (d) Wait until the sol travels through the full length of each capillary and droplets may be seen at the open / free end of the capillaries. (e) The free end of each of the activated capillaries is pushed through the lid of the GC vial and immersed into the sol, and the unactivated capillary (which connects the GC vial to the helium cylinder) is pulled out of the GC vial. The GC vial holding the leftover sol and the filled, activated capillaries (with both capillary ends immersed into the remaining sol) is then placed in the oven for gelation.

Appendix 4. Summary of additional achiral PMO capillary monolith syntheses.

T_{gel} [°C]	Vol. of BTESBP [mL][a]	Amount of Additive[a]	Mass of F127 [g][a]	Vol. of DMA [mL][a]	Average Macropore Diameter [μm][b]	Average Skeleton Thickness [μm][b]	Ratio of Pore Size / Skeleton Size	Resultant Structure
40	0.10	N / A	0.055	0.40	4.7	1.4	3.4	isolated macropores
40	0.10	N / A	0.065	0.40	5.5	1.9	2.9	co-continuous (not uniform)
40	0.10	N / A	0.075	0.40	N / A	5.7[c]	N / A	nanoparticulate aggregate
40	0.10	N / A	0.085	0.40	N / A	5.0[c]	N / A	nanoparticulate aggregate
40	0.10	0.0143 g urea	0.100	0.40	3.5	1.2	2.9	co-continuous
80	0.10	N / A	0.040	0.40	N / A	N / A	N / A	non-porous / nanoporous gel
80	0.10	N / A	0.060	0.40	0.81	0.42	1.9	co-continuous
80	0.10	N / A	0.070	0.40	1.8	0.72	2.4	co-continuous
80	0.10	N / A	0.080	0.40	N / A	2.4[c]	N / A	nanoparticulate aggregate

[a] – Quantity of a given reagent used in a sol containing 0.025 mL of 1 M $HNO_{3(aq)}$ as the catalyst for silane hydrolysis and condensation. [b] – Macropore diameter and skeleton thickness each determined as an average of measurements at 6 different points within a cross-sectional SEM image of a given sample. [c] – Average diameter of nanoparticle.

Appendix 5. Summary of additional achiral and chiral PMO capillary monolith syntheses (in all instances, T_{gel} = 60 °C).

Vol. of BTESBP [mL][a]	Amount of Additive[a]	Mass of F127 [g][a]	Vol. of DMA [mL][a]	Avg. Macropore Diameter [μm][b]	Avg. Skeleton Thickness [μm][b]	Ratio of Pore Size / Skeleton Size	Resultant Structure
0.090	0.0142 g *R*-**2** (10 mol% Si)	0.055	0.40	N / A	N / A	N / A	non-porous / nanoporous gel
0.091	0.0126 g *rac*-**2** (9 mol% Si)	0.080	0.40	0.50	0.22	2.3	co-continuous
0.090	0.0139 g *R*-**2** (10 mol% Si)	0.110	0.40	1.7	0.51	3.2	co-continuous
0.090	0.010 mL (10 mol%) **γ-MAPS**[d]	0.060	0.40	N / A	N / A	N / A	non-porous / nanoporous gel
0.090	0.010 mL (10 mol%) **γ-MAPS**[d]	0.090	0.40	3.0	1.0	2.9	co-continuous
0.090	0.010 mL (10 mol%) **γ-MAPS**[d]	0.120	0.40	N / A	2.0[c]	N / A	nanoparticulate aggregate
0.090	0.0075 mL (10 mol%) **DMDES**	0.090	0.40	2.6	0.92	2.8	co-continuous[e]
0.090	0.0075 mL (10 mol%) **DMDES**	0.120	0.40	N / A	1.5[c]	N / A	nanoparticulate aggregate
0.070	0.0225 mL (30 mol%) **DMDES**	0.090	0.40	N / A	N / A	N / A	non-porous / nanoporous gel

[a] – Quantity of a given reagent used in a sol containing 0.025 mL of 1 M $HNO_{3(aq)}$ as the catalyst for silane hydrolysis and condensation. [b] – Macropore diameter and skeleton thickness each determined as an average of measurements at 6 different points within a cross-sectional SEM image of a given sample. [c] – Average diameter of nanoparticle. [d] – Amount of **V88** added = 1 mg. [e] – Borderline nanoparticulate aggregate.